JPL PUBLICATION 82-77

Shuttle Imaging Radar-A (SIR-A) Experiment

J.B. Cimino and C. Elachi
Editors

December 15, 1982

National Aeronautics and
Space Administration

Jet Propulsion Laboratory
California Institute of Technology
Pasadena, California

JPL PUBLICATION 82-77

Shuttle Imaging Radar-A (SIR-A) Experiment

J.B. Cimino and C. Elachi
Editors

December 15, 1982

National Aeronautics and
Space Administration

Jet Propulsion Laboratory
California Institute of Technology
Pasadena, California

The research described in this publication was carried out by the Jet Propulsion Laboratory, California Institute of Technology, under contract with the National Aeronautics and Space Administration.

FOREWORD

This report gives an assessment of the SIR-A system performance during the second Shuttle flight, and some preliminary scientific results. The preliminary scientific results are reported by the SIR-A team members and their collaborators. The sensor performance sections were written by the SIR-A implementation and operations team members, mainly J. Granger (Cognizant Engineer), E. Caro, H. Harris, B. Huneycutt, and S. Wall.

The report was edited by the Principal Investigator, Dr. C. Elachi and the Science Experiments Coordinator, Dr. J. B. Cimino.

ACKNOWLEDGMENT

The success of the SIR-A Experiment is the result of the efforts of many people at JPL who are part of the radar programs. In particular, special credit should be given to the Cognizant Engineer J. Granger and Task Manager G. Sisk. The SIR-A team and particularly the Principal Investigator would like to acknowledge the support of the Office of Earth and Planetary Exploration at NASA Headquarters and its staff, in particular, J. Taranik (Program Scientist), K. Carver, J. Moore, B. Schardt, M. Settle, P. Thome, and J. Welch. Special thanks are given to D. E. Fulton, J. W. Kempton, and M. F. Buehler of the Documentation Section, S. Conrow, A. Holmes, and D. Harrison of the Imaging Radar Geology Group, and B. Trinh and W. Fiechter of the Radar Processing Group, all of whom cooperated closely with the editors throughout the different phases in the preparation of this report.

ABSTRACT

The main objective of the SIR-A Experiment was to acquire radar data over a variety of regions to further our understanding of the radar signatures of various geologic features. A complementary objective was to assess the capability of the Shuttle as a scientific platform for observation of the Earth's resources.

The SIR-A sensor operated nominally and the full data acquisition capacity of the optical recorder was used. The data acquired will allow us to meet all the stated objectives.

CONTENTS

EXECUTIVE SUMMARY ---------- xi

I. INTRODUCTION AND OVERVIEW ---------- 1-1

II. THE SIR-A SYSTEM ---------- 2-1

A. SYSTEM DESCRIPTION ---------- 2-1
B. RESOLUTION ---------- 2-8
C. AZIMUTH ANTENNA PATTERN AND RETURN ECHO PROFILE ---------- 2-11

III. SIR-A HARDWARE PERFORMANCE ---------- 3-1
A. SUMMARY ---------- 3-1
B. PERFORMANCE BY SUBSYSTEM ---------- 3-1
1. Antenna ---------- 3-1
2. Transmitter ---------- 3-1
3. Receiver ---------- 3-3
4. Logic and Control ---------- 3-3
5. Power Converter ---------- 3-3
6. Optical Recorder ---------- 3-3
C. SHUTTLE SYSTEMS ---------- 3-3
1. Power ---------- 3-3
2. Command ---------- 3-4
3. Status Monitors ---------- 3-4
4. Radio-Frequency Interference ---------- 3-4
5. Attitude Stability ---------- 3-4
6. Cooling ---------- 3-4

IV. DATA ANALYSIS ---------- 4-1
A. OVERVIEW (C. Elachi, JPL) ---------- 4-1
B. ANALYSIS OF THE IMAGERY OVER THE EGYPTIAN EASTERN DESERT (T. Dixon, JPL) ---------- 4-2
C. ANALYSIS OF SIR-A AND SEASAT SAR IMAGES OF KENTUCKY-VIRGINIA (J. Ford, JPL) ---------- 4-10
D. VOLCANIC FIELD EAST OF RATON, NEW MEXICO (H. Masursky, U.S.G.S.) ---------- 4-19
E. GEOLOGIC FEATURES NEAR BATTLE MOUNTAIN, NEVADA (H. Masursky, U.S.G.S.) ---------- 4-22
F. X- AND L-BAND IMAGERY ALONG THE MOTAGUA FAULT, EASTERN GUATEMALA: A COMPARISON (L. Dellwig, U. of Kansas) ---------- 4-22
G. COMPARISON OF SIR-A IMAGERY AND AIRCRAFT RADAR IMAGERY, PANAMA (H. MacDonald, U. of Arkansas) ---------- 4-24
H. THE VIRGINIA DALE RING-DIKE COMPLEX: A COMPARISON OF LANDSAT, SEASAT, AND SIR-A IMAGERY (H. MacDonald, U. of Arkansas) ---------- 4-30
I. SEASAT/SIR-A DIGITAL REGISTRATION OVER NORTHEASTERN ALGERIA (Ph. Rebillard, NRC-JPL Research Associate) ---------- 4-35

J. PRELIMINARY EVALUATION OF SIR-A IMAGES OF EASTERN NORTH CAROLINA (M. D. Krohn and N. M. Milton, U.S.G.S.) ---- 4-43
K. DUNES ON SIR-A IMAGES (C. S. Breed, J. F. McCauley, G. G. Schaber, A. S. Walker, and G. L. Berlin U.S.G.S.) ---- 4-52
L. COREGISTRATION OF SIR-A AND SEASAT IMAGES OF THE SAN RAFAEL SWELL AND THE SANTA YNEZ RANGE (D. Evans and J. B. Cimino, JPL) ---- 4-87
1. The San Rafael Swell (Utah) ---- 4-87
2. Santa Ynez Range, Santa Barbara (California) ---- 4-92

V. SIR-A IMAGE EXAMPLES ---- 5-1
A. GEOLOGY ---- 5-3
1. Lu-Liang Shan (China) ---- 5-4
2. Serra Imeri (Venezuela) ---- 5-6
3. Pakaraima and Merume Mountains (Guyana) ---- 5-8
4. Nile River Basin (Egypt) ---- 5-11
5. Hamersley Mountain Range (Western Australia) ---- 5-14
6. Lengguru Fold Belt (Irian Jaya) ---- 5-16
7. Precambrian Outcrop (Western Algeria) ---- 5-19
8. Faulted Area (East Coast of Belize) ---- 5-23
B. HYDROLOGY ---- 5-27
9. Berau River Emptying Into the Celebes Sea (Borneo) ---- 5-28
10. Meta Province (Colombia) ---- 5-30
11. Ilhas Macuapanim and Surrounding Rivers (Central Brazil) ---- 5-33
12. Mississippi Floodplain (Mississippi) ---- 5-36
C. URBAN AND AGRICULTURAL REGIONS ---- 5-39
13. Brasilia (Brazil) ---- 5-41
14. Cultivated Fields in Central New South Wales (Australia) ---- 5-44
15. Villages and Cultivated Fields (China) ---- 5-46
D. OCEANOGRAPHY ---- 5-49
16. Ocean Patterns Off Isla Coiba (Panama) ---- 5-50
17. Internal Waves (Andaman Sea) ---- 5-52
18. Coral Reefs Near Hai Nan Tao and Palawan ---- 5-54
19. Wind Patterns Off Sardinia ---- 5-57
20. Oil Rigs and Vessels (Persian Gulf) ---- 5-60

VI. SIR-A/SMIRR CROSSINGS ---- 6-1

VII. COVERAGE ---- 7-1

REFERENCES ---- 8-1

APPENDIXES
A. SUMMARY OF RADAR PARAMETERS ---- A-1
B. SWATH LOCATIONS ---- B-1

Figures

1-1. SIR-A Coverage ---------- 1-3

2-1. Location of SIR-A System Aboard OSTA-1 Pallet ---------- 2-2

2-2. Functional Diagram for the SIR-A System ---------- 2-3

2-3. SIR-A Timing Diagram ---------- 2-6

2-4. Variation of STC, ESG, Calibration Level, and PRF with Altitude ---------- 2-7

2-5. Dimensions of SIR-A Image Film ---------- 2-9

2-6. SIR-A Signal Film Data ---------- 2-10

2-7. Corner Reflectors Deployed Near Lake Henshaw, California: (a) Location ---------- 2-12

2-7. Corner Reflectors Deployed Near Lake Henshaw, California: (b) SIR-A Image of Reflectors ---------- 2-13

2-8. Strip-Chart Recording of Echo Sample Gate Telemetered Values ---------- 2-14

2-9. SIR-A Data Flow ---------- 2-16

2-10. SIR-A Image of Los Angeles Basin, California ---------- 2-17

2-11. Transfer Curves for Three Segments of the SIR-A System -------- 2-18

3-1. Comparison of Antenna Patterns ---------- 3-2

4-1. SIR-A Image of the Southeastern Desert in Egypt ---------- 4-3

4-2. Lithologic Map of the Southeastern Desert in Egypt ---------- 4-5

4-3. Structural Interpretation of the Radar Image of the Southeastern Desert in Egypt ---------- 4-6

4-4. Lithologic Interpretation of the Radar Image of the Southeastern Desert in Egypt ---------- 4-7

4-5. SIR-A Image of the Appalachian Plateau in Kentucky and Virginia ---------- 4-11

4-6. Digitally Correlated Seasat SAR Images of Kentucky and Virginia ---------- 4-12

4-7. Lineament Map of Appalachians From SIR-A Image ---------- 4-14

4-8. Images of Appalachian Plateau, Kentucky and Virginia ---------- 4-18

4-9. SIR-A Image of Volcanic Field West of Raton, New Mexico ------- 4-20

4-10. Geologic Map of Volcanic Field West of Raton, New Mexico ------ 4-21

4-11. SIR-A Image of Battle Mountain, Nevada ---------- 4-23

4-12. Eastern End of the Motagua Fault Along the Rio Motagua, Guatemala ---------- 4-25

4-13. Schematic Diagram Showing the Manner in Which an Otherwise Concealed Drainage Control is Revealed in a Radar Image ------- 4-26

4-14. Rio Motagua, Guatemala ---------- 4-27

4-15. Darien Province, Panama ---------- 4-28

4-16. Enlargement of Figure 4-15 Imagery ---------- 4-31

4-17. Virginia Dale Ring-Dike Complex: (a) Landsat Imagery (Band 7) ---------- 4-32

4-17. Virginia Dale Ring-Dike Complex: (b) Seasat Imagery ---------- 4-33

4-17. Virginia Dale Ring-Dike Complex: (c) SIR-A Imagery ---------- 4-34

4-18. Seasat SAR and SIR-A Coverage Over Northeastern Algeria ------- 4-36

4-19. Topographic Map of the Chott Merouane and Chott Melrhir Areas (Algeria) ---------- 4-37

4-20. Seasat SAR/SIR-A Digitally Registered Images of Chott Merouane, Chott Melrhir Area, Algeria ---------- 4-39

4-21. Seasat SAR/SIR-A Digital Registration Images at Full Resolution: (a) the Southern Boundary of the Chott Melrhir ---------- 4-40

4-21. Seasat SAR/SIR-A Digital Registration Images at Full Resolution: (b) the Town of Mrhaier ---------- 4-41

4-21. Seasat SAR/SIR-A Digital Registration Images at Full Resolution: (c) the Northern Boundary of the Chott Merouane ---------- 4-42

4-22. Color Image of the Coregistered Data ---------- 4-44

4-23. SIR-A Image of the North Carolina Coastline ---------- 4-46

4-24. Optically-Correlated Seasat Image of the North Carolina Coastline ---------- 4-50

4-25. Taklimakan Shamo, China: (a) SIR-A Image ---------- 4-54

4-25. Taklimakan Shamo, China: (b) Landsat Image ---------- 4-55

4-26. SIR-A Image on Eastern Edge of An Nafud, Saudi Arabia --------- 4-56

4-27. Badan Jaran Shamo, China: (a) SIR-A Image ---------- 4-57

4-27. Badan Jaran Shamo, China: (b) Landsat Image ---------- 4-58

4-28. Badan Jaran Shamo, China: (a) Enlarged SIR-A Image ---------- 4-59

4-28. Badan Jaran Shamo, China: (b) Enlarged Landsat Image --------- 4-60

4-28. Badan Jaran Shamo, China: (c) Enlarged Landsat Image of Snow-Mantled Southwest Edge ---------- 4-61

4-29. Kara Kum Desert, Turkmen, S.S.R.: (a) SIR-A Image ---------- 4-62

4-29. Kara Kum Desert, Turkmen, S.S.R.: (b) Landsat Image ---------- 4-63

4-30. SIR-A Image of Dark Dunes and Bright Interdune Flats in Chad Basin ---------- 4-64

4-31. Grand Erg Occidental, North Africa: (a) SIR-A Image ---------- 4-65

4-31. Grand Erg Occidental, North Africa: (b) Landsat Image -------- 4-66

4-32. SIR-A Image of Mu Us Shadi, China ---------- 4-67

4-33. Kelpin Tagh, China: (a) SIR-A Image ---------- 4-76

4-33. Kelpin Tagh, China: (b) Landsat Image ---------- 4-77

4-34. Lop Nor, China: (a) SIR-A Image ---------- 4-79

4-34. Lop Nor, China: (b) Landsat Image ---------- 4-80

4-35. SIR-A Image of the Great Kavir (West), Iran ---------- 4-81

4-36. SIR-A Image of the Great Kavir (East), Iran ---------- 4-82

4-37. SIR-A Image of Harrat Al Uwayrid ---------- 4-85

4-38. SIR-A Image of Limestone Plateau, Egypt ---------- 4-86

4-39. South San Rafael Swell, Utah: (a) SIR-A Image ---------- 4-88

4-39. South San Rafael Swell, Utah: (b) Geologic Map ---------- 4-89

4-39. South San Rafael Swell, Utah: (c) Seasat SAR Image ---------- 4-90

4-39. South San Rafael Swell, Utah: (d) Coregistered SIR-A and Seasat Images ---------- 4-91

4-40. Santa Ynez Range, Santa Barbara, California:
(a) SIR-A Image ---------- 4-93

4-40. Santa Ynez Range, Santa Barbara, California:
(b) Mosaicked Seasat SAR Image ---------- 4-94

4-40. Santa Ynez Range, Santa Barbara, California:
(c) Coregistered SIR-A and Seasat Images ---------- 4-95

6-1(a). SIR-A/SMIRR Intersecting Swaths — North America ---------- 6-2

6-1(b). SIR-A/SMIRR Intersecting Swaths — Africa ---------- 6-3

6-1(c). SIR-A/SMIRR Intersecting Swaths — Asia ---------- 6-4

7-1. SIR-A Mission Swaths ---------- 7-2

7-2. North America ---------- 7-3

7-3. Central America ---------- 7-4

7-4. South America ---------- 7-5

7-5. Africa ---------- 7-6

7-6. Asia ---------- 7-7

7-7. Indonesia ---------- 7-8

7-8. Australia ---------- 7-9

Tables

1-1. Orbital Geometry ---------- 1-1

1-2. SIR-A Investigators ---------- 1-4

2-1. SIR-A System Characteristics ---------- 2-4

4-1. Directional Trends of Appalachian Lineaments ---------- 4-15

5-1. Image Examples ---------- 5-2

EXECUTIVE SUMMARY

The SIR-A Experiment was successfully conducted during the STS-2 flight of the Space Shuttle Columbia in November 1981. The main objective of the SIR-A Experiment was to acquire radar data over a variety of regions to further our understanding of the radar signatures of various geologic features. A complementary objective was to assess the capability of the Shuttle as a scientific platform for observation of the Earth's resources.

The SIR-A sensor operated nominally and the full data acquisition capacity of the optical recorder was used. Ten million square kilometers were imaged over all continents except Antarctica. The data acquired will allow us to meet the stated objectives. The analysis of the data is ongoing and the results to date are reported here as well as in two papers that will be published shortly (Elachi et al., 1982; McCauley et al., 1982). Some of the key results include: (1) imaging of buried drainage channels in a hyperarid region of Southern Egypt. The channels are buried under sand and are not visible on Landsat images or from the ground; (2) demonstration that many morphologic features in arid regions are better depicted on radar images than Landsat images; (3) verification that the addition of radar data to Landsat data enhances the capability of rock discrimination in the latter; (4) acquisition of radar images over tropical regions that have been rarely imaged by Landsat because of cloud cover; (5) repetitive observations of dynamic ocean phenomena with estimations of the upper limits of their time constants.

Results of the work of an international team of about 40 scientists will be presented at the Spaceborne Imaging Radar Symposium, which will be held at JPL during the week of January 17, 1983.

SECTION I

INTRODUCTION AND OVERVIEW

On November 12, 1981, the Shuttle Columbia flew in space for the second time. It carried the first shuttle-borne scientific payload, Office of Science and Technology Applications - 1 (OSTA-1), selected for remote sensing of land resources, ocean conditions, environmental quality, and meteorological phenomena. A sensor in this payload, the Shuttle Imaging Radar (SIR-A), was a synthetic-aperture imaging radar. One SIR-A Experiment objective was to acquire and analyze radar images of a variety of regions to further our understanding of the use of spaceborne imaging radars for geologic mapping. Another objective was to demonstrate use of the Shuttle as a platform for scientific investigations.

Launch occurred at 9:10 a.m. Houston time. The average altitude achieved by the Shuttle was 259 km and all data were taken in -ZLV (+ZLV is Z-axis local vertical) at a look angle of 47 deg from nadir in a northward direction perpendicular to the ground track of the Shuttle. The orbit was nearly circular with an inclination of about 38 deg. This allowed imaging of areas between latitudes of 40.8°N and 35.6°S. Table 1-1 describes the SIR-A orbital geometry. Appendix B (a summary of which appears in Appendix A) lists the altitude of the Shuttle and the latitudes and longitudes of the center of the ground swath as functions of time in 1-min intervals for each data take. (A "data take" is a unit of radar data one radar swath wide, or about 50 km, whose length depends on the on/off times commanded for that particular imaging period.)

Table 1-1. Orbital Geometry

Parameter	Value
Mean Altitude	259 km (140 nmi)
Altitude Range	255.2 to 265.8 km
Orbital Inclination	38 deg
Orbital Eccentricity	0.0008
Maximum Latitude Imaged	40.83°N
Minimum Latitude Imaged	35.59°S

The SIR-A Experiment was a complete success. The sensor operated as expected and met all of its design goals. All 1100 m of signal film were used and imagery was acquired over a total surface area of about 10 million km^2 (Figure 1-1) with a resolution of slightly better than 40 m. The exact location of the coverage was partially modified from that originally planned because of the shortened mission (from 4 days to 2-1/2 days). However, the updated coverage included examples of all regions of interest, and the data acquired will allow us to meet all the scientific objectives of the experiment.

The Shuttle's capability as a scientific platform and the payload's operational capability were also successfully demonstrated. SIR-A required very tight control of the platform attitude and a fair amount of operational in-flight control. This was made even more critical by the shortened mission and a slightly higher orbit than originally planned. Replanning of the radar configuration and data collection strategy was required in near-real time. These updated commands were generated by the SIR-A Operations Team and uplinked to the Shuttle by the Johnson Space Center Payload Operations Control Center (POCC) Team.

After landing, the signal film was retrieved by JPL personnel at Edwards Air Force Base, flown to JPL, and processed at the SIR-A Data Processing Facility. Eight hours later, processing of the first data take was successfully completed. All the data acquired were processed by the end of March 1982. These data were sent to the National Space Science Data Center (NSSDC) (at Goddard Space Flight Center) and are available to the general scientific community.

The analysis of the SIR-A data is just beginning. The SIR-A Science Team, as well as other investigators, is in the process of analyzing the data, and a SIR-A science report will be published in early 1983 following a SIR-A workshop to be conducted in January 1983. Preliminary results will be published (Elachi et al., 1982; McCauley et al., 1982). Table 1-2 is a list of science investigators who are in the process of analyzing the data as of the date of this publication.

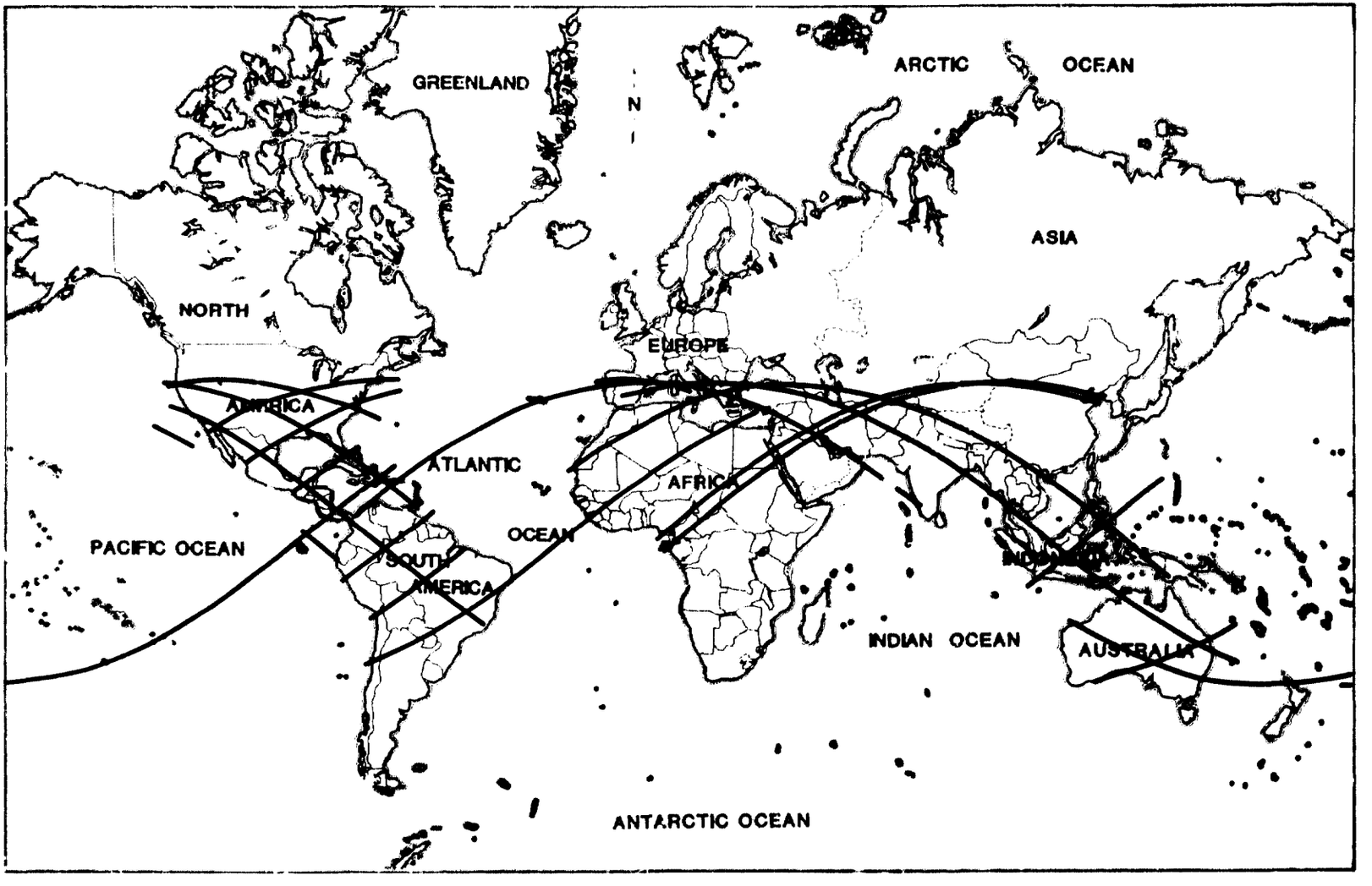

Figure 1-1. SIR-A Coverage

Table 1-2. SIR-A Investigators

Investigator	Affiliation	
L. Berlin	U.S.G.S.	Flagstaff, AZ
R. Blom	JPL	Pasadena, CA
C. Breed	U.S.G.S.	Flagstaff, AZ
C. Brockmann	Purdue University	West LaFayette, IN
W. Brown	JPL	Pasadena, CA
L. Bryan	JPL	Pasadena, CA
J. Cimino	JPL	Pasadena, CA
M. Cole	Bedford College	London, England
L. Dellwig	University of Kansas	Lawrence, KS
T. Dixon	JPL	Pasadena, CA
J. Douglas	Department of Environment & Planning	Hindmarsh, S. Australia
S. Drury	The Open University	Milton Keynes, England
C. Elachi	JPL	Pasadena, CA
F. El-Baz	Smithsonian Institution	Washington, D.C.
D. Evans	JPL	Pasadena, CA
T. Farr	JPL	Pasadena, CA
J. Ford	JPL	Pasadena, CA
P. Francis	Lunar and Planetary Institute	Houston, TX
R. Girdler	University of Newcastle Upon Tyne	Newcastle, England
M. Grolier	U.S.G.S.	Flagstaff, AZ
C. Haynes	University of Arizona	Tucson, AZ
D. Henninger	Johnson Space Center	Houston, TX
F. Honey	CSIRO Western Australia Laboratories	Wembley, Australia
B. Issawi	Egyptian Geological Survey	Cairo, Egypt
B. Koopmans	International Institute for Aerial Survey and Earth Sciences (ITC)	The Netherlands
D. Krohn	U.S.G.S.	Reston, VA
L. Laidet	Groupment pour le Development de la Teledection Aerospatiale	Toulouse, France
K. Lambeck	The Australian National University	Canberra, Australia
D. Lichy	Corps of Engineers	
A. Lind	University of Vermont	Burlington, VT
R. Lyon	Stanford University	Stanford, CA

Table 1-2. SIR-A Investigators (cont'd)

Investigator	Affiliation	
J. McCauley	U.S.G.S.	Flagstaff, AZ
H. MacDonald	University of Arkansas	Fayetteville, AR
D. Mallick	Institute of Geological Sciences	Nottingham, England
P. Martin-Kaye	Hunting Geology and Geophysics, Ltd.	Herts, England
H. Masursky	U.S.G.S.	Flagstaff, AZ
J. Ormsby	Goddard Space Flight Center	Greenbelt, MD
K. Raney	Energy, Mines and Resources Canada	Ontario, Canada
Ph. Rebillard	JPL	Pasadena, CA
F. Sabins	Chevron Oil Field Research Company	La Habra, CA
S. Saunders	JPL	Pasadena, CA
G. Schaber	U.S.G.S.	Flagstaff, AZ
E. Schanda	University of Bern	Bern, Switzerland
J. Taranik	University of Nevada	Reno, NV
F. Ulaby	University of Kansas	Lawrence, KS
A. Walker	U.S.G.S.	Reston, VA
R. Walker	CSR Limited	Sydney, Australia
S. Wu	National Space Technology Laboratories	NSTL Station, MS

This report is published with the following objectives:

(1) To give a brief assessment of the sensor performance.

(2) To provide a description of some of the ongoing scientific investigations.

(3) To give a sample of the type of images acquired.

(4) To provide sufficient data coverage and format information to be of use to investigators.

Section II describes the system and its performance. Section III describes the sensor performance. Section IV gives a brief report on some of the ongoing scientific investigations. Section V contains a broad sample of SIR-A images as illustrations of the available data, and Section VI gives the areas where the Shuttle Multispectral Infrared Radiometer (SMIRR) and SIR-A data are available for complementary analysis.

SECTION II

THE SIR-A SYSTEM

A. SYSTEM DESCRIPTION

The SIR-A Experiment utilized a synthetic-aperture technique to generate a long antenna in the along-track direction. The system consisted of the antenna, the radar sensor, the optical recorder, and the optical processor. The SIR-A system is shown mounted on the OSTA-1 pallet in Figure 2-1. A functional diagram is shown in Figure 2-2. During the mission, the SIR-A Experiment Team provided sensor parameters to the Mission Operations Team. The corresponding commands were then routed through the Shuttle's general purpose computer (GPC) to the SIR-A radar sensor to set up the radar configuration. In a few cases, the Shuttle crew also sent commands to the radar sensor directly through the GPC. Low-rate telemetry information was routed in the opposite direction, and downlinked to the Mission Operations Team for real-time monitoring of the sensor performance. The main characteristics of the SIR-A system are given in Table 2-1.

The radar sensor consisted of the transmitter, receiver, calibrator, and control computer. These were contained in the electronics module, which was coupled to a cold plate and mounted on the pallet deck. The dimensions of the electronics were 1.5 m by 1 m by 25 cm, with a total weight of 136 kg. The transmitter generated a 1-kW frequency-modulated (chirped) RF pulse. The transmitter pulse was centered at 1278 MHz and had a 6.0-MHz bandwidth. The peak power transmitted was 1000 W, and cabling losses between the transmitter and antenna were 0.5 dB. The receiver filtered, range-gated, amplified, and down-converted the return echo to a video signal. The receiver contained a variable-gain amplifier to control the instrument's sensitivity and compensate for the antenna pattern as a means to maintain a relatively constant amplitude in the signal output to the optical recorder. The calibrator generated a controlled-amplitude signal that was fed to the receiver and used to measure the intensity of the echo. The control computer controlled all operating modes for the radar. It contained the sequencer that was made up of a collection of canned sets of parameters. For a given average altitude, a canned set of radar parameters could be accessed with a single command from the ground.

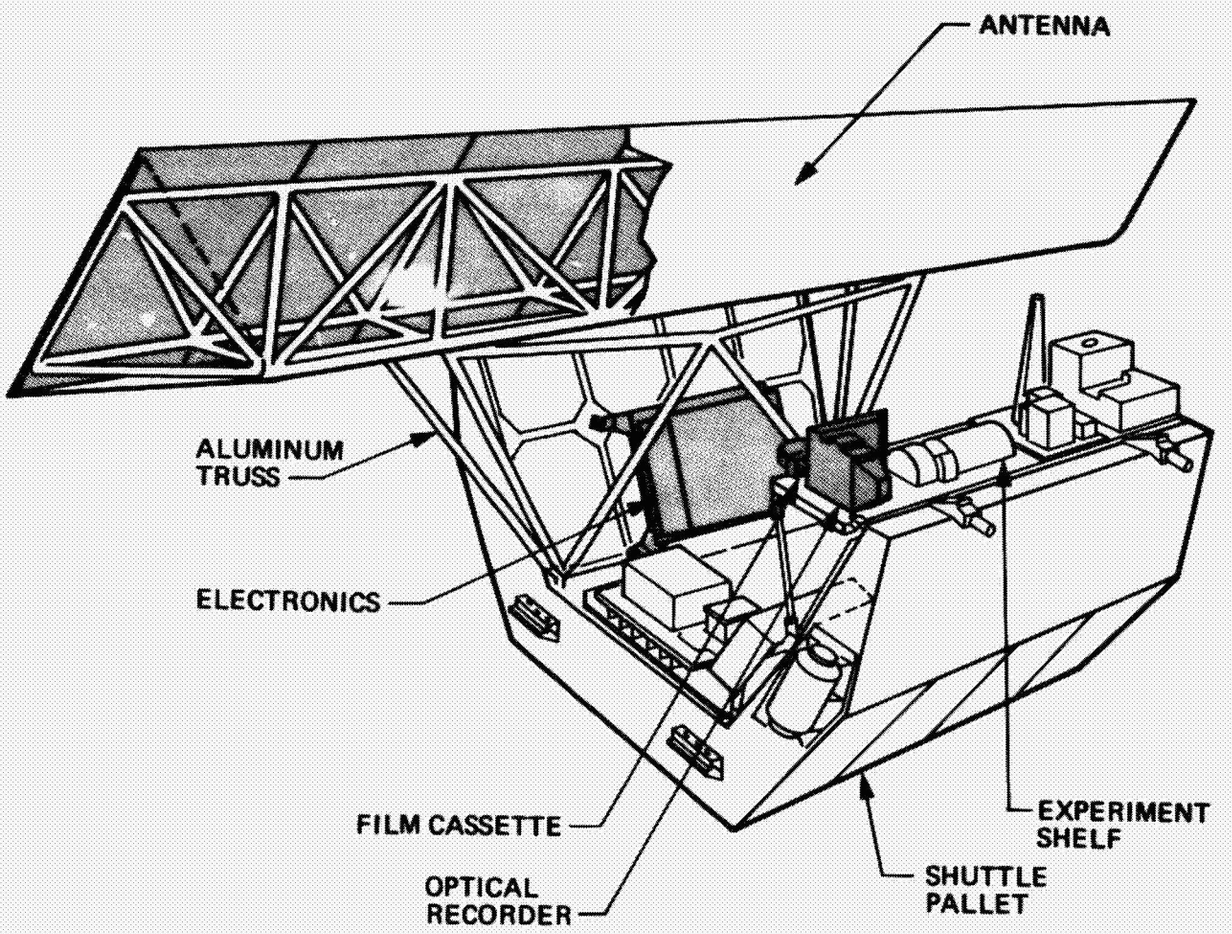

Figure 2-1. Location of SIR-A System Aboard OSTA-1 Pallet. The Antenna, Electronics, and Optical Recorder are Part of the SIR-A System

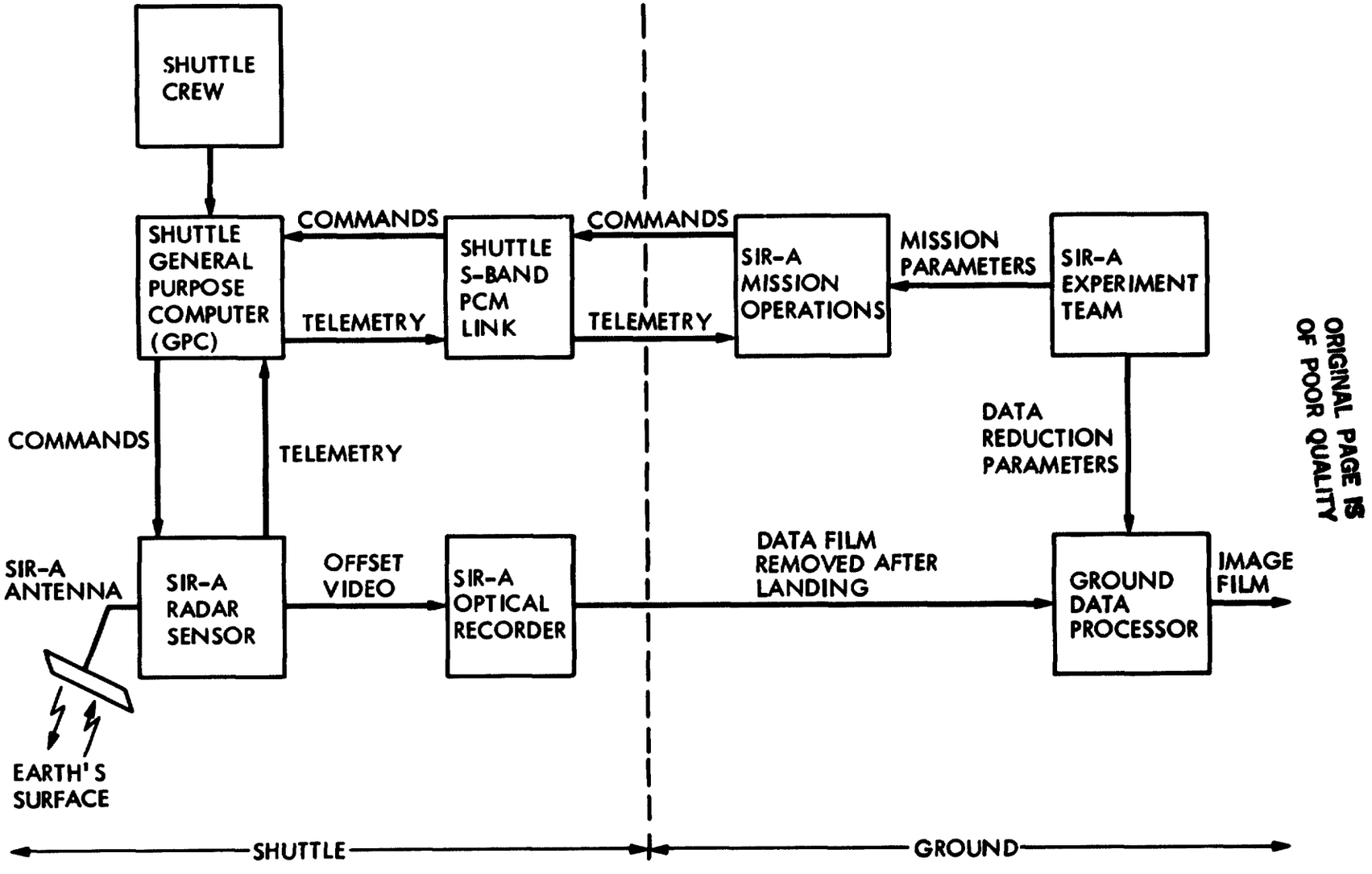

Figure 2-2. Functional Diagram for the SIR-A System

Table 2-1. SIR-A System Characteristics

Subsystem Element	Characteristic	Value
Orbit	Average Altitude	259 km
	Inclination	38 deg
Antenna and Pointing	Antenna Dimensions	9.4 × 2.16 m
	Antenna Gain	33.8 dB
	Polarization	HH
	Look Angle	47 deg
	Attitude Uncertainty (3σ)	±2 deg
Radar Sensor	Center RF Frequency	1278.3 MHz
	Transmit Pulse Width	30.4 μs
	RF Bandwidth	6 MHz
	Radar Transmitter Peak Power	1000 W
	Pulse Repetition Frequency	1464 to 1824 Hz
	Radar Receiver Gain	80 to 101 dB
	Sensitivity Time Control Range	5 dB
	Range Offset Frequency	0.6 MHz
Optical Recorder	Linear Dynamic Range	12 dB
	Range Bandwidth	36 cycles/mm
	Azimuth Bandwidth	26 cycles/mm
	Record Window Width	272 μs
Ground Processor	Processor Bandwidth	1300 Hz
	Azimuth Looks	6 to 8

For a given altitude and look angle, the round-trip delay time delay from transmission to reception varies; therefore, timing considerations were very important. Figure 2-3 is a timing diagram showing the various parameters that must be changed as altitude changes. The pulse rate frequency (PRF) was set to prevent the instrument from transmitting while signals were being received. PRF values used for each data take are listed in Appendix A. The transmitted pulse length was 30.4 μs, thus setting the interpulse period (IPP) at (t - 30.4) μs, where t is the inverse of the PRF or the time between transmit events. This time, t, was divided into 64 parts such that each of the 64 divisions was t/64 μs long. These are the sensitivity time control (STC) positions. The STC was triggered at one of the 64 positions such that a V-shaped waveform 290 μs in length was produced in the receiver, which coarsely compensated for the antenna gain pattern in range. When the STC was on during a data take, the gain was increased by about 5 dB to compensate for the attenuation by the STC. STC position and receiver gain were also controllable from the ground. Values for each data take are listed in Appendix A. Figure 2-4 shows how the STC, echo sample gate (ESG), and PRF vary as a function of altitude.

The data output from the SIR-A electronics was recorded on the optical recorder, which was a modified spare from the Apollo 17 Lunar Sounder Experiment. The recorder dimensions were 60 by 60 by 50 cm; it weighed 68 kg and contained 1100 m of signal film (8 h). The intensity of the echoes controlled the brightness of a spot tracing a line across a CRT. An overlapping succession of these lines was recorded on a strip of signal film moving past the CRT at a rate proportional to the speed of the Shuttle. Thus the terrain echo was recorded on the signal film with the cross-track dimension across the width of the film and the along-track dimension along the length of the film.

The exposed signal film can be regarded as a radar hologram. Once back on the ground, the film was processed in an optical correlator at JPL. Using a coherent light source, a cylindrical lens was used to bring the cross-track direction in focus and in line with the along-track direction. A conical lens was used to correct for tilt resulting from the oblique angle of the side-looking radar. In the range direction, one look was used, and in the azimuth direction, eight looks were used. Finally, the light was trained on the image film to create a two-dimensional image.

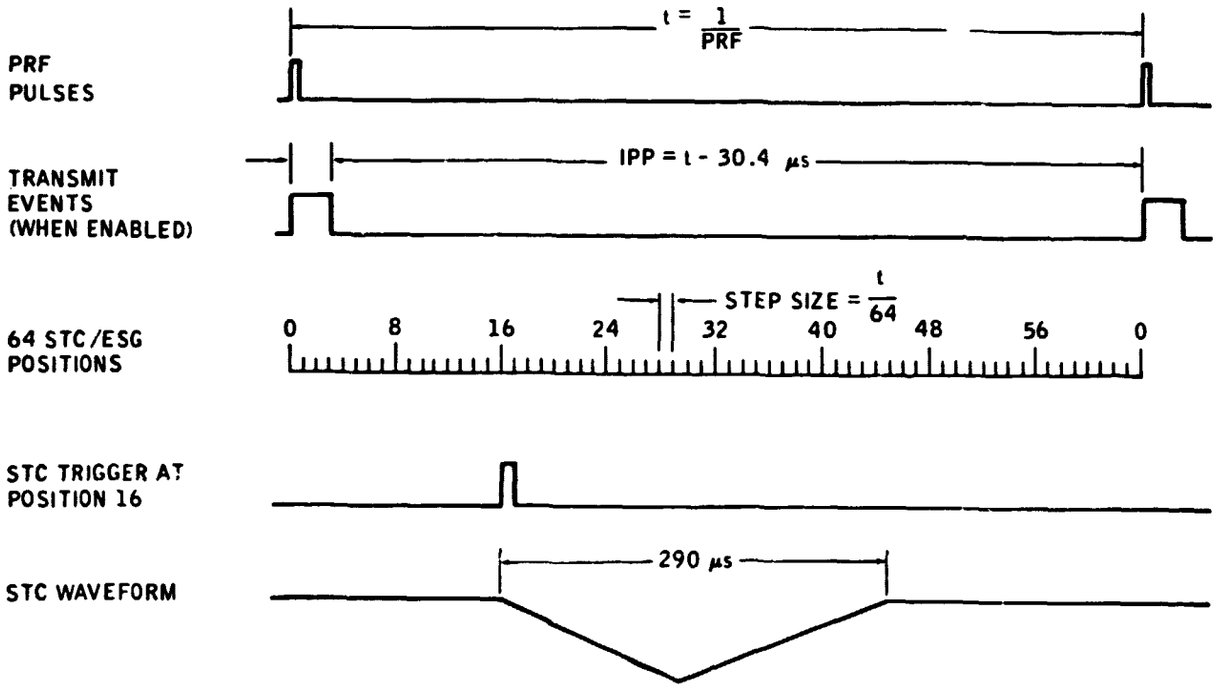

Figure 2-3. SIR-A Timing Diagram

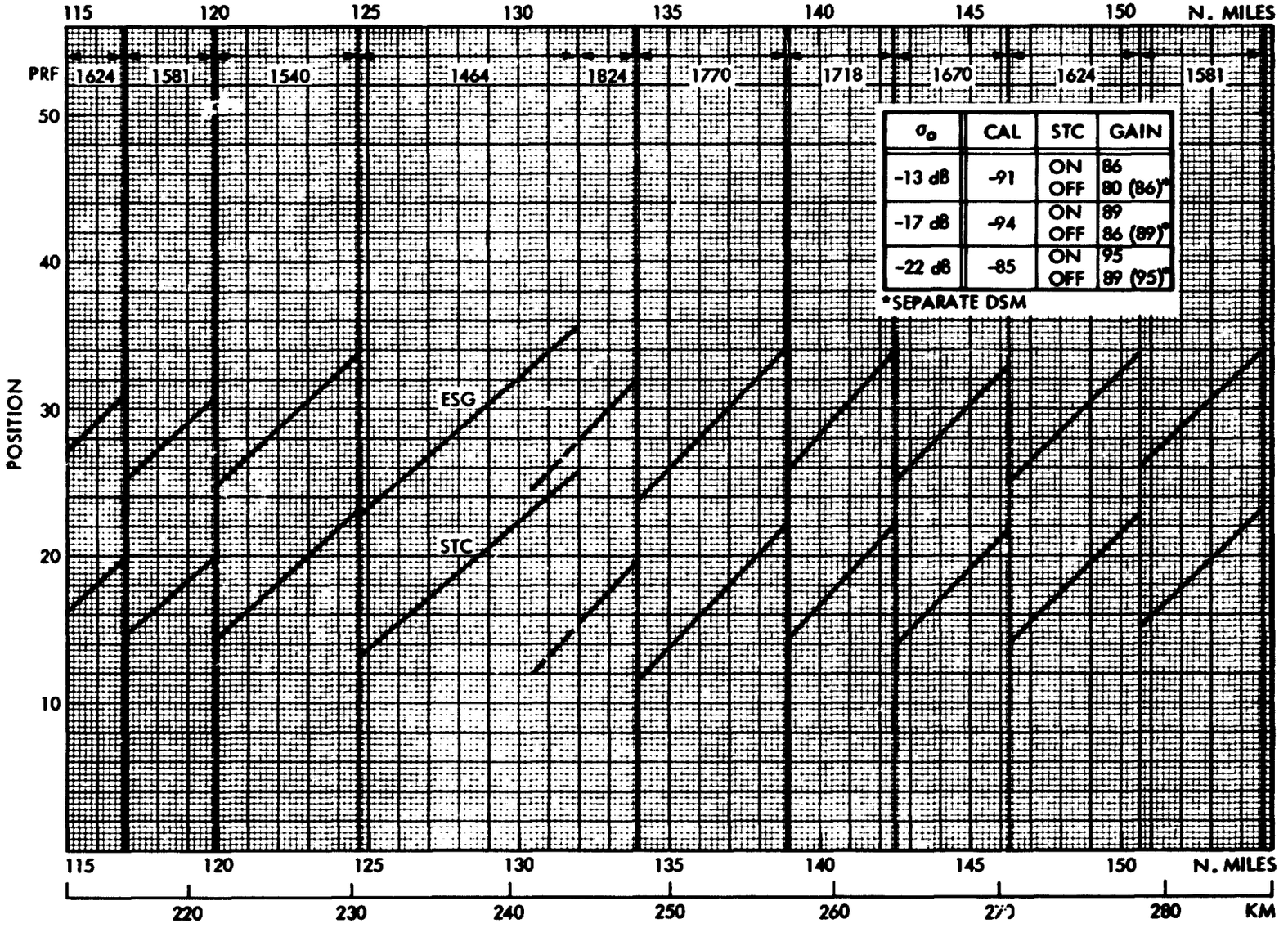

Figure 2-4. Variation of STC, ESG, Calibration Level, and PRF with Altitude

Figure 2-5 shows the dimensions of the SIR-A image film and the time interval between the tick marks. The tick marks are always on the southward edge of the film. The resolution of the image is slightly better than 40 m. The look angle varies from 50 deg at the northward edge of the film to 44 deg at the southward edge (including Earth-curvature effects). The scale of the image is 1:500,000. An image is identified by data-take number and geographic location.

B. RESOLUTION

The SIR-A synthetic-aperture radar system presents a maplike representation of the radar backscatter from the Earth's surface. One important performance parameter of the radar imaging system is its resolving capability. Fine resolution in the along-track direction is accomplished using a synthetic-aperture technique, whereby the amplitude and phase of successive returns are used to synthetically generate a long antenna (Elachi, 1980). For a given point target on the surface, successive returns along the synthetic aperture are Doppler shifted in frequency. As the radar moves along a linear trajectory, the returns yield a signal that is frequency modulated in azimuth; the signal is recorded on signal film. This film is then processed in the optical correlator to produce the final image. Fine resolution in the crosstrack direction is accomplished by using a short-pulse technique and time gating the returns. A pulse compression technique, in which the transmitted pulse is linearly swept in frequency, was used to yield a signal that is linearly modulated and frequency modulated in range.

The system's resolution can be characterized by the frequency content of the raw data recorded on the signal film and by the width of the point-spread function[1] on the image film. This resolution was determined using a corner reflector array deployed in the Lake Henshaw area of California; the array was imaged in data take (DT) 24C. The corresponding areas on the signal and image film were scanned using a microdensitometer, recorded digitally and analyzed both for frequency content (signal film) and point-spread response (image film). Figure 2-6 shows the frequency transform both in azimuth (a) and range (b) of the signal-film

[1]The signal film's frequency content determines the system resolution of a properly focused correlator. The width of the point target response on image film relates to the system resolution actually accomplished for that particular correlation.

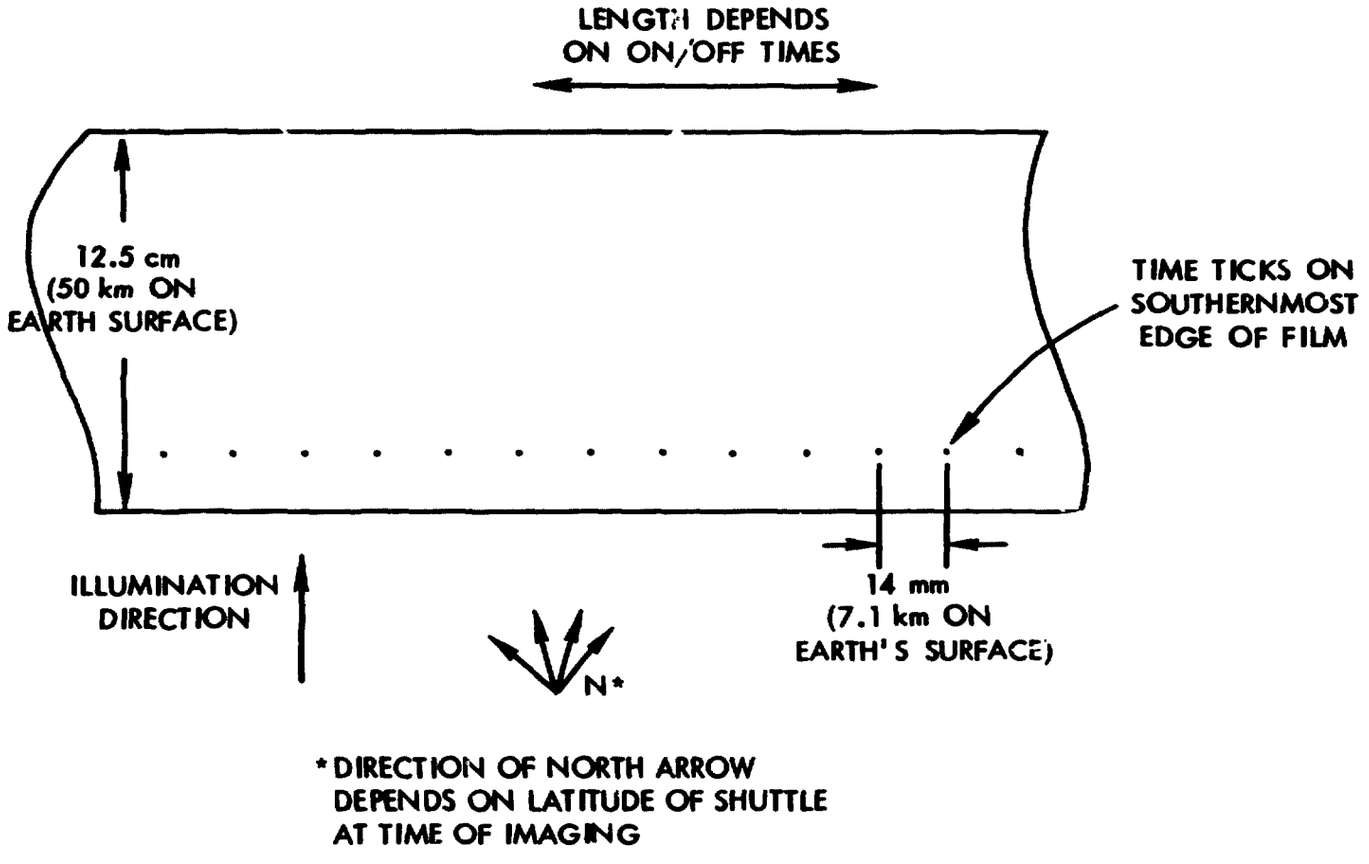

Figure 2-5. Dimensions of SIR-A Image Film

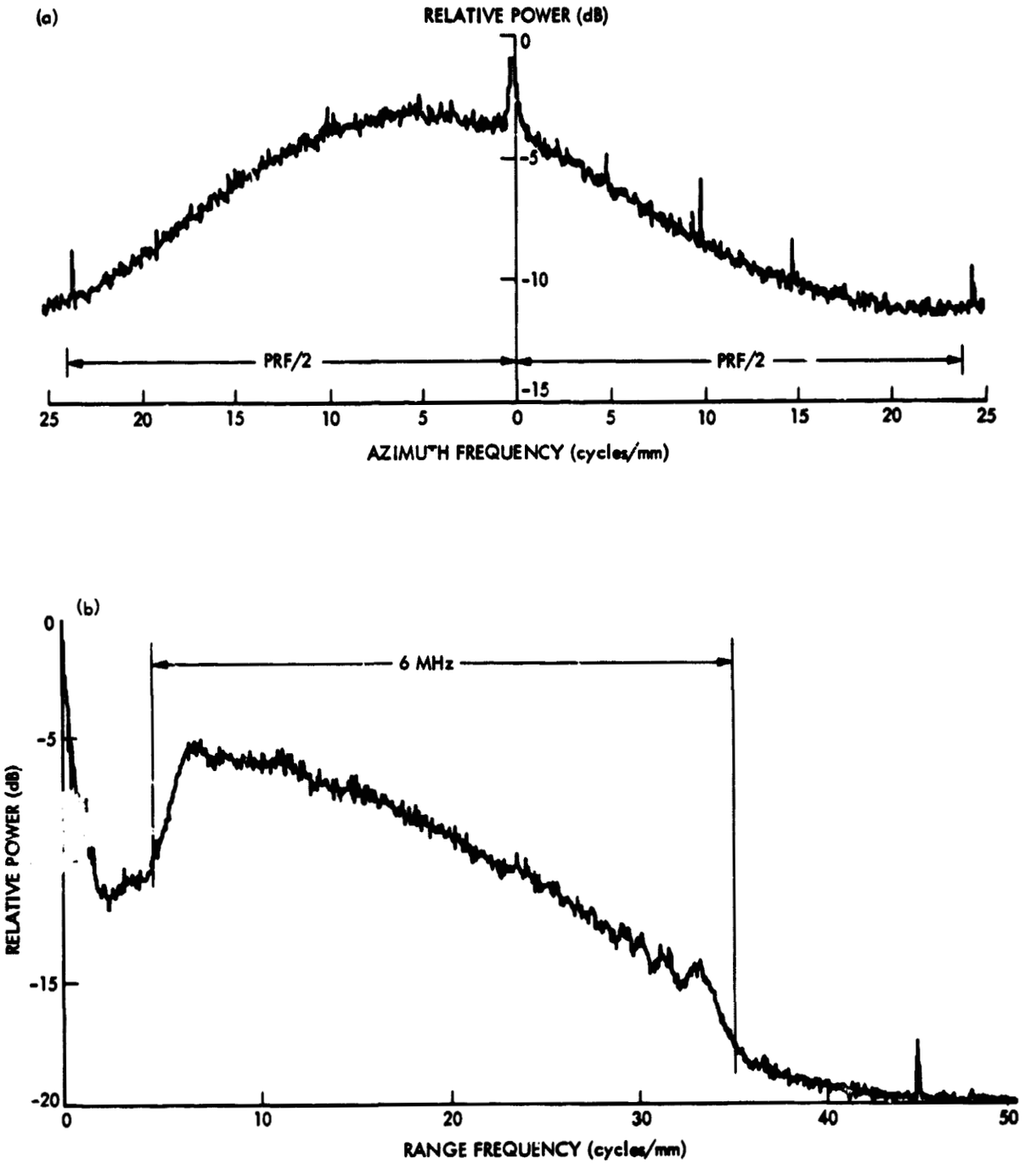

Figure 2-6. SIR-A Signal Film Data: (a) Azimuth Spectrum; (b) Range Spectrum

data. The ordinate represents ten times the common log (dB) of the fast Fourier transform values of the data numbers (DNs) taken from the microdensitometer (transmission mode). In Figure 2-6(a), the amplitude modulation of the azimuth antenna pattern is evident. The spikes seen in the data correspond to frequency components near zero-range frequency; these spikes are caused by optical recorder film drive noise. In Figure 2-6(b), the effect of the modulation transfer function can be seen over the 6-MHz bandwidth of the echo. Again, the noise spike close to zero-range frequency corresponds to optical recorder drive noise.

The corner reflector array (Fig. 2-7(a)) can be readily identified on the output image film (Fig. 2-7(b)). The reflector array was deployed to resemble a cross, with seven reflectors aligned in a north-to-south direction, and three reflectors in an east-to-west direction. The sizes of the trihedral reflectors were 2, 4, 6, and 8 feet. All reflectors, except the smallest, are clearly visible on the output image. The sizes of the reflectors' images correspond to approximately a point response of 40 × 40 m, which is the expected resolution.

C. AZIMUTH ANTENNA PATTERN AND RETURN ECHO PROFILE

The SIR-A hardware did not include a calibration capability, and no attempt was made to calibrate the sensor end to end to derive the absolute backscatter cross section. However, it is still useful to consider how that transfer takes place and what uncertainties and variations exist in the data reduction. An understanding of the transfer mechanism aids in qualitative interpretation of the data, and some limited quantitative analysis can be done.

The radar sensor employed an echo sample gate (ESG) to sample and average a portion of the RF echo amplitude within the interpulse period (IPP). In the ESG scan mode, the gate was automatically and continuously stepped across the IPP, dwelling at each of 64 positions for about 1/4 s. For a uniformly-distributed target such as a smooth ocean, the ESG scan roughly traced the antenna pattern in range. An example of such data is shown in Figure 2-8. Data of this type were acquired during the whole period of SIR-A image acquisition. It is possible to use these data to infer (uncompressed) radar backscatter, and thus avoid the calibration problems associated with photographic film and processing.

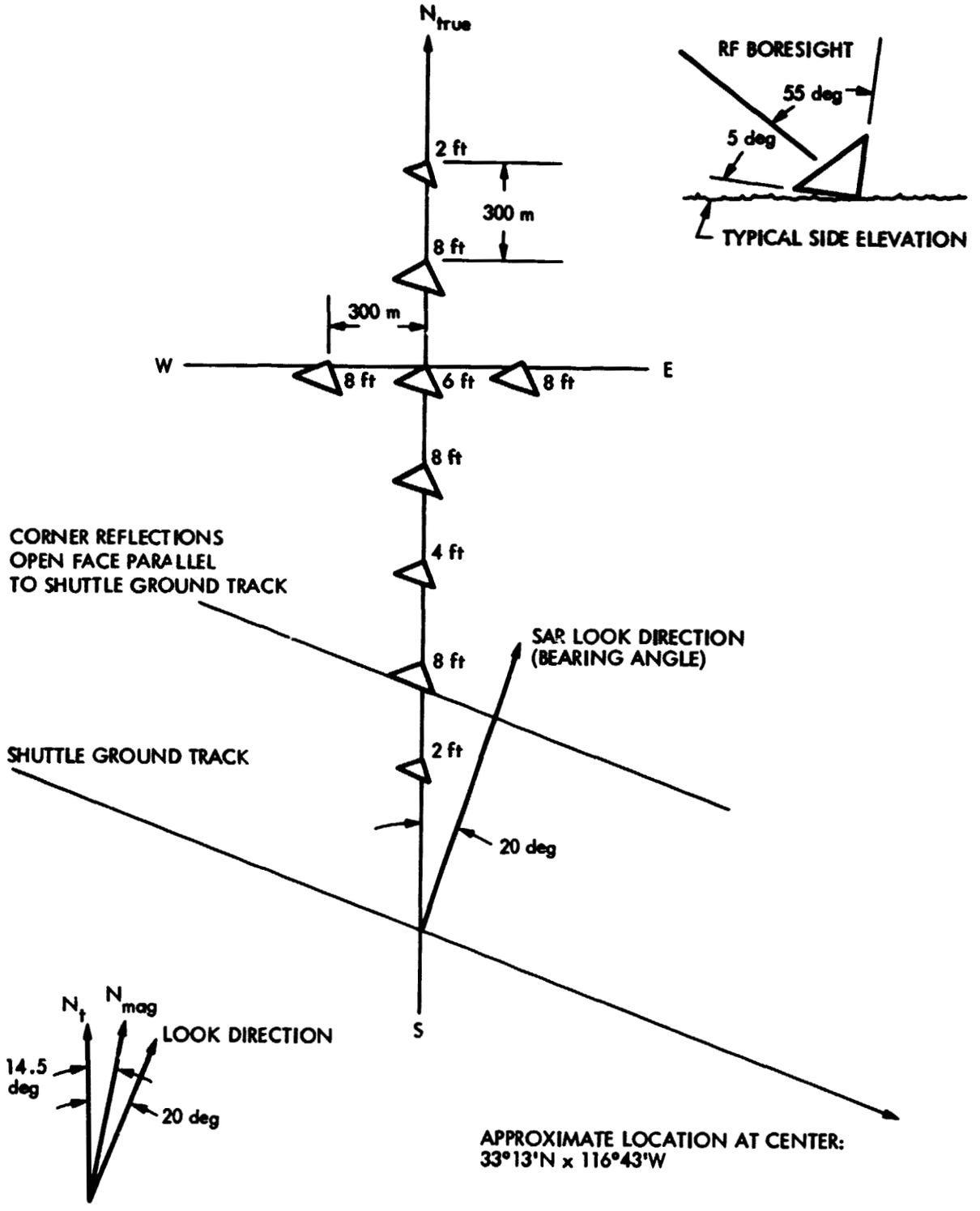

Figure 2-7. Corner Reflectors Deployed Near Lake Henshaw, California: (a) Location

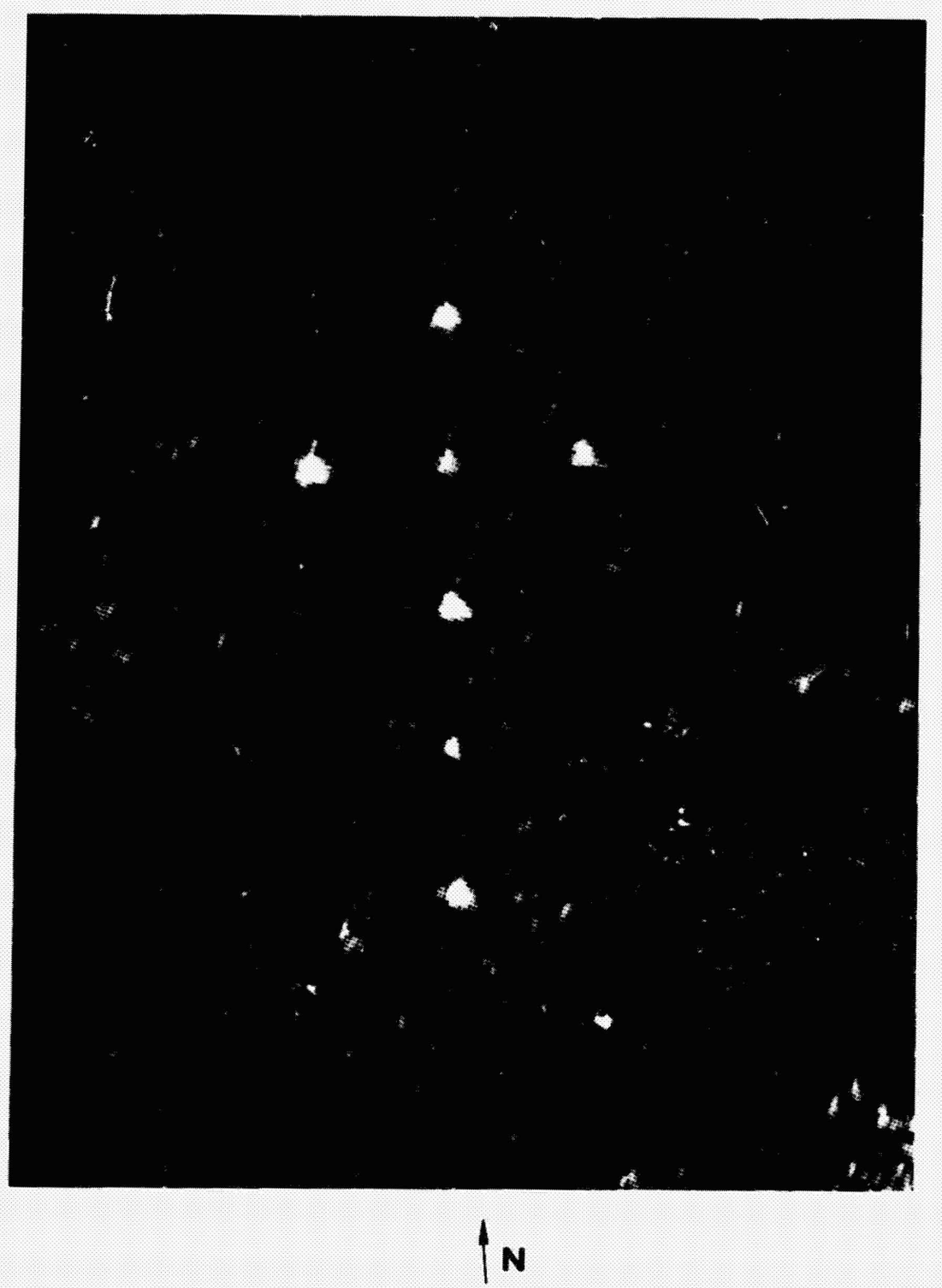

Figure 2-7. Corner Reflectors Deployed Near Lake Henshaw, California: (b) SIR-A Image of Reflectors

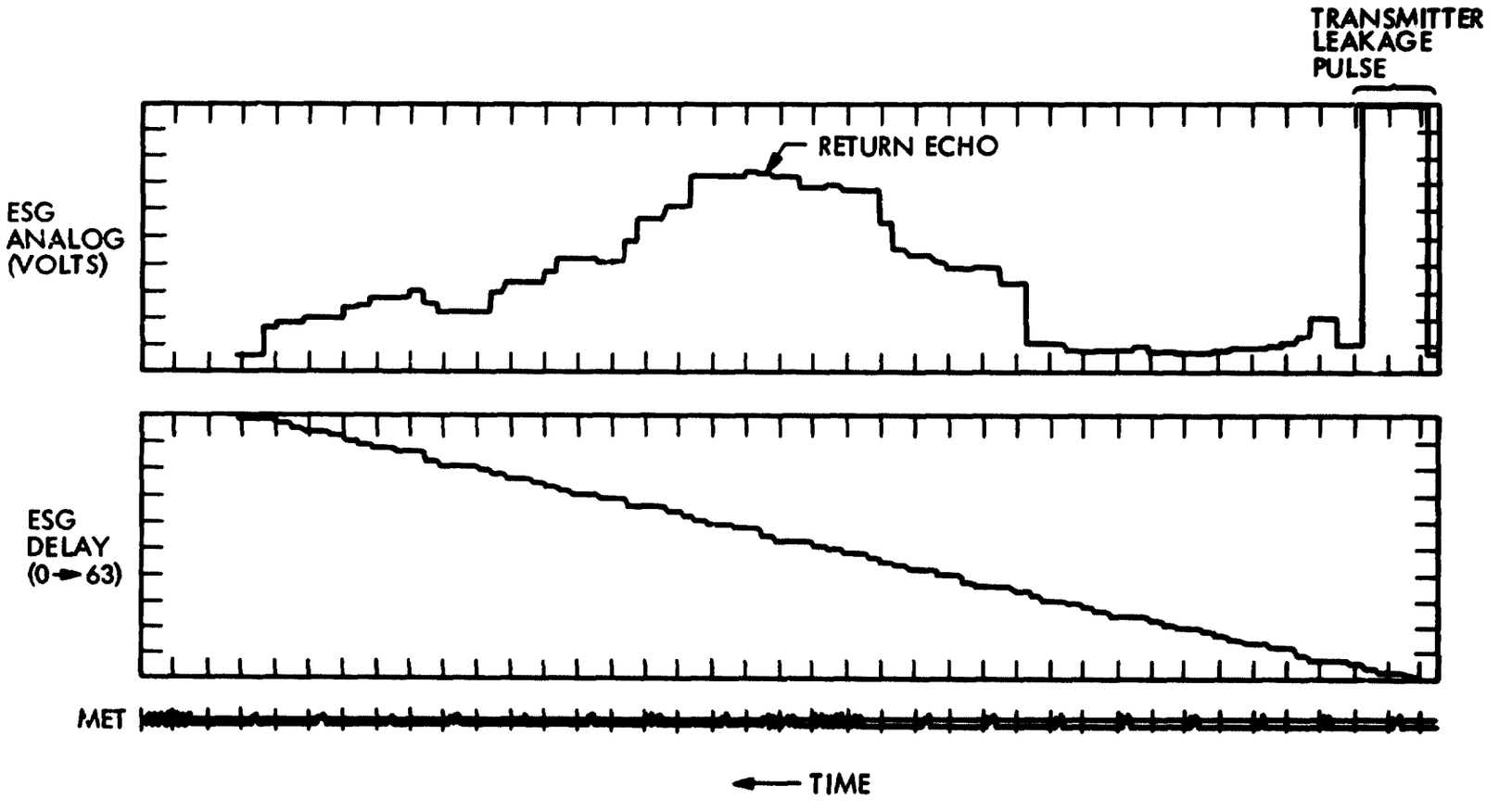

Figure 2-8. Strip-Chart Recording of Echo Sample Gate (ESG) Telemetered Values

Details of the amplitude transfer are shown in Figure 2-9.[2] The backscatter coefficient controls the strength of the radar returned signal, which is amplified and fed to the optical recorder. The intensity of the light used by the recorder to expose the signal film is related to the returned strength.

After the flight, the developed signal film was used to modulate the laser light in the optical correlator; the laser light was optically filtered and compressed to create an image. The image was exposed on the image film negative (IFON), which, when developed, was used to create various film products or digitized for computer analysis.

To describe the transfer from backscatter coefficient to image film density, it is more convenient to divide the system into segments, between which lie points where the signal is available for measurement. Figure 2-9 shows the divisions used for this analysis: (1) the receiver and associated electronics that condition the returned signal prior to delivery to the optical recorder; (2) the optical recorder, signal film and its development, and the optical correlation; and (3) the image film and its development. The segment prior to the receiver has been modeled but not measured. Segment (1) starts at the receiving antenna port. The division between (1) and (2) is the input connector to the optical recorder, whose label is 7J5. The division between (2) and (3) is the laser radiant power in the image film plane.

Both the SIR-A flight hardware and the ground processing system are adjusted to place the range of radar returns in the most linear portion of the system's dynamic range. For illustration we will assume the system is aligned for the range of backscatter coefficients encountered in the segment of data take 24C over Southern California, shown in Figure 2-10. Maximum and minimum image film densities observed in this segment will be traced through the system as an example. Figure 2-11 shows the combination of segments 1 through 3 aligned for that data take. Note that this figure is not necessarily representative of SIR-A data in general, and that large deviations from these curves may exist in the actual data reduction scheme. In addition, only areas homogeneous over a synthetic aperture can be traced through them. The upper left graph shows the receiver amplitude transfer function with STC off and a commandable gain of

[2]Note that in the production of SIR-A NSSDC and experimenter data products, a signal film master positive (SFMP) step was added that is not included in this analysis.

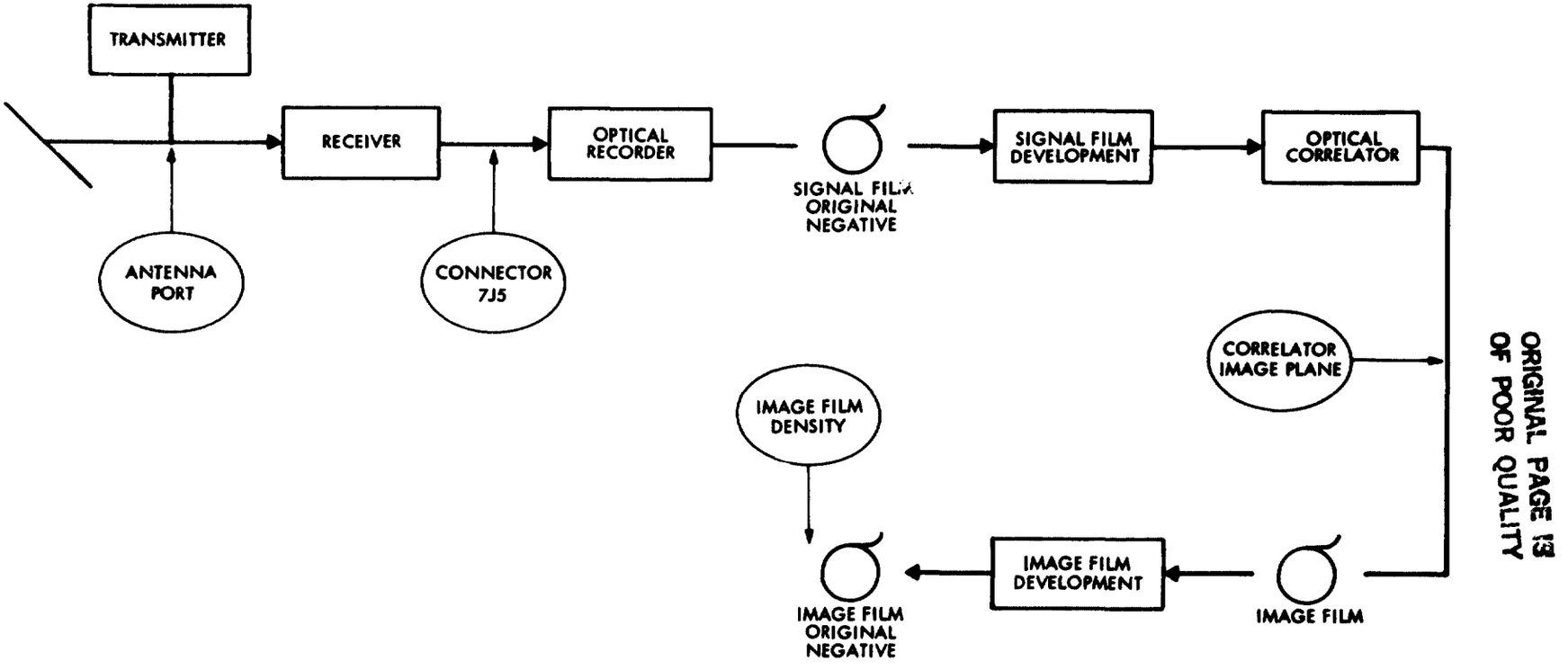

Figure 2-9. SIR-A Data Flow Showing Divisions Used for the Transfer from Backscatter Coefficient to Image Film Density

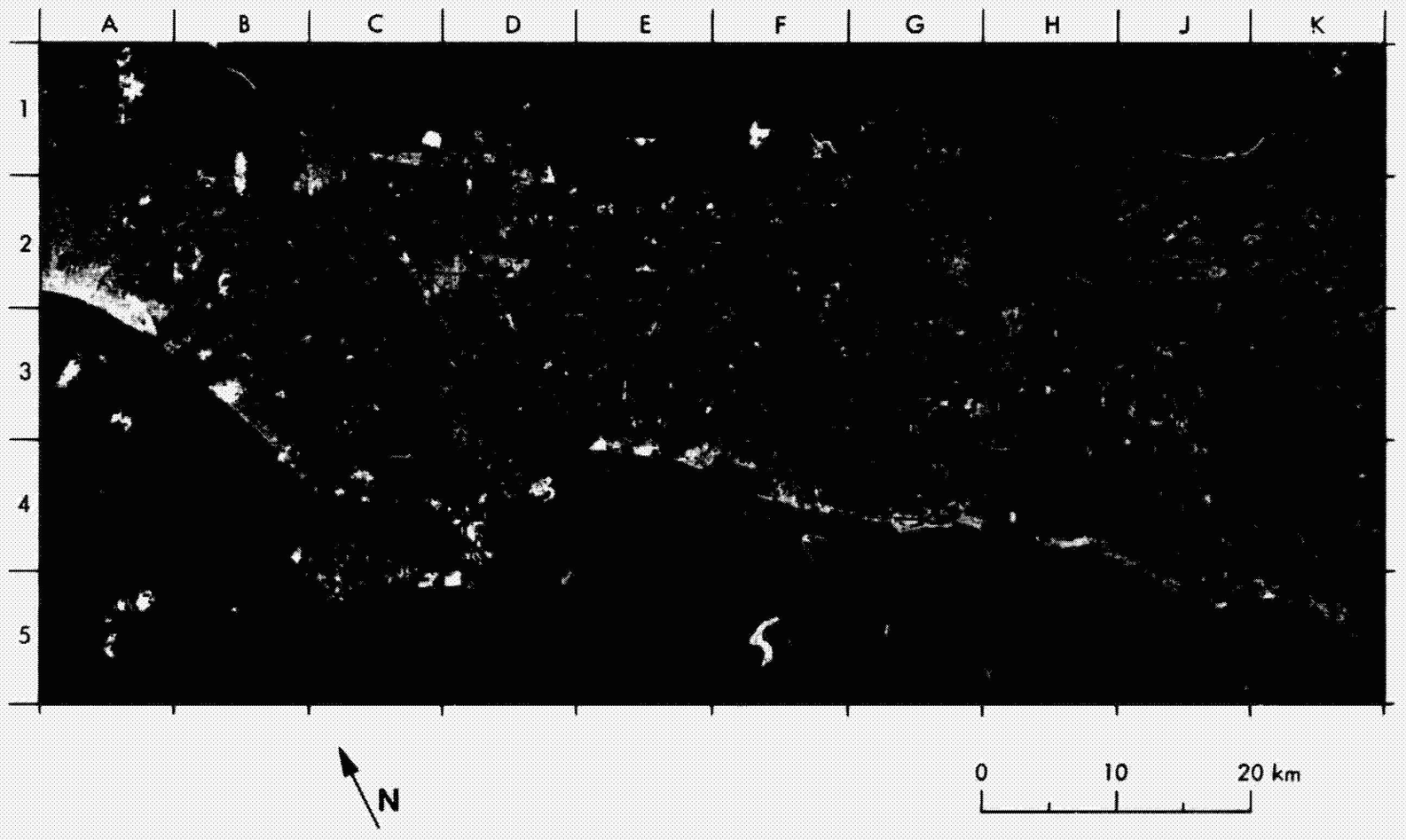

Figure 2-10. SIR-A Image of Los Angeles Basin, California (Data Take 24C)

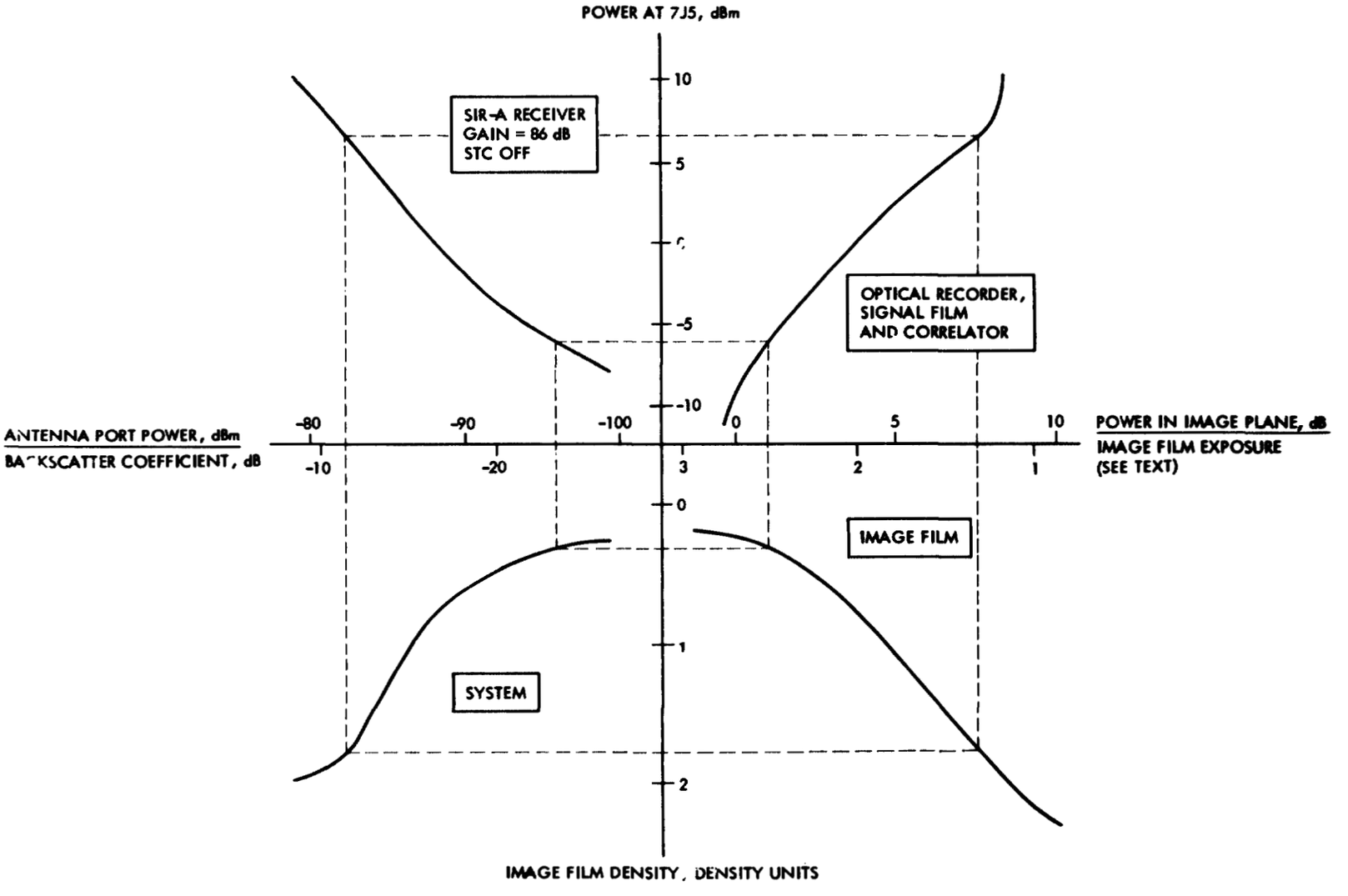

Figure 2-11. Transfer Curves for Three Segments of the SIR-A System as Outlined in Figure 2-9

89.3 dB (86-dB title). The abscissa of this graph is linearly related to backscatter coefficients, but the proportionality depends on shuttle altitude, transmitter power, STC, and position in the swath. For typical values of these parameters, the relationship has been computer modeled and shown on the lower scale of the abscissa. Thus, under these assumptions, backscatter coefficients between -24 and -11 dB will produce an output between -6 and +6.5 dBm at connector 7J5. The ESG analog data are extracted at this point and relayed to strip-chart recorders on the ground. Although the telemetry data cannot be compressed into imagery, it is possible to infer uncompressed (large-area) backscatter from it.

Figure 2-11 shows the transfer curves for the three segments of the SIR-A system as outlined in Figure 2-9. The curves are arranged so that the most linear portions of the three curves align with the dynamic range observed in the image of Figure 2-10.

The upper-right graph in Figure 2-11 shows the transfer from 7J5 to power that is incident on the image film in the optical correlator. The abscissa of this graph is marked with both power in dB and the equivalent exposure of the IFON, measured as the logarithm of the reciprocal of the exposure in relative units. The absolute relationship between the two scales is changed when the correlator laser power is adjusted. The adjustment shown here will expose the image film for the Figure 2-10 imagery to provide the best results from the relatively limited dynamic range of this film. This graph also assumes perfect development of the signal film and no latent image degradation or other predevelopment chemistry variations in the signal film emulsion. Additional variations in power across the swath may be produced by vignetting in the correlator. Under these assumptions, our original backscatter coefficient range of -24 to -11 dB has now been transferred to image film exposures from 2.5 to 1.4 (relative units).

In the lower-right corner of Figure 2-11 is the development curve for the image film, which transfers the exposure into variations in density on the developed IFON. Except for the variations in this film development discussed below, this step is relatively straightforward. The exposure range of 2.5 to 1.4 has been mapped into the image film density range of 0.3 to 1.8 density units, which is the observed density variation in the segment of data take 24C.

In the lower-left corner of Figure 2-11 is the system transfer function between backscatter coefficient (the abscissa for the upper-left graph) and image film density (the ordinate for the lower-right graph), which results under all of the above assumptions. This curve was generated by tracing points through the other three graphs. The system dynamic range as shown is about 11 dB, in good agreement with prelaunch predictions. Note that the range is limited at the lower end by the noise (base plus fog) of the image film, and at the upper end by the optical recorder, signal film, and correlator component. Upstream of the optical recorder, the available dynamic range goes beyond the limits of this graph. Actual limits of the receiver are about 30 dB, and if the data were recorded on some other medium, this range could have been preserved. As it is, it is clear that the system is far from linear, and that the nonlinearities are mostly due to the data recording system employed.

SECTION III

SIR-A HARDWARE PERFORMANCE

A. SUMMARY

The SIR-A flight hardware performed flawlessly during the STS-2 mission, gathering nearly 8 hours of data. All engineering specifications of the instrument were met or exceeded.

The OSTA-1 pallet was removed from the Shuttle in December 1981, and the SIR-A electronics and optical recorder were shipped to JPL in January, 1982. The electronics and optical recorder are at JPL awaiting their next flight into space as part of the SIR-B Experiment in the summer of 1984. The SIR-A antenna was shipped to Ball Aerospace Systems Division, Boulder, Colorado, in March 1982 where it will undergo extensive modification for the SIR-B Experiment.

B. PERFORMANCE BY SUBSYSTEM

1. Antenna

Based on quick-look analysis of the available data, the antenna appears to have performed nominally in all aspects. Amplitude responses for the azimuth pattern of the antenna were received by JPL portable ground receivers, specifically deployed for that purpose, during data takes 24B and 24C over northern California. The SIR-A antenna pattern in azimuth was obtained by recording the received signal intensity on a strip chart recorder as the Shuttle passed by the receiver site. Figure 3-1(a) shows the preflight calibration data of the antenna pattern in azimuth and Figure 3-1(b) shows the recorded azimuth pattern for one particular pass.

2. Transmitter

The transmitter performed satisfactorily during the mission with only one unexplained phenomenon — a slight decrease followed by an increase of power during each data take. This behavior appears to be due to unequal heating of the three transmitter power amplifiers.

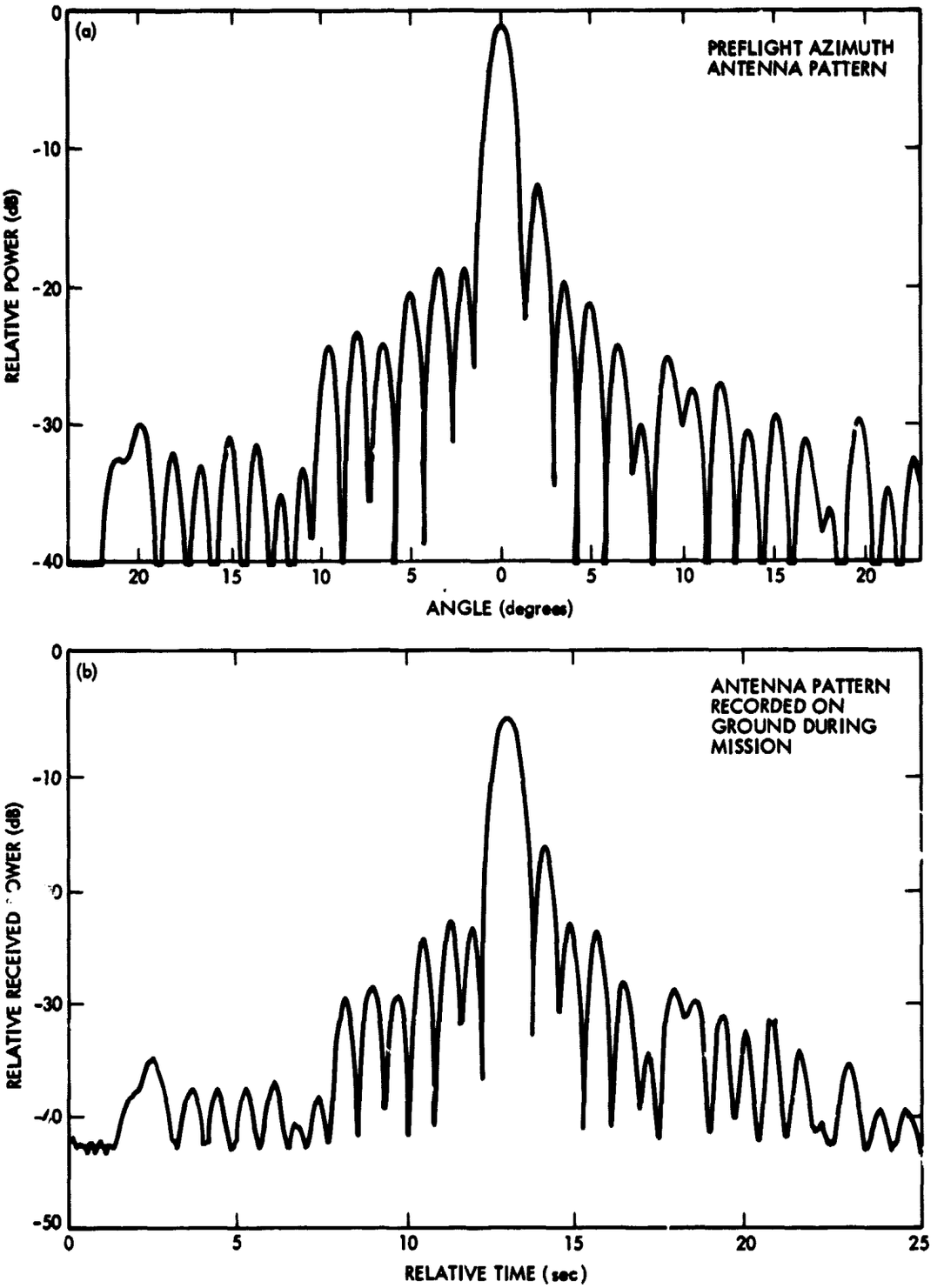

Figure 3-1. Comparison of Antenna Patterns: (a) Preflight Calibration of the Azimuth Antenna Pattern; (b) Azimuth Antenna Pattern Recorded on the Ground During the Mission

3. Receiver

The receiver subsystem performed perfectly throughout the mission and even sustained a high reflected input power of 200 W for 2 s during a Shuttle water dump. The high reflected power was due to a cloud of water crystals migrating in front of the antenna during transmitter operation.

4. Logic and Control

The SIR-A sequencer performed as planned throughout the flight. Its flexibility was appreciated when immediate replanning was necessary for the minimum mission. Some concern was voiced at JPL over the ability of the sequencer's memory to remain intact under cosmic-ray bombardment. A test performed at Kennedy Space Center (KSC) after removing the instrument from the OSTA-1 pallet indicated that the memory was 100% intact. Not one bit out of 45,056 bits had changed during the flight.

5. Power Converter

The SIR-A power converter experienced no problems during the flight. An unexplained, operate-bus failure during testing at KSC, prior to installation on the pallet, never reappeared during testing on the pallet or during the flight.

6. Optical Recorder

Our greatest reliability concern during the flight was the optical recorder, primarily because of its age (14 years) and the severe launch vibration environment. No visible damage was sustained by the optical recorder during the launch. The recorder produced crisp, clear data with no evidence of degradation. Small damage to the take-up cassette occurred when removing its safety harness, but not enough to impair its usefulness in further flights. The dynamic range and frequency response of the recorder were as expected.

C. SHUTTLE SYSTEMS

1. Power

The dc voltage at the instrument varied from 29.8 volts at the start of the mission to 28.5 volts at the end. A voltage below 26.0 volts would have caused the optical recorder CRT to unfocus.

2. Command

The command system through the Shuttle's general purpose computer (GPC) and pallet flex multiplexer demultiplexer (MDM) operated perfectly.

3. Status Monitors

The analog and discrete status monitors through the pallet flex MDM and the Shuttle's GPC operated nominally. In the future, we will set caution and warning limits only for safety-threatening failures.

4. Radio-Frequency Interference

No evidence of interference from UHF, S-band, TACAN, or any other RF source on the orbiter was found in the SIR-A data.

5. Attitude Stability

An attitude deadband of ±0.10 deg and a drift rate of ±0.02 deg/s for all axes were adequate for the SIR-A instrument.

6. Cooling

Active cooling for the SIR-A electronics was adequate. Passive cooling for the optical recorder was inadequate for data takes longer than 25 min.

SECTION IV

DATA ANALYSIS

A brief summary of the early results is given in this section as well as in two papers soon to be published: Elachi et al. (1982) gives an overview of the SIR-A preliminary science results, and McCauley et al. (1982) presents one of the most exciting results related to subsurface imaging.

This section is composed of subsections written by the original SIR-A Science Team members or their collaborators.

A. OVERVIEW (C. Elachi, JPL)

It is well established that imaging-radar data are important elements in the morphological and structural mapping of tropical regions. The SIR-A preliminary data analysis clearly indicates that radar data are also of unique importance in mapping structures in hyperarid and arid regions, and provide additional information (relative to Landsat) in semiarid and temperate regions.

Analysis of the data acquired in the hyperarid region of southern Egypt clearly shows the SIR-A imaged subsurface drainage elements and geologic structures that are covered by a layer of dry sand. These results are reported by McCauley et al. (1982). Dixon (Subsection B) used the SIR-A data to acquire additional information on the tectonics of the Eastern Desert of Egypt relative to what is available on the most recent geologic maps. Breed, McCauley, Schaber, Walker, and Berlin from the U.S.G.S. (Subsection K) give assessments of the capability of mapping the morphology of sand dunes, desert regions, and arid regions using radar data, and present a comparison with Landsat data. It is clear that the radar data provide additional information. In many cases, surface morphology is better depicted on the SIR-A images, particularly where sand cover tends to reduce variations in the visible and IR reflections. Masursky (Subsections D and E) discusses the results of using SIR-A data to map volcanic features and illustrates a case where some information could be acquired from SIR-A data about the cooling and silica content of lava flows. These phenomena affect the blockiness of the surface, which, in turn, strongly affects the radar return. Rebillard (Subsection I) presents the use of the SIR-A data in conjunction with Seasat data to map dry lake beds in northwestern Algeria, and

illustrates variations in the surface signature due to the radar illumination geometry and temporal variations on the surface.

In their analysis of some of the SIR-A data over the U.S., Ford and MacDonald (Subsections C and H) clearly show that because of differences in illumination geometry, the SIR-A, Seasat, and Landsat data contain complementary information about surface morphology and structure. This illustrates the need for multisensor observations to acquire a more detailed picture of surface geology.

Dellwig and MacDonald (Subsections F and G) present a comparison of the SIR-A and airborne radar data acquired over tropical forested areas in Panama and Guatemala. Krohn and Milton (Subsection J) present their results of using SIR-A data, in connection with Seasat and Landsat data, to map surface geology in heavily forested areas, based on the distribution of surface vegetation.

B. ANALYSIS OF THE IMAGERY OVER THE EGYPTIAN EASTERN DESERT (T. Dixon, JPL)

SIR-A provided the first radar images obtained over the Eastern and Western Deserts of Egypt. The Eastern Desert of Egypt is a peneplained Precambrian Shield, which has, for the most part, remained tectonically inactive for the last 500 million years. The continental rifting associated with formation of the Red Sea in post-Cretaceous time has left little tectonic imprint, but two effects are noteworthy. Mild uplift of the basement and subsequent erosion of a thin Phanerozoic sediment cover has exposed the Precambrian rocks. This uplift is presumably related to subcrustal heating and related thermal expansion of the crust associated with the initial stages of Red Sea rifting (e.g., Falvey, 1974). In addition, strike-slip faults associated with the Red Sea rift-transform system appear to be affecting the shield.

This section describes the signature of major rock types exposed in the Eastern Desert of Egypt as observed in the Shuttle radar imagery. Fault-related lineaments are also observed in the imagery, some of which have not been previously described. These observations allow some new generalizations concerning tectonic trends in the shield.

The synthetic-aperture radar image from data take 28 of SIR-A is shown in Figure 4-1. A lithologic map modified from El Ramly and Hermina (1978) is shown

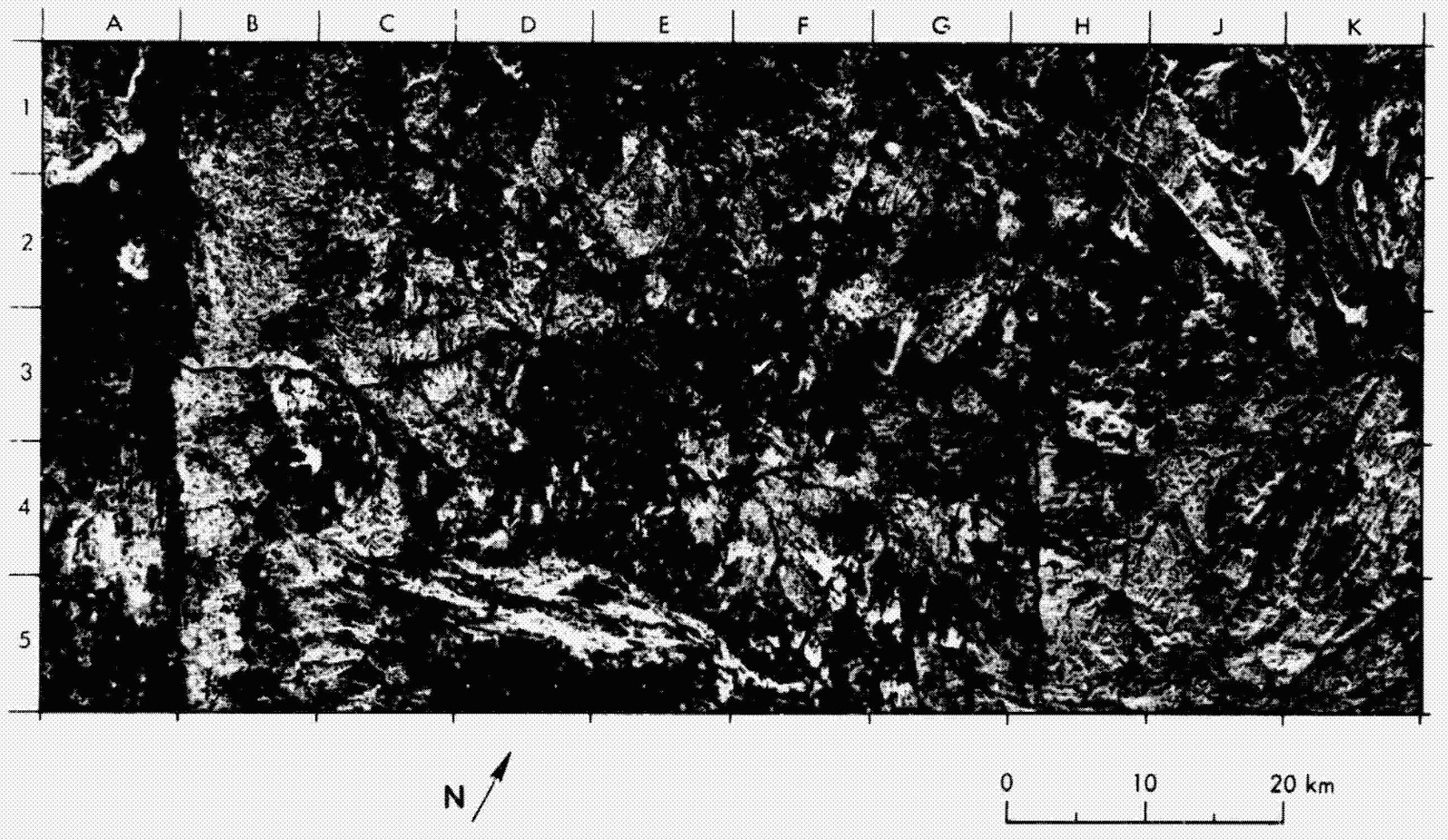

Figure 4-1. SIR-A Image of the Southeastern Desert in Egypt (Data Take 28)

in Figure 4-2. Figures 4-3 and 4-4 are structural and lithologic interpretations of the radar image.

Five major lithologic units can be distinguished in the radar image; they are described below from the youngest to the oldest:

(1) Recent accumulations of relatively flat sand and gravel occur in narrow "wadis" and in wider areas, especially west of the Nile River. These areas are dark on the radar image because the surfaces are smooth at the radar wavelength, and very little energy is back-scattered to the receiver. The wadis often mark the location of major faults because erosion proceeds rapidly within the sheared rocks.

(2) The Cretaceous Nubian Sandstone group laps against the Precambrian Shield on its western edge. This unit has a relatively high radar albedo, and a distinctive dendritic drainage. Lower albedo Tertiary sediments crop out in a narrow zone along the Red Sea coast.

(3) At least ten granitic plutons can be observed on the radar image, with diameters ranging from about 5 to 15 km. Two groups of plutons have previously been distinguished on the basis of petrologic and chronologic data: older granodiorites (600 to 650 Myr) and a younger granite-adamellite group (570 to 590 Myr). Two plutons visible in the radar image have been dated by the whole rock Rb-Sr technique. Stern (1979) obtained an age of 671 ±33 Myr for the Wadi Miah granodiorite. Fullagar and Greenberg (1978) report an age of 594 ±8 Myr for the Gebel Kadobora granite.

Granitic plutons are easily distinguished on the radar image because of three characteristics. First, they are more or less circular in shape. Second, many of the plutons vary in resistance to erosion relative to the country rock. For example, plutons may be defined by wide sandy areas or wadis that appear dark in the radar image. This is most apparent in the case of the older granodiorites, e.g., Wadi Miah and Wadi Beizah. The intense weathering and erosion of some of the older granodiorites may be related to a pervasive foliation that characterizes many of these synorogenic plutons. In contrast, the Gebel Kadabora and Gebel El Sibai younger granites are characterized by an outer ring of high hills, but a strongly weathered, hence, dark

Figure 4-2. Lithologic Map of the Southeastern Desert in Egypt
Modified from El Ramly and Hermina (1978)

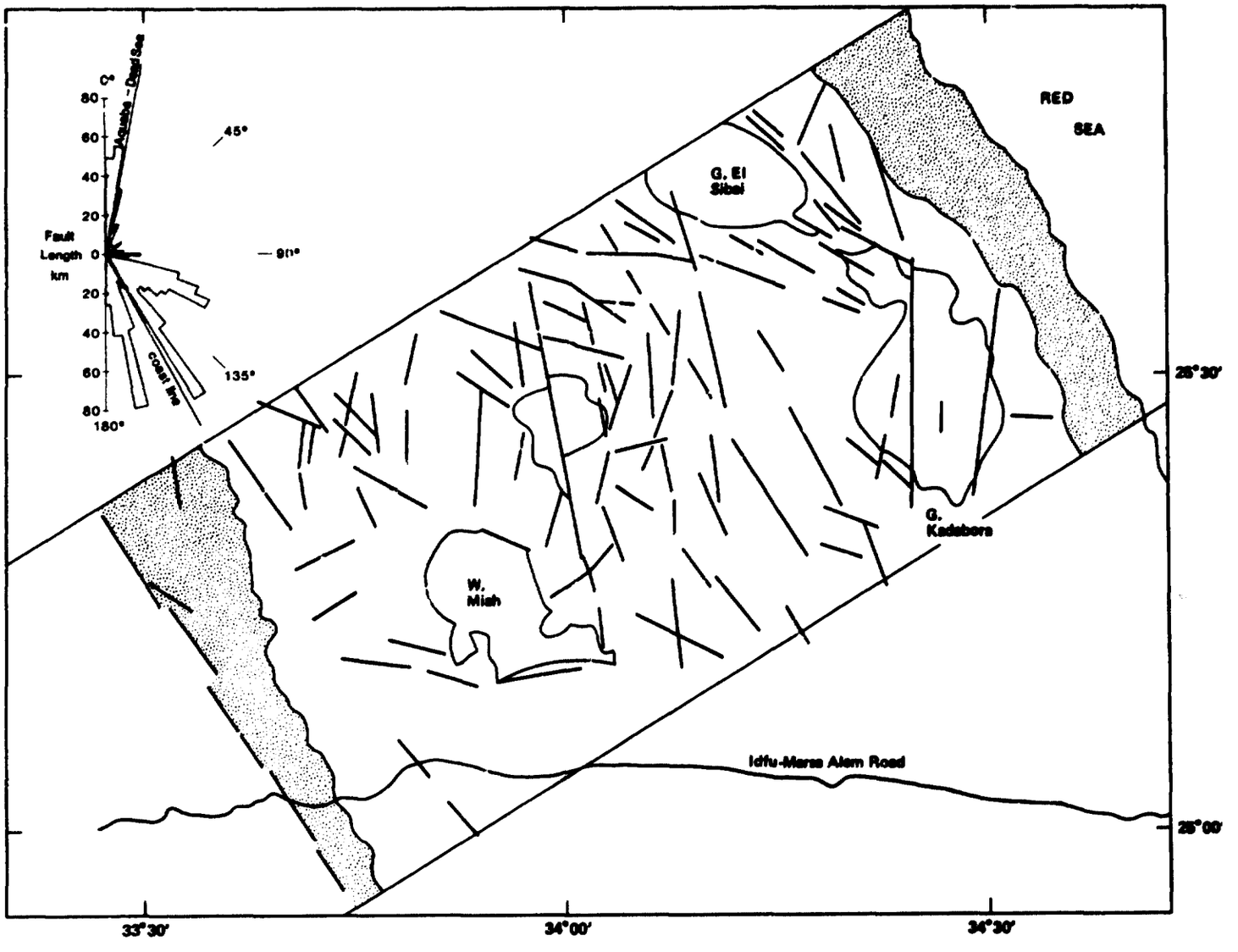

Figure 4-3. Structural Interpretation of the Radar Image of the Southeastern Desert in Egypt; Insert is the Rose Diagram

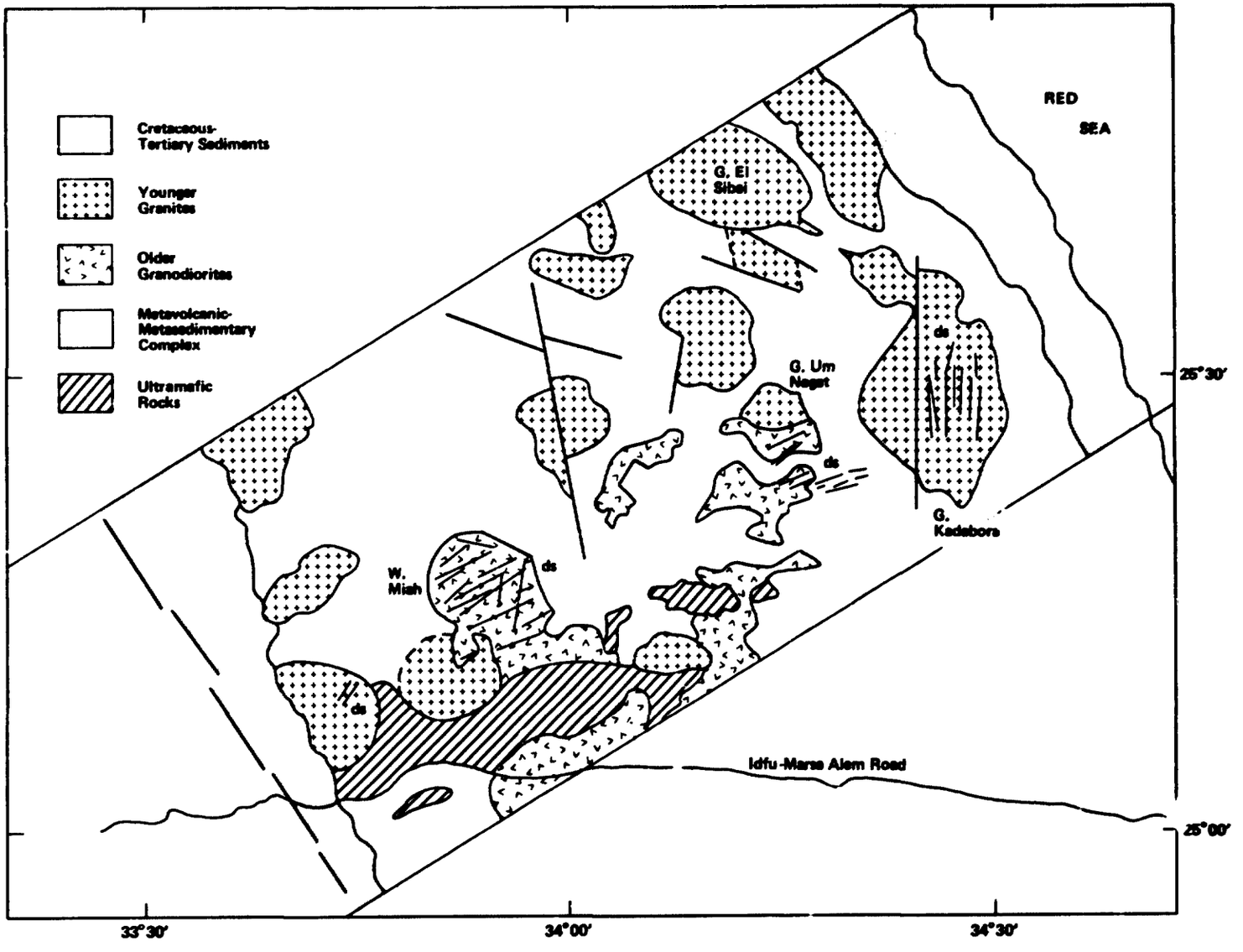

Figure 4-4. Lithologic Interpretation of the Radar Image of the Southeastern Desert in Egypt

core. Neary, Gass, and Cavanagh (1976) noted similar dichotomous topography in the younger granites of the NE Sudan. The coarse-grained nature of the granite plutons, especially in the cores, may contribute to their rapid erosion, since water percolation along grain boundaries might be enhanced. Third, some of the plutons are characterized by dike swarms or parallel joint fractures that are prominent on the radar image. They are most apparent in the Wadi Miah granodiorite (southwest-northeast), and the Gebel Umm Nagat (southwest-northeast) and the Gebel Kadabora (north-south) younger granites. Felsic or siliceous dyke swarms are of considerable interest in the Egyptian Shield. Their emplacement is probably related to the later stages of granitic magmatism. They are therefore favorable sites for the concentration of uranium-bearing fluids (e.g., Rogers et al., 1978). Several such occurrences in the Central Eastern Desert contain significant levels of uranium mineralization (e.g., Hussein and El Kassas, 1980).

(4) The country rock intruded by the granitic plutons consists of basaltic to andesitic volcanic rocks, related sedimentary material, and associated ultramafic rocks, now metamorphosed to greenschist facies. This sequence is thought to be indicative of a late-Precambrian oceanic and island arc environment (Engel, Dixon, and Stern, 1980; Stern, 1981). In terms of radar image discrimination, the metavolcanic-metasedimentary rocks represent a single unit, and appear as a moderate-relief terrane with moderate-to-high radar albedo.

(5) The ultramafic rocks can be distinguished from the metavolcanic-metasedimentary unit by their high relief and high relative brightness. The strong topographic expression indicates resistance to weathering. Although the original mineralogy of these rocks (mainly olivine and orthopyroxene) is highly susceptible to weathering and erosion, the rocks are now composed almost completely of a dense mixture of serpentine and carbonate (mainly ankerite), which is very resistant to weathering in the desert climate. The Barramiya serpentinite is the largest such body and is strongly lineated in the east-west direction. These lineations probably reflect the influence of tectonic emplacement or remobilization; however, no obvious faults or other lineaments are apparent in the adjacent country rock.

Figure 4-3 contains a rose diagram of major lineaments visible in the radar image. Linear features smaller than 5 km and the previously discussed dyke swarms and joint fractures were not plotted. Most of the remaining features are probably faults because they are all relatively long, well-defined lineaments. Actual offsets are apparent in some cases (e.g., Figure 4-1, location F2).

Three major lineament directions are apparent; the oldest trends are east-southeast to west-northwest. The age assignment is based on the observation that lineaments in this group do not cut any of the granitic plutons, and, in turn, are offset by a younger north-south fault set. This older lineament set may be related to tectonism associated with collapse and emplacement of the metavolcanic-metasedimentary complex.

A second, younger lineament set trends northwest-southeast, or approximately parallel to the Red Sea coast (e.g., Youssef, 1968). This lineament group probably represents faults that have experienced post-Mesozoic movement because they displace outcrops of the Nubian sandstone, or at least strongly control its deposition. A similar fault may even control the position and trend of the Red Sea coast. The strongest linear feature on the radar image, with the exception of the coastline, is the northwest-trending boundary in the Nubian sandstone near the southwest boundary of the shield (Figures 4-1 and 4-4). Some normal movement has occurred on this fault because the southwest side of the fault has been downthrown, and the Nubian outcrops there are covered with a thin veneer of recent alluvial material. This obvious boundary probably represents an extension of previously mapped faults to the north and south (e.g., El Ramly and Hermina, 1978). It is one of the longest well-defined lineaments in the Eastern Desert, with a strike length of at least 250 km.

A north-south (±15 deg) group of lineaments also probably represents faults that have been active in the Phanerozoic, though exact age relations to the previously described northwest-southeast fault set are not clear. A north-northeast to south-southwest fault cuts Gebel Kadabora, suggesting that this fault group as a whole has an absolute age younger than 594 Myr. Another well-developed fault in this group trends north-northwest to south-southeast and cuts a small unnamed pluton northwest of the Wadi Miah granodiorite, where about 2 km of left lateral displacement is observed. This fault also displaces an older lineament immediately north of the pluton, also with about 2 km left-lateral

displacement. It is noteworthy that this locale is on strike with the Dead Sea-Gulf of Aqaba fault, an active left-lateral transform fault associated with a Tertiary-to-Recent opening of the Red Sea. The overall alignment with the Aqaba trend, the available age constraints, and the observed left-lateral motion for the north-south fault set all suggest that this group of faults is associated with the tectonics of the Red Sea rift. Alternately, this fault set could have been active in the Precambrian, and was reactivated during initiation of the Red Sea rifting. In this case, preexisting tectonic trends in the shield controlled the orientation of the Red Sea rift.

C. ANALYSIS OF SIR-A AND SEASAT SAR IMAGES OF KENTUCKY-VIRGINIA (J. Ford, JPL)

The terrane covered by this study represents a small portion of each of two widely differing geomorphic provinces. The Appalachian Plateau in southwest Kentucky is extensively covered by a dense forest of mixed deciduous and coniferous trees. It is deeply dissected. Slopes are steep to very steep. Valley bottoms are mostly very narrow and winding. Bedrock consists of coal-bearing sedimentary sequences that include much sandstone and shale. Most rocks of this regional structure dip gently toward the Appalachian Basin in the southeast.

The adjacent Ridge and Valley terrane in southwest Virginia is strongly oriented in elongate subparallel strips. The ridges have steep slopes that are densely forested. The intervening major valleys are wide, relatively level, and largely cultivated; they extend linearly for many tens of kilometers. Bedrock consists of carbonate and clastic shelf-rock sequences that have been extensively folded and faulted into thrust slices (Rogers, 1949). The bedrock in both the Plateau and Ridge and Valley areas is covered by a thick mantle of soil and vegetation. Outcrops are few and the landforms are controlled more by structure than the underlying lithology. Drainage is structurally controlled. A major structural feature is the Pine Mountain overthrust. This thrust has carried a thin plate of Plateau rocks northwest for a distance of about 6.4 km over Ridge and Valley rocks (Harris and Milici, 1977). The feature is prominent on the SIR-A and Seasat SAR images (Figures 4-5 and 4-6, respectively).

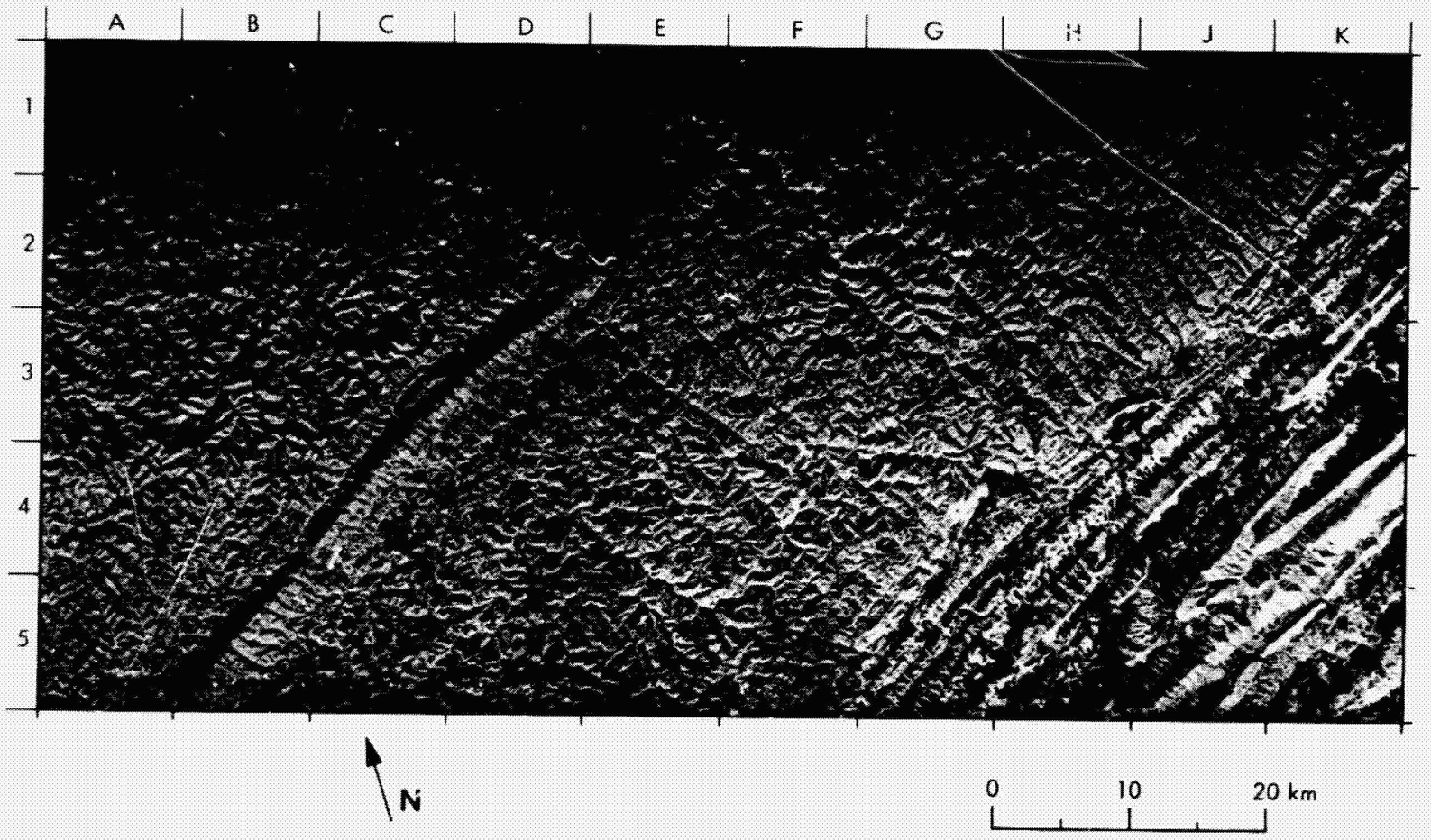

Figure 4-5. SIR-A Image of the Appalachian Plateau in Kentucky and Virginia (Data Take 24A)

Figure 4-6. Digitally Correlated Seasat SAR Images of Kentucky and Virginia: (a) From Rev. 874 Acquired on August 27, 1978; (b) From Rev. 793 Acquired on July 31, 1978. Direction of Scene Illumination is Shown by Arrows: (a) N67°W and (b) N67°E

Lineament mapping and structural interpretation are made from the contrast in tone, texture, and pattern on each of the SIR-A and the Seasat SAR images. The range of gray levels on the two sets of radar images is broadly similar. The gray levels cannot be compared quantitatively because the data are uncalibrated. In both cases, however, the abrupt linear changes of image tone denote corresponding changes in radar backscatter. Geomorphic features reflected by the abrupt changes include linear valleys or alignments of valley segments in the Appalachian Plateau, and major ridges in the Ridge and Valley area. Bedding is perceived locally from tonal variations along the scarp slope of Pine Mountain. The local direction of dip is determined from the pattern of flatirons on the dip slope (Figures 4-5 and 4-6, F2/E2 to B4). However, the tonal variations provide no discrimination or identification of the bedrock lithology. The textures on the SIR-A image (Figure 4-5) and the Seasat SAR image (Figure 4-6) differ in corresponding image areas. This effect enhances or suppresses local topographic features differentially on the respective images. It results in part from differences in backscatter that are due to the different radar look angles used on the SIR-A and the Seasat SAR systems. In part, it results from differences in the direction of scene illumination. These two factors combine to produce a significant difference in the local incidence angle of the SIR-A and the Seasat SAR imaging beams at corresponding localities on the respective images.

Topographic lineaments observed on the SIR-A image (Figure 4-5) are mapped in Figure 4-7. Linear valleys or alignments of valley segments in the Appalachian Plateau area that are 15 km or greater in length correspond mostly with mapped faults from published sources. The faults and directional trends mapped in Figure 4-7 are listed in Table 4-1. Numerous lineaments in the Plateau area that range from 1 to 12 km are oriented parallel to a fault trend. Six linear valleys or aligned valley segments that range in length from 6 to 14 km are labeled in Figure 4-7 and tabulated as major lineaments (Table 4-1). Large numbers of minor linear valley segments mapped in Figure 4-7 range from 1 to 4 km in length.

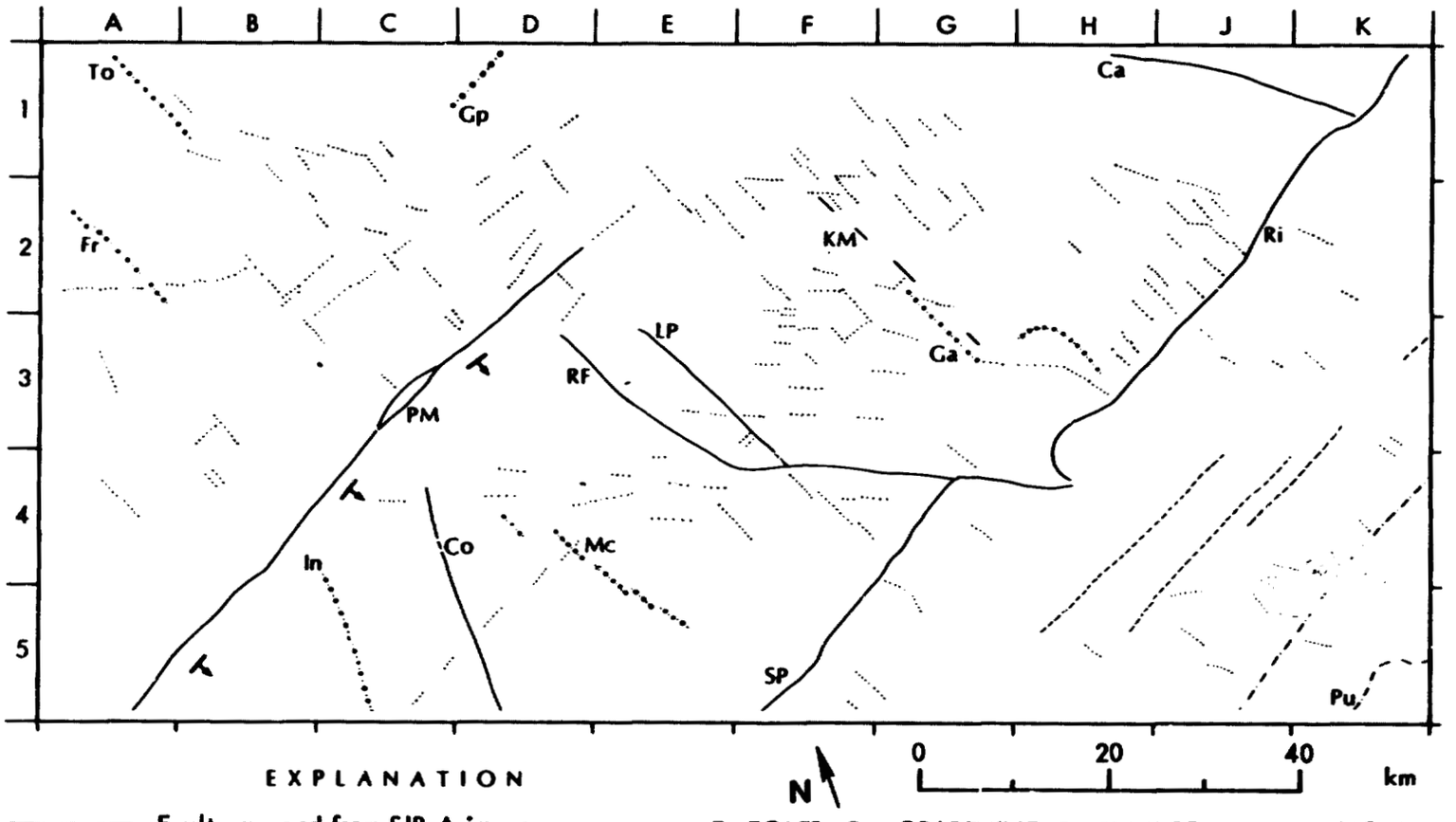

Figure 4-7. Lineament Map of Appalachians From SIR-A Image

Table 4-1. Directional Trends of Appalachian Lineaments

Fault	Trend	Length of Major Topographic Lineaments, km	Minor Topographic Lineaments	
			No.	Av. Length, km
Canebrake (NW segment)	N67°W	–	36	1.8
Russel Fork (SE segment)	N67°W			
Canebrake (SE segment)	N58°W		13	2.6
Russel Fork (NW 6 km)	N28°W	Toler, 8 Frasure, 10	65	2.0
Little Paw Paw	N28°W	McClure, 12		
Keen Mountain	N28°W	Garden, 6		
Coeburn	N7°E	Indian Creek, 14	5	2.6
Pine Mountain (SW segment)	N59°E	Grapevine, 6	14	1.9
Pine Mountain (NE segment)	N71°E		12	2.3
Richlands St. Paul Saltville Pulaski	N64°E ↓ N64°E	*Major ridge crests (15 km upward)		

*Major ridge crests are omitted on Figure 4-7.

The parallelism of the major and minor lineaments with the mapped faults suggests that the lineaments are structural in origin. This is supported from the observations that the Toler Creek, Grapevine Creek, and Frasure Creek lineaments (Figures 4-5 and 4-7, A1, D1, and A2) are oriented approximately parallel to structural contours drawn on the subsurface Ohio Shale (Fulton, 1979). These three lineaments also trend nearly parallel to corresponding linear segments of a strong magnetic gradient in the basement shown on the aeromagnetic map of Kentucky (Johnson, 1980). The intersections of major and minor lineaments adjacent to the Keen Mountain Fault (Figures 4-5 and 4-7, F2 and G2) have been reported to coincide with zones of shattering and exceptionally weak roof rock in

subsurface coal mines in the area (Elder, Jeran, and Keck, 1974). Field work by J. Muskat (1981) has shown that the Indian Creek Lineament (Figures 4-5 and 4-7, C5) is the site of faulted rocks. However, the extent and magnitude of the faulting remains unknown at the time of this writing.

The abrupt change of image tone and texture that extends from K1 to F4 in Figure 4-5 marks the fault zone that bounds the Ridge and Valley area. Major lineaments in the area are formed by the subparallel repetition of the ridges. The pattern denotes the regional strike and suggests repetition of the underlying rock sequences by folding and faulting. For clarity, the major linear ridges are omitted from the map in Figure 4-7. The axes of plunging folds are inferred from lines that join the centers of the curvature patterns on the images. There is no evidence of bedding along the ridges in Figure 4-5, and the distinction between scarp slopes that are steep relative to dip slopes that are more gentle is obscured by the bright radar returns from the foreslopes. The above factors prevent recognition of the dip directions from the image. Numerous short lineaments up to about 5 km in length are formed by narrow valleys that transect the major ridges. If these lineaments have a structural significance, it is not apparent from this study.

A map of linear features (not shown here) was drawn from the Seasat SAR images (Figure 4-6) for comparison purposes. The map shows that most of the major topographic lineaments that are mapped in Figure 4-7 from the SIR-A image (Figure 4-5) were also perceived and mapped from the Seasat SAR images. However, most lineaments that are less than 15 km in length in the Appalachian Plateau cannot be located on the Seasat SAR image because of layover. The minor lineaments in the Ridge and Valley area that transect the direction of regional strike are rotated on the Seasat SAR image (Figure 4-6) relative to their corresponding position on the SIR-A image (Figure 4-5) because of image distortion, which is extreme in the Seasat case.

Drainage mapping from the SIR-A image (Figure 4-5) provides an incomplete distribution of the stream channels in the area. Segments of the low-order channels are not perceptible on the image if they are narrower than the image resolution (40 m), or if they are oriented nearly parallel to the direction of scene illumination. In both instances, there is insufficient tonal contrast on the image for channel perception. This prevents the identification of many

headwaters that rise in both the Plateau and the Ridge and Valley areas. Drainage divides cannot be located and consequently the directions of regional drainage cannot be determined from the image. Drainage mapping from the Seasat SAR image (Figure 4-6) by contrast is virtually impossible. Layover and rotation of the slopes distorts or obliterates channels of the low-order streams. Only portions of the trunk streams in the Ridge and Valley area are more readily perceptible. This is probably due to the higher resolution (25 m) of the Seasat SAR.

Numerous Landsat Multispectral Scanner (MSS) and Return Beam Vidicon (RBV) images of areas that correspond to SIR-A and Seasat SAR coverage were examined for comparison. The best images for lineament and drainage mapping are those where the topography is enhanced by low-angle solar shadowing. This occurs on cloud-free images acquired between November and February when the local sun elevation angle ranges between 22 and 28 deg at the time of image acquisition. Examples of the best MSS and RBV images are given in Figure 4-8. Lineament mapping from these images generally shows an equivalent or better perception of the major and minor topographic features mapped from the SIR-A image (Figure 4-5). A notable exception occurs where minor features strike in a sector that is within about ±5 deg of the sun illumination (about N30°W). In this narrow sector, the minor linear features are suppressed because of insufficient image contrast. In this instance, the narrow sector coincides with the strike of the major proportion of lineaments mapped from the SIR-A image in the Appalachian Plateau area (Figures 4-5, 4-7, and Table 4-1). The selective suppression of linear topography that strikes in this sector is more severe on the MSS image (80-m resolution) than on the RBV image (30-m resolution). During March through October, when the sun illumination direction is further to the east at image acquisition time, the sun elevation angle is higher and topographic enhancement by shadowing is less effective.

This analysis of SIR-A and Seasat SAR images of uniformly forested, steeply sloping surfaces shows that the relationship between the radar look angle (at the antenna) and the angle of surface slope in the direction of radar illumination is of prime importance to the perception of linear topographic features. Maximum topographic enhancement occurs at low incidence angles, where the radar is most sensitive to slope effects. The radar look angle must always exceed the surface

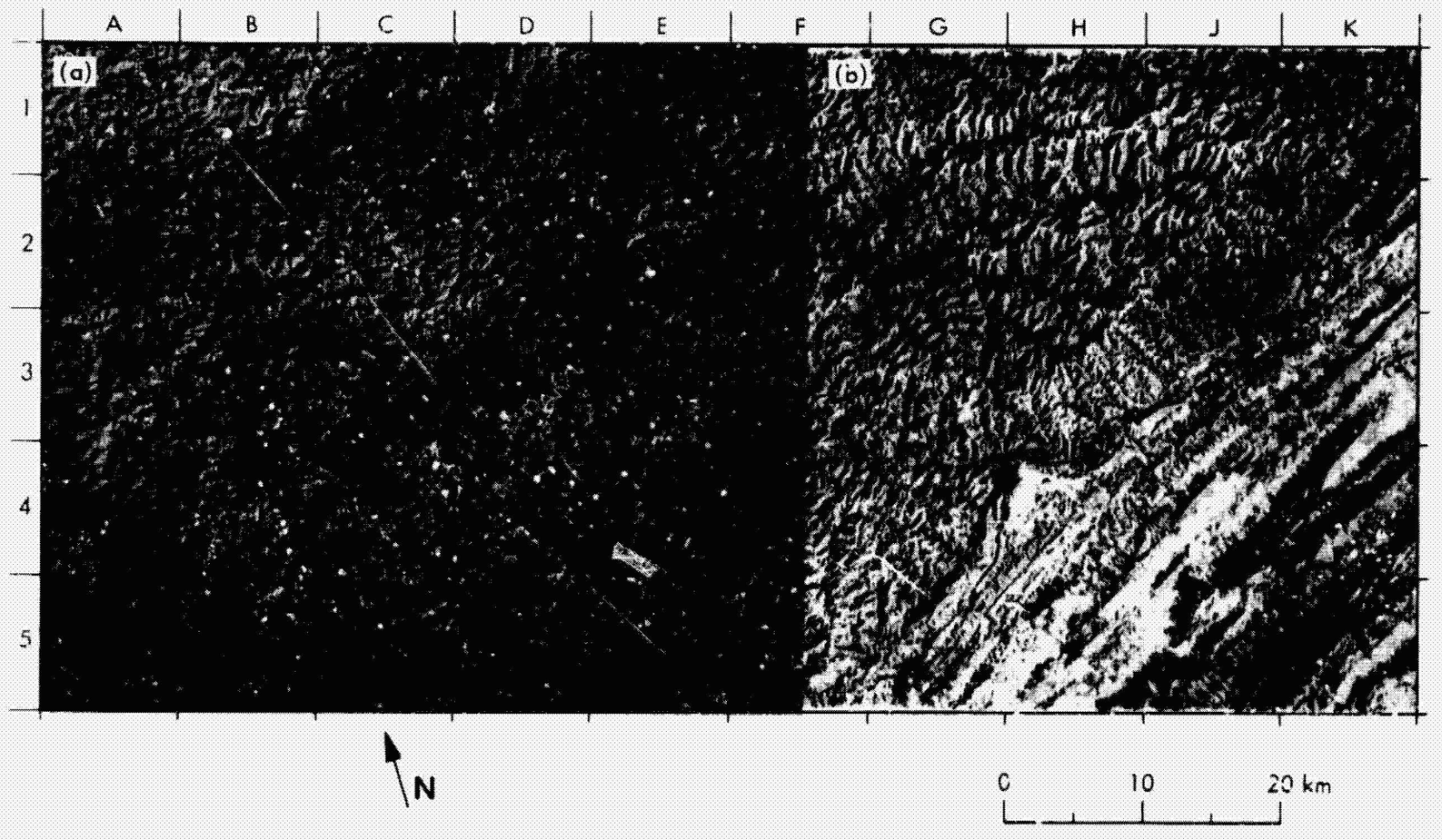

Figure 4-8. Images of Appalachian Plateau, Kentucky and Virginia: (a) Landsat RBV Subscene, ID 30319-15321-b, Acquired January 18, 1979; (b) MSS Band 5 Subscene, ID 1173-15371-5, Acquired January 1, 1973. Sun Elevation 24°, Azimuth 149° (N31°W)

slope angle by a discrete amount to avoid layover or excessive relief displacement. An imaging radar with a variable look angle is required to obtain a uniformly low range of incidence angle through the variable range of slope angle that occurs in terranes such as the Appalachian Plateau and the Ridge and Valley areas. The comparisons of the geological mapping capability made here from the SIR-A and the Seasat SAR images (Figures 4-5 and 4-6), and the Landsat RBV and MSS images (Figure 4-8), further emphasize that feature perception depends strongly in each case on the geometry and direction of scene illumination.

D. VOLCANIC FIELD EAST OF RATON, NEW MEXICO
(H. Masursky, U.S.G.S.)

The radar image in Figure 4-9 shows the volcanic field east of Raton, New Mexico (C3). The brightest feature in the area is Sierra Grande (G3/H3), a large extrusive mass of dacitic volcanic rocks, which have a higher silica and alumina content than common basaltic lava flows. The coarse fragments (several centimeters) that form the talus are of the proper size to produce a bright radar return. Southwest of this feature is Eagle Tail Mountain (C5), a volcanic center surrounded by lava flows of basaltic composition. The outer edges of the lava flows chilled during eruption and broke up under the pressure of subsequent flows (autobrecciation) to produce the bright outline of each lava flow or eruptive center. Smaller masses of dacite (some of which are vents, some intrusive bodies, D4 and D5) also give bright radar returns due to the coarse fragment size. The basaltic flows have a low return except for the outer rims. Basaltic dikelike bodies, vent areas, and pyroclastic cones have bright radar returns also because of similar autofragmentation and mass wasting that produce the proper block size. Thus, two factors in the igneous rocks affect the radar brightness: (1) increasing silica content produces larger, brighter fragments, and (2) physical parameters like cooling and autofragmentation produce larger, brighter blocks. Some of the Mesozoic sedimentary rocks at the west end of the area and Recent stream-channel deposits near the east end also give bright returns. Figure 4-10 is a geologic map of the Raton area.

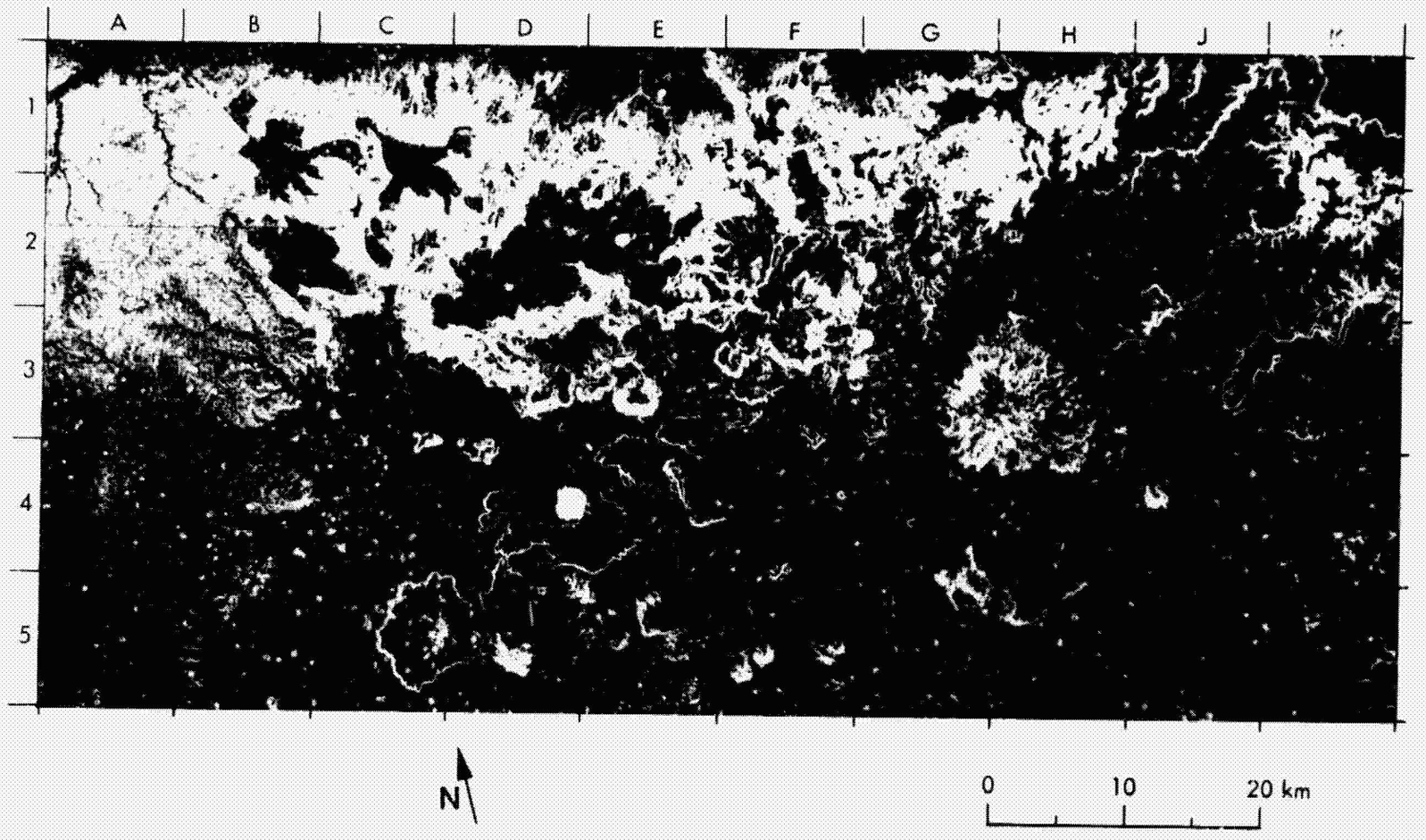

Figure 4-9. SIR-A Image of Volcanic Field West of Raton, New Mexico (Data Take 24B)

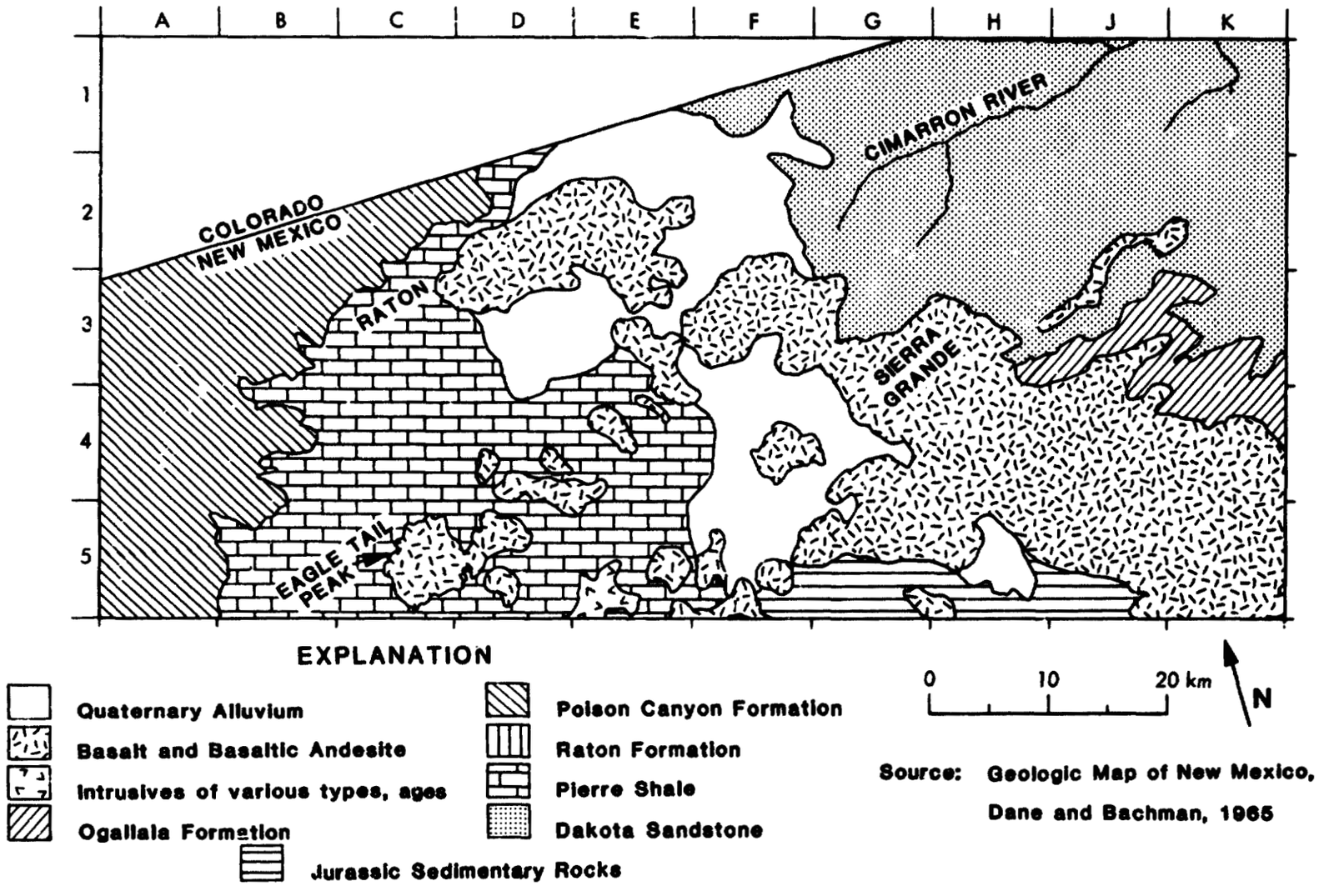

Figure 4-10. Geologic Map of Volcanic Field West of Raton, New Mexico

E. GEOLOGIC FEATURES NEAR BATTLE MOUNTAIN, NEVADA (H. Masursky, U.S.G.S.)

The radar image (Figure 4-11) from data take 24A beautifully displays the basaltic rocks east of Battle Mountain (H4), Nevada, in the Sheep Creek Range (J2 to K2 through J3 to K3). This is the thickest section (about 300 m) of basaltic lava flows (Malpais Basalt) in the north-south trough that extends for about 200 km to the south. These flows and feeder dikes exhibit one of the largest magnetic anomalies in North America and have a radiometric age of 14 million years (Miocene). The basaltic trough is transected by the Humboldt River (G2/H2 to J4); its valley is filled with Pleistocene and Recent sediments. Stream meander patterns in the valley show nicely on the image. South of the river, outcrops of the Slaven Chert (J4/J5) of Devonian age, part of the upper plate of the Roberts thrust, are shown. Barite deposits occur in quarries in the chert south of Argenta Point (K4). Tilted basaltic flows are exposed in the cliffs along the Argenta Rim (K4) where they uncomformably overlie the Paleozoic cherts. The range front faults of Pliocene to Recent age cut these rocks and are defined by the cliff faces. The siliceous sinter deposited by the Beowawe geysers lies near the south edge of the image. These rocks near the geysers have been drilled as a possible source of geothermal energy. The thick basaltic flows have been studied as a possible repository for nuclear wastes. The high heat flow and the mobile hot ground water in this region make this use unlikely.

To the east and west of Battle Mountain, the linear mountain ranges and sediment filled valleys of the Basin-Range system are displayed. There has been movement at places along these young bounding faults in the last several years.

F. X- AND L-BAND IMAGERY ALONG THE MOTAGUA FAULT, EASTERN GUATEMALA: A COMPARISON (L. Dellwig, U. of Kansas)

As a result of the Guatemalan earthquake of February 4, 1976, interest in the use of radar imagery to study the effects of faulting and to identify faulting not recorded by other remote sensing devices led to the acquisition of airborne X-band radar imagery along the Motagua Fault southwestward from the Gulf of Honduras.

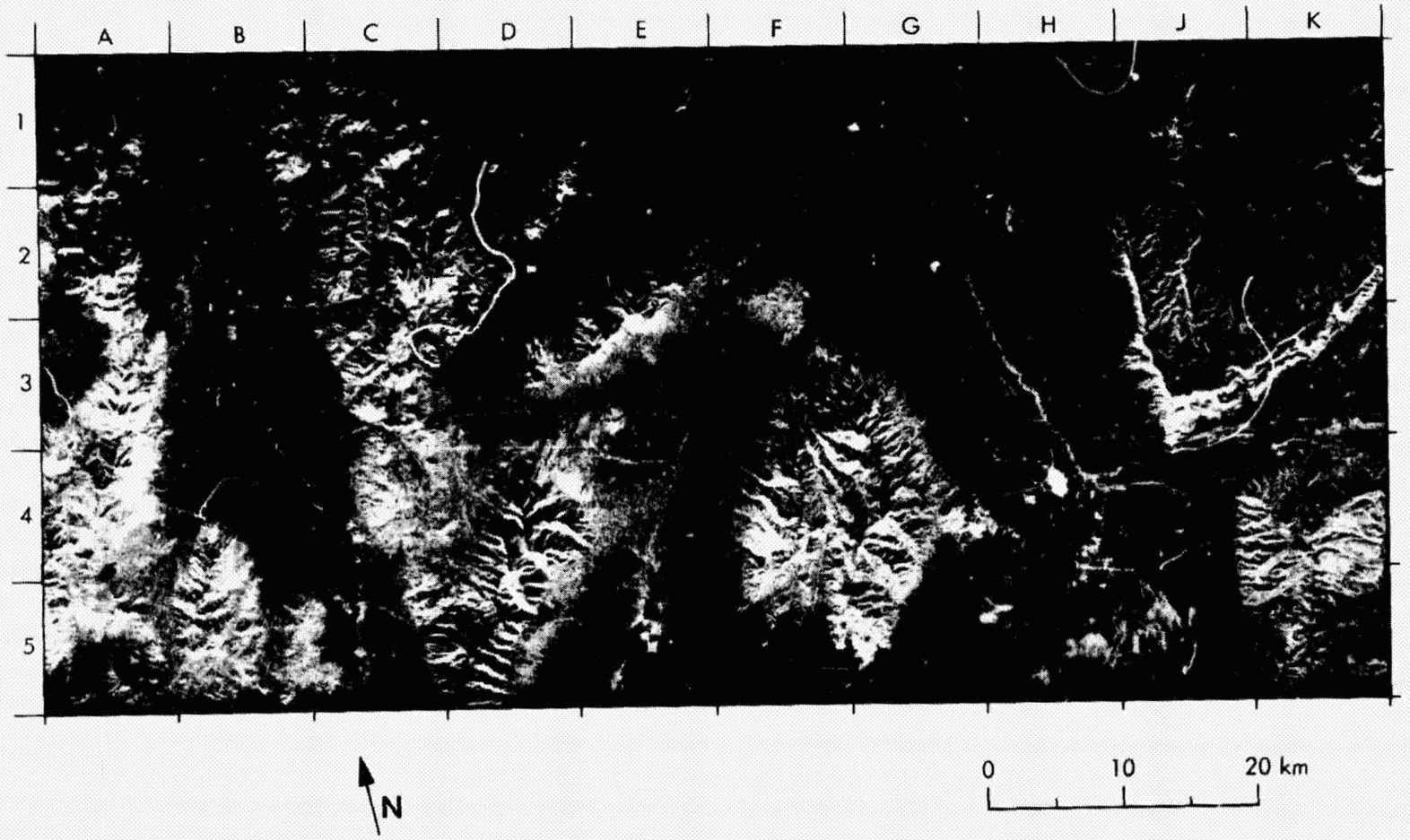

Figure 4-11. SIR-A Image of Battle Mountain, Nevada (Data Take 24A)

Figure 4-12(a) shows the X-band image and Figure 4-12(b) shows the SIR-A (L-band) image north of Rio Motagua along the Gulf of Honduras. The higher look angle of the X-band airborne imager results in enhancement of the drainage network in an area of low relief by providing a strong return from the near-range side and a shadow on the far range side of the high vegetation adjacent to the drainage channels (Figure 4-13) (Dellwig, Bare, and Gelmett, 1978). Along only a single stream channel (other than the Rio Motagua) is it possible to map the drainage on the SIR-A image. In this instance, identification apparently results from partial penetration of the vegetation and specular reflection from the channel itself, but this channel is more precisely defined on the airborne radar image by a high return-shadow signature.

However, north of the river at the eastern end of the Montanas del Mico (X-band, Figure 4-14(a) and SIR-A L-band, Figure 4-14(b)) where elevations reach up to 1000 m, the advantage of the 50-deg incidence angle is obvious. This area, viewed in the far range (up to 76-deg incidence angle) of the X-band image, is subject to a high percentage of shadowing and a consequent data loss. Although the incidence angle of the SIR-A image approaches grazing on some slopes, there is almost no data loss in the far-range portion of the L-band image.

In the near-range portion of the X-band image, the incidence angle of approximately 45 deg approximates that of the SIR-A image (approximately 50 deg) and the percentage of shadow is significantly reduced. Although there is only a small difference in incidence angle, the SIR-A image suffers significantly less data loss without a noticeable increase in foreshortening.

Recognizing the possibility of vegetative changes between the overflights, a 180-deg difference in look direction, and the contrasting system parameters, comparison of these two images well documents the need for variable incidence angles for maximum data extraction. Continuing analysis and comparison of these images will result, hopefully, in the development of an understanding of the strongly contrasting tone-texture vegetation signatures throughout the images.

G. COMPARISON OF SIR-A IMAGERY AND AIRCRAFT RADAR IMAGERY, PANAMA (H. MacDonald, U. of Arkansas)

The SIR-A imagery illustrated in Figure 4-15(a) is from the Darien Province in east-central Panama. The climate is tropical, the vegetation canopy continuous,

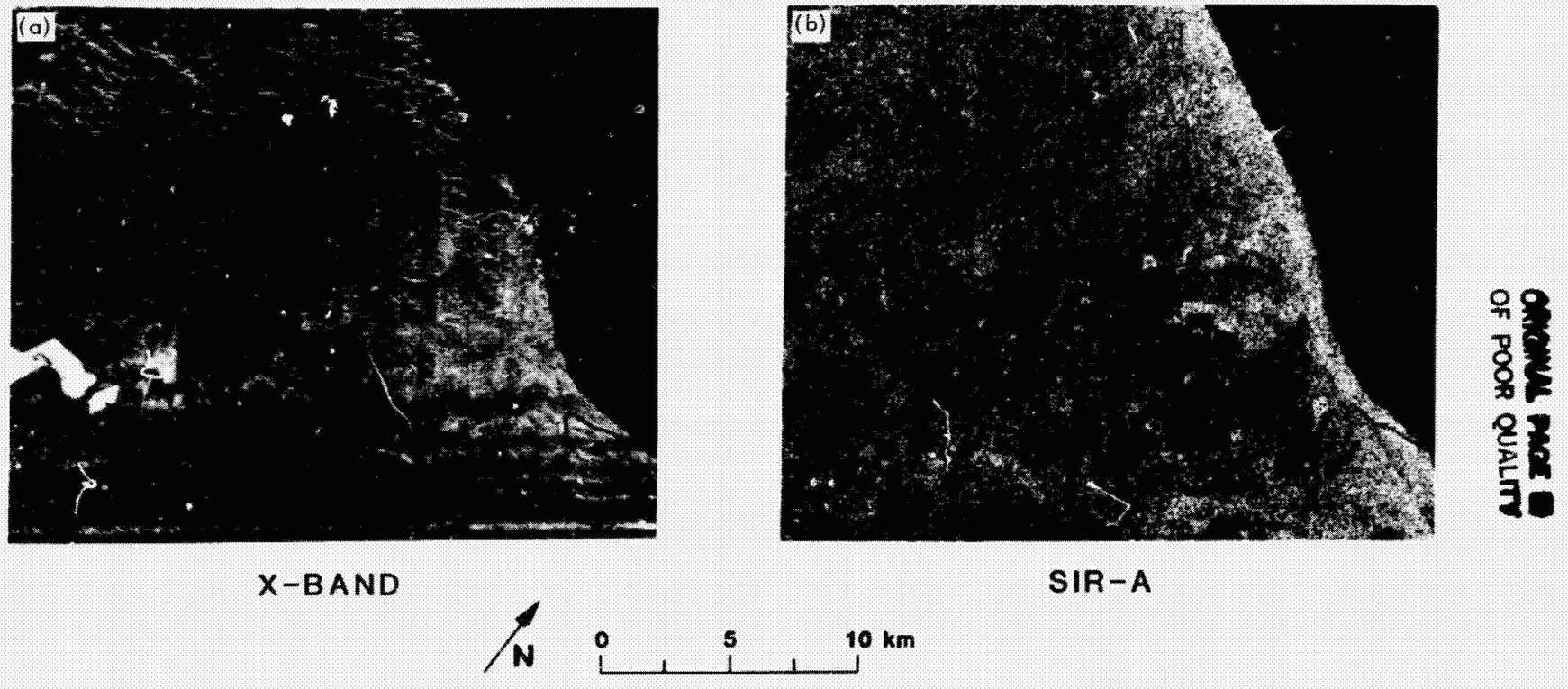

Figure 4-12. Eastern End of the Motagua Fault Along the Rio Motagua, Guatemala: (a) X-Band Image; (b) L-Band Image (SIR-A Image is From Data Take 18)

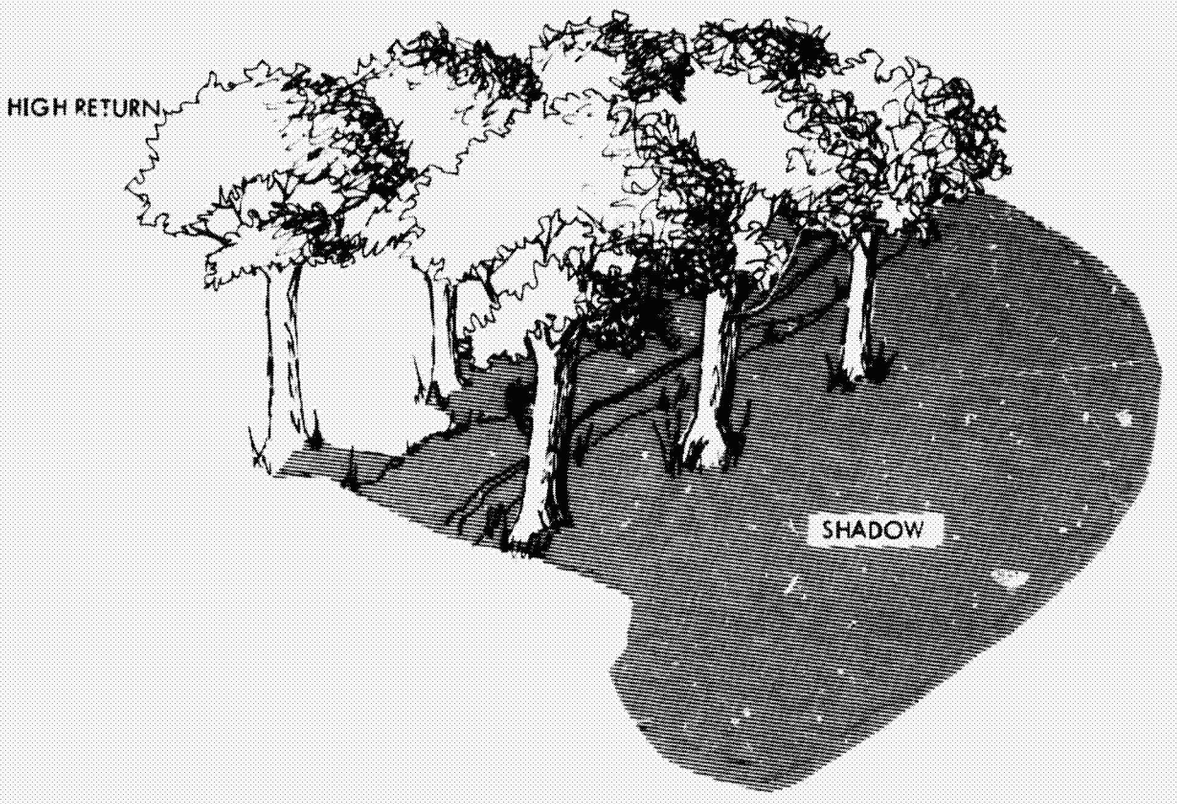

Figure 4-13. Schematic Diagram Showing the Manner in Which an Otherwise Concealed Drainage Control (Shown by Lines on Ground Between Trees) is Revealed in a Radar Image by the Combination of a High Return From the Near-Range Side and a Shadow Zone on the Far-Range Side of the Bordering Vegetation

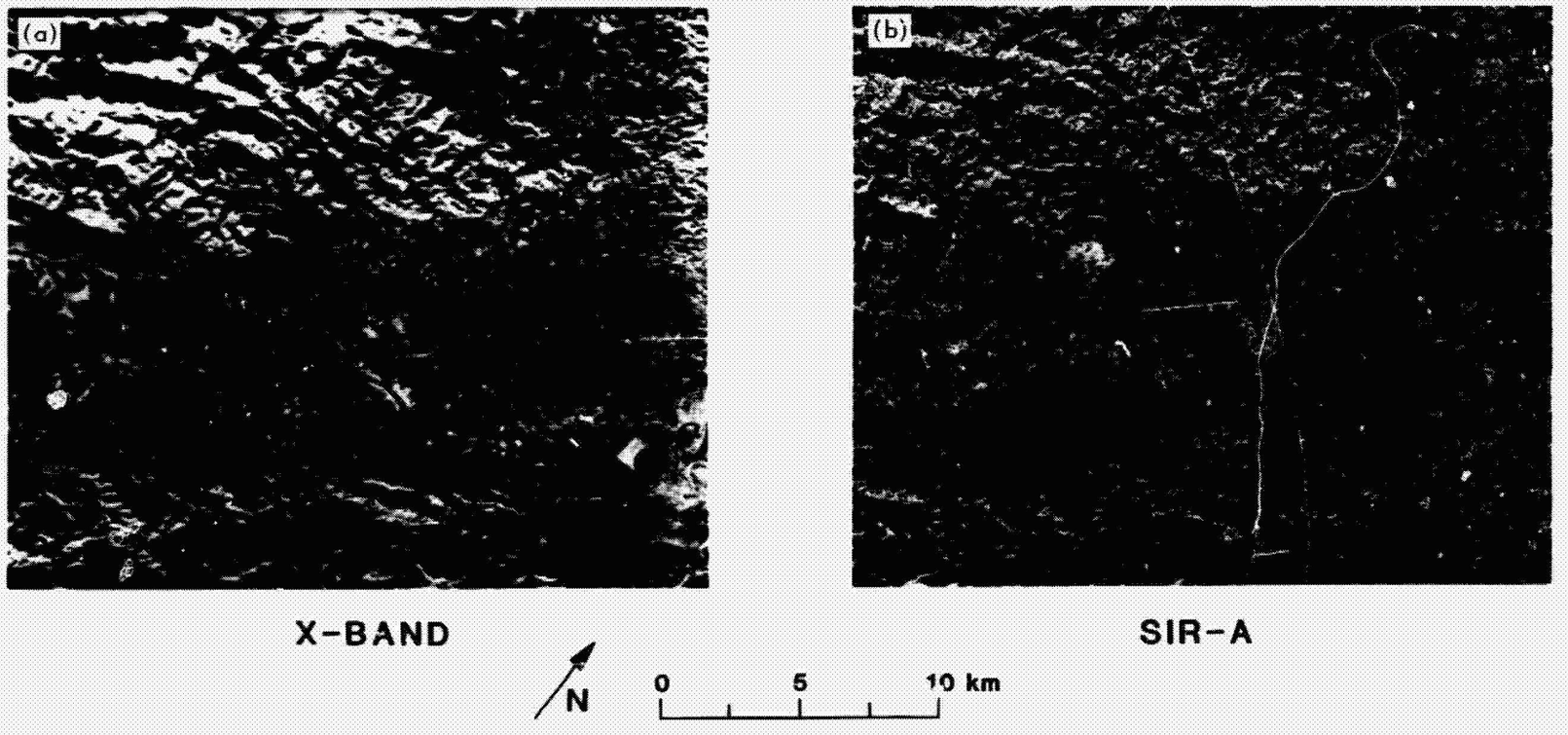

Figure 4-14. Rio Motagua, Guatemala, approximately 10 km West of the Area Shown in Figure 4-12(a): (a) X-Band Image; (b) L-Band Image

Figure 4-15. Darien Province, Panama: (a) SIR-A Image (Data Take 24C); (b) K-Band Aircraft Radar Image

and the terrain marked by extremes of inaccessibility. Roads do not exist in most of the region; even the Pan American Highway has not been constructed through this part of Panama. Obtaining Landsat imagery or photography for geologic mapping in Darien Province has met with minimal success because of the almost perpetual cloud cover. This part of Central America serves adequately as an area typical of the tropical, cloudy environments with dense vegetal cover characteristic of many countries in equatorial latitudes where adequate geologic mapping is lacking.

The Rio Turia flows around an isolated anticline (center of Figure 4-15(a)), which may be genetically related to a fold belt of north-trending en echelon anticlines (lower right, Figure 4-15(a)). Although there have been no significant oil or gas discoveries in this part of Panama to date, these anticlinal features represent classical examples of the landform expression of geologic structures commonly associated with hydrocarbon accumulation.

Figure 4-15(b) is the product of a high-resolution K-band radar system. This imagery, obtained from an aircraft, provides a slant-range display that progressively incorporates compression of scale in the near range; thus the differing geometries of Figures 4-15(a) and 4-15(b). In the middle part of the K-band imagery (anticline at top center of Figure 4-15(b)), the look angles range from 67 to 63 deg. In contrast, the same terrain was imaged with the Shuttle radar at a look angle of approximately 47 deg (Figure 4-15(a)). The more shallow "illumination" angle provided by the aircraft radar allows enhancement of the subtle terrain features by radar shadowing. This aspect is especially evident on the K-band imagery (Figure 4-15(b), left center), where several steeply dipping, thinly-bedded rock units are expressed as distinctive hogback landforms. These same features are not well expressed on the Shuttle SIR-A imagery (Figure 4-15(a)).

The use of radar imagery to identify plant communities often requires identification keys comparable to those used for photo interpretation of the same features, namely tone and texture. Relatively short-wavelength radar systems (K-band, for example) are generally more sensitive to the uppermost surface roughness of a vegetation canopy. In contrast, longer-wavelength systems, such as the SIR-A L-band radar, are more influenced by a combination of initial surface and the underlying vegetation volume. What appears to be a decrease in the perception of tonal and textural contrasts at longer wavelengths is event when

comparing Figures 4-16(a) and 4-16(b). Boundaries between mangrove swamps (upper left, just north of the rivers), swamps with grasses and low trees (left center), and jungle vegetation are better defined on the K-band imagery than on the Shuttle SIR-A imagery.

The higher resolution of the K-band radar (15 m), as contrasted with the SIR-A radar (40 m), does not appear to significantly impact geologic interpretation. However, smaller streams with narrow channels that are detectable on the K-band imagery are not obvious on the Shuttle radar. See, for example, the small streams entering the Rio Turia, especially in the upper left of Figures 4-16(a) and 4-16(b).

H. THE VIRGINIA DALE RING-DIKE COMPLEX: A COMPARISON OF LANDSAT, SEASAT, AND SIR-A IMAGERY (H. MacDonald, U. of Arkansas)

The purpose of this study is to compare SIR-A imagery with Landsat and Seasat imagery for the interpretation of geologic features within the Virginia Dale ring-dike complex along the Colorado-Wyoming Front Range. The complex is centered astride the extreme south end of the Laramie Range, at its junction with the Colorado Front Range, on the Colorado-Wyoming border. The ring-dike complex intrudes folded metamorphic rocks and is deeply eroded.

On both the Landsat image (Figure 4-17(a)) and the Seasat image (Figure 4-17(b)), a lineament approximately 30 km in length is detected between points E and F. This same lineament does not appear on the SIR-A imagery (Figure 4-17(c)). Its nondetectability on the SIR-A imagery is directly related to the Shuttle radar's look direction. The lineament is oriented at approximately N13°E. The SIR-A radar look direction is N10°E, or nearly parallel to the linear feature. The Landsat look direction (solar azimuth) is N31°W, and the Seasat radar look direction is N68°E. Both Landsat and Seasat images provide enhancement of landforms as the angle between illumination (look direction) and landform increases from parallelism to orthogonality.

An additional example of look-direction bias can be seen within the ring-dike complex on Figure 4-17(c). The arrows on the SIR-A image show the trend (N50°W) of fracture patterns in this igneous complex. However, this same fracture pattern is completely suppressed on the Landsat image where the solar azimuth (look direction) is nearly parallel to the fracture pattern. Similar to

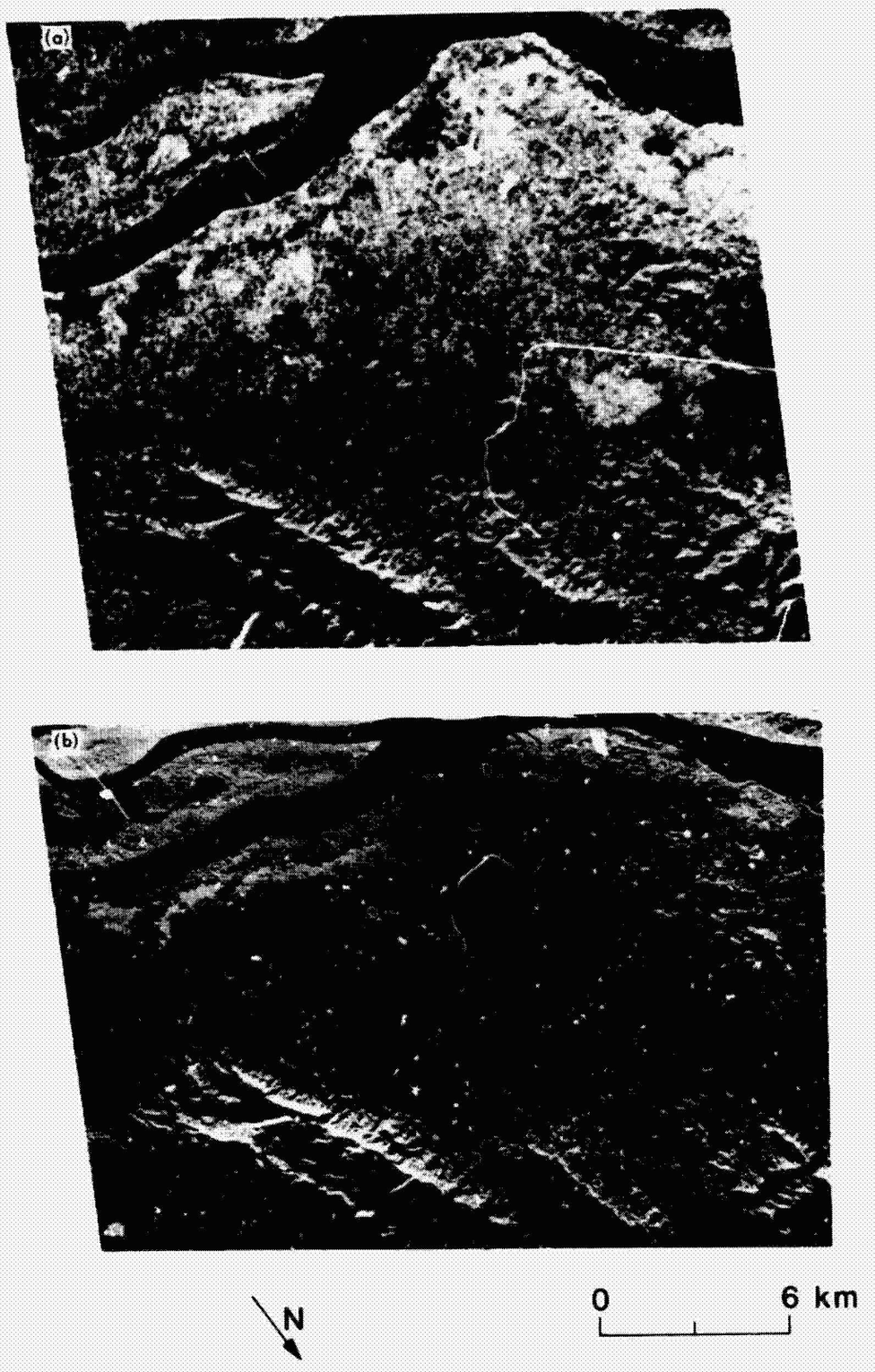

Figure 4-16. Enlargement of Figure 4-15 Imagery: (a) SIR-A; (b) K-Band

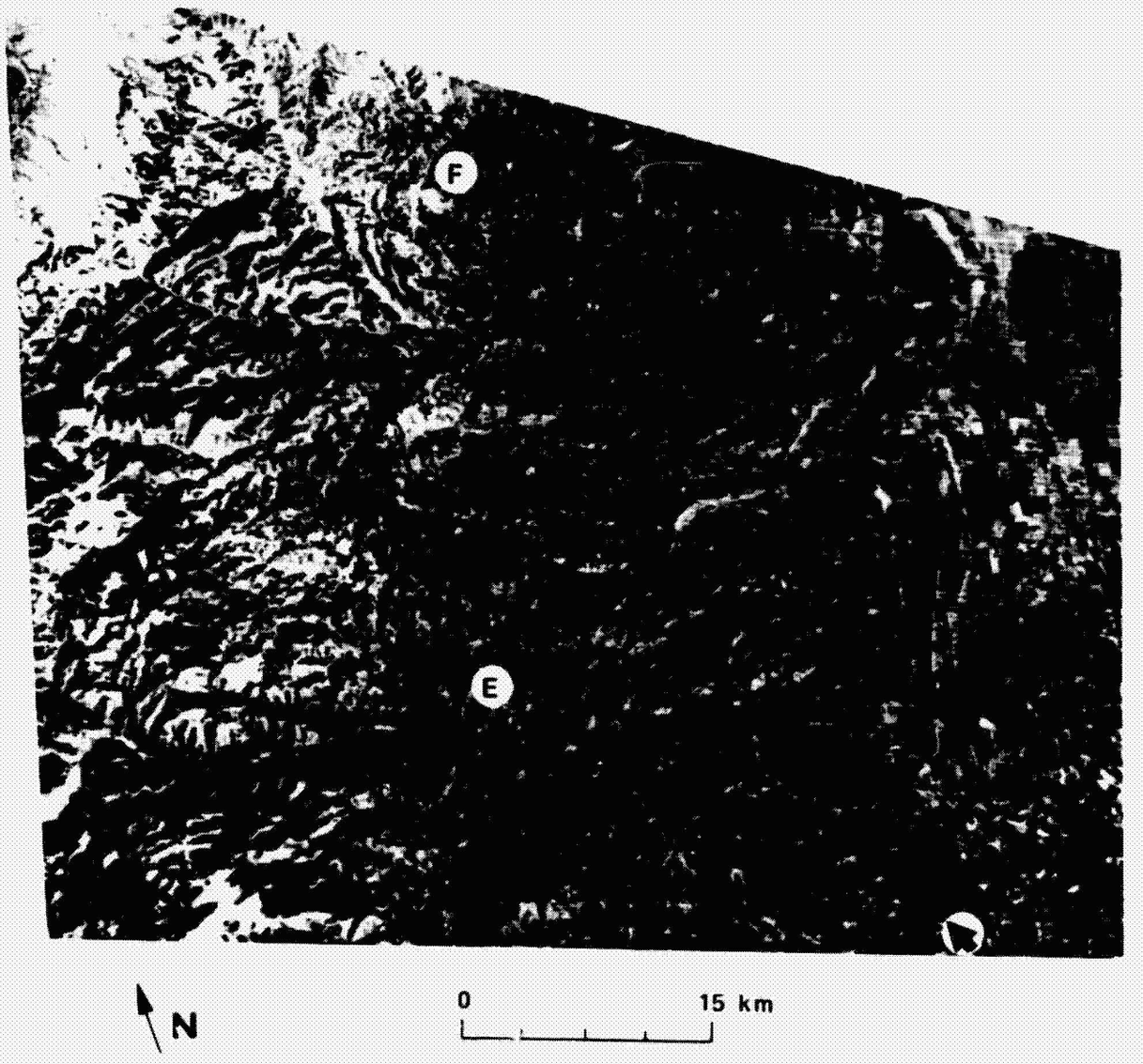

Figure 4-17. Virginia Dale Ring-Dike Complex: (a) Landsat Imagery (Band 7) Taken December 1976; The Solar Elevation was 20 deg Above the Horizon With an Azimuth of 149 deg (Indicated by Arrow, Lower Right Corner); ID 2690-16500

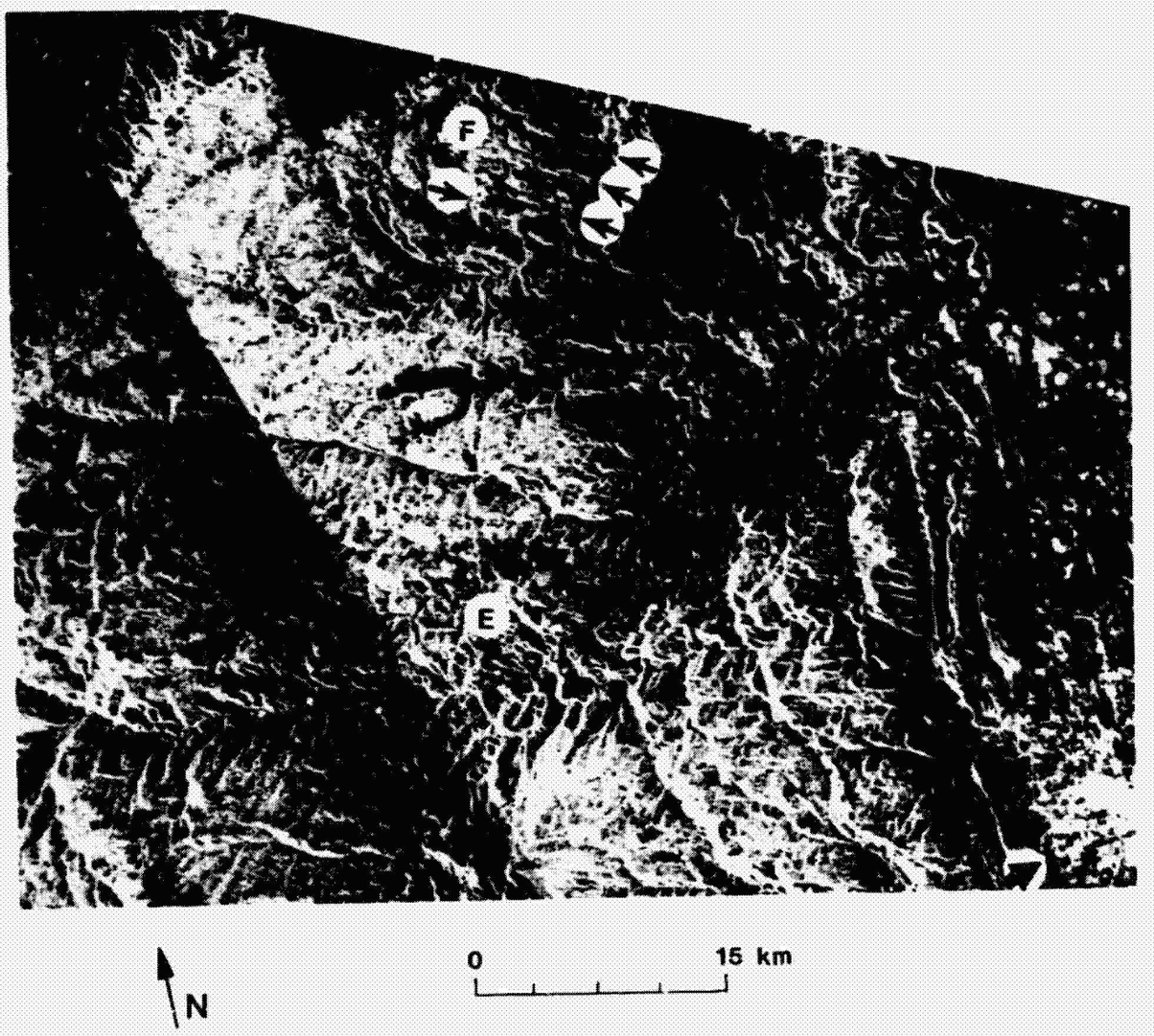

Figure 4-17. Virginia Dale Ring-Dike Complex: (b) Seasat Imagery Taken August 1978 (Rev. 580); The Depression Angle was Centered Around 67 deg With a Look Direction Toward N68°E (Indicated by Arrow, Lower Right Corner)

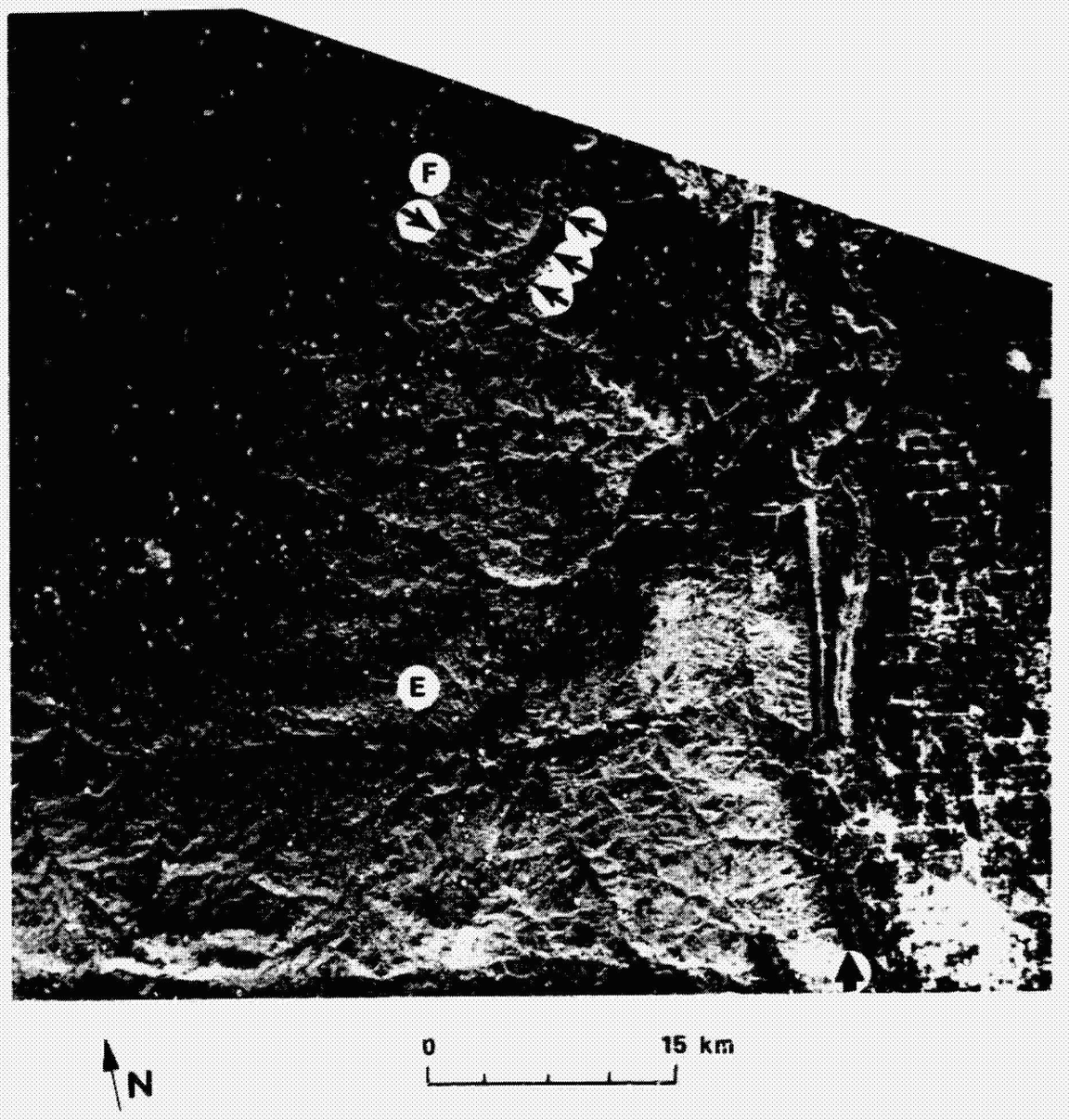

Figure 4-17. Virginia Dale Ring-Dike Complex: (c) SIR-A Imagery, Data Take 24A; The Depression Angle was Centered Around 40 deg With a Look Direction Toward N10°E (Indicated by Arrow, Lower Right Corner)

the SIR-A image, the Seasat image provides these fracture patterns because the angle between look direction and feature is approximately 60 deg.

Topographically expressed lineaments were mapped from the entire area on all three images. A total of 435 lineaments were interpreted from the Landsat imagery, while the Seasat and SIR-A imagery produced totals of 226 and 217 lineaments, respectively. The differences in the number of lineaments is related to differences in both look directions and depression angles. Landsat had a relatively low solar elevation of 20 deg (equivalent to the radar depression angle), which enabled subtle topographic relief to be enhanced by shadowing. Seasat and SIR-A both had relatively smaller look angles (23 and 40 deg, respectively), which decreased shadowing and, therefore, suppressed the enhancement of subtle relief.

Observations from this study indicate that in situations where the SIR-A and Landsat look directions approach orthogonality, they serve to complement each other.

I. SEASAT/SIR-A DIGITAL REGISTRATION OVER NORTHEASTERN ALGERIA

(Ph. Rebillard, NRC-JPL Research Associate)

Few places outside the U.S. were covered by both Seasat and SIR-A, among them the Chott Merouane and the Chott Melrhir (Northeastern Algeria) are intersected by Seasat Rev. 791 and SIR-A data take 32-33 (Figure 4-18).

The Chott Merouane and the Chott Melrhir are located on the northeastern boundary of the Algerian Sahara, 100 km south of the town of Biskra. Center coordinates of the area are 6°30'E and 34°10'N (Figure 4-19). The chotts (or playas) are interior desert basins 40 m below sea level. These salt playas may be covered with a sheet of water in the winter.

This area is of interest because of: (1) the absence of relief, (2) the well-delineated interface between the chotts and sand, and (3) the different backscatterings from the chott floors due to the fact that Seasat and SIR-A data were not taken at the same time of the year.

Since SIR-A was operated in an optical mode, the SIR-A swath covering the area was scanned with a Perkin Elmer microdensitometer PDS (pixel size: 50 μm), digitized (recorded on 256 gray levels), and registered to the Seasat data

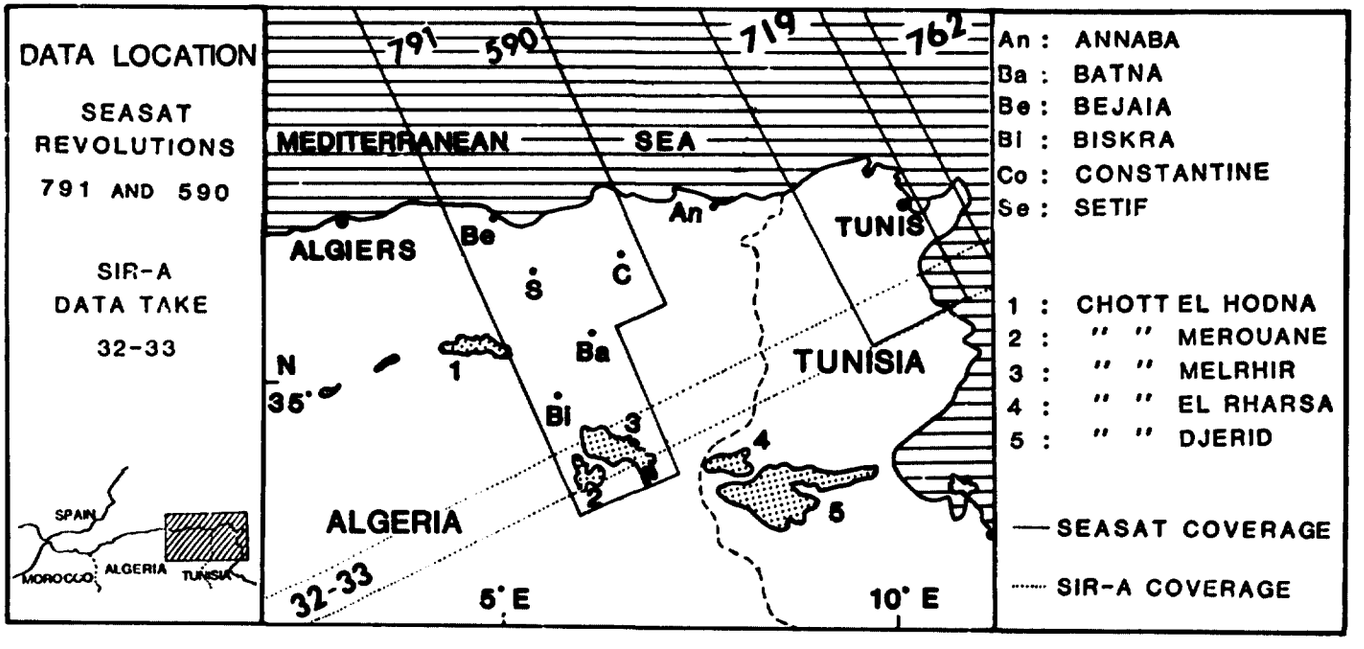

Figure 4-18. Seasat SAR and SIR-A Coverage Over Northeastern Algeria

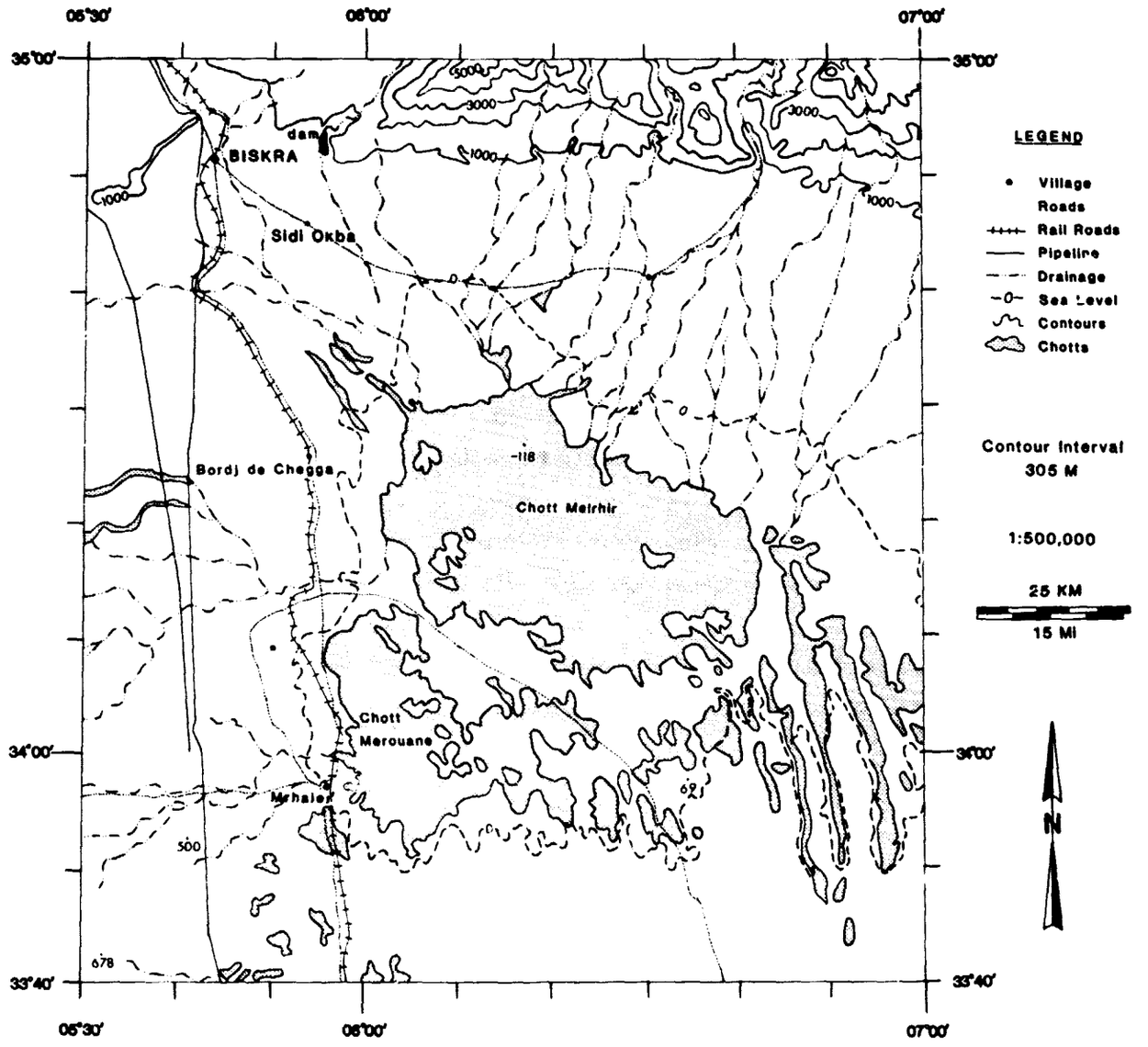

Figure 4-19. Topographic Map of the Chott Merouane and Chott Melrhir Areas, Algeria (From Defense Mapping Agency (1979))

(4800 lines and 2400 samples) using JPL's VICAR image processing program. The registration process consisted of finding common tie points for rotating and sizing one image (SIR-A) to another one (Seasat). About 120 tie points were used at full resolution. The angle between the two paths was 93 deg, but, in the process, the necessary rotation was only 3 deg (due to the way the images were scanned); so from two radar pictures we produced a single radar picture that was taken by two sensors whose look directions were almost perpendicular to each other.

The final product (Figure 4-20) is two images at the same scale emphasizing the role of each imaging radar system. Over this picture, we chose three subareas displayed at full resolution as shown by Figures 4-21(a), (b), and (c).

Figure 4-20 displays the Chott Merouane-Chott Melrhir area as seen by Seasat (top) and SIR-A (bottom). From the left to the right are the Chotts Merouane (B2/C2 through B5/C5) and Melrhir (D1 to H1 through D4 to H4). These salty depressions are surrounded by Quaternary deposits (A1 to B1 through A5 to B5, and D2 to F2 through D4 to F4), or by dunes (F5 through K5). Running north to south from the Aures Mountains, several channels bring alluvium in the Chott Melrhir; some of them are seen in the upper right corner of the figure (J1 to K1). Even though the climate is very arid, some places are inhabited; the Bordj Oum el Thiou- (A1), the Bordjs Ourir and Mraier (A3/B3), and the Bordj Khelil (A5) are examples. These villages are connected by small roads (A1 to A2) or railroads (A1 to B1 and A2 to B2).

There are few changes in the shape of the objects on the two images, which were taken three years apart. A small chott at E5/F5, however, seems to have larger boundaries on the SIR-A data, suggesting a little expansion over the years. The reason for, or the process of, this expansion is not known.

The sandy areas (F5 through J5, and A1 through A5) look the same on both images: they have a coarse texture. At the left, the area presents some lineations with little vegetation.

There is no major change in delineating the Chott Merouane (B3 to C3) according to Seasat or SIR-A data, but the floor of the Chott Melrhir (G1 to J1 through G3 to J3) appears as a dark surface on Seasat data and as a bright surface on the SIR-A picture. A likely explanation is flooding in that region. Also, the change

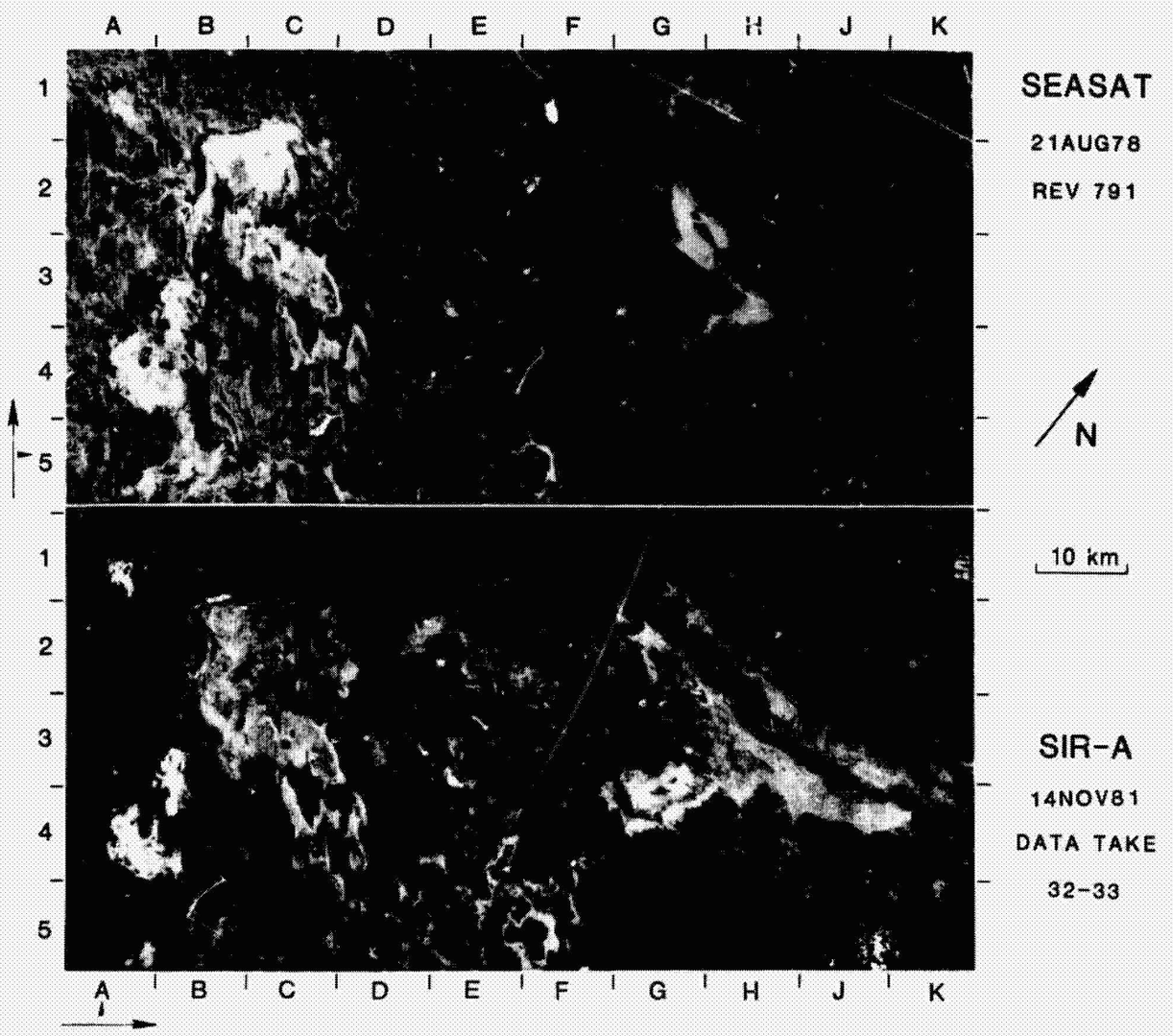

Figure 4-20. Seasat SAR/SIR-A Digitally Registered Images of Chott Merouane, Chott Melrhir Area, Algeria (SIR-A Image is From Data Takes 32 and 33)

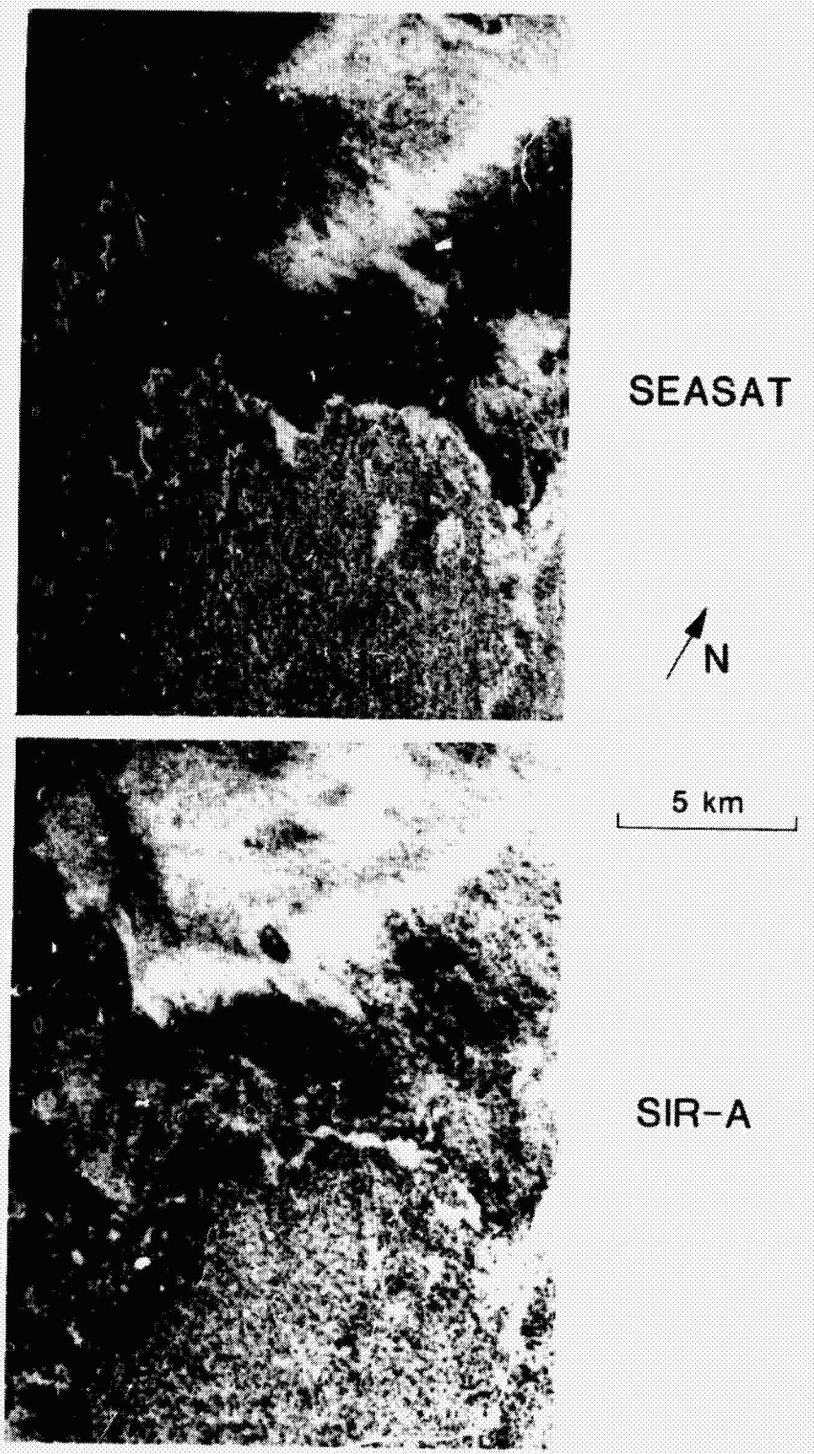

Figure 4-21. Seasat SAR/SIR-A Digital Registration Images at Full Resolution: (a) the Southern Boundary of the Chott Melrhir (Area F4 to G4 on Figure 4-20)

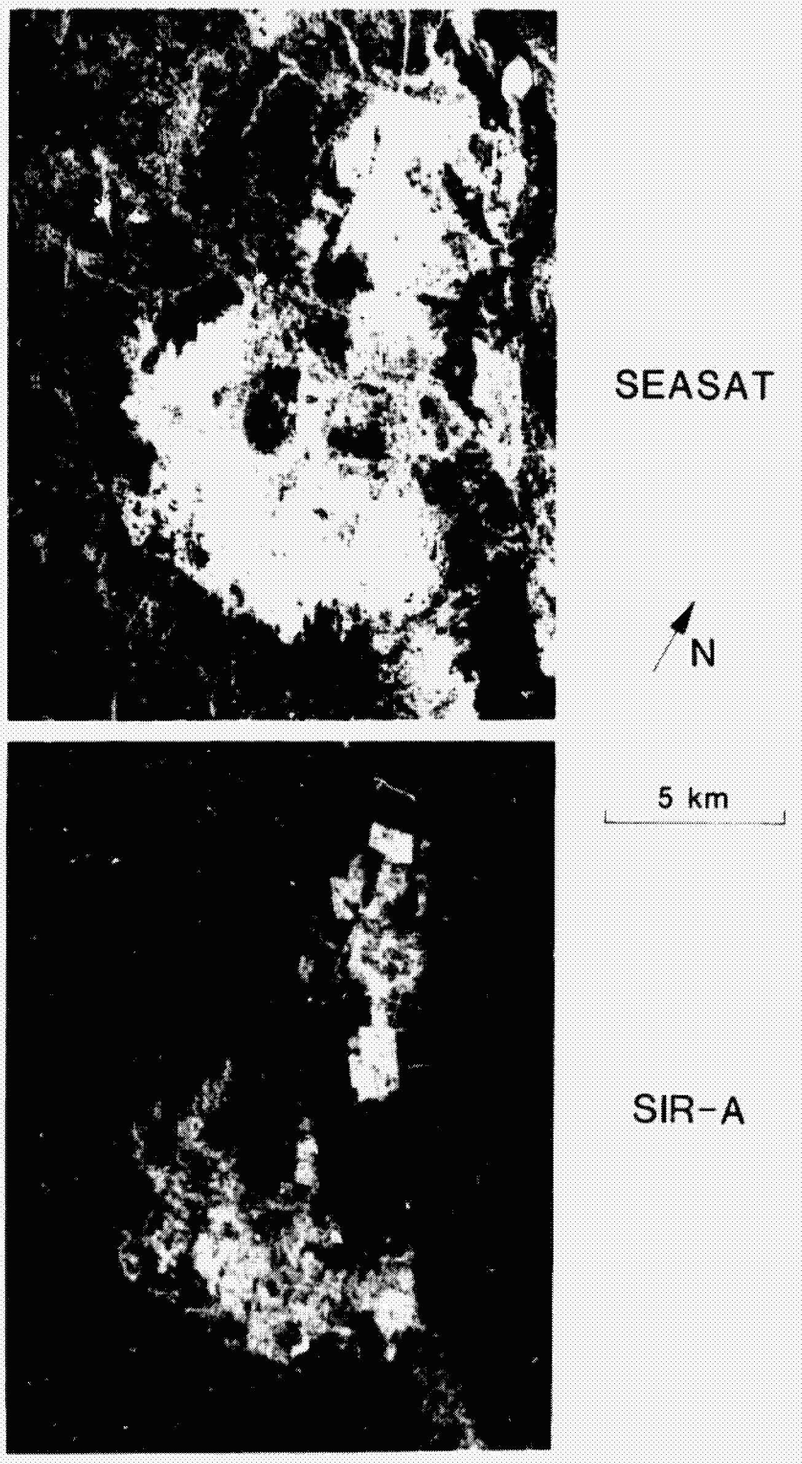

Figure 4-21. Seasat SAR/SIR-A Digital Registration Images at Full Resolution: (b) the Town of Mrhaier (Area A5 to B5 on Figure 4-20)

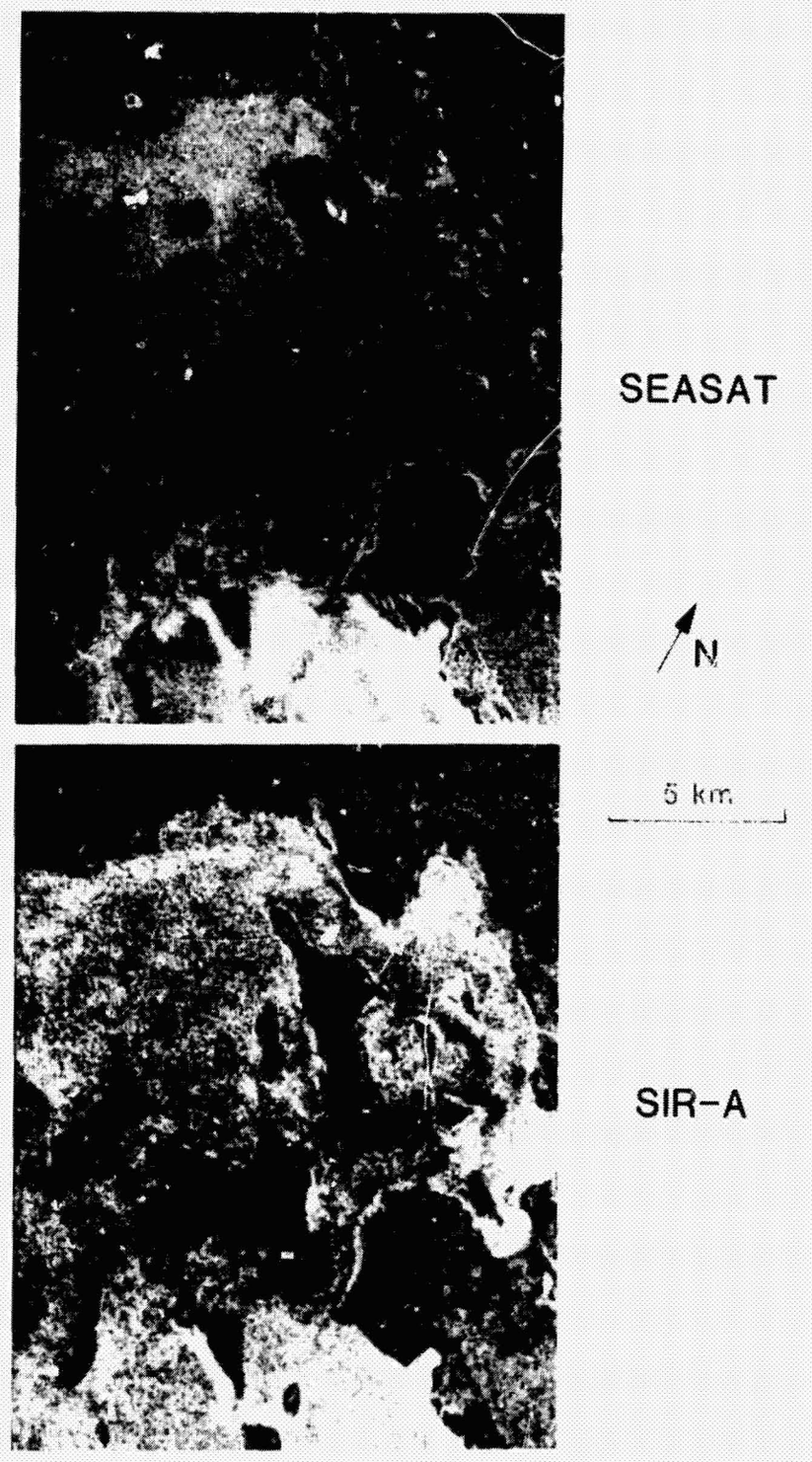

Figure 4-21. Seasat SAR/SIR-A Digital Registration Images at Full Resolution: (c) the Northern Boundary of the Chott Merouane (Area C2 to D2 on Figure 4-20)

in surface appearance could be due to the scattering mechanisms, which give different returns at a 50-deg incidence angle (SIR-A) and a 20-deg incidence angle (Seasat).

Railroads and roads north of the town Mraier are very prominent on the Seasat radar picture (A1 to B1 and A2 to B2) because they are almost perpendicular to the illumination direction. Those bright lines do not appear on the SIR-A data because they are parallel to the SIR-A illumination direction; two other lines (F2 to G2), however, are detected in the SIR-A data and not in the Seasat radar picture. No explanation is presently available for those two lines detected by SIR-A.

Each of the subareas of Figure 4-21 (a through c) is displayed at full resolution and emphasizes the differences between the two radar systems. For instance, three parameters were not the same. They are (1) the resolution, (2) the illumination direction, and (3) the look angle (or depression angle). To display the pictures at the same scale (full resolution), the SIR-A data were expanded to twice that used for the Seasat image; this also amplified the speckle noise that is evident in a comparison of the two. The influence of illumination direction is clearly seen in Figure 4-21(b) at the town of Mraier. The difference between the two incidence angles (Seasat 20 deg and SIR-A 50 deg) may explain the main difference in the aspect of the Melrhir floor in the two pictures. The other possibility would be changes in the surface conditions, such as flooding.

A color image of the registered data was made by displaying Seasat data, SIR-A data, and the ratio (Seasat/SIR-A) in red, green, and blue, respectively (Figure 4-22). Filtering, to remove very-low spatial frequencies, was applied to reduce large-scale shading gradients. Brown-red areas correspond to sand outcrops, blue and yellow colors mark the floor of the chotts, and villages are displayed in yellow.

J. PRELIMINARY EVALUATION OF SIR-A IMAGES OF EASTERN NORTH CAROLINA

(M. D. Krohn and N. M. Milton, U.S.G.S.)

A 50-km swath of the Piedmont and Coastal Plain of North Carolina is covered by data take 24A of the SIR-A mission. The image area extends from north of Winston-Salem on the west, through Durnam, to Ockracoke, a town on the barrier

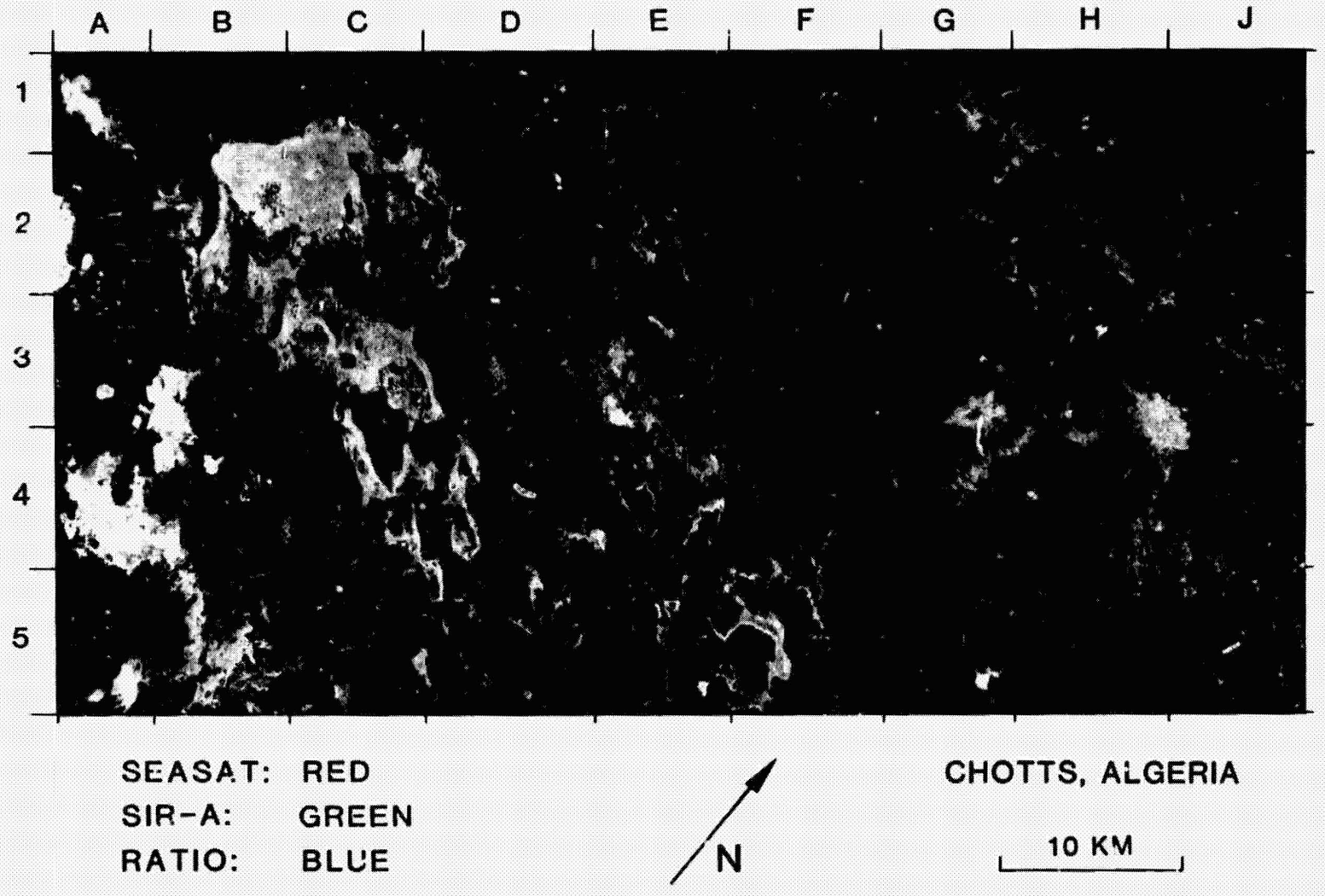

Figure 4-22. Color Image of the Coregistered Data Where Seasat Data, SIR-A Data, and the Ratio (Seasat/SIR-A) are Displayed in Red, Green, and Blue, Respectively

islands along the eastern coastline (Figure 4-23, G4 to H4 and G5 to H5). The SIR-A images are being analyzed as part of an experiment to test the use of radar as an aid to geologic mapping in heavily vegetated areas of low relief. Our hypothesis is that certain forest types, which are recognized by the presence or absence of a single species, have a distinctive relationship to the geology and can be observed on digitally-processed imagery. Prior work with Landsat, Seasat, L-band, and X-band SLAR data was centered in eastern Virginia, approximately 500 km to the north. In this area, two geologic features have been recognized based on the distribution of a chestnut oak forest (Quercus prinus): the Chopewamsic formation, a metavolcanic rock that is a host rock for gold deposits near Mineral, Virginia, and a northwest-southwest linear zone of upland gravel deposits that may be related to a zone of seismicity along the James River (Krohn et al., 1981).

The SIR-A image (Figure 4-23) covers two major physiographic provinces of the eastern United States. The Piedmont Province is composed of metamorphic rocks, primarily argillite, slate, and metavolcanic rocks interspersed with bodies of granite. In this portion of North Carolina, the Piedmont can be subdivided into four belts; from west to east these are the Inner Piedmont, the Carolina Slate, the Raleigh, and the Eastern Slate. In addition, two Mesozoic sedimentary basins are located in this section of the Piedmont: the Durham basin, approximately 20 km wide, and the Dan River basin, approximately 8 km wide. A thick layer of saprolite blankets most of the Piedmont rocks in this section. The Coastal Plain Province is composed of flat-laying sedimentary rocks that extend approximately 200 km inland from the coast. The Province can be subdivided into a western section, composed primarily of the Miocene Yorktown Formation, and an eastern section composed of younger Quaternary sedimentary rocks.

In general, the Piedmont shows less contrast than the Coastal Plain areas in the SIR-A image. This may be due partly to the look direction of the SIR-A radar, which was approximately parallel to the northeast direction of the metamorphic foliation. However, neither the Mesozoic basins nor any of the four metamorphic belts in the Piedmont can be discerned with any degree of confidence. Certain streams, such as Troublesome Creek southeast of Reidsville, North Carolina, appear bright on the radar image, perhaps due to backscattering from vegetation

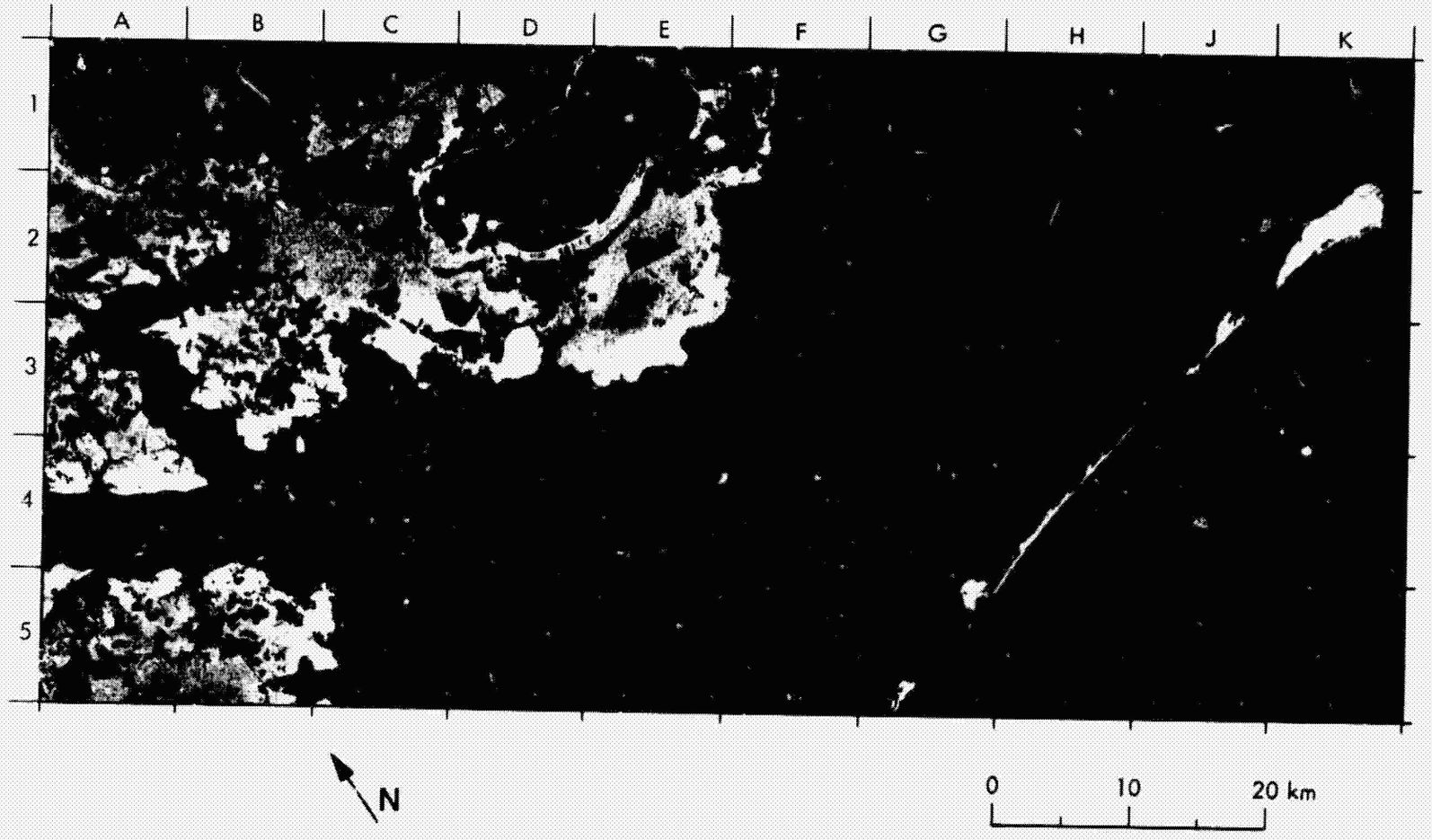

Figure 4-23. SIR-A Image of the North Carolina Coastline (Data Take 24A)

along the stream bottom. However, the effect is not displayed consistently enough to be useful in structural interpretation. To analyze such areas more effectively, digital radar data are needed to enhance subtle backscatter differences that may be present.

Geologic and physiographic features in the Coastal Plain are better displayed than those in the Piedmont because of the wider range of gray levels present in the radar image. The distinction between the Miocene rocks on the west and the Quaternary rocks on the east is generally visible on the SIR-A image; however, the boundary between the two areas corresponds to the soil map (Tant, Byrd, and Horton, 1974) more than to the geologic map (Stuckey, 1958). The soil map separates the southern Coastal Plain on the west, characterized by loamy and clayey soils of upland surfaces, from the Atlantic Coastal Flatwoods on the east, characterized by similar soils of wet lowlands, organic soils of shallow lake beds, and the river swamps.

Stream drainage patterns appear highlighted in the western portion of the Coastal Plain on the SIR-A image. The broad vegetated valleys of the Tar River system appear bright in contrast to the dark surrounding farmed upland areas. Such a presentation emphasizes the whole drainage valley and provides a different interpretation of lineaments from Landsat, which tends to emphasize the river channel itself (Trask, Rowan, and Krohn, 1977).

The Quaternary portion of the Coastal Plain to the east is a marshy lowland. Like Seasat, the SIR-A image shows a wide brightness range in lowlands, which are not distinguishable on Landsat images. Experience with Seasat has shown that many of these features are related to a vegetation canopy over a standing water surface (Engheta and Elachi, 1981; Waite et al., 1981). The marshy area southeast of Lake Mattamuskeet (Figure 4-23) illustrates this effect. Preliminary field investigations suggest that a deciduous forest characterized by sweetgum (Liquidambar styraciflua) and red maple (Acer rubrum) (the bright circular feature at the lower left of F1) may be discernible from the more prevalent loblolly pine (Pinus taeda) forest (the darker features in F1). In general, variations in the bright areas are seen more easily on the negative image than on the positive image.

In the vicinity of Pamlico Sound, marshes are readily distinguished from other parts of the shoreline. The marshes depicted on SIR-A show excellent agreement with marshes mapped on the N.O.A.A. (1980) navigation charts and the U.S.G.S. (1978) topographic maps. The marshy area near Wysocking Bay (the gray area in the top center of F2, Figure 4-23) is a good example of this vegetation type. The primary marsh plant in this area is Juncus roemerianus, a short grass with stems 1.0 to 1.3 m tall. Zizania aquatica, a marsh plant that grows to 2.0 to 2.5 m tall and has broad flat leaves that resemble those of a corn plant, was also observed; it may be responsible for some of the gray-scale variation observed in the marshy areas on the SIR-A images. On Seasat images, corn fields generally appear bright. Because of the wide variety of plant morphologies, marshy areas may be suitable places to examine the complex scattering of L-band radar from a vegetation canopy.

Because both a barrier beach and a lowland marsh are present, the eastern coastline of North Carolina is a good subject in the study of SIR-A radar response to shoreline features. The image (Figure 4-23) covers a section of the Outer-Banks of North Carolina that include portions of Hatteras Island (J2 through K2), Ocracoke Island (J3 through H5) and Portsmouth Island (G5). The ocean-facing foreshore of the beach appears dark on the image, whereas the vegetated dune areas on the sound side of the barrier island appear bright. Several different gray levels can be observed in the vegetated dune areas. One of the brightest areas is on the small peninsula where the town of Ocracoke is located (G5). The town area has a fairly dense canopy of live oak (Quercus virginiana). The dark areas observed on the image between Ocracoke and Hatteras Islands are mud flats without vegetation (J center of 3). Similar gray levels south of the town of Ocracoke suggest a similar morphology. The curving northern part of Portsmouth Island is also well depicted on the image (G5). The SIR-A image agrees with the N.O.A.A. (1978) navigational charts, which show a beach area on the east, an interior lagoon, and a vegetated dune area on the west.

Some offshore features of interest are also visible on the SIR-A image. Two shoal areas, Howard Reef (H4) and Clam Shoal (J2), are visible as thin white lines west of the barrier islands. At ground level, these shoals appear as a line of breakers on the water surface. Similar patterns appear at Diamond Shoal off the tip of Cape Hatteras and at Ocracoke Inlet between Portsmouth and Ocracoke Islands. The presence of such offshore features on the SIR-A image suggest that

radar systems with incidence angles larger than those designed for Seasat's geological applications may have some potential coastal mapping applications as well.

The images received during Rev. 378 of July 23, 1978, as Seasat passed over a portion of the Outer Banks enable comparison of the two L-band systems at different times of the year. The Seasat image (Figure 4-24) looks remarkably different from the SIR-A image (Figure 4-23) along the coastline. The vegetated dune areas on the barrier islands appear dark; the small peninsula with the town of Ocracoke (G5) is barely distinguishable on the Seasat image. The gray level from the peninsula matches the gray level from the water surface. However, the vegetated dune areas on the main part of Hatteras Island still appear bright on the Seasat image. Gray levels on the Coastal Plain portion of the Seasat image generally appear darker than they do on the SIR-A image. Part of this darkening may be due to photographic differences between the two prints; however, the marsh vegetation areas in the Seasat image appear too dark to be accounted for simply by differences in exposure of the prints. The reason for the difference between the Seasat and the SIR-A images has not been determined at this time. A partial explanation may be the different incidence angles of the two radar systems. However, environmental conditions may exert a strong influence on the L-band returns, especially in shoreline and lowland areas where the presence of standing water can significantly increase the strength of a return signal. Successive radar coverage would help distinguish between local environmental factors and factors inherent in the vegetated terrain.

Because of its flatness, the high contrast between its land and water, and the presence of numerous man-made linear features, the North Carolina coastline is a good subject for the measurement of the geometric precision and resolution of the SIR-A radar. Two types of linear features were measured in a preliminary field reconnaissance of the area. The bright line across Lake Mattamuskeet (D2, Figure 4-23) is a causeway for the two-lane North Carolina Route 94. The causeway is 33 m wide and has a variety of lowland vegetation approximately 4 m high along the banks. The causeway corresponds well to the predicted 40-m resolution of the SIR-A system. The Seasat image (Figure 4-24), with a nominal 25-m resolution, shows the causeway as a dark line rather than a bright line.

ORIGINAL PAGE
BLACK AND WHITE PHOTOGRAPH

Figure 4-24. Optically-Correlated Seasat Image of the North Carolina Coastline (Rev. 378, July 23, 1978)

Numerous straight lines visible in the field patterns of the SIR-A image are drainage canals. The drainage canal at A-1 (Figure 4-23), faintly visible in the original SIR-A transparencies, was measured in the field. The canal itself is 3 m wide, dug approximately 1.5 m below the ground surface with steep sloping bands on either side, and has vegetation approximately 2 m tall along the banks. Canals that are both parallel and perpendicular to the radar beam appear bright on the image. The canals show that for certain situations, the SIR-A radar can detect features that are much smaller in dimension than the stated resolution size.

The geometric precision of the SIR-A image was measured from a paper print using a Mann Manocomparator. Sixty-five points were located on the image and plotted with UTM coordinates on U.S.G.S. (1978) topographic maps. Of the 65 points plotted, only 19 points were measured on the comparator; the rest were not used because of the limited aperture of the comparator or because of mislocation of the control points. The precision of measuring points on the comparator was estimated at 25 to 30 μm; location of points on the map was estimated to be within 15 m. The results of a sixth-degree affine transformation showed that the image had a scale of almost exactly 1:500,000 along the direction of flight, but had a scale of approximately 1:463,000 across the flight direction. The second number is a linear approximation of a nonlinear range correction. A nonorthogonality angle of approximately 1 deg was computed for the image, which was skewed toward the east — the forward direction of the spacecraft. Because of the possible distortion of the paper print image, the results given here are only preliminary and will be measured again using the original positive transparency.

In summary, a preliminary evaluation of the SIR-A radar was conducted for the Piedmont and Coastal Plain of eastern North Carolina. In general, more geologic features are observed in the Coastal Plain than in the Piedmont, primarily because of the wider range of gray levels present in that portion of the image. The western Miocene portion of the Coastal Plain can be differentiated from the younger Quaternany area to the east, but the boundary between the two areas is better represented on the soil map than on the geologic map. Coastline features stand out particularly well in the SIR-A image and appear significantly different from those on a Seasat image. The interaction of the L-band radar

signal with a vegetation canopy over standing water may be a partial explanation for the increased dynamic range observed along the coastline areas.

Prior studies with Seasat in the Virginia Piedmont have shown that features observed in the digitally-enhanced Seasat images could not be seen in earlier optically-correlated versions. Thus the limited applications of SIR-A to the Piedmont geology may be a limitation of the type of data available. In general, however, the SIR-A radar seems to show many of the same types of features that were apparent in Seasat images of the flat-lying Coastal Plain. This is an important consideration because the larger incidence angles, which are more useful in areas of high relief, may not preclude applications of radar images in the Coastal Plain.

K. DUNES ON SIR-A IMAGES (C. S. Breed, J. F. McCauley, G. G. Schaber, A. S. Walker and G. L. Berlin, U.S.G.S.)

Observations of dunes in North American deserts imaged by Seasat and airborne radar (Blom and Elachi, 1981) show that these features give a dark response typical of smooth surfaces unless the dunes have steep slopes oriented normal to the incident radar beam. Dunes with slipfaces (avalanche slopes that stand at an angle of about 32 deg) that are so oriented give a very bright specular response. These authors also demonstrate that the illumination direction of the radar beam is critical to imaging the pattern of dune slope distribution, which defines dune morphologic type; such morphologic identification is essential if dunes are to be used to interpret causative wind regimes.

These conclusions from earlier experiments are confirmed and strengthened by the results of SIR-A imaging of large dunes in Africa and Asia. The SIR-A imaging experiment succeeded in recording dunes in parts of several major Old World deserts, including the Taklimakan, Badan Jaran, Ulan Bah and Mu Us, in the People's Republic of China, the Kara Kum Desert in Turkmen S.S.R., the An Nufud of the northern Arabian Peninsula, and the Sahara of Northern Africa. Images were also acquired of lesser dune fields in North American deserts such as White Sands, New Mexico, and the Gran Desierto of Sonora, Mexico. However, the North American dunes are small in comparison with those of Asia and Africa. Although the star dunes of the Gran Desierto are more than 100 m high and have active slipfaces, they give only a minor response on the SIR-A images.

The Old World dunes, which are commonly 2 km or more in width or diameter and as much as 200 to 300 m high, are readily discernible on the SIR-A images. The bedforms recorded on SIR-A images include both active dunes with steep avalanche slopes in hyperarid to arid regions, and dunes that are stabilized by vegetation in arid to semiarid regions.

Such large dunes were imaged by radar even when their slopes were subparallel to the direction of the beam, as, for example, in the Taklimakan Shamo of the Tarim Basin, China (Figure 4-25(a) and (b)). Diffuse scattering from vegetation and specular responses from slipfaces on the secondary bedforms that commonly develop on the stoss slopes of such large dunes (Breed and Grow, 1979) apparently combined to give a salt-and-pepper tone that permits these large dunes to be recorded. Very large compound and complex dunes recorded by SIR-A are in the Badan Jaran Shamo of northwest China (Figures 4-27(a) and (b), and 4-28(a), (b), and (c)), the Kara Kum Desert near Mary, Turkmen S.S.R. (Figure 4-29(a) and (b)), the Chad Basin (Figure 4-30), the Grand Erg Occidental of the Sahara (Figure 4-31(a) and (b)), and Mu Us Shadi, China (Figure 4-32). Large sand streaks just east of the An Nafud in Saudi Arabia were also imaged by the SIR-A (Figure 4-26).

The overall tone that delineates the extent of sand seas on SIR-A is highlighted by several small but very bright patches that match south-facing segments of major slipfaces shown on Landsat (compare Figure 4-27(a) with 4-27(b)). Active slipfaces such as those on the dunes imaged by SIR-A do not have a vegetative cover or layers of large pebbles that might explain this very bright radar response. The dune surfaces generally consist of very dry, loose sand that forms very smooth but steep avalanche slopes of about 32 deg (angle of repose). A specular response from the dune slipfaces is suggested by these very bright radar reflections. At first glance, given a SIR-A depression angle centered on 43 deg and a slipface angle of about 32 deg, the resulting angle of reflection (about 75 deg) would not provide a mirrorlike return of the radar beam to the Shuttle sensor. However, the slipfaces of these dunes are not flat planes; their curved, parabola-shaped surfaces offer a variety of angles to the incident radar beam and may act to concentrate the incident beam in a mirrorlike fashion.

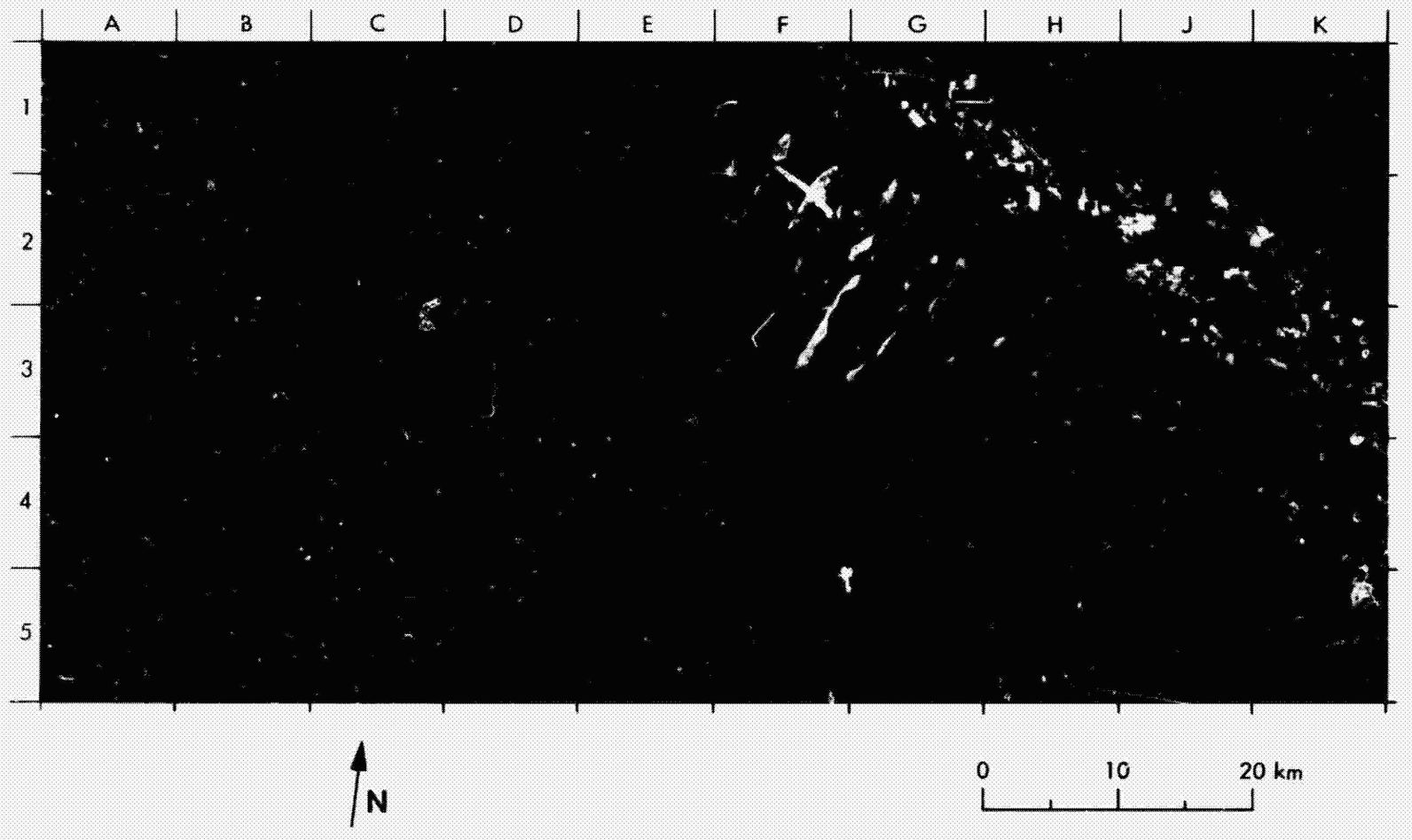

ORIGINAL PAGE
BLACK AND WHITE PHOTOGRAPH

Figure 4-25. Taklimakan Shamo, China: (a) SIR-A Image of Dunes on Northeast Edge (Data Take 28)

Figure 4-25. Taklimakan Shamo, China: (b) Landsat Image of Dunes on Northeast Edge (ID E-1146-04251-6)

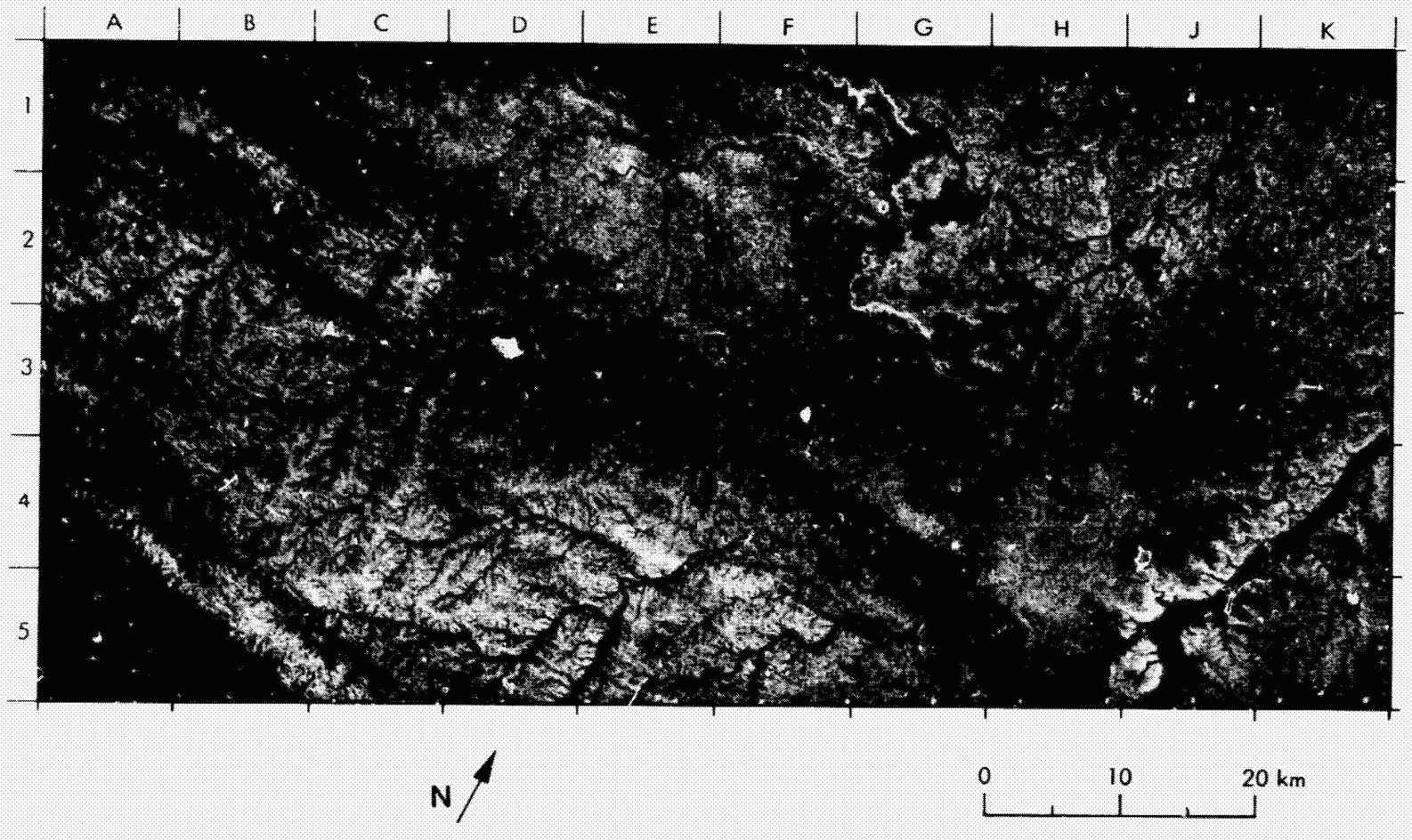

Figure 4-26. SIR-A Image on Eastern Edge of An Nafud, Saudi Arabia (Data Take 28)

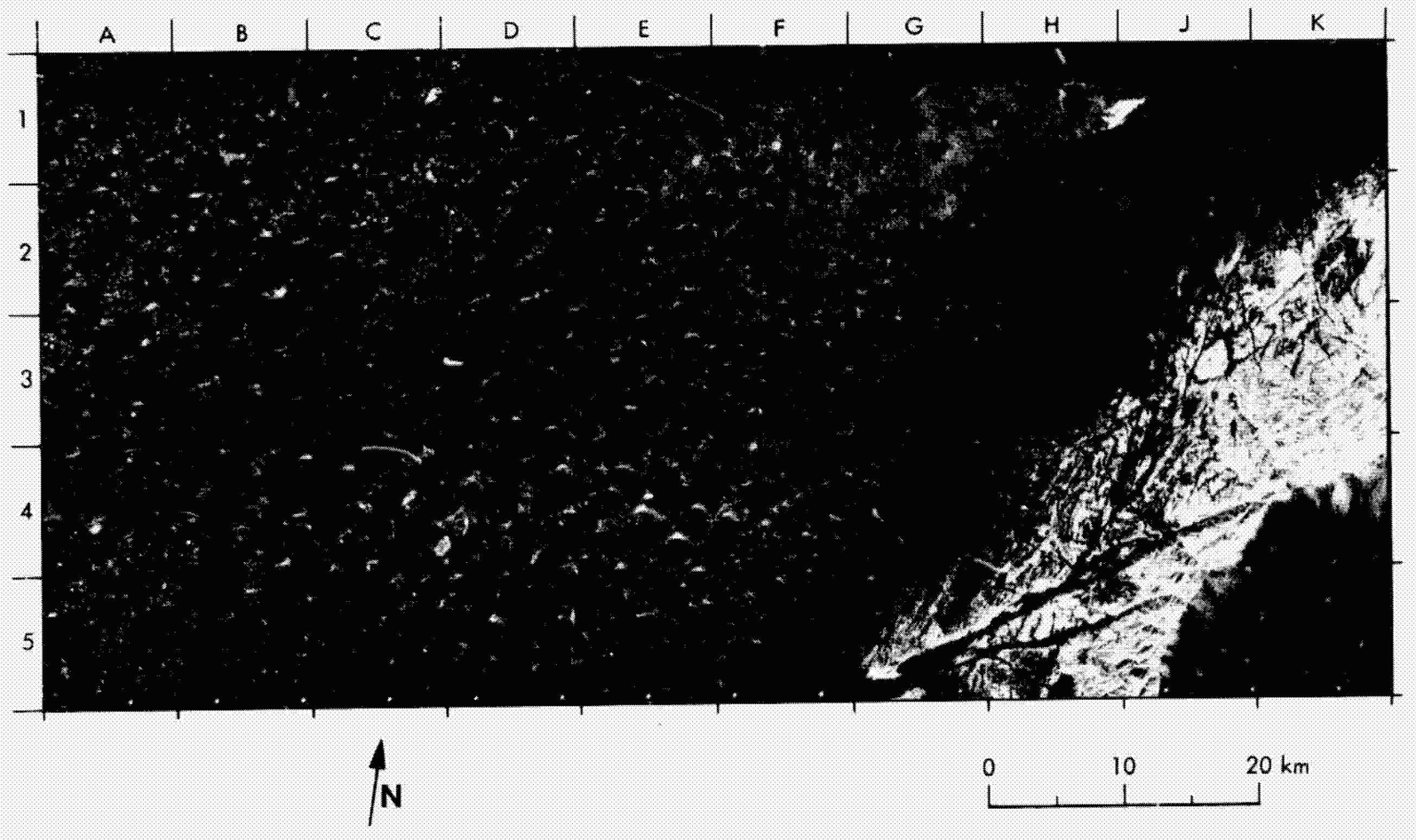

Figure 4-27. Badan Jaran Shamo, China: (a) SIR-A Image of Dunes on East Edge (Data Take 28)

Figure 4-27. Badan Jaran Shamo, China: (b) Landsat Image of Dunes on East Edge (ID 1117-03222-6)

Figure 4-28. Badan Jaran Shamo, China: (a) Enlarged SIR-A Image of Southwest Edge (Data Take 28)

Figure 4-28. Badan Jaran Shamo, China: (b) Enlarged Landsat Image of Southwest Edge (ID E-1209-03340-4)

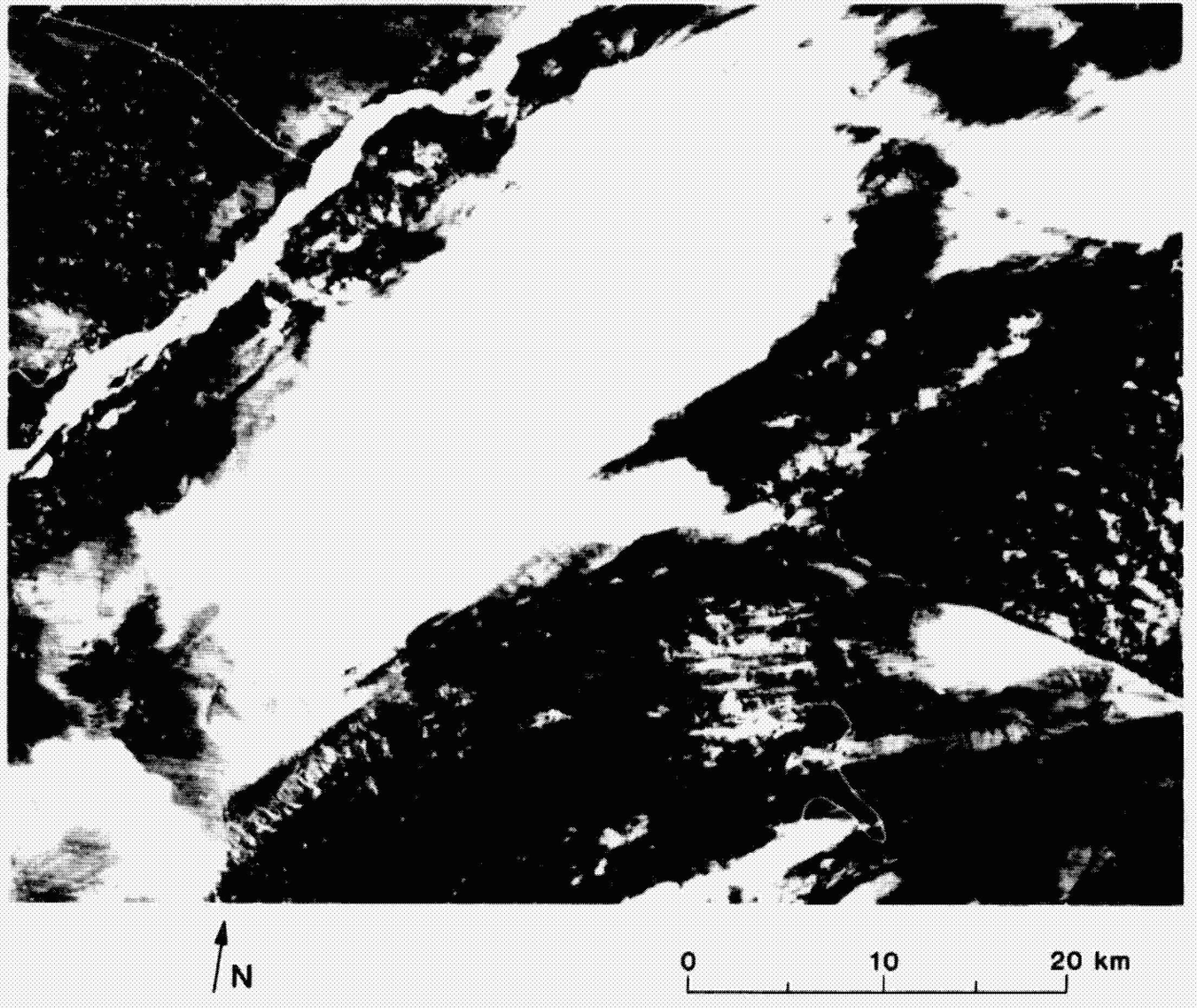

Figure 4-28. Badan Jaran Shamo, China: (c) Enlarged Landsat Image of Snow-Mantled Southwest Edge (ID E1191-03334-5)

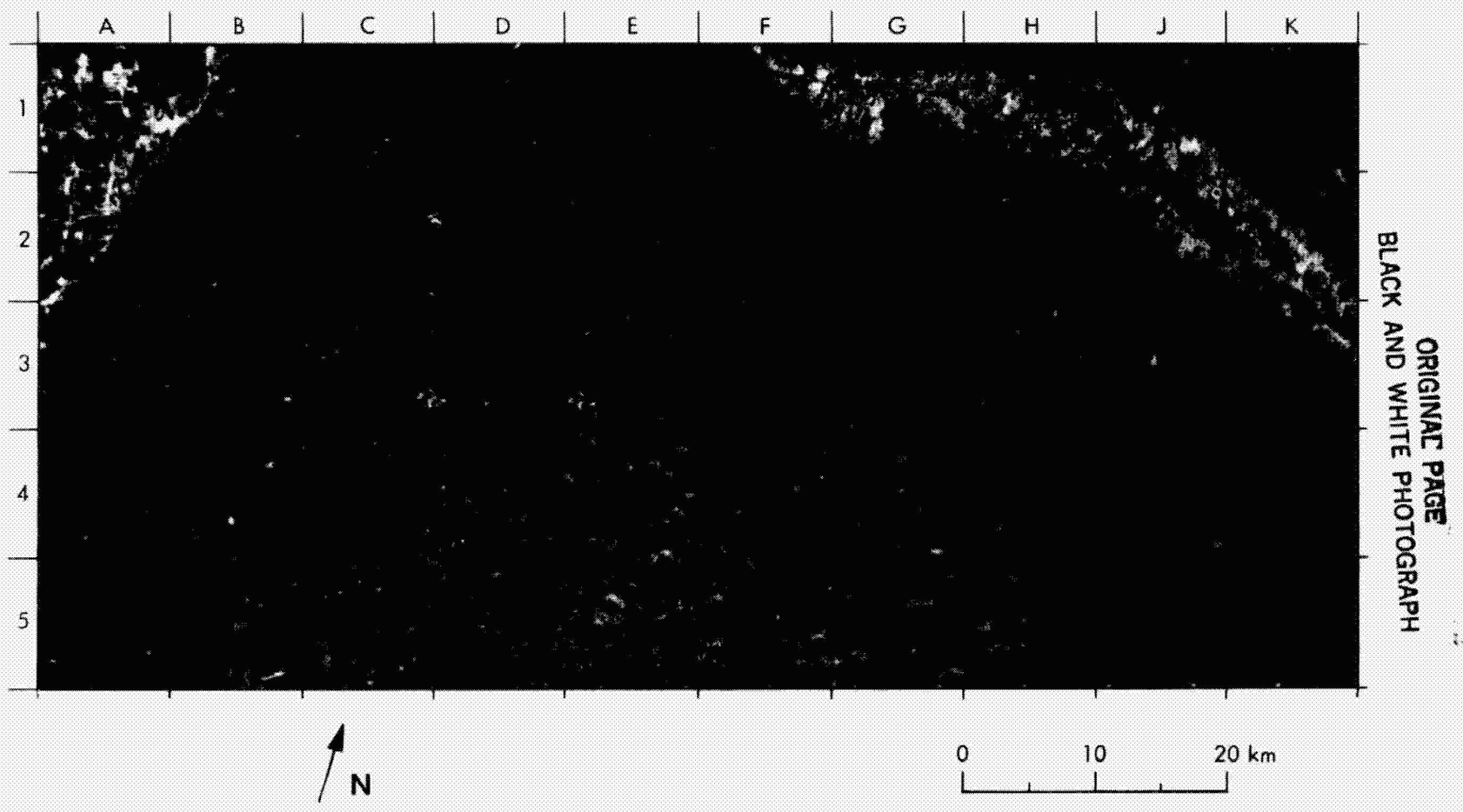

Figure 4-29. Kara Kum Desert, Turkmen, S.S.R.: (a) SIR-A Image of Radar-Facing Megabarchanoid Dunes (Data Take 28)

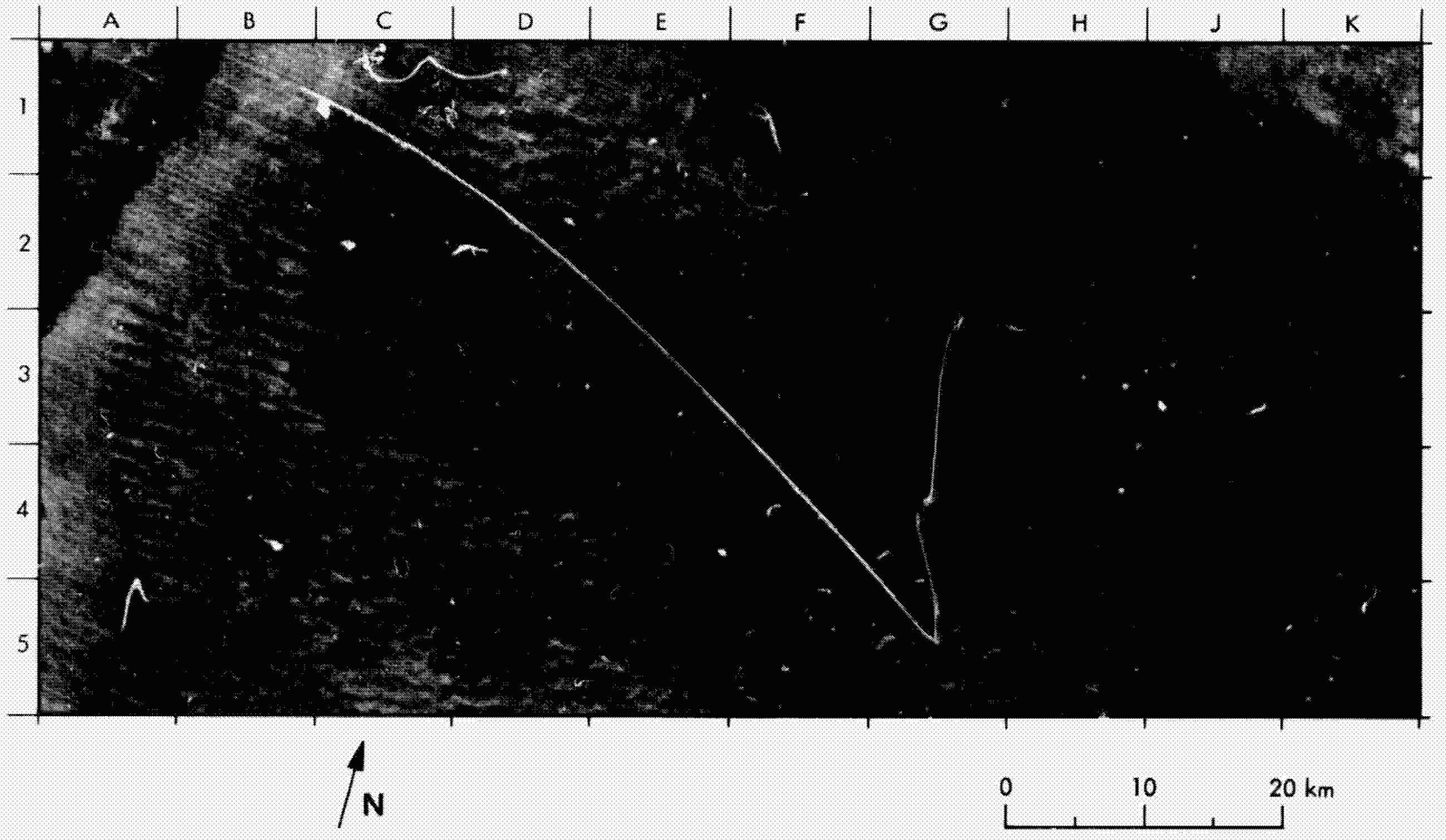

Figure 4-29. Kara Kum Desert, Turkmen, S.S.R.: (b) Landsat Image of Megabarchanoid Dunes (ID E1126-05581-6)

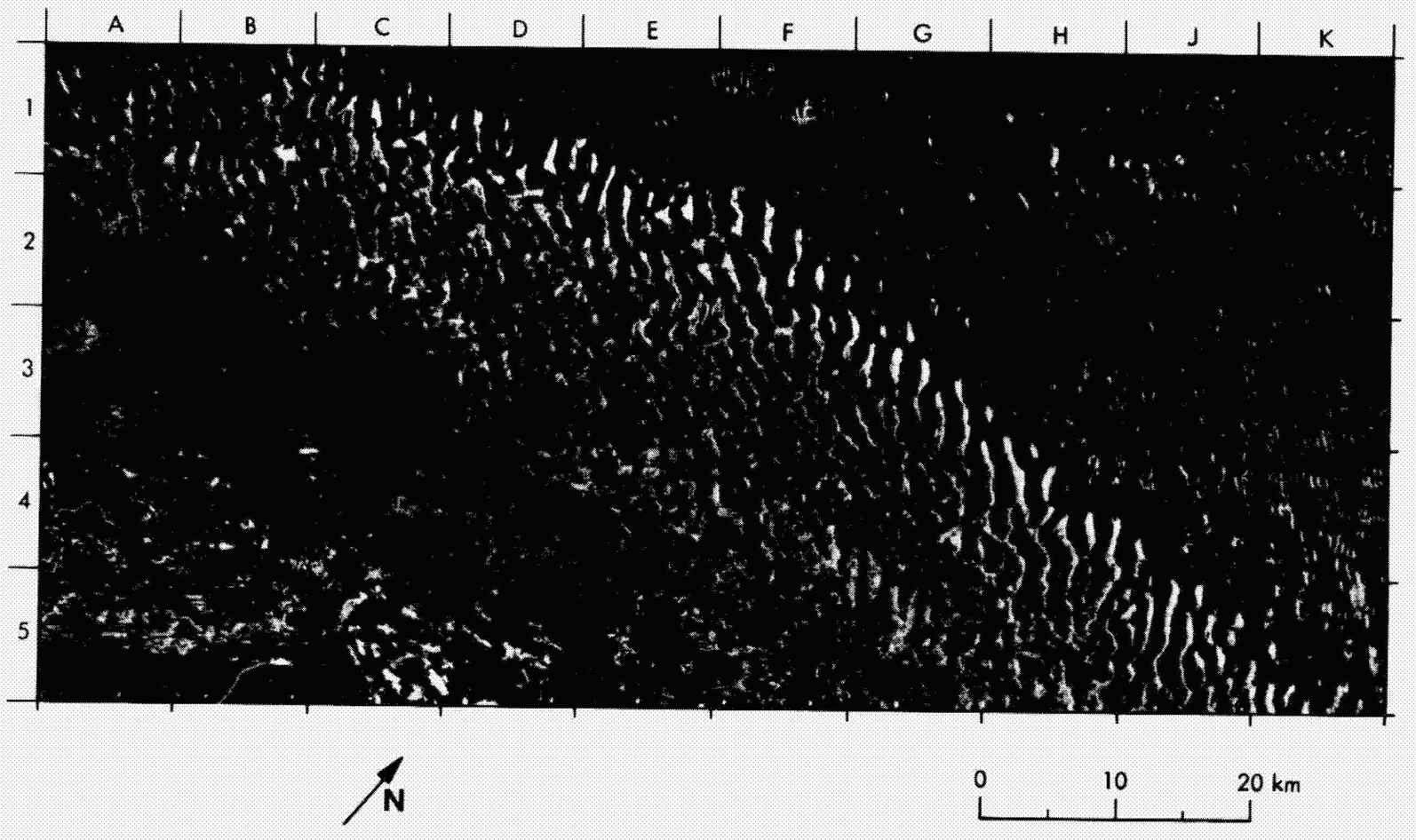

Figure 4-30. SIR-A Image of Dark Dunes and Bright Interdune Flats in Chad Basin (Data Take 28)

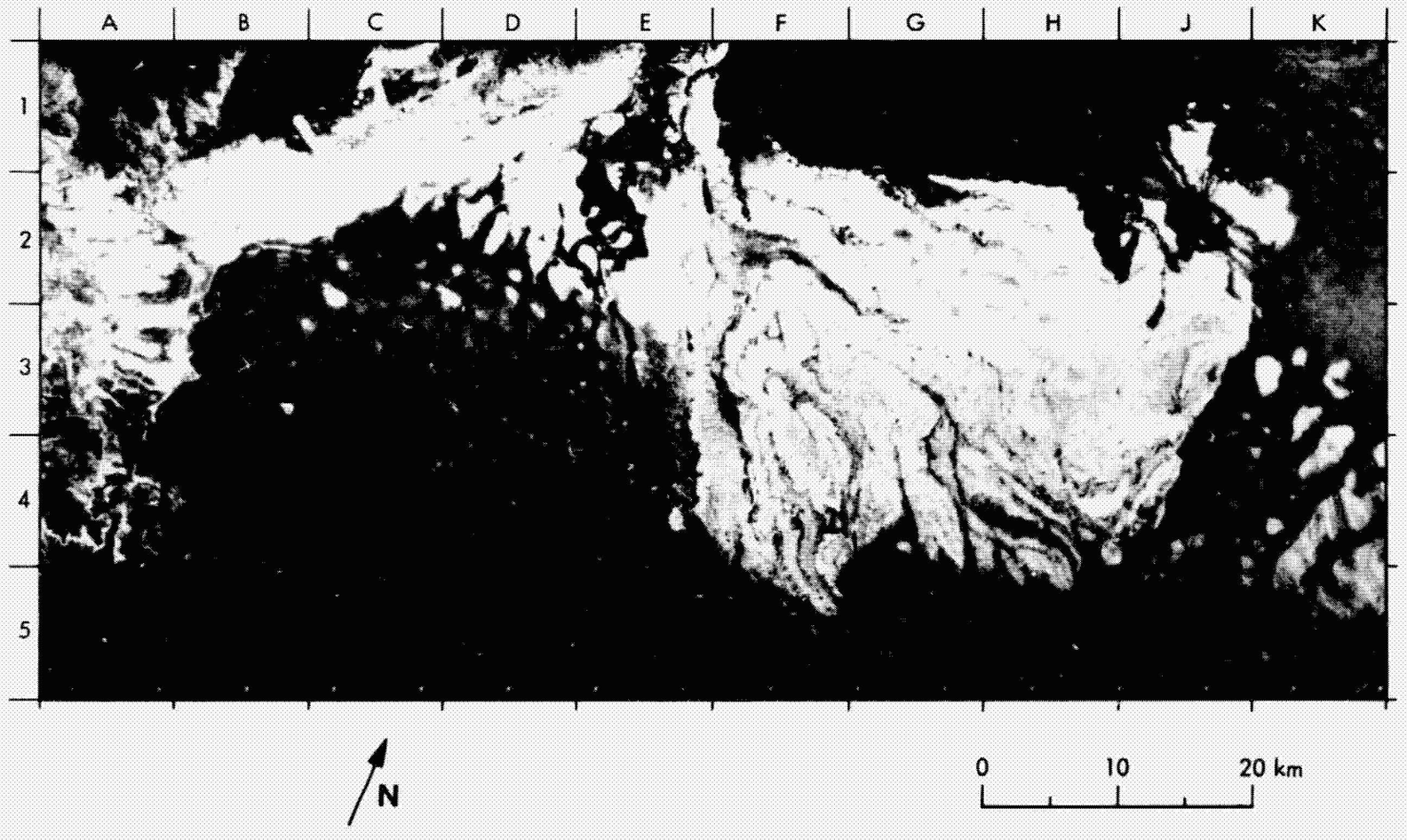

Figure 4-31. Grand Erg Occidental, North Africa: (a) SIR-A Image of Northwest Edge (Data Takes 32 and 33)

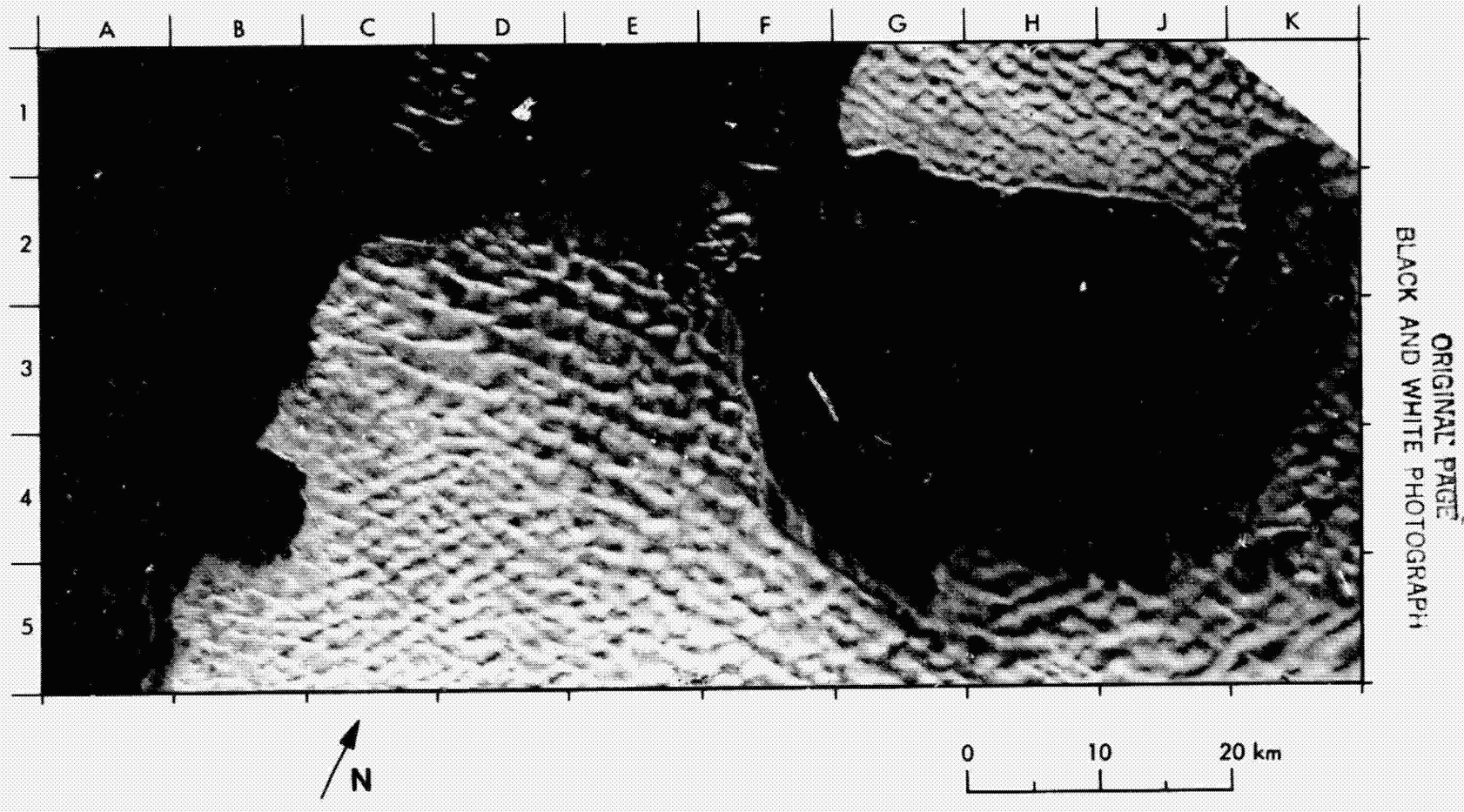

Figure 4-31. Grand Erg Occidental, North Africa: (b) Landsat Image of Northwest Edge (ID E1116-10123-6)

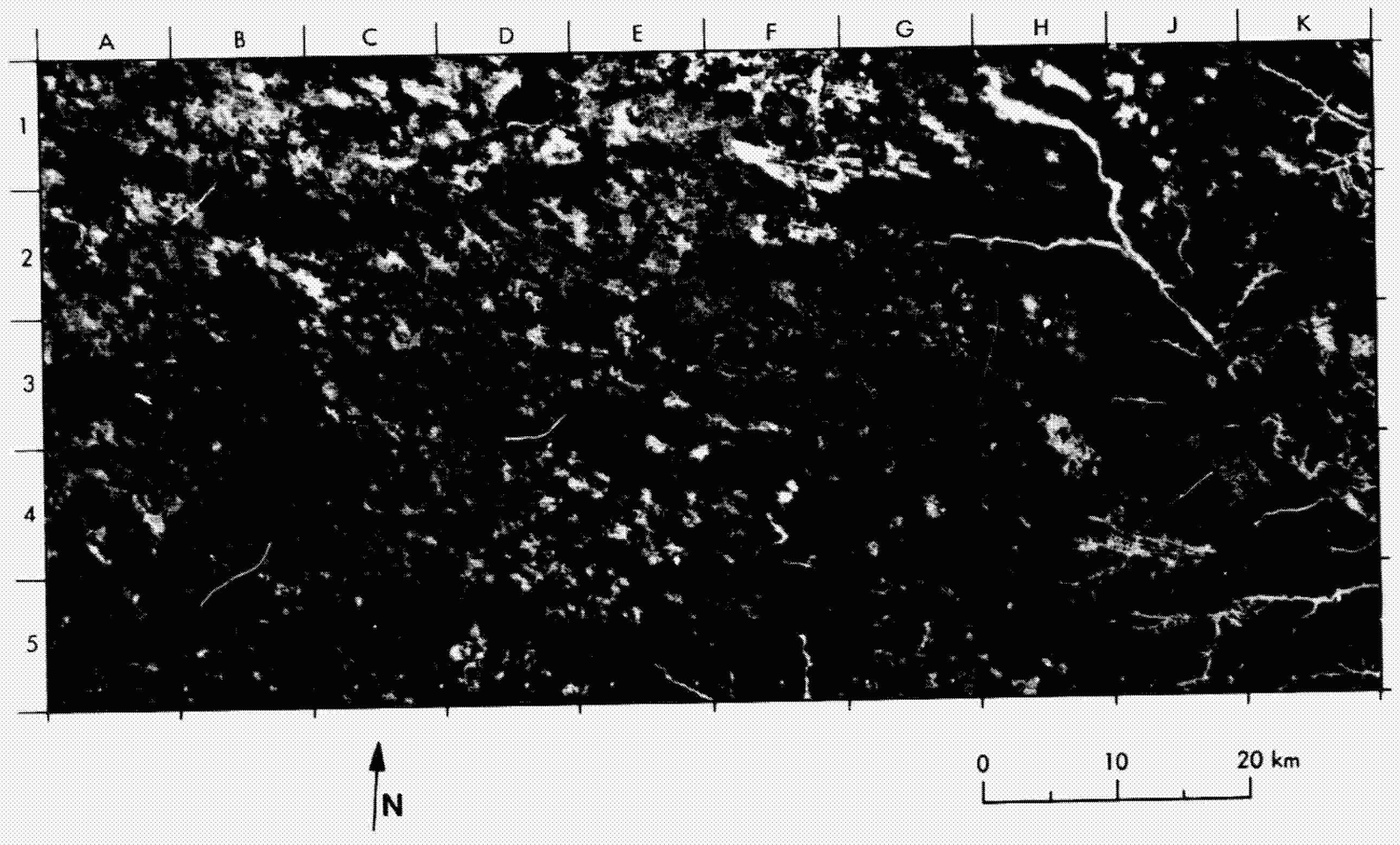

Figure 4-32. SIR-A Image of Mu Us Shadi, China (Data Take 28)

Only some south-facing parts of the slipfaces shown on Landsat give a very bright response and thus are imaged by SIR-A. As a result, the impression SIR-A gives of dune-slope orientations is ambiguous or misleading. Probably because only one radar look direction is available, the dunes of the Badan Jaran Shamo appear on SIR-A (Figure 4-27(a)) to have south-facing slipfaces (formed by dominantly northerly winds), whereas on Landsat (Figure 4-27(b)) their actual east-southeast-facing directions are obvious. Where the radar look direction is normal to both the primary and secondary dune slipfaces, as in the Kara Kum dunes image (Figure 4-29(a)), the bright gray tone that apparently results either from the integration of specular responses from the slipfaces or from vegetation on the stoss slopes give an almost photographically faithful rendition of the dune shapes. This SIR-A image shows the potential for discrimination of dunes by SIR-A under the best combination of circumstances.

Another possible explanation for the apparent specular return from the dune slipfaces is that the radar beam penetrates the loose, dry avalanche sand at the dune surface (as described by McCauley et al., 1982). The radar beam is then refracted at the air-sand interface (Elachi, Roth, and Schaber, in press) and thus impinges on buried slipface laminae (foreset beds in the dune) at a higher angle. A refraction angle of only 15 deg added to the 75-deg reflection angle would permit a mirrorlike return of the radar beam to the SIR-A sensor. Specular reflection thus might occur from buried, subparallel slipface laminae, inclined about 32 deg, that are semiconsolidated, encrusted, or moist.

Besides dune vegetation and specular response from slipfaces, a third factor that allows recognition of even rather minor dune fields on SIR-A images is the tone contrast between the dunes and the adjacent surface: gravel or sandy plains, bedrock, interdune lakes, and so on. Even where slipfaces are absent, too small to be detected, or not aligned normal to the radar beam, dunes can be detected by their patterns of regularly repeated, dark, wavy ridges on the SIR-A images. The bright parts of these patterns represent heavily vegetated dunes and interdune flats whose surfaces may range from rough salt deposits and wind-eroded lake beds (yardangs) to heavily vegetated marshes (Figure 4-30). The high contrast between dark dunes and bright vegetated interdune surfaces is useful for discriminating even the small dune ridges of the Mu Us Shadi on the semiarid Ordos Plain, China (Figure 4-32).

Although at first glance the Landsat images of desert dune regions appear superior to the SIR-A images, the SIR-A images have at least three distinct advantages over Landsat. One is the capability of radar to penetrate cloud cover and low-density, very-dry sand cover (see McCauley et al., 1982); another is the excellent discrimination of bedrock relief and structures by radar; and the third is the capability of radar to image cultural features, ranging in scale from whole settlements that are not visible on standard Landsat images to roads, canals, railroad ties, and even the barbed-wire enclosures ("kuluns") of the Chinese pasture lands (Figure 4-32). This capability provides a new view of the relations between man-made features and the dunes, salt flats, yardang fields, and other natural desert features that man must contend with in these arid and semiarid regions. The radar view of the deserts thus provides a new way to examine problems of land reclamation, groundwater utilization, population pressures, dune encroachment, wind erosion of soils, salinization, and other aspects of geodynamics generally associated under the heading of "desertification."

The SIR-A image (Figure 4-26) shows the sand streaks (A1 to B1 through E3/F3) and sand-choked wadis (dendritic intermittent stream channels) of the Al Labbah plateau (29°30'N, 41°15'E) just east of the An Nafud sand sea (dark area on west end of image). The large sand streaks originating from the Nafud are shown as extremely dark tones on the image because of the fine-grained nature of the material and the absence of pebble-to-boulder-size scatterers on these surfaces that would increase the diffuse component of the radar return. The Al Labbah upland is underlain by the Aruma Formation of Upper Cretaceous age and is described as flat-lying, light gray-tan, locally fossiliferous, and limestone interbedded with marly limestone and marly dolomite; in the upper sections, the formation is a yellowish-brown shale.

The dendritic pattern of the wadis is strongly enhanced on the image because the stream valleys act as traps for windblown sand, which is characterized on the SIR-A image by dark image tones. The larger wadi (J5 to K4, Figure 4-26) on the extreme east side of the image is also choked with sand from the Nafud. The largest, best-defined dark sand streak appears to have its local source associated with a small circular mesa (F3/F4). The well-developed dendritic wadi pattern indicates that the underlying rocks are flat-lying sedimentary materials. The absence of any highly scattering surface materials within the wadi floors and

valley slopes indicates that sand encroachment is proceeding at a higher rate than any downcutting due to water erosion.

Figure 4-27(a) is a SIR-A image of compound crescentic (megabarchanoid) dune ridges in the Badan Jaran (formerly Badan Jiling or Badan Dzareng) Shamo (desert) of the Ala Shan Plain, north-central China. It is paired with a Landsat image (Figure 4-27(b)) of the same area at the same scale. The dunes in this sand sea are among the tallest on Earth, reaching heights of more than 300 m above the interdune flats (Zhu, Zheng, and Shu, 1980). Comparison of the two images shows that the very bright returns from the dunes recorded on the radar image (left half) are solely from the south-facing components of the major east-southeast-facing slipfaces on the crescentic dune segments, which are clearly defined on the Landsat image. Inspection of the radar image alone suggests that the potential direction of sand dune migration is southward, driven by northerly winds. Inspection of the dunes on the Landsat image, however, shows that each wavy dune ridge consists of numerous adjacent crescentic segments. Each segment is as wide as 2 km or more from horn to horn, and each has a gentler west-facing stoss slope, and a steeper, east-southeast-facing avalanche slope. Linear "thresholds" of sand (Hedin, 1905), extend east-southeastward across the interdune flats from one parallel wavy ridge to the next. The entirely different appearance of these dunes on the SIR-A image occurs because only the south-facing part of each curved slipface was oriented toward the radar beam, and only those parts of the major slipfaces were imaged, giving a false impression of the dune morphology.

Interpretations of effective wind direction from slipface orientations can be tested against the annual resultant direction of sand-driving winds calculated from the World Meteorological Organization wind measurements (Fryberger. 1979; Breed et al., 1979). The east-southeastward resultant direction of potential sand migration at Maomu (formerly Ting-Hsin), at the western ridge of the Badan Jaran sand sea, is apparent in Figure 4-27(a). This direction closely agrees with that of the overall sand migration pattern interpreted from the dune morphology in the main part of the sand sea (left half of image). Near the Yabrai Shan (Mountains) and also along the southern and northeastern margins of this sand sea, the megabarchanoid ridges grade into isolated sharp-crested reversing dune

ridges and star dunes, probably in response to the topographic effects on the effective winds caused by mountain ridges along the edges of the sand sea (Breed, 1977). The change in dune shapes was not detected by SIR-A because the long axes of the narrow, reversing ridges near the mountains lie almost parallel with, rather than normal to, the direction of the radar beam.

Numerous spring-fed interdune lakes, which are mostly filled with water on the Landsat image at A4 to A5 and B4 to B5 (Figure 4-27(b)), give a response as dark as that of the dunes on the radar image (Figure 4-27(a)). However, the lakes are outlined by thin bright lines that probably represent thickets of reeds and other marsh vegetation, as described by Petrov (1966). The tone of various parts of the large playa at H1 is reversed from light to dark on the Landsat and radar images. This difference occurs because the smooth, unvegetated parts of the playa, whether filled with water (dark) or dry (light) on Landsat images, are dark on the radar image.

The radar signature of the semiarid Mu Us Shadi (sandy land) in the Central part of the Ordos Plain (Figure 4-32), northwest China, is distinctively different from that of more arid regions such as the Badan Jaran Shamo (Figure 4-27(a)). The Mu Us receives 400 to 440 mm of rainfall per year; groundwater levels lie only 1 to 3 m below the surface, and numerous lakes (mainly saline) dot the surface (Zhu, Zheng, and Shu, 1980). Settlements, such as at F1, support a population density of about 22 people per km^2. The radar image shows many enclosures called "kuluns," which are constructed of earthen walls and barbed wire to protect and cultivate natural pastures, to control the movement of grazing animals, and to prevent sand drift (Walker, 1982).

Fields of parallel wavy dune ridges, as at D2/D3, B4/C4, and B1/C1/B2/C2, can be seen in dark contrast to the steppe vegetation of the interdune plains. One field of dunes (J4), located between one of the larger kuluns and the vegetated Tuwei He, a tributary to the Huang Ho (Yellow River), gives a bright rather than dark response that indicates that these dunes, unlike those that give a dark response, are heavily vegetated, perhaps with trees. The encroachment of dunes into the pastureland of this region is considered a result of "desertification" or degradation of arid and semiarid land. Many Chinese scientists consider

the Mu Us sandy land to be a man-made desert, rather than a desert formed by natural causes (e.g., Zhu, Zheng, and Shu, 1980).

Figure 4-28(a) is an enlarged part of SIR-A data take 28 (Figure 4-27(a)) showing the western margin of the Badan Jaran Shamo, paired with parts of two Landsat images (Figure 4-28(b) and (c)). The radar image shows a bright response from bedrock pediments that, on the Landsat image are obscured by blown sand. The enhancement of the underlying bedrock pattern by radar imaging may be due to subtle differences in relief, much as a light drift of snow enhances subtle textures on an earlier Landsat image (Figure 4-28(c)). The pattern of bedrock ridges on Figure 4-28(a) does not, however, closely match the snow-enhanced surface texture on Figure 4-28(c), especially in the bedrock of the lower left quarter of the image. A possible alternative explanation for the high contrast of the bedrock areas on Figure 4-28(a) may be that if the buried surfaces are covered by only a thin veneer of loose, dry sand (perhaps a few centimeters to 0.3 m thick), some penetration by the radar beam occurs and gives a response from the underlying material.

The SIR-A radar and the Landsat images of Figure 4-25 are presented at the same scale; they show some of the largest dunes on Earth, in the Taklimakan Shamo (sand sea) of Xinjiang Uygur province, northwest China. This sand sea lies in one of the largest intermontane depressions on Earth, the Tarim Basin, bounded on the north by the braided streams of the Tarim He. Sediments carried into the basin by glacier-fed streams from the surrounding mountains have been winnowed and reworked by winds dominantly from the northeast, but also from the north and northwest (Hedin, 1905; Breed et al., 1979; Zhu, Zheng, and Shu, 1980). These complex wind regimes have built complex crescentic dune ridges with linear "thresholds" (shown on the Landsat image) extending from one ridge to the next. These thresholds provided ramps for camel traverses from one dune ridge to the next during the expedition to this region by the great Swedish explorer, Sven Hedin, in 1899 to 1900. Many of the dune thresholds, which are oriented normal to the incident radar beam, give narrow, bright specular responses on the SIR-A image. Other bright responses come not from the slopes of the large dunes at B4/B5, but from parallel rows of smaller barchanoid dune ridges at B1/C1 near the Tarim He; these smaller dunes probably have active slipfaces oriented toward the radar beam.

The larger dune ridges, which have segments measured in kilometers (Breed and Grow, 1979; Breed et al., 1979) are imaged because their tone contrasts with that of the interdune basins. Some of these basins (the "bahirs" of Hedin, 1905) are vegetated, others contain yardangs (wind-eroded dry lake beds), and several near the river contain water (G2 to G3 on both images). The shapes of these basins have not changed (at the resolution of these images) since they were mapped by Hedin (1905). Note that the village of Tarim' Nongchang, clearly shown on the radar image, is not visible on the Landsat image.

The transverse (barchanoid) dunes northeast of Fort Lamy in the Lake Chad Basin (Figure 4-30) are part of a sand sea built by Saharan winds from reworked alluvium during one or more episodes of aridity when Lake Mega-Chad, which at its maximum extent was about the size of the Caspian Sea (Grove, 1970), receded. When humid climatic conditions returned, the lake rose again, flooding the dunes and leaving behind diatomaceous deposits in the interdune hollows. Later, as the lake again gradually receded by evaporation, limy beds were left capping the diatomaceous deposits. Dating of shells in the lake beds indicates that Lake Mega-Chad may have stood at an elevation of 320 m above sea level as recently as 5000 years ago (Grove and Warren, 1968).

Recession of the lake has left widespread arrays of large dune ridges standing above interdune flats, which are characterized by abandoned or ephemeral drainage channels, wind-eroded lake beds, rough salt playas, and vegetation. This wide variety of surfaces gives various roughness responses on the SIR-A image, as at E4/E5, A3/A4, A2, and G4 (Figure 4-30). The dune ridges, whose long axes are aligned parallel to the direction of the incident radar beam, are mostly dark; the identification of dune patterns on the SIR-A image results largely from the bright response of the vegetated interdune flats. The overall irregularity of the large sand ridges, which are dark gray on SIR-A, is typical of old, vegetated, inactive dunes that have been weathered and eroded under conditions of climatic oscillation. Blurred patches of brightness in the pattern (F1) may represent areas of heavy vegetation both on the dunes and in the interdune flats.

Complex crescentic dunes are imaged in the northern part of the Grand Erg Occidental, near the border of Algeria with Morocco (Figure 4-31). As in other

Old World sand seas, the dark tones of the dune pattern on the radar image (Figure 4-31(a)) are the reverse of the bright tones on the Landsat image (Figure 4-31(b)), and the bedrock, dark on Landsat, is bright on the radar image. The dark-gray dunes on the SIR-A image are recognizable because of tone contrasts with various interdune surfaces, including sabkhas (containing saline flats and wind-eroded silt and clay deposits), bedrock, and vegetation. The dunes themselves are mostly narrow ridges, grading into reversing ridges and star dunes near the topographic barriers that confine the sand sea on the north and west. The complex pattern reflects the complex wind regime recorded at Beni Abbes, about 40 km south of Igli (Fryberger, 1979; Breed et al., 1979). Bedrock units, obscure on the Landsat image, are mappable from the SIR-A image.

Figure 4-29 is of the southern part of the Kara Kum (sandy desert) that lies east of Mary in Turkmen S.S.R., on an alluvial plain between the mountains that border Iran and Afghanistan. Precipitation in this arid region is less than 100 mm/y and the cotton-farming oasis towns such as Mary (Merv) and Bayram-Ali depend on irrigation water brought in by the Kara Kum Canal (Nalivkin, 1973).

Dunes of the Kara Kum consist of reworked alluvial sands deposited thousands of years ago by the ancient Amu Darya, whose course has gradually shifted to the east of the area shown (Suslov, 1961; Nalivkin, 1973). The barchanoid form of these dune ridges (Suslov, 1961, Figure 14-3) resembles that of the much higher dunes in the central Badan Jaran Shamo (Figure 4-27(a)), and also dunes of many other regions, including both the fixed Nebraska dunes (Smith, 1965) and the active Algodones Dunes of the U.S. (Breed and Grow, 1979). This type of wavy dune ridge consists of adjacent crescentic segments whose size, from horn to horn, may range from a few tens of meters, as at White Sands (McKee, 1966), to kilometers, as in the Ala Shan Shamo (Figure 4-27(a)). It is probably the most common form on Earth; interestingly, it is also the most common on Mars (Breed, 1977; Breed, Grolier, and McCauley, 1979).

The large Kara Kum dunes at D4/D5 to E4/E5 (Figure 4-29(a)) are clearly imaged by SIR-A, with photographic fidelity to the dune form, doubtless because these ridges, though only about 25 m high, are aligned with their long axes (and thus their major slopes) normal to the direction of the incident radar beam.

These dunes have major south-facing slipfaces that give a bright, apparently specular response. The ridges also have myriads of small, secondary barchanoid dunes on their stoss (back) slopes (Suslov, 1961, Figure 14-3) and these secondary dunes, which have slip-faces oriented toward the radar beam, also apparently give specular responses. Thus the geometry of these compound dune ridges results in an integrated bright response that gives a true representation of the dune morphology on the SIR-A image. Here, also, the interdune flats give a darker response than the sand dunes, just as on the Landsat image (Figure 4-29(b)). Possibly this contrast occurs because the flats are floored with smooth deposits of alluvial silt and clay (Nalivkin, 1973). The importance of topographic relief and radar look angle are emphasized by the lack of response, on the SIR-A image, from the smaller and differently oriented dune ridges at J4.

Figure 4-33, the SIR-A image from data take 28 and the Landsat MSS (band 5) image, shows large-scale faulting (B1 through B5, F1 through F5, and G3 through G5), structure, and stratigraphy in Ordovician-Silurian limestones, sandstones, and shales in the northwest Xinjiang Uygur Province of northern China. The tectonic region is the Kelpin Tagh Uplift of the Northern China-Korean Platform. The major faults cut the sedimentary rock cuestas (hogbacks), and are normal faults with the upthrown side to the west (left side on the image).

Delineation of the horizontal bedded sandstones, limestones, and shales exposed on the upper portions of the cuestas is better on the SIR-A image than the Landsat image. The detail on small drainage patterns is superior on the SIR-A image. The alluvial fans that are pervasive below the cuestas are better defined on the SIR-A image because of the sensitivity of L-band radar to small changes in gravel sizes and the rapid onset of Rayleigh scattering at about the 4- to 6-cm mean relief scale for surface roughness as described by Schaber, Berlin, and Brown (1976).

Flat playa deposits in the valley floors (D3, C4, F3/G3, K5) are bright on the Landsat image but dark on the SIR-A image; this occurs because of the extreme smoothness of these surfaces to the long wavelength radar sensor and the presence of highly reflecting salt and silt deposits affecting the Landsat sensor response. A small lake (F3) in one of the valley playas appears dark on both the Landsat and SIR-A images. A bright halo at the lake edge on the SIR-A image is thought to be caused by vegetation roughness (probably small trees).

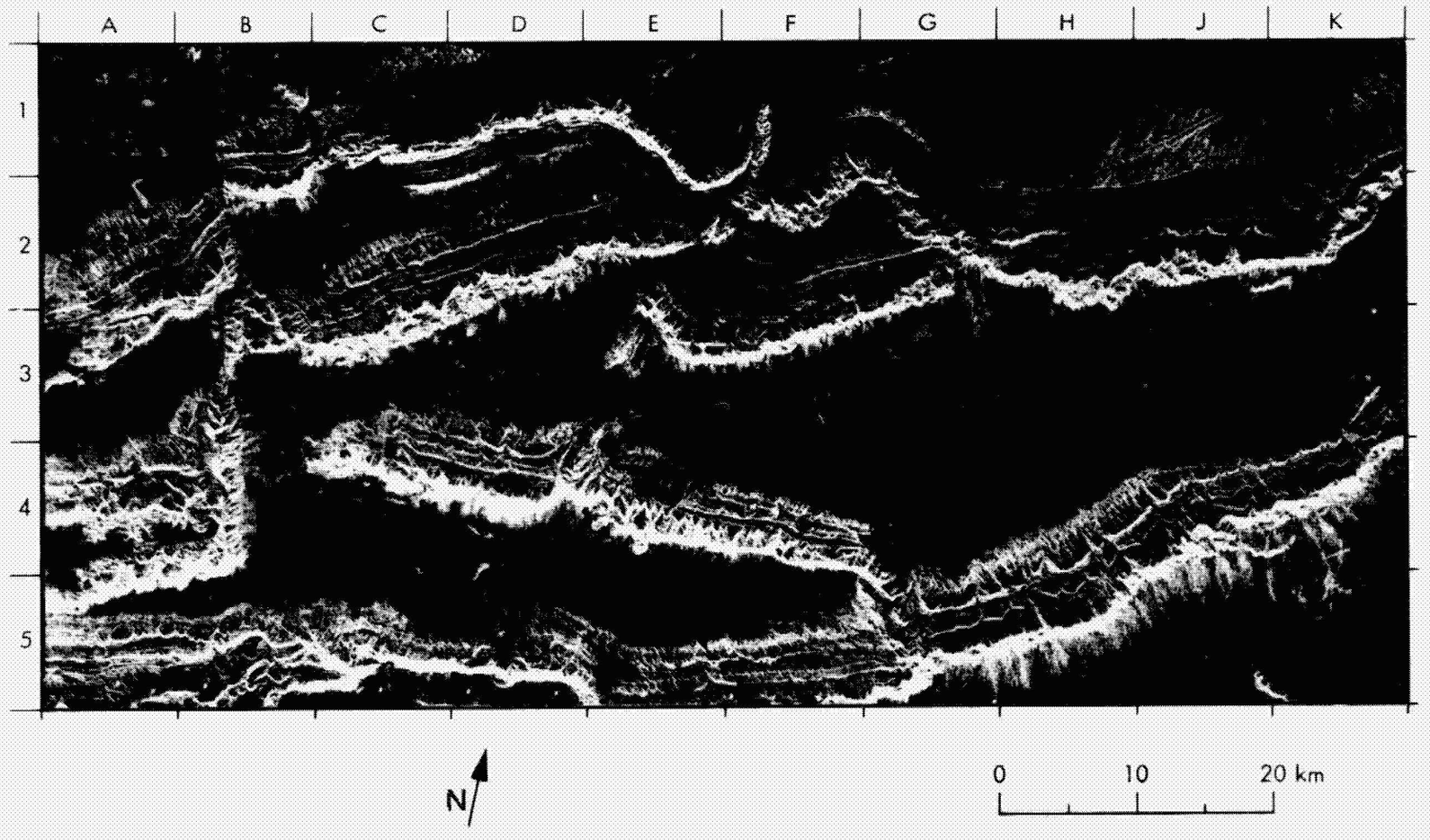

Figure 4-33. Kelpin Tagh, China: (a) SIR-A Image (Data Take 28)

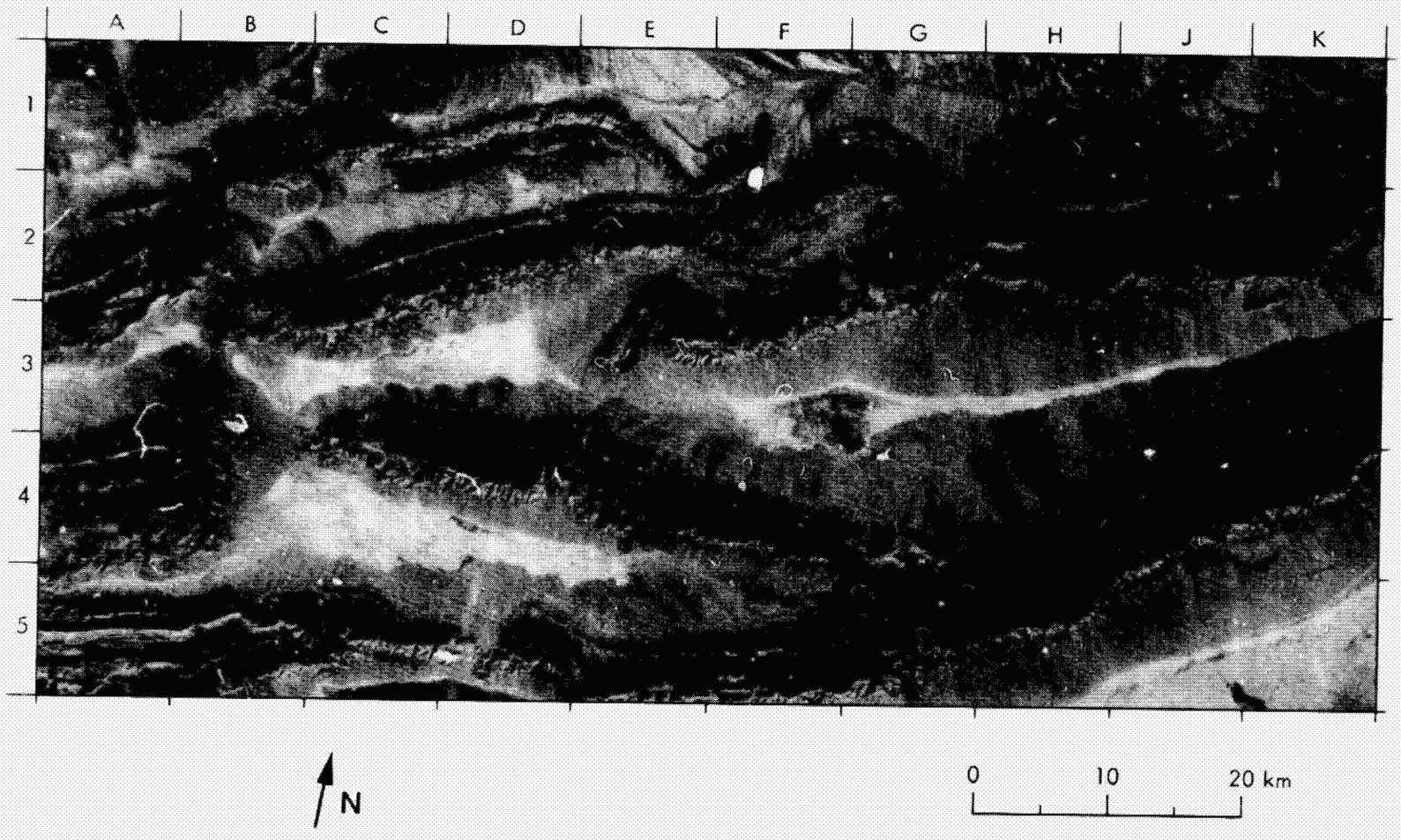

Figure 4-33. Kelpin Tagh, China: (b) Landsat Image (ID 1116-04595-5)

It is clear that the SIR-A image of this region would provide a photointerpreter with a considerable amount of information above that available from the Landsat image alone. Specifically, the SIR-A image provides excellent stratigraphic and structural characterization, in addition to extreme sensitivity to small-scale surface roughness changes.

The area of northwest China near the north edge of Lop Nor at the edge of the Taklimakan Desert (SIR-A data take 28, Figure 4-34(a)) is of interest because it has played an important role in the history of desert research. In areas to the west and east of the present Lop Nor, the Swedish explorer Sven Hedin (1905) first described closely spaced, aerodynamically-shaped ridges and troughs commonly several hundreds of meters long. They were called yardangs from the local dialect and ascribed to wind erosion.

Yardangs were, until recently, thought to be rare, invariably small desert features, limited in distribution to weakly consolidated lacustrine beds. McCauley, Grolier, and Breed (1977) have shown that they are far more common in the hyperarid parts of the world than previously realized. They can range up to tens of kilometers in length and occur in materials ranging from crystalline igneous and metamorphics through Mesozoic sandstones and shales, to tough recrystallized Eocene limestones and well-indurated Quaternary sediments.

The yardangs in this locality show considerably better on the SIR-A image than on the Landsat image (H2 to J1 and A2/A3) (Figure 4-34(b)), possibly because of their extreme roughness at the meter and smaller scale and the abrupt topography of the yardangs. Individual yardangs several kilometers in length can be identified on the SIR-A image, whereas only faint streaks show in the Landsat image. These yardangs trend north-northeast into the strong prevailing wind of this region, and are undoubtedly surrounded by swarms of smaller, elongate, "inverted canoe-shaped" ridges at or near the limit of resolution of the SIR-A and Landsat images.

The utility of the SIR-A data for desert studies is particularly evident in the images of the northern part of the Great Kavir Desert of Central Iran, centered near 35°N and 55°E (Figures 4-35 and 4-36). The Kavir is a giant salt desert, about 50,000 km^2 in extent, that consists of a subtle combination of salt-encrusted playa basins enclosed by folded and eroded Miocene rocks. These

ORIGINAL PAGE
BLACK AND WHITE PHOTOGRAPH

Figure 4-34. Lop Nor, China: (a) SIR-A Image of the Northern Part of the Eastern Edge of the Taklimakan Desert (Data Take 28)

Figure 4-34. Lop Nor, China: (b) Landsat Image of the Northern Part of the Eastern Edge of the Taklimakan Desert (ID E1359-04074-7)

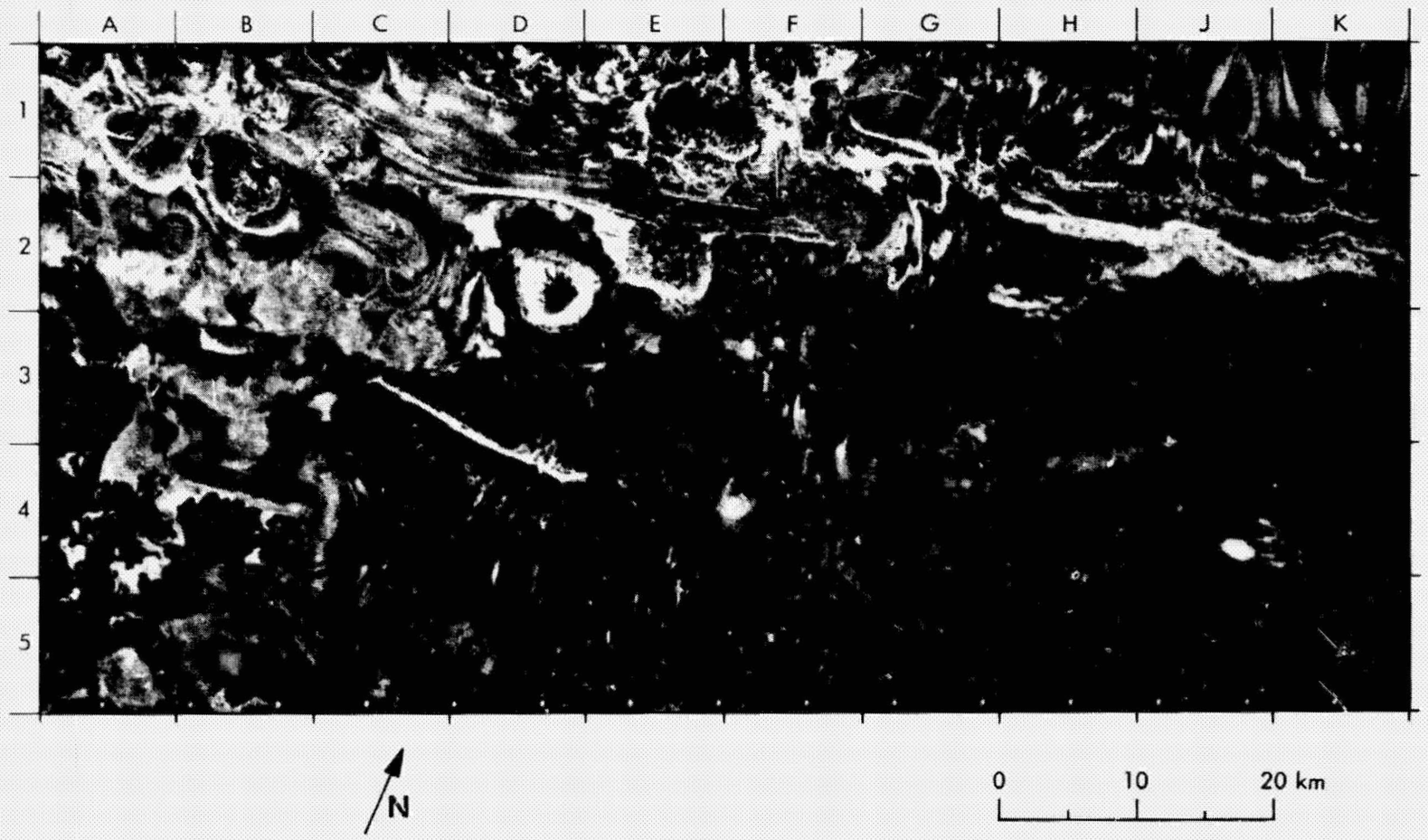

Figure 4-35. SIR-A Image of the Great Kavir (West), Iran (Data Take 28)

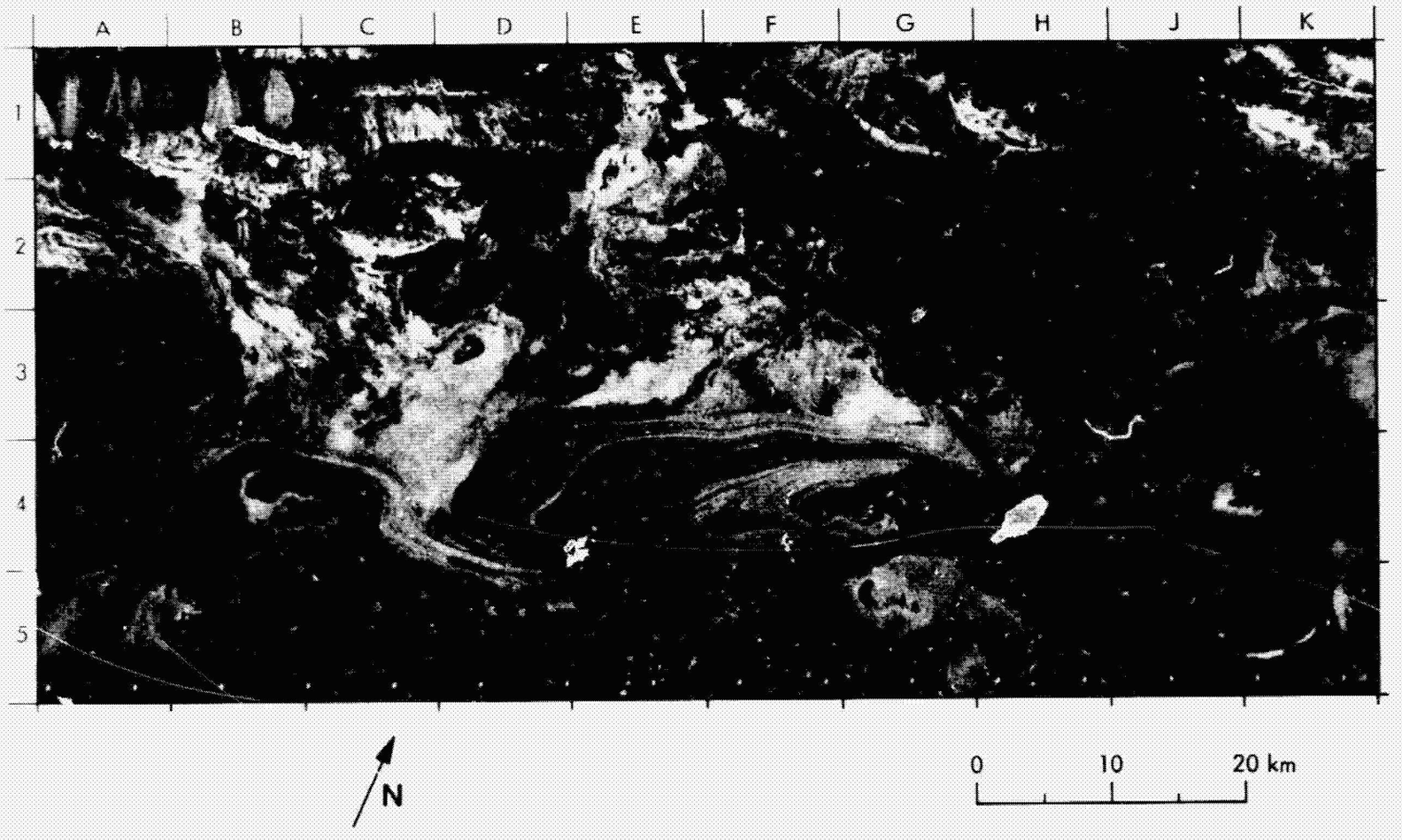

Figure 4-36. SIR-A Image of the Great Kavir (East), Iran (Data Take 28)

rocks are mostly evaporites. They are covered by a regolith as much as a meter thick; this "puffy ground" was created by alternate wetting and drying of the weathered bedrock and consequent churning of the silts and clays that make up the surface (Krinsley, 1970). Locally, the surface is punctured by spectacular salt diapirs. The extensive salt wastes of this region are still controversial in origin. They are considered now by most workers to be derived by weathering, erosion, and redistribution of the Miocene evaporites that floor the basin. Geological exploration of the region has been severely limited by the treacherous salt crusts that overlie briny mud and extensive patches of wet ground, which make much of its surface accessible only by helicopter.

The salt flats at A4/B4, E3/E4, and J4 (Figure 4-35) show varying degrees of roughness. Typically, the crust consists of a rough, jumbled mass of sharp, angular blocks, slabs, and pinnacles. The salt flat at A4/B4 is very dark to the L-band (23-cm wavelength) SIR-A radar, suggesting that its surface has a relatively smooth, mean relief (less than 2 or 3 cm), perhaps smoother than the average for this region. The material is light gray on Landsat images of the area. The gray tone of the salt flat at E3/E4 (10- to 20-cm mean relief) is more typical of the radar reflectance of the salt playas in the Kavir. The extremely bright, but small, playa at J4 is very dark on Landsat and aerial photographs, and actually consists of "black salt" (Krinsley, 1970, Figure 59). This is one of the roughest salt surfaces (greater than 50-cm mean relief) so far observed on the Kavir, and is somewhat rougher than the massive halite deposits at the Devil's Golf Course in Death Valley, California.

Folded Miocene bedrock covered by one meter or more of light, yellowish, puffy ground can be seen at H4. Individual strata are well seen on the radar image, but difficult to discern on the ground because of the in situ regolith. Numerous salt plugs or diapirs that intruded into the Miocene bedrock from underlying evaporite horizons are seen at B1/B2 and D2. The flanks of these structures are often very bright suggesting extreme roughness or steepness in the direction of the radar look. The steep slopes of an anticlinal structure at H2 are also bright to the radar. The small village of Hoseyan is located at J1/J2 and K1/K2; north of the village and to the east and west are numerous steep, conical fans of the Kuh E Darestan range. These consist of coarse, immature, angular cobbles typical of the edge of the tectonically active Kavir Basin.

Part of data take 28 (Figure 4-36) shows the region of the Great Kavir Desert immediately east of that just discussed. At F4/G4 is a very pronounced anticlinal structure with a dark pluglike feature along its crest, possibly an incipient or juvenile salt diapir. Salty clay pans that are covered with 10- to 20-cm-wide polygonal desiccation cracks are present at G5; they seem to have a more uniform radar brightness than the other units described. Compare the saltpans at G5 with the mottled light and dark radar response of the large salt pan at J3/J4 to K3/K4.

An enlarged section of SIR-A data take 28 (Figure 4-37) shows a Quaternary-Tertiary volcanic field in the Harrat Al Uwayrid region of Saudi Arabia (27°27'N, 37°15'E). Numerous cinder cones (small circular features in upper left of image) and lava flows (bright region in upper center) are observed; the wide variation of image tone within the volcanic field indicates a diversity of surface roughness (dark-smooth, bright-rough). The areas of lowest radar return (left portion of image) (quasi-specular reflection) are associated with the underlying Ram and Umm Sahm sandstones of Ordovician and Cambrian age, and alluvial deposits (dark linear features in right of image) in focal wadi floors (ephemeral stream channels). The large, shallow crater forms (small dark dots in lower left of image) may be maars (explosive vents), perhaps with lakes or lake sediments filling the crater floors.

Part of data take 28 shows the extremely rough crystalline limestone of Eocene age where it caps the Sin el Kaddah Plateau west of Aswan in Southwest Egypt (Figure 4-38). The barren, windswept surface of this extremely arid plateau gives a unique signature on the SIR-A radar image. Several large fractures (arrows) intersect in a rectangular grid pattern that has been etched by winds, which are dominantly from the north. Only a few large drainage channels are preserved on the limestone surface, in contrast to the intricate patterns of the dendritic drainage preserved on the sandstones and shales of Upper Cretaceous age that crop out along the east edge of the plateau.

The limestone is heavily wind-eroded, with roughness scales varying from grooves and ridges with pinnacles on the order of a few centimeters, to yardangs tens of meters wide and up to hundreds of meters long (Grolier et al., 1980).

Figure 4-37. SIR-A Image of Harrat Al Uwayrid (Data Take 28)

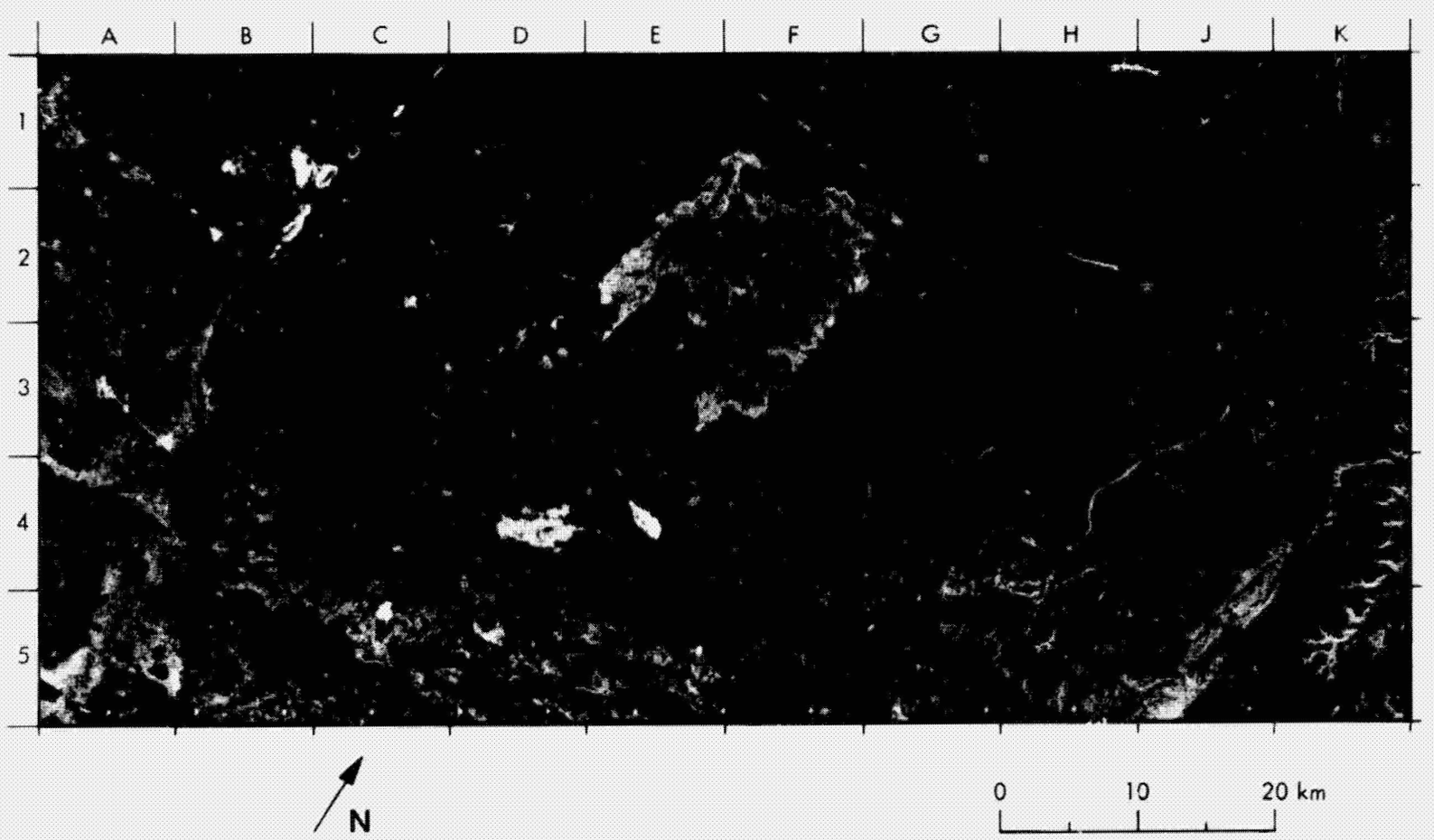

ORIGINAL PAGE
BLACK AND WHITE PHOTOGRAPH

Figure 4-38. SIR-A Image of Limestone Plateau, Egypt (Data Take 28)

This type of desert terrain was referred to as "kharafish" by early explorers (Beadnell, 1909; Gautier and Mayhew, 1935). These varying scales of roughness probably account for the peculiar distribution of gray tones and bright patches on the SIR-A image.

L. COREGISTRATION OF SIR-A AND SEASAT IMAGES OF THE SAN RAFAEL SWELL AND THE SANTA YNEZ RANGE (D. Evans and J. B. Cimino, JPL)

Incidence angle, polarization, and wavelength are all radar instrument parameters that may be varied to extract information from a scene using microwave techniques. By comparing SIR-A data with Seasat data, the effect of a variable incidence angle on the radar backscatter may be examined. Seasat had a small incidence angle of about 20 deg; therefore, backscatter was dominated by slope or topography. SIR-A, however, had a much larger incidence angle (about 50 deg); therefore, the backscatter was dependent primarily on local roughness and relatively independent of slope.

Both SIR-A and Seasat images of the San Rafael Swell region in Utah and the Santa Ynez Range in California will be used to illustrate the advantage of having multiple incidence angles for the interpretation of the local geology.

1. The San Rafael Swell (Utah)

Figure 4-39(a) is an image of the southern portion of the San Rafael Swell, a large, sedimentary dome in eastern Utah. Geologic units of interest can be traced over large areas (Figure 4-39(b)). The dome is made up of continental and marine sediments uplifted during the early Tertiary ($\sim$50 million years ago). The repeated transgression and regression of the seas in this region resulted in the deposition of units of economic importance. For example, coal beds have been found in the Ferron Sandstone (B2 and G3). Other economically important units such as the uranium-bearing Salt Wash Sandstone (D4 and E4) are found in this area because the permeable nature of the sedimentary rocks allows the flow of mineralizing fluids.

The SIR-A image was digitized and registered to a Seasat SAR image (Figure 4-39(c)) by finding common tie points in the images, and rotating and sizing the SIR-A image to fit the Seasat image. The coregistered images were

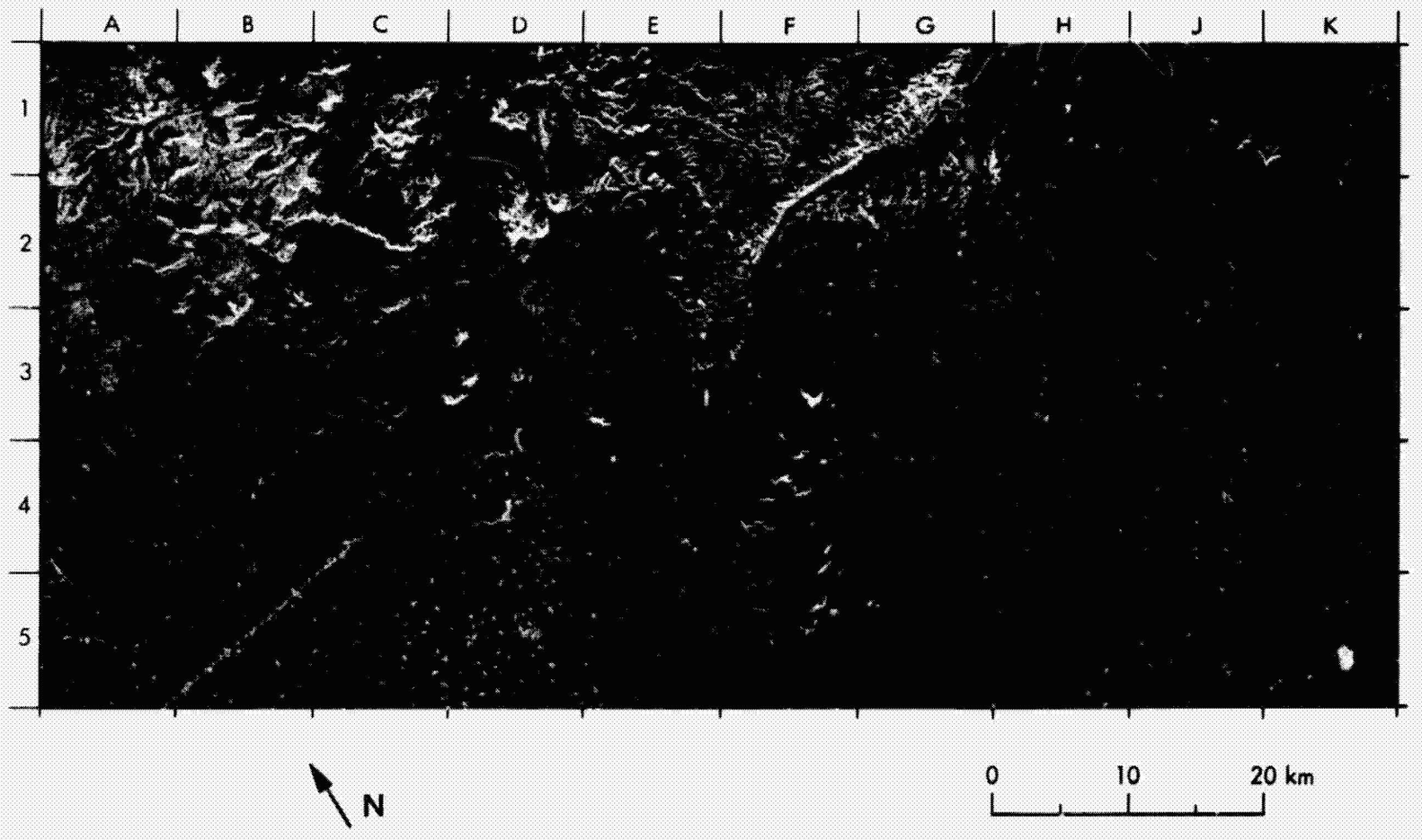

ORIGINAL PAGE
BLACK AND WHITE PHOTOGRAPH

Figure 4-39. South San Rafael Swell, Utah: (a) SIR-A Image (Data Take 24C)

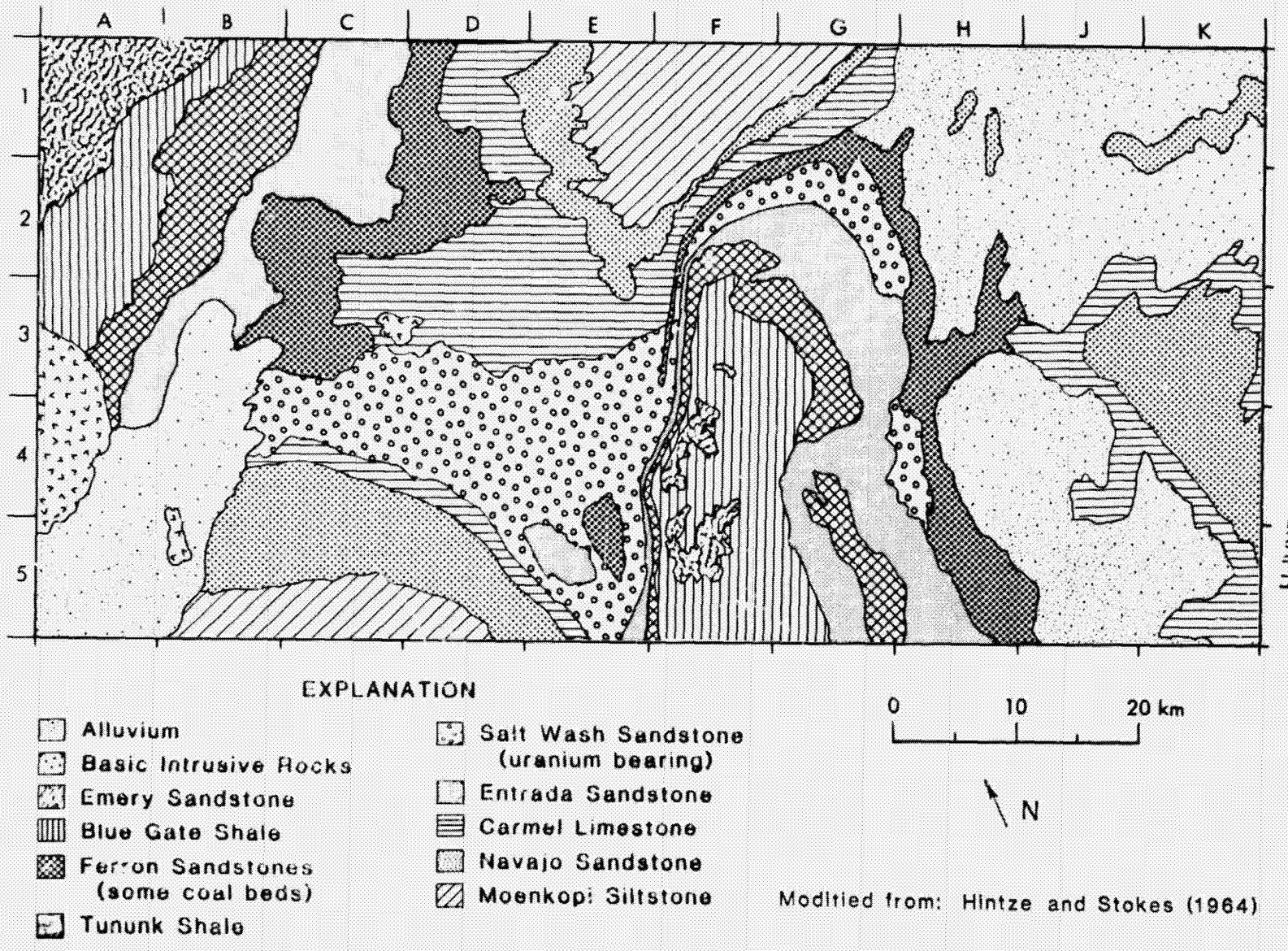

ORIGINAL PAGE
BLACK AND WHITE PHOTOGRAPH

Figure 4-39. South San Rafael Swell, Utah: (b) Geologic Map Modified From a Map by Hintze and Stokes (1964) Using the Data of Figure 4-39(a)

Figure 4-39. South San Rafael Swell, Utah: (c) Seasat SAR Image (Rev. 853)

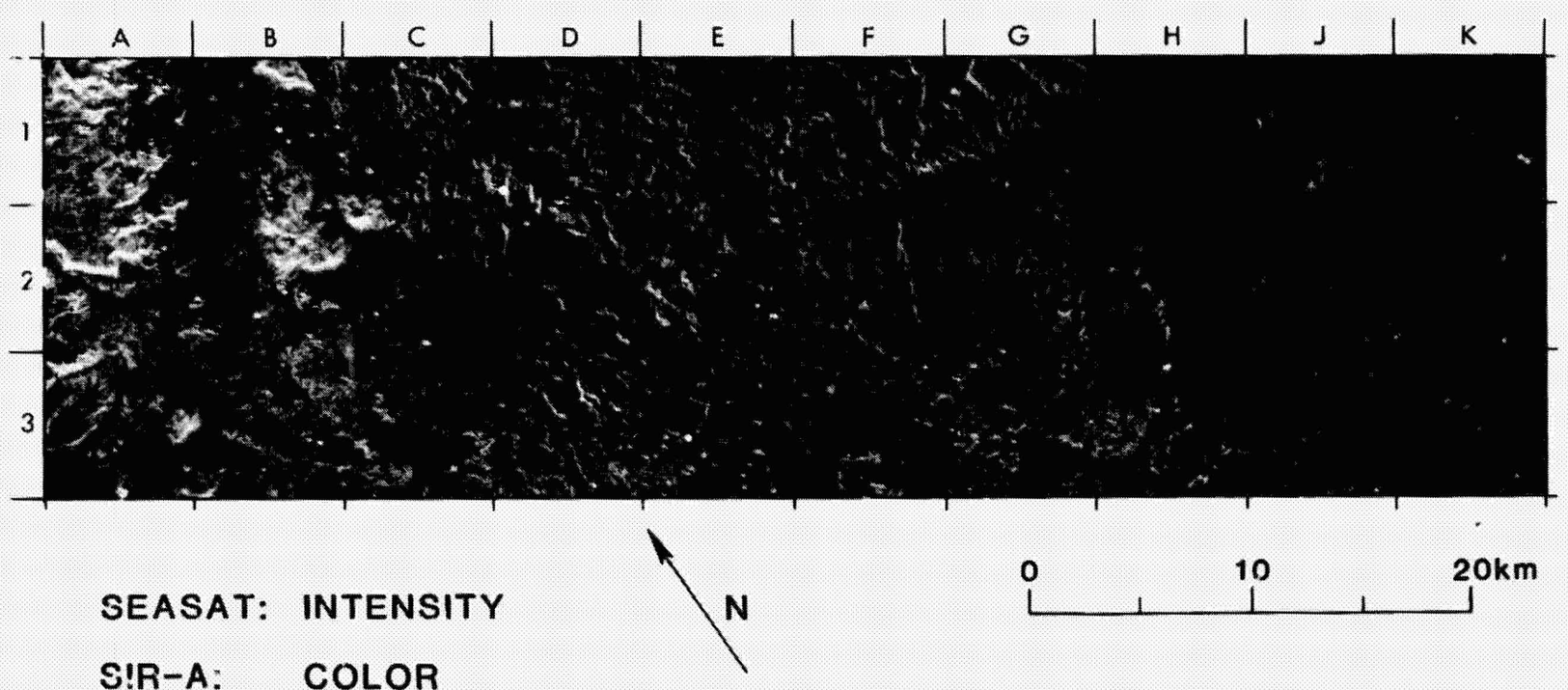

ORIGINAL PAGE
COLOR PHOTOGRAPH

Figure 4-39. South San Rafael Swell, Utah: (d) Coregistered SIR-A and Seasat Images

then displayed as shown in Figure 4-39(d) using the SIR-A image to produce color and the Seasat image to modulate the intensity of the color where the images overlapped. Because of the difference in incidence angles of the two sensors, SIR-A images are most sensitive to small-scale roughness properties of the surface, while Seasat images are more sensitive to changes in local slope. Therefore, in this image, variations in color are related to roughness variations, and variations in intensity are related to topography.

The combination of surface roughness and topographic information shown in Figure 4-39(d) allows better discrimination of the lithologic units present. For example, in the cliff at D2, it is possible to see sedimentary layers (coded as brown and blue in this rendition) that cannot be seen in either the SIR-A or Seasat image alone. This is a significant result, because it shows how subtle details can be brought out in combined image data sets.

2. Santa Ynez Range, Santa Barbara (California)

The California coastline from Point Conception (A5) to Ventura (K3) is shown in Figure 4-40. The geology is dominated by folded sedimentary layers of the Santa Ynez Range. The stratification terminates abruptly at the Santa Ynez Fault on the inland side of the mountains (C4 to K1). The Santa Clara River traces the Oak Ridge Fault, seen as a bright linear feature east of Ventura (K1 to K2). Cachuma and Casitas Lakes are the large dark areas at D2/E2 and K2, respectively. The city of Santa Barbara (G3) is visible in the center of the figure (bright region along the coast line). The row of bright spots in the ocean (H3) are oil drilling platforms in the Santa Barbara Channel, while random bright points in the channel are vessels.

The brightness of the terrain in the SIR-A image (Figure 4-40(a)) varies significantly from location to location, suggesting changes in local surface roughness. The Little Pine Fault running from C1 to E2, for example, shows up as a change in brightness from dark on the ocean side of the fault to bright on the mainland side. This is because the smoother Plio-Pleistocene nonmarine deposits on the southern side of the fault specularly reflect the radar beam, while the more rugged Mesozoic ultrabasic intrusive rocks and the

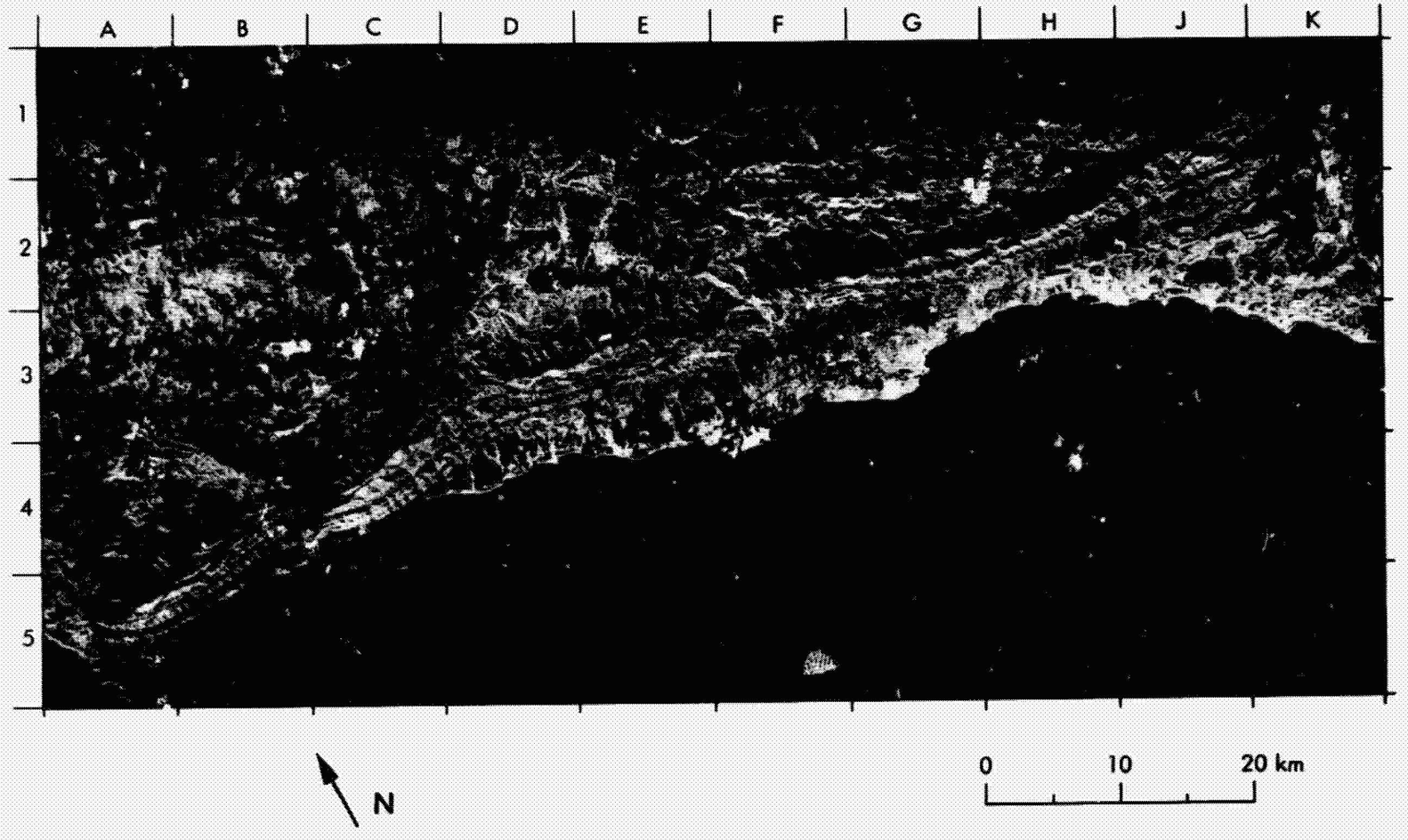

Figure 4-40. Santa Ynez Range, Santa Barbara, California: (a) SIR-A Image (Data Take 24C)

Figure 4-40. Santa Ynez Range, Santa Barbara, California: (b) Mosaicked Seasat SAR Image

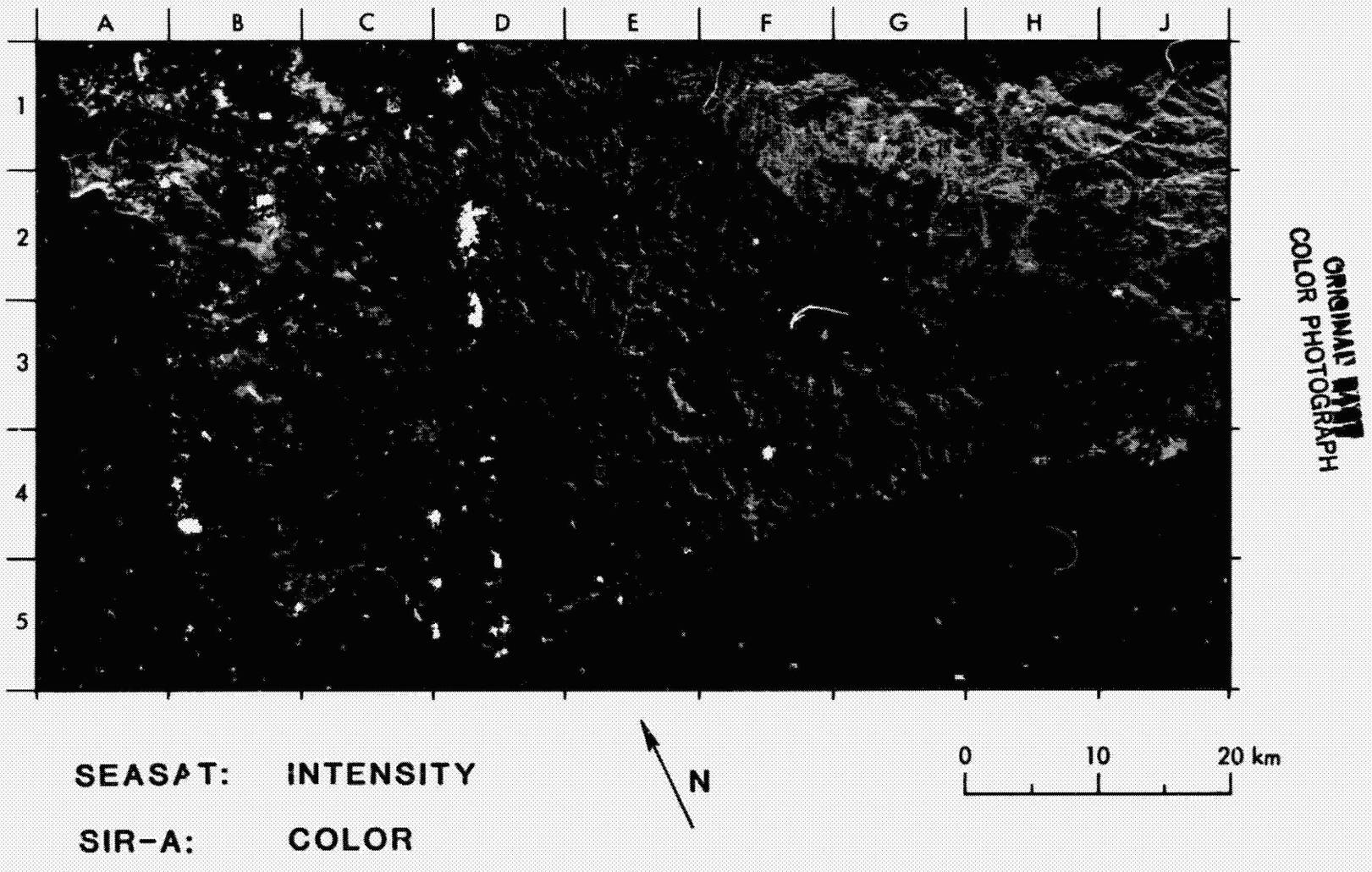

Figure 4-40. Santa Ynez Range, Santa Barbara, California (c) Coregistered SIR-A and Seasat Images

Franciscan Formation on the northern side scatter the radar beam, producing the bright radar return. The fault is not obvious in the Seasat image.

The mosaicked Seasat image (Figure 4-40(b)) of the same area shows some significant differences in the imagery. These differences are demonstrated in many regions throughout the image, but the most apparent is in the ocean where the Seasat incidence angle enables detection of roughness in the waters; however, the larger SIR-A incidence angle produces specular reflection. Differences are also notable along the Santa Ynez Range. Although in many cases there is extensive layover in the Seasat image, topography is well defined throughout the image. There are only a few places, for example, along the crests of the Santa Ynez Range where topography is apparent in the SIR-A image. This is because the local slopes are so steep that the incidence angle becomes small and topography dominates over surface roughness along the mountain crests. The bedding along the Santa Ynez Range is camouflaged by the dominant return of the drainages in the Seasat image, but very pronounced in the SIR-A image. The bedding can be easily followed from the most recent Upper Miocene Marine layer, which is that closest to the ocean, through the Middle and Lower Miocene Marines, the Oligocene Marine, and the Eocene Marine to Upper Cretaceous Marine, which is toward the inland side of the mountains. This bedding is cut abruptly by a small fault at D5/E5.

There are, of course, advantages to both incidence angles. The sedimentary layers along the coastline are easily traceable in the SIR-A image, but are lost in the layover of the Seasat image. On the other hand, the drainage patterns at C2 in the Seasat image are obvious, but are not seen in the SIR-A image. This is due to the difference in local slope in the two regions.

The color coregistered image of the Santa Ynez Range (Figure 4-40(c)) provides even more information. As with the San Rafael images, the SIR-A image is used to produce color and the Seasat image is used to modulate the intensity of the color where the images overlap. The combination of surface roughness and topographic information shown in this image allows better discrimination of the lithologic units present. The topographic information provided by the Seasat data enhances the image texture, which can be used to differentiate rock types.

For example, the linear and fine-scale texture pattern at G1 is related to non-marine unconsolidated conglomerates. Due west, at E2/F2 to E3/F3, is a coarse mountainous texture related to marine sandstones.

SECTION V

SIR-A IMAGE EXAMPLES

The SIR-A mission recorded data covering approximately 10 million km^2 of the Earth, including terrain from all continents except Antarctica. In this section, a sample of images is presented to give the reader examples of the wide variety of features imaged by the radar (Table 5-1). The section is divided into four parts: geology, hydrology, urban and agricultural regions, and oceanography.

All images cover an area 50 km (range direction) by 100 km (azimuth direction). The horizontal top and bottom margins are parallel to the Shuttle orbital path during acquisition of the data. The look angle of the radar antenna was always 47 deg from nadir in a northward direction perpendicular to the Shuttle ground track. The illumination direction is from the southernmost horizontal edge of the image to the northernmost horizontal edge. In some cases, Landsat and Seasat images are shown for comparison. Geologic maps are also shown for several images.

Table 5-1. Image Examples

A. Geology

1. Lu-Liang Shan (China)
2. Serra Imeri (Venezuela)
3. Pakaraima and Merume Mountains (Guyana)
4. Nile River Basin (Egypt)
5. Hamersley Mountain Range (Western Australia)
6. Lengguru Fold Belt (Irian Jaya)
7. Precambrian Outcrop (Western Algeria)
8. Faulted Area (East Coast of Belize)

B. Hydrology

9. Berau River Emptying into the Celebes Sea (Borneo)
10. Meta Province (Colombia)
11. Ilhas Macuapanim and Surrounding Rivers (Central Brazil)
12. Mississippi Flood Plain

C. Urban and Agricultural Regions

13. Brasilia (Brazil)
14. Cultivated Fields in Central New South Wales (Australia)
15. Villages and Cultivated Fields (China)

D. Oceanography

16. Ocean Patterns off Isla Coiba (Panama)
17. Internal Waves (Andaman Sea)
18. Coral-Reef Patterns Near Nai Nan Tao and Palawan
19. Wind Patterns (Sardinia)
20. Oil Rigs and Vessels (Persian Gulf)

A. GEOLOGY

1. Lu-Liang Shan (China)

The extensive dendritic patterns shown in this image in the Shanxi Province of China are drainages from the Hei-ch'a Shan (mountains) (F4, F5, G4, and G5) and the Lu-liang Shan (G1, G2, J1, and J2), which run into the Fen Ho (river) (K1 to K5) and the Huang Ho or Yellow River (A1 to A5). Smaller rivers including the Lan-i Ho (D1/D2 to A2), the K'u-yeb Ho (A5 to B5), and the Yu-fen Ho (F3 to A4/B4) contribute to this network. The more mountainous region in the center of the image is about 1000 m higher than the Huang Ho valley and 500 m higher than the Fen Ho valley. Bedrock consists mostly of Triassic sedimentary rocks that overlie an ancient platform.

The SIR-A image is very bright in the vegetated uplands because of the roughness of the canopy relative to the radar wavelength. Vegetation is also prevalent in the valleys that join the Huang Ho. Agriculture in this hot, dry region is supported by some irrigation. Winter wheat, millet, and koaling are the primary crops. Near-surface and deeply-buried coal deposits have been mined to some extent in this region of China. The river banks have a population density of about 50 people per square kilometer. The city of Lan-hsien is at H4 and Lao-ch'eng is at H3/H4.

(Data take 28; 38°27'N, 111°30'E.)

LU-LIANG SHAN (CHINA)

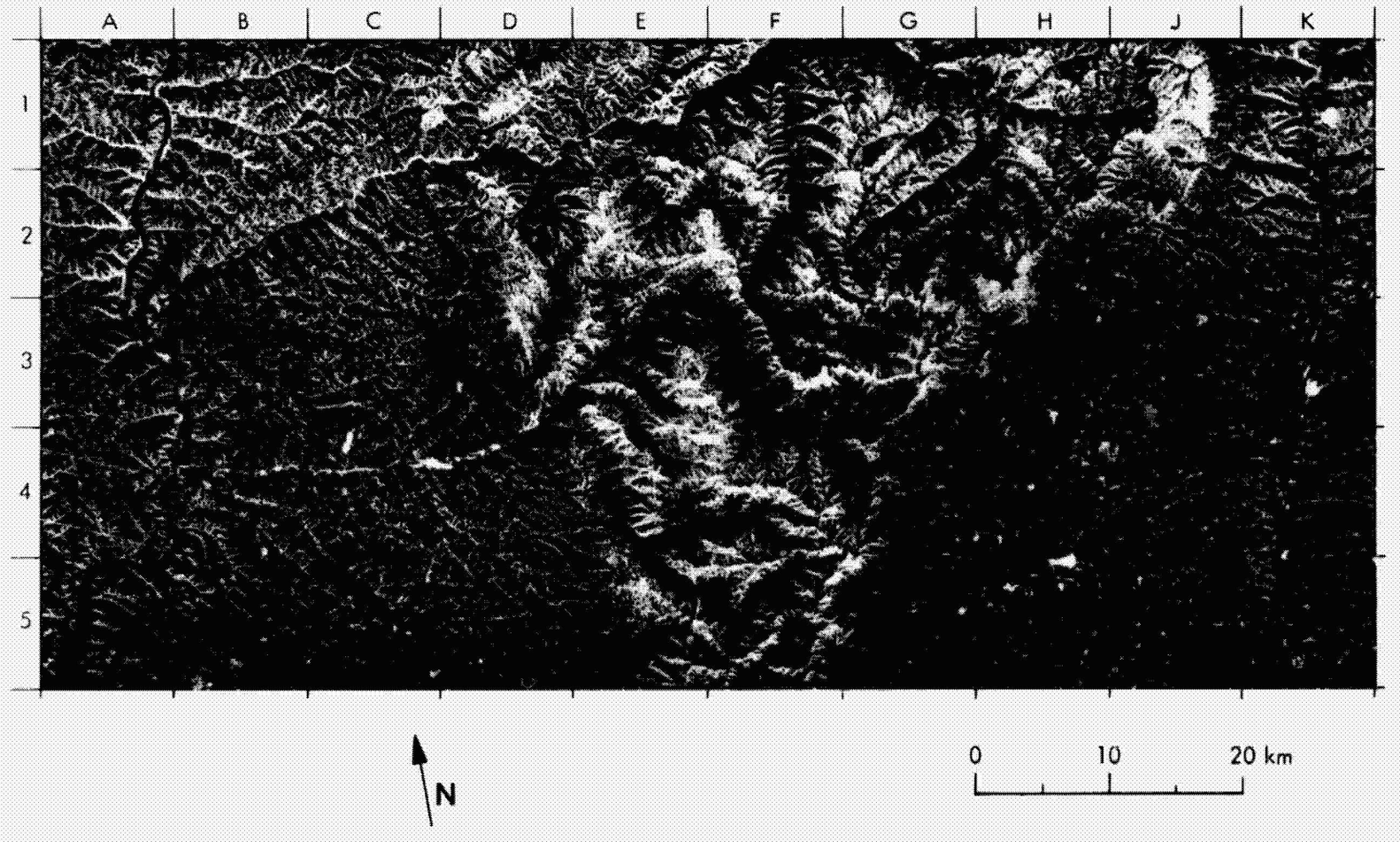

ORIGINAL PAGE
BLACK AND WHITE PHOTOGRAPH

2. Serra Imeri (Venezuela)

The dominant geological structure in this SIR-A image is the cross-cutting fracture pattern of lineaments in the Serra Imeri on the southern border of Venezuela. The range is on the south edge of a huge plateau that is part of the Guyana Shield. Aircraft charts warn of the abrupt cliffs that appear in the left portion of the image. The Yatua River runs through the center of the image (F1 to F5) and the city of Santa Isabel sits on the edge of the river (E4).

(Data take 34; 1°36'N, 65°30'W.)

SERRA IMERI (VENEZUELA)

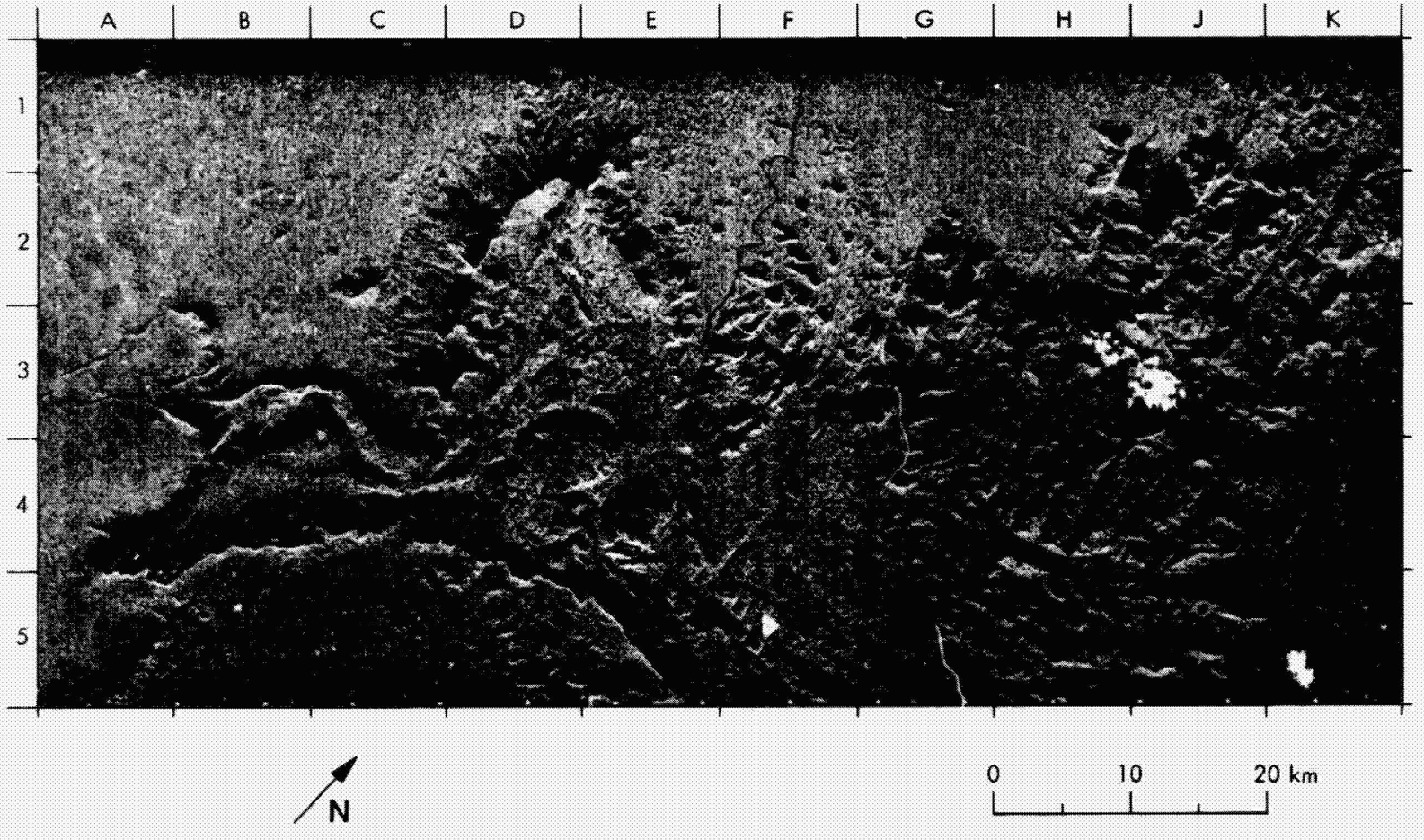

ORIGINAL PAGE
BLACK AND WHITE PHOTOGRAPH

3. Pakaraima and Merume Mountains (Guyana)

The mountain ranges dominating this SIR-A image are the Pakaraima Range in the left of the image and the Merume range in the right. The ranges are located in Guyana near the Venezuelan border just north of the Imbiamada. They are part of the Roraima Plateau in the Gran Sabana. The Mazarume River flows through the center and upper right of the image (G5 to J1). The tributary that connects with the Mazaruni at G3/G4 and flows to D2/E2 is the Kamurang River.

(Data take 34; 5°45'N, 60°51'W.)

PAKARAIMA AND MERUME MOUNTAINS (GUYANA)

ORIGINAL PAGE
BLACK AND WHITE PHOTOGRAPH

4. Nile River Basin (Egypt)

This SIR-A image shows a section of the Nile River just north of the Aswan Dam in Egypt. The major city of Kom Ombo sits just to the east of the lower bend in the river (H5). The Kom Ombo plain is covered by thick alluvial floodplain deposits containing shells, bones, and Stone-Age flint implements. The straight, bright vertical lines running along the broad, dry valley west of the river are power lines leading from the dam northward. The mountainous area to the west of the valley was overflown by the SMIRR experiment aboard STS-2.

The Quaternary sediments to the west of the Nile River are alluvial gravels, sand, and mud with a veneer of windblown sand. The Nubia Group to the east of the Nile and surrounding the Gebel el-Barga at D4/E4 is Mesozoic Taref Sandstone and Queseir Variegated Shale. The Upper Cretaceous/Paleocene Dakhla Formation, which shows up as a bright (rough) outcrop in several places throughout the image, consists of shale, marl, and limestone. The Paleocene outcrops also include the Tarawan Chalk and Esna Shale. The lower Eocene outcrops in the far left of the image are limestones of the Dungal Formation, containing flint concretions.

(Data take 28; 24°20'N, 32°35'E.)

NILE RIVER BASIN (EGYPT)

ORIGINAL PAGE
BLACK AND WHITE PHOTOGRAPH

GEOLOGIC MAP OF NILE RIVER BASIN

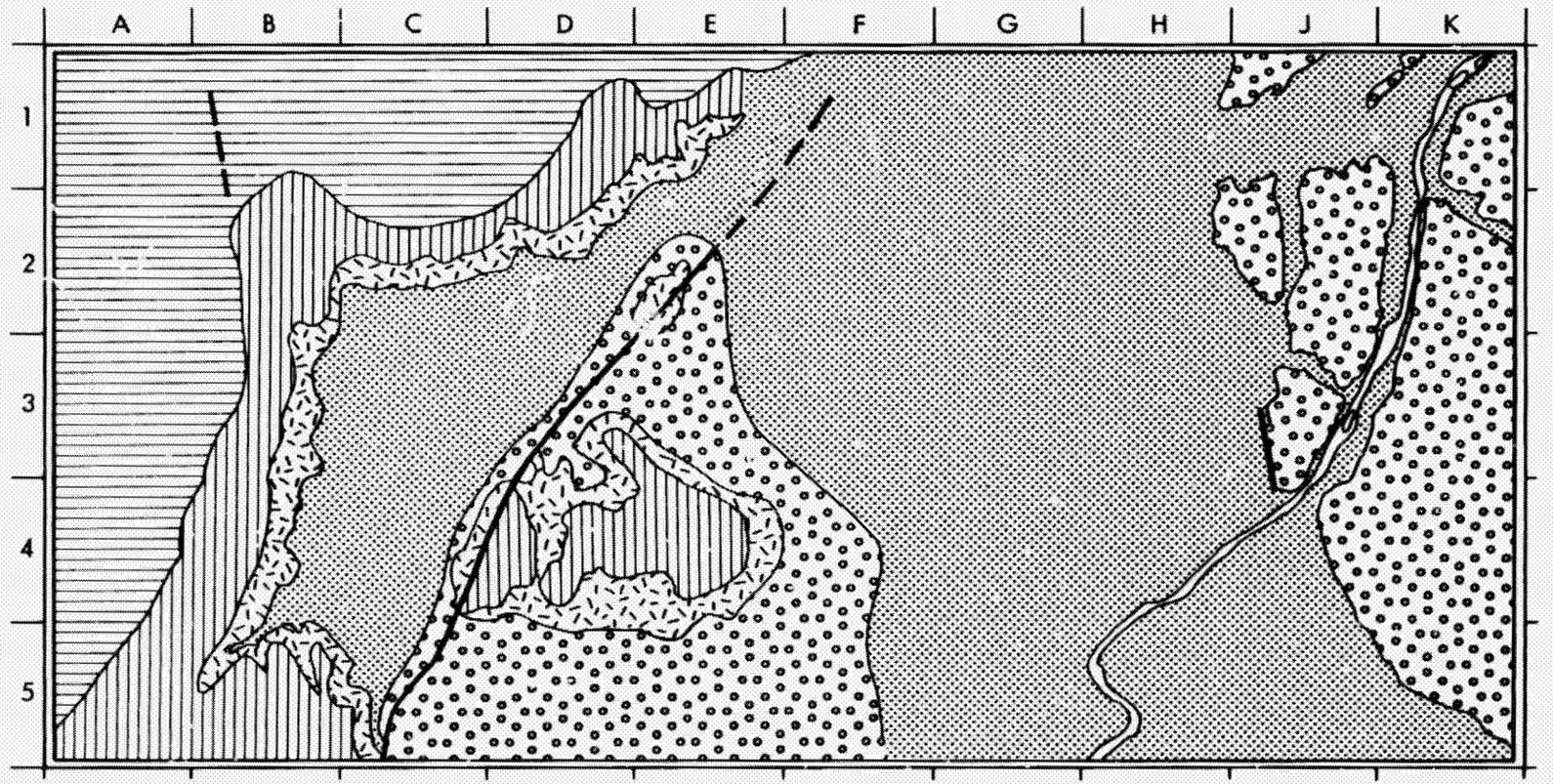

EXPLANATION

- Quaternary
- Lower Eocene
- Paleocene
- Dakhla Formation
- Nubia Group

Contact — Fault

N

0 10 20 km

Modified from: Geologic Map of the Aswan Quadrangle, Egypt, 1978, USGS

5. Hamersley Mountain Range (Western Australia)

The Hamersley Mountain Range in Western Australia is the dominant geologic structure in this SIR-A image. Volcanic rocks and sediments appear as eroded folds exposed at the surface. These rocks are approximately 1.5 billion years old. The central circular feature is a large intrusive granite and gneiss dome, which is part of a large anticline extending across most of the image. The Hardey River runs vertically to the right of the central circular dome (D1/E1 to B5), and the Beasley River runs southward in the lower left-hand corner of the image. Mount Turner is in the top center of the image. The region in the upper left quarter of the image is severely faulted. The bright linear feature cutting across the center of the dome is a dolerite dike.

(Data take 38; 22°52'S, 117°28'E.)

HAMERSLEY MOUNTAIN RANGE (WESTERN AUSTRALIA)

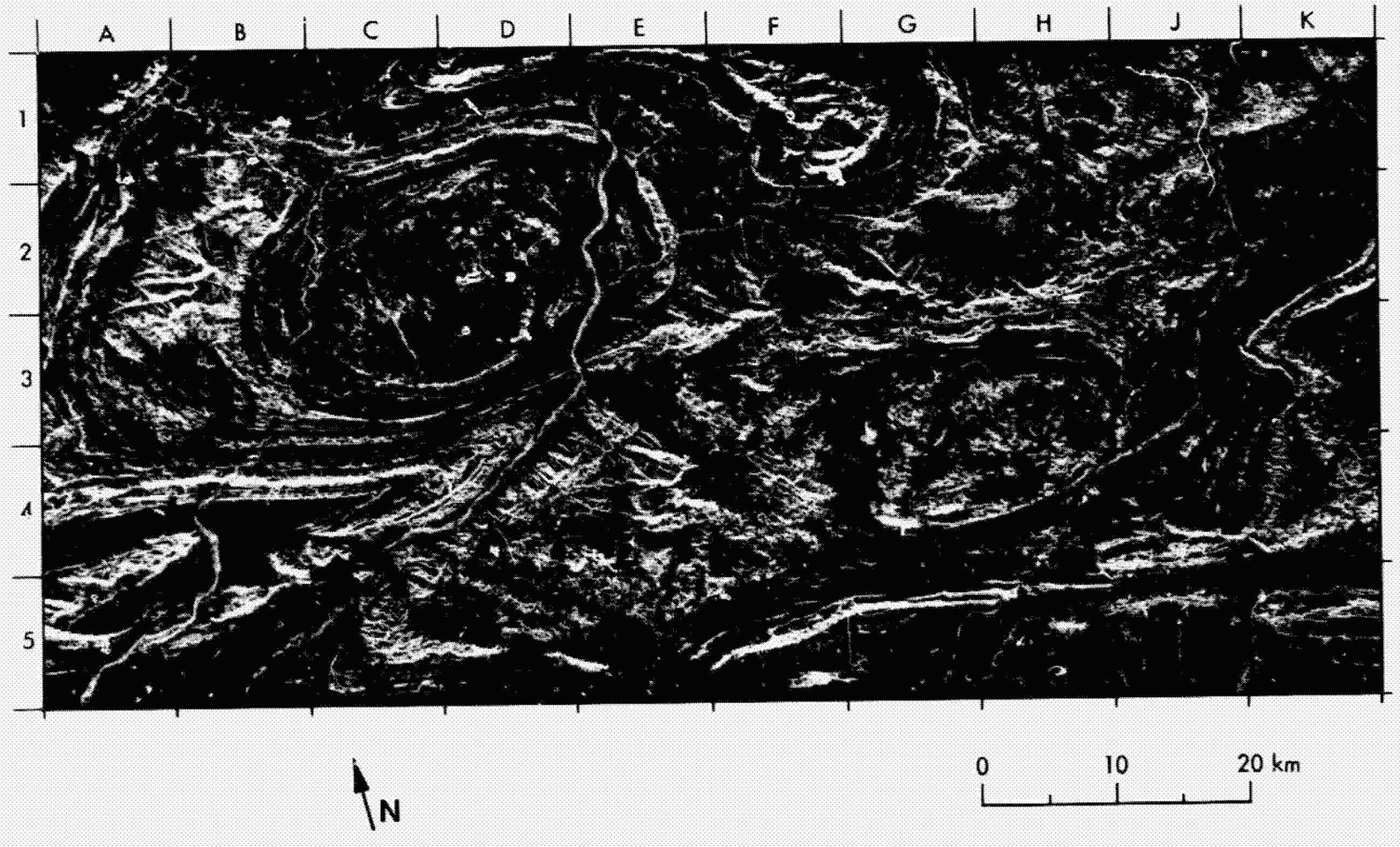

ORIGINAL PAGE
BLACK AND WHITE PHOTOGRAPH

6 engguru Fold Belt (Irian Jaya)

The Lengguru Fold Belt (the large "boomerang" structure, F3) shown dramatically in this SIR-A image is on the northwestern peninsula of Irian Jaya (western New Guinea). The pitted and grooved unit at K5 may be limestone that has developed karst topography common in tropical areas. Units at H1, H2, K1, and K2 appear to be thin, tilted, and eroded sedimentary beds with their outcrop pattern affected by folding and jointing. The two smaller islands are Rumberpon (A4) and Mios Wear (D5). The estuaries at E1 flow into the Teluk Benturi off the Ceram Sea. The water in the left of the image is the Teluk Sarera. The area is adjacent to the oil-producing Salawati Island region, where heavy jungle and cloud cover make radar images an economical method of exploration.

(Data take 32-33; 1°50'S, 133°54'E.)

LENGGURU FOLD BELT (IRIAN JAYA)

ORIGINAL PAGE
BLACK AND WHITE PHOTOGRAPH

7. Precambrian Outcrop (Western Algeria)

This SIR-A image shows an area west of Beni Abbes (not in image) in Western Algeria. In the far left of the image are some star dunes of the Erg El Raoui. The large cylindrical feature to the right of the dunes is the Jebel Guettara, a north-northwestern oriented Precambrian outcrop dissected by many crossing faults. The smaller circular features (E4) are part of an eroded anticline showing Silurian and Cambrian exposures. The feature is known as Dra El Kelba. These outcrops could be either due to plunging folds or to differential erosion following the topography. A large depression dominates the center of the image. This area is known as Hama du Guir and is characterized by Pliocene outcrops. To the right of the image is the western border of the Grand Erg Occidental, a sand sea characterized by barchans and star dunes. In the upper right corner of the image is a region of carboniferous outcrops showing well delineated bedding.

(Data take 32-33; 30°00'N, 0°15'W.)

PRECAMBRIAN OUTCROP (WESTERN ALGERIA)

ORIGINAL PAGE
BLACK AND WHITE PHOTOGRAPH

GEOLOGIC MAP OF PRECAMBRIAN OUTCROP (WESTERN ALGERIA)

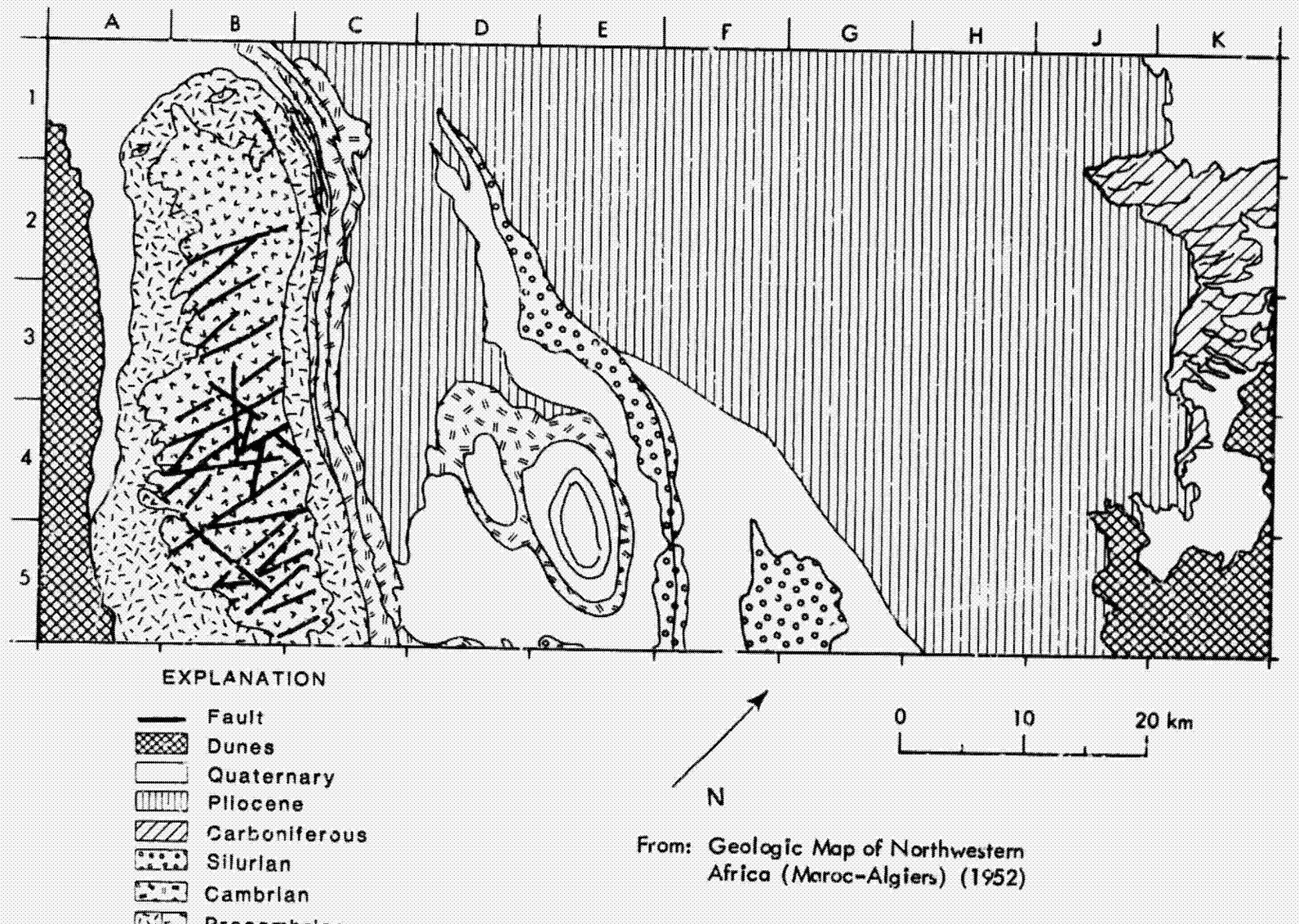

From: Geologic Map of Northwestern Africa (Maroc-Algiers) (1952)

8. Faulted Area (East Coast of Belize)

This SIR-A image of central Belize covers an area of diverse lithology cloaked in a nearly continuous vegetation canopy. Differences in lithology are therefore recognized in the image on the basis of texture. Areas of alluvium, such as along the coast, and intrusive plutonic rocks at D1 and H1 have smooth, even textures. The center of the image is composed of the coarse mountainous texture of metamorphic rocks and old continental sediments. In tropical regions, carbonates such as limestones often produce the unique knobby topography known as karst. This is best seen at F5 and G4.

(Data take 24C; 17°02'N, 88°31'W.)

FAULTED AREA (EAST COAST OF BELIZE)

ORIGINAL PAGE
BLACK AND WHITE PHOTOGRAPH

GEOLOGIC MAP OF CENTRAL BELIZE

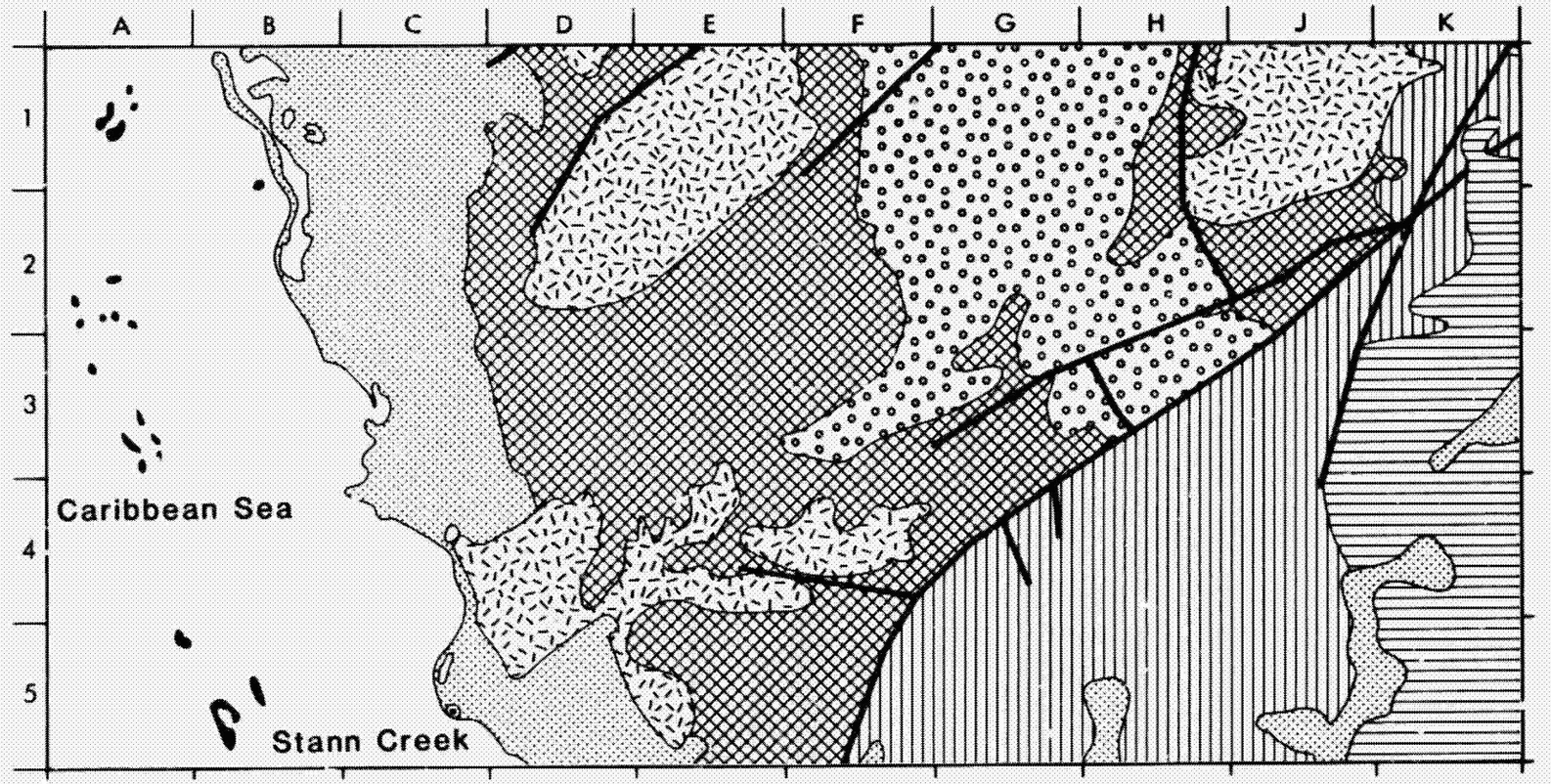

EXPLANATION

- Quaternary Alluvium
- Paleocene-Eocene Marine Sediments
- Cretaceous Carbonates
- Carboniferous-Permian Continental Sediments
- Undivided Plutonic Rocks
- Paleozoic Undivided Metamorphic Rocks
- Contact
- Fault

N

0 10 20 km

Modified from: Instituto Geográfico Nacional (1970)

ORIGINAL PAGE IS OF POOR QUALITY

B. HYDROLOGY

9. Berau River Emptying Into the Celebes Sea (Borneo)

The intricate drainage patterns shown in this SIR-A image are created by the Berau River as it empties into the Celebes Sea in Tanjungbata on the east coast of Borneo. Some interesting ocean patterns are apparent throughout the Celebes Sea. The bright white linear pattern (K5) may be associated with coral reefs.

(Data take 24BB; 2°10'N, 117°40'E.)

BERAU RIVER EMPTYING INTO CELEBES SEA (BORNEO)

ORIGINAL PAGE
BLACK AND WHITE PHOTOGRAPH

10. Meta Province (Colombia)

This SIR-A image of the Meta Province shows the Amazon Basin just east of the Cordillera Oriental near Bogotá, Colombia. The Amazon Basin region is covered by vegetation and appears bright to the radar in the right portion of the image. The left portion of the image is dominated by very steep drainage canyons. These canyons empty into major rivers (brightest patterns) such as Rio Manacacias (A2 to A5), Rio Planas (C1 to C5) and Rio Vichada (E1 to D4). The darkest linear features in the left of the image are ridges; however, the dark intensity of the region in general is unusual and is associated with the flatness of the savanas. The darker region is higher in elevation by about 200 m and thus probably contains different vegetation than the jungle region to the right. In the right portion of the image, it is difficult to recognize features; however, Rio Siare is apparent, flowing from F5 to K2.

(Data take 24C; 3°18'N, 71°58'W.)

META PROVINCE (COLOMBIA)

ORIGINAL PAGE
BLACK AND WHITE PHOTOGRAPH

11. Ilhas Macuapanim and Surrounding Rivers (Central Brazil)

A complex network of rivers surrounds the island of Ilhas Macuapanim in central Brazil in the lower right quarter of these SIR-A and Landsat images. The north-south trending river is Rio Japurá and the river arching in at the bottom of the image is the Amazon. The SIR-A image was acquired in November 1981 and the Landsat image was acquired in September 1973. In general, the main stream channels have changed very little in 8 years; however, closer examination discloses some significant alterations in the minor connecting channels. In 1973, the Rio Japura was connected to the Amazon primarily at A5/B5. At point A5 in the Landsat image, however, there was a thin channel connecting the two rivers. In 1981, the connection at point A5/B5 in the SIR-A image is almost extinct and the two rivers now connect at point A5. This rerouting has decreased the size of the large island in the Amazon significantly. Other nearby islands in the Amazon have also been altered by the change in course. Note that the arm just above the Amazon River has become only a skeleton in the 1981 SIR-A image.

It is significant that few Landsat images with less than 20% cloud cover have been obtained of this area. The L-band radar, however, is not influenced by cloud cover because of the longer wavelength of the sensor. In fact it is likely the area was covered at least partially by clouds when this SIR-A image was acquired. Therefore, to monitor the courses of rivers in cloudy regions of the world such as Brazil, it is beneficial to use radar techniques.

(SIR-A data take 24C; 2°36'S, 65°00'W. Landsat ID No. 1424-13583, band 7, September 20, 1973.)

ILHAS MACUAPANIM (CENTRAL BRAZIL)

ORIGINAL PAGE
BLACK AND WHITE PHOTOGRAPH

LANDSAT IMAGE OF ILHAS MACUAPANIM (SEPTEMBER 1973)

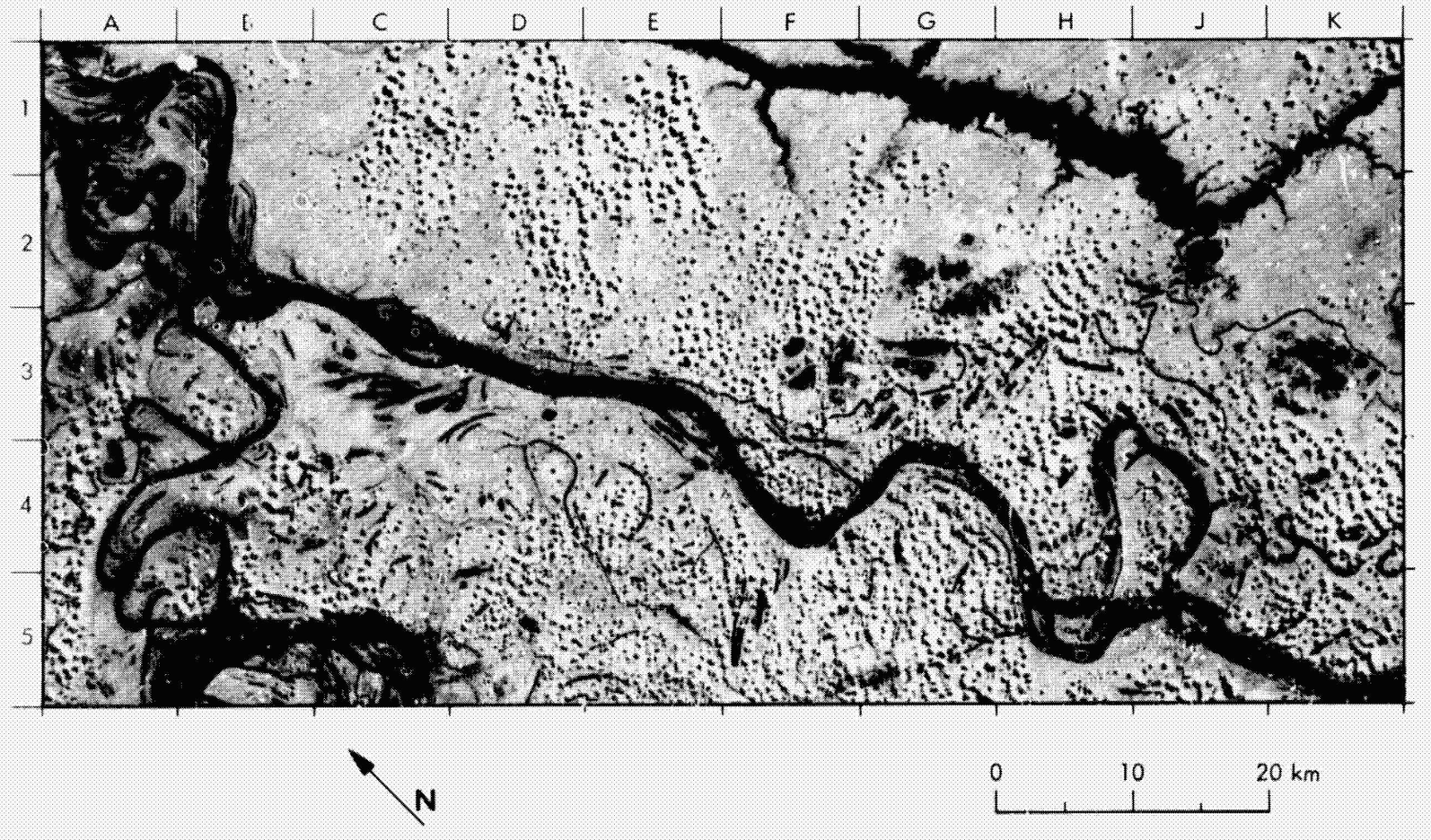

ORIGINAL PAGE
BLACK AND WHITE PHOTOGRAPH

12. Mississippi Floodplain (Mississippi)

The portion of the Mississippi River shown in this SIR-A image is just south of Vicksburg. The floodplain extends from the far left of the image to just right of the river (H/J). The floodplain edge east of the river shows up as a change in intensity from bright in the floodplain to darker in the uplands. The larger bright area in the center of the image and the smaller bright area at C3 are wooded areas. Surrounding these areas are agricultural regions through which many smaller creeks, bayous, and rivers flow. The horseshoe-shaped sections of the Mississippi (H5 and H6) are oxbow lakes or abandoned meanders of the main river. The thin bright lines outlining the oxbows are vegetated levees that show high backscatter, especially in contrast to the specular scattering of the smooth river.

(Data take 24B; 32°16'N, 91°20'W.)

MISSISSIPPI FLOOD PLAIN (MISSISSIPPI)

ORIGINAL PAGE
BLACK AND WHITE PHOTOGRAPH

C. URBAN AND AGRICULTURAL REGIONS

13. Brasilia (Brazil)

The city of Brasilia dominates the patterns seen in this image. The black line from E1 to G5 in the center of the figure is the Pan American Highway. The dark lake at F2 is Lago de Brasilia. The curved pattern to the west of the lake (E2/F2) (E/F-2) is a large residential area composed primarily of apartments. Other urban features are shown in the map.

(Data take 24C; 15°52'S, 47°57'W.)

BRASILIA (BRAZIL)

ORIGINAL PAGE
BLACK AND WHITE PHOTOGRAPH

URBAN MAP OF BRASILIA (BRAZIL)

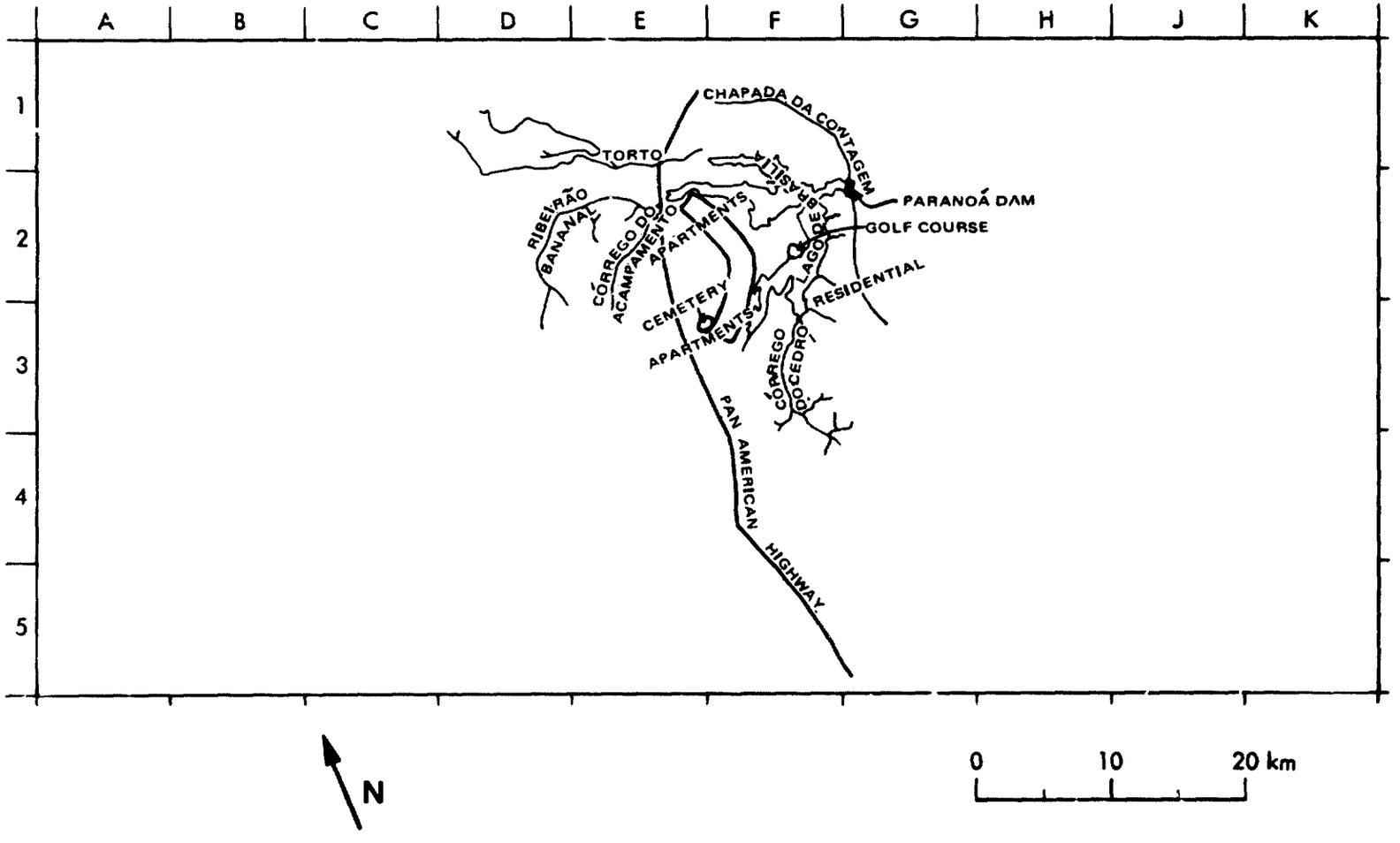

ORIGINAL PAGE IS OF POOR QUALITY

14. Cultivated Fields in Central New South Wales (Australia)

This SIR-A image shows a cultivated region of central New South Wales, Australia. Lake Brewster appears at A2 as an oval feature. The city of Ungarie appears as a bright spot at K1/K2. The rectangular regions are crops. The bright lines dividing the crops are probably metal fences or rows of trees, which are often planted to block winds. The brightness of a crop depends on the type of crop, the stage of growth, and the direction of the rows of plants relative to the look direction of the radar.

(Data take 38; 33°38'S, 146°23'E.)

CULTIVATED FIELDS IN CENTRAL NEW SOUTH WALES (AUSTRALIA)

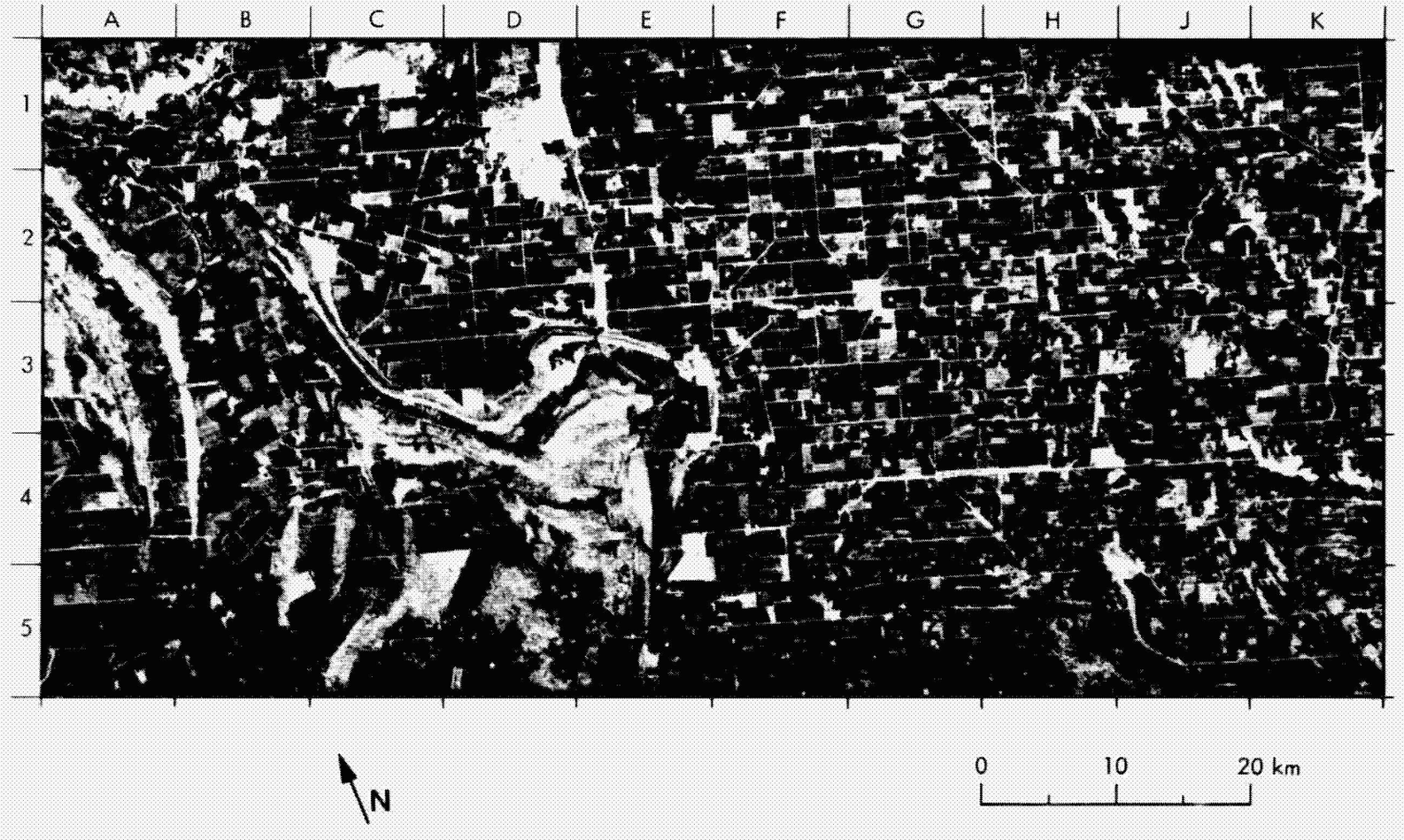

ORIGINAL PAGE
BLACK AND WHITE PHOTOGRAPH

15. Villages and Cultivated Fields (China)

The intricate maze of rectangular patterns and hundreds of bright spots covering this SIR-A image are cultivated fields and small villages in the province of Shantung and Hopeh in eastern China. The Yun-ho (Grand Canal) running from K1 to G5/H5 divides the two provinces (Hopeh is to the left). The larger cities of Te Chou, located at K2, Heng Shui at E1/F1, and Nan-kung at C5 are extremely bright. The region is about 150 km north of China's largest river, the Huang Ho. The Fu-yang Ho running from E1 to A4/A5 looks like a double river. Actually, the river is the southernmost feature, and the northernmost feature is a levee. The Yun-ho also appears to be a double river; however, close comparison shows that the river runs between two brighter levees.

This region is part of the North China Plain and has a hot, dry summer climate with cold, dry winters. The average precipitation is low, however there may be a torrential summer maximum or no precipitation at all. The summer rains cause severe flooding due to the flatness of the near-sea-level alluvial soils. Fine, fertile loess from the river's sources in the provinces of Inner Mongolia, Shanxi, Shaanxi, and Gansu muddy the waters in the rivers. When the rivers flood, this silt is trapped in sedimentation basins. When the basins are filled, they are cultivated. An example of this is shown at C2/D2 where a lake that existed in 1976 (seen on Landsat image) has been cultivated in 1981 when the SIR-A image was acquired. The deposition of silt from the flooding of the rivers has made the North China Plain fertile.

The density of villages in this region is roughly one per square kilometer. Over half the total land area in this region is cultivated to feed the more than 200 people per square kilometer. Winter wheat is the primary crop in this area with koaling and millet also important resources. Soy beans, sweet potatoes, cotton, and maize are also common.

(Data take 28; 37°30'N, 115°42'E.)

VILLAGES AND CULTIVATED FIELDS (CHINA)

ORIGINAL PAGE
BLACK AND WHITE PHOTOGRAPH

D. OCEANOGRAPHY

16. Ocean Patterns Off Isla Coiba (Panama)

Although the primary objective of the SIR-A mission was to image geologic features over land, some data were taken over the ocean. This image just southwest of Isla Coiba off the southern coast of Panama shows some internal wave patterns. These waves are generated by disturbances created within the ocean and propagate within stratified subsurface layers defined by temperature and salinity variations. The wave-generated currents interact with the surface, leading to periodic variations of the surface roughness. The radar images of these variations provide information about the spatial properties of the wave train. The image was obtained on November 14, 1981, at a GMT of 11 h, 47 min.

(Data take 37; 6°56'N, 82°06'W.)

OCEAN PATTERNS OFF ISLA COIBA (PANAMA)

ORIGINAL PAGE
BLACK AND WHITE PHOTOGRAPH

17. Internal Waves (Andaman Sea)

The large curvilinear patterns shown in this SIR-A image are internal waves in the Andaman Sea 150 km southeast of North Andaman Island. This area is well known for the presence of large internal waves. The upper right area of the image corresponds to the location of a subsurface sea mount. It is possible that the wave is generated by the interaction of currents with the mount. The image was obtained on November 14, 1981, at a GMT of 10 h, 56 min.

(Data take 35-36; 12°28'N, 94°00'E.)

INTERNAL WAVES (ANDAMAN SEA)

ORIGINAL PAGE
BLACK AND WHITE PHOTOGRAPH

18. Coral Reefs Near Hai Nan Tao and Palawan

Although the 47-deg look angle used for the SIR-A mission was chosen to emphasize land topography rather than ocean patterns, some unusual oceanic features were imaged. The white patterns seen in this image are coral reefs associated with the Parcel Islands. They are located in the South China Sea between the islands of Hai Nan Tao and Palawan in the Phillipines. The reefs shown in this image are part of the Discovery Reef, and the islands (A3/A4) (small white spots) are part of the Crescent group. The linear streaks in the ocean are the result of wind interaction with the surface. The image was acquired on November 13, 1981, at a GMT of approximately 16 h and 26 min.

(Data take 32-33; 15°50'N, 111°40'E.)

CORAL REEFS NEAR HAI NAN TAO AND PALAWAN

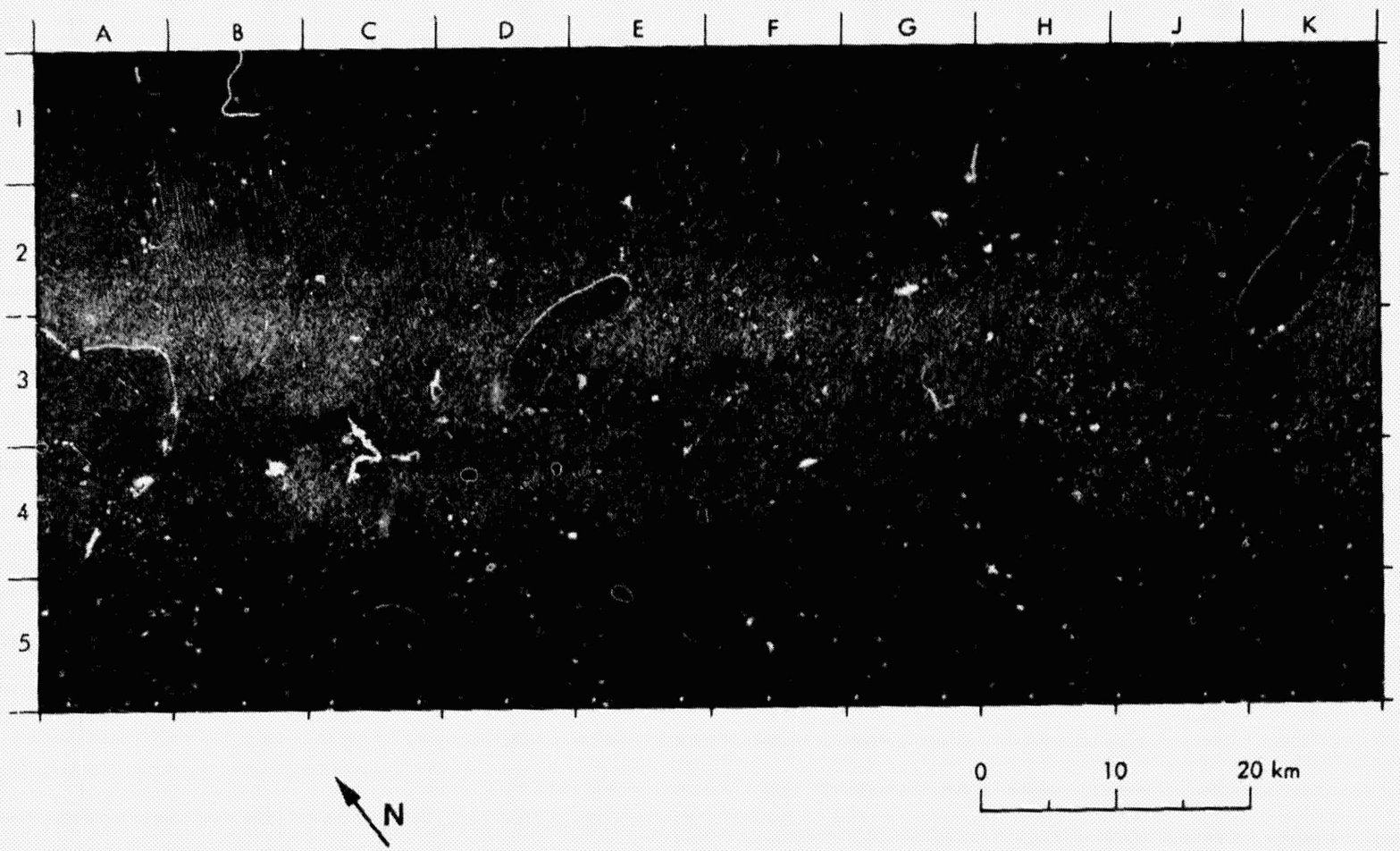

ORIGINAL PAGE
BLACK AND WHITE PHOTOGRAPH

19. Wind Patterns (Sardinia)

This area of the Mediterranian just off Sardinia was imaged twice by SIR-A during the STS-2 flight. Changes in the ocean patterns over a 90-min period are apparent. In the right portion of the image the ocean has become rougher and distinct eddies appear near the coast. The rough pitches are most likely due to a localized wind's interaction with the surface. These two images allow us to establish an upper limit of 90 min as the time constant for the generation of the bright (rough) patches. Data take 35-36 was imaged on November 14, 1981, at a GMT of 10 h and 36 min, and data take 37A was imaged at a GMT of 12 h and 10 min.

(Data takes 37A and 35-36; 40°10'N, 10°00'E.)

WIND PATTERNS OFF SARDINIA (DATA TAKE 35-36)

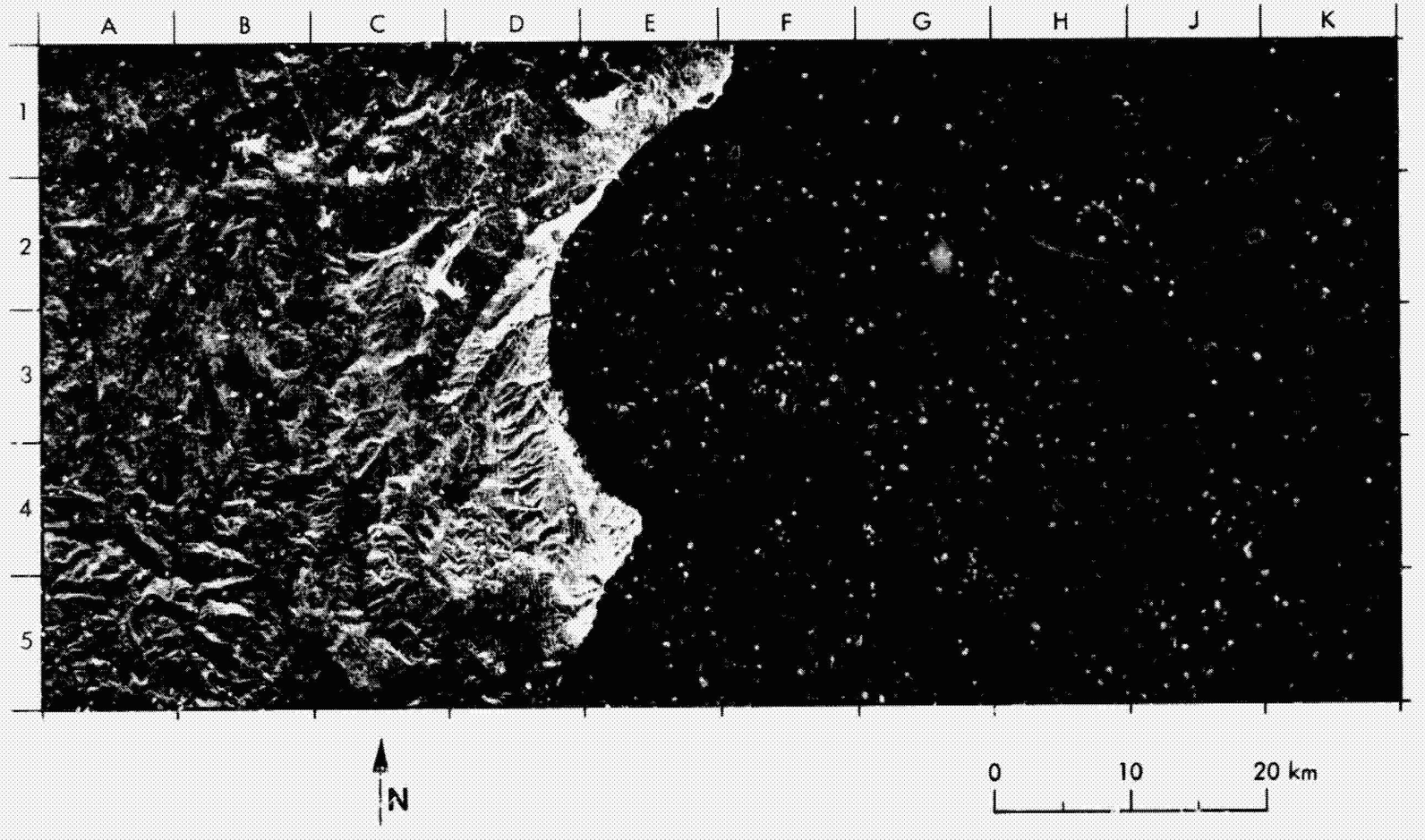

ORIGINAL PAGE
BLACK AND WHITE PHOTOGRAPH

WIND PATTERNS OFF SARDINIA (DATA TAKE 37A)

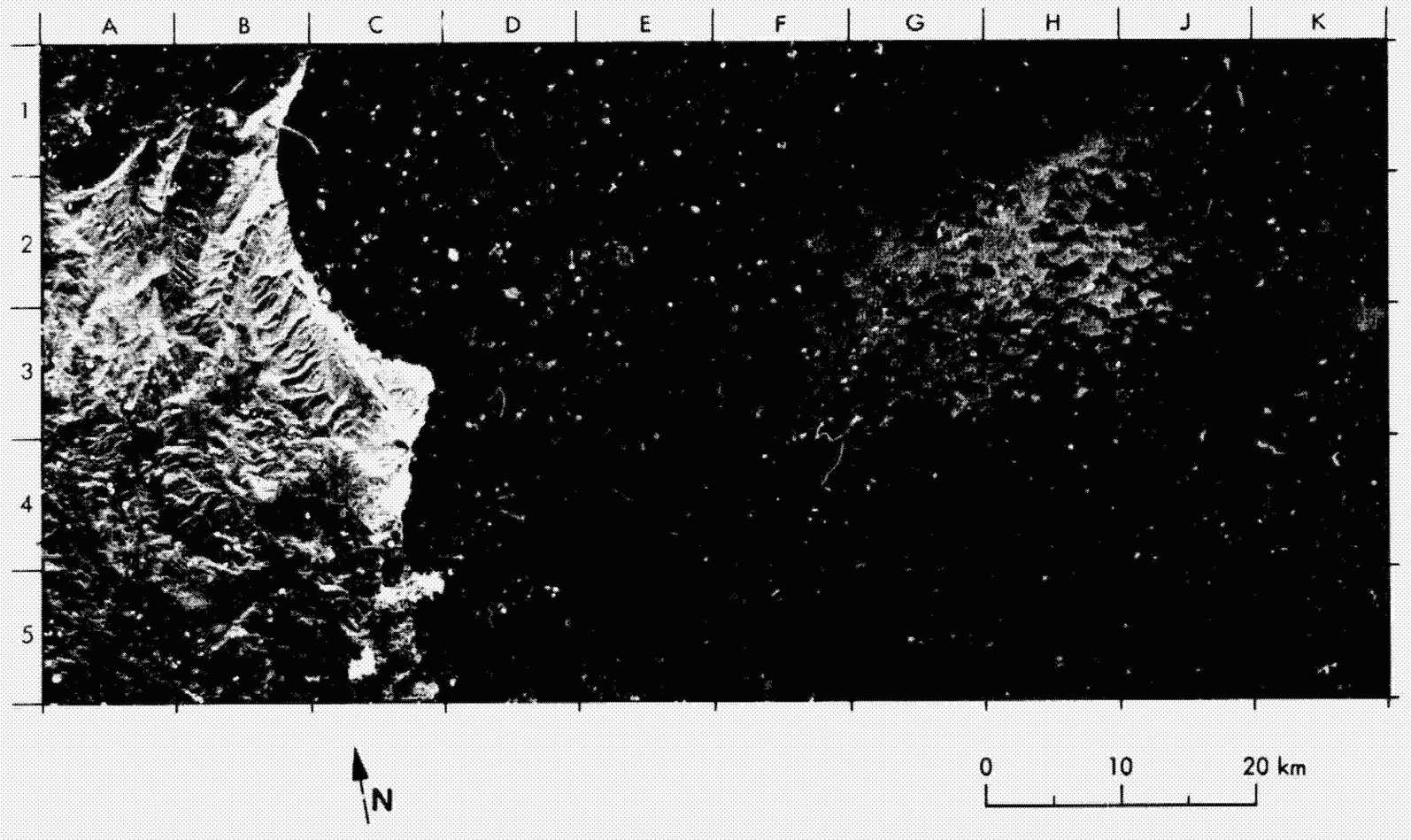

ORIGINAL PAGE
BLACK AND WHITE PHOTOGRAPH

20. Oil Rigs and Vessels (Persian Gulf)

Ships and oil rigs appear in this SIR-A image as bright point targets in the Persian Gulf. The waters in the right of the image are rough — that is, the wave spectrum has signified components with wavelengths of the same order of magnitude as the radar wavelength (0.235 m). The darker patterns throughout the rougher waters are probably oil slicks. The increased density of the water at the surface where the oil slicks are located tends to damp the formation of shorter wavelengths. Abu Dhabi is just off the lower right of the figure. The image was obtained on November 14, 1981, at a GMT of 12 h and 20 min.

(Data take 37A; 24°10'N, 54°10'E.)

OIL RIGS AND VESSELS (PERSIAN GULF)

ORIGINAL PAGE
BLACK AND WHITE PHOTOGRAPH

SECTION VI

SIR-A/SMIRR CROSSINGS

The primary information derived from SIR-A data is surface structure and surface roughness. If the geologic structures imaged by the radar could also be identified by rock type, more refined interpretations of the geology would be possible. Such data are available from the Shuttle Multispectral Infrared Radiometer (SMIRR), a JPL experiment conducted by A. Goetz; the SMIRR was also aboard STS-2. SMIRR collected spectra in the 0.5- to 2.5-μm range in an attempt to discriminate geologic units using their spectral properties. Figure 6-1 (a, b, and c) shows locations on the Earth where the SIR-A and SMIRR tracks overlap. SIR-A produced images at a look angle of 47 deg from nadir and SMIRR recorded line data from a 100-m swath pointed toward the nadir; therefore, all data overlaps are at locations where the two tracks cross. It is possible to locate the SMIRR track along the SIR-A swath using photographs taker by the SMIRR with two 16-mm cameras.

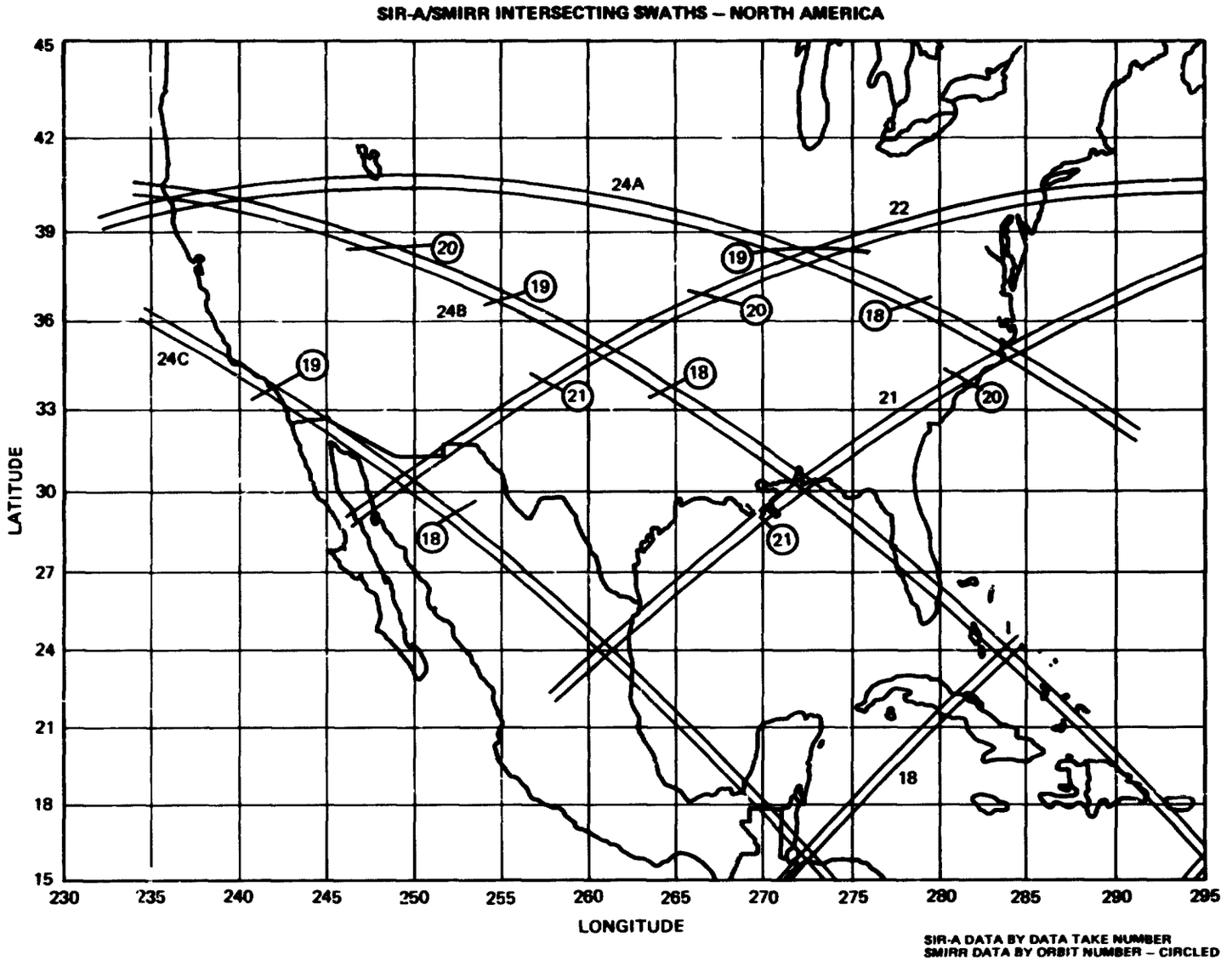

Figure 6-1(a)

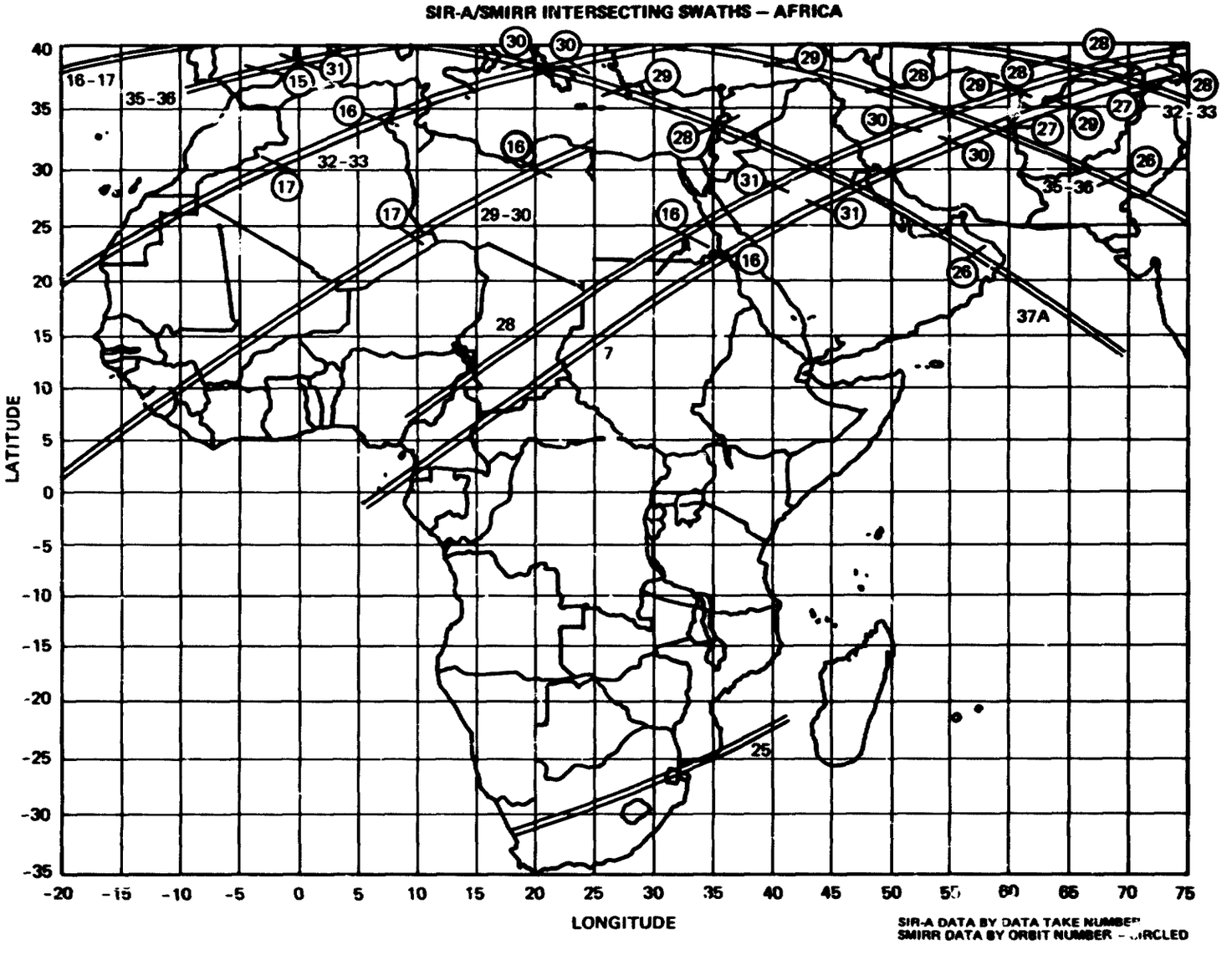

ORIGINAL PAGE IS
OF POOR QUALITY

Figure 6-1(b)

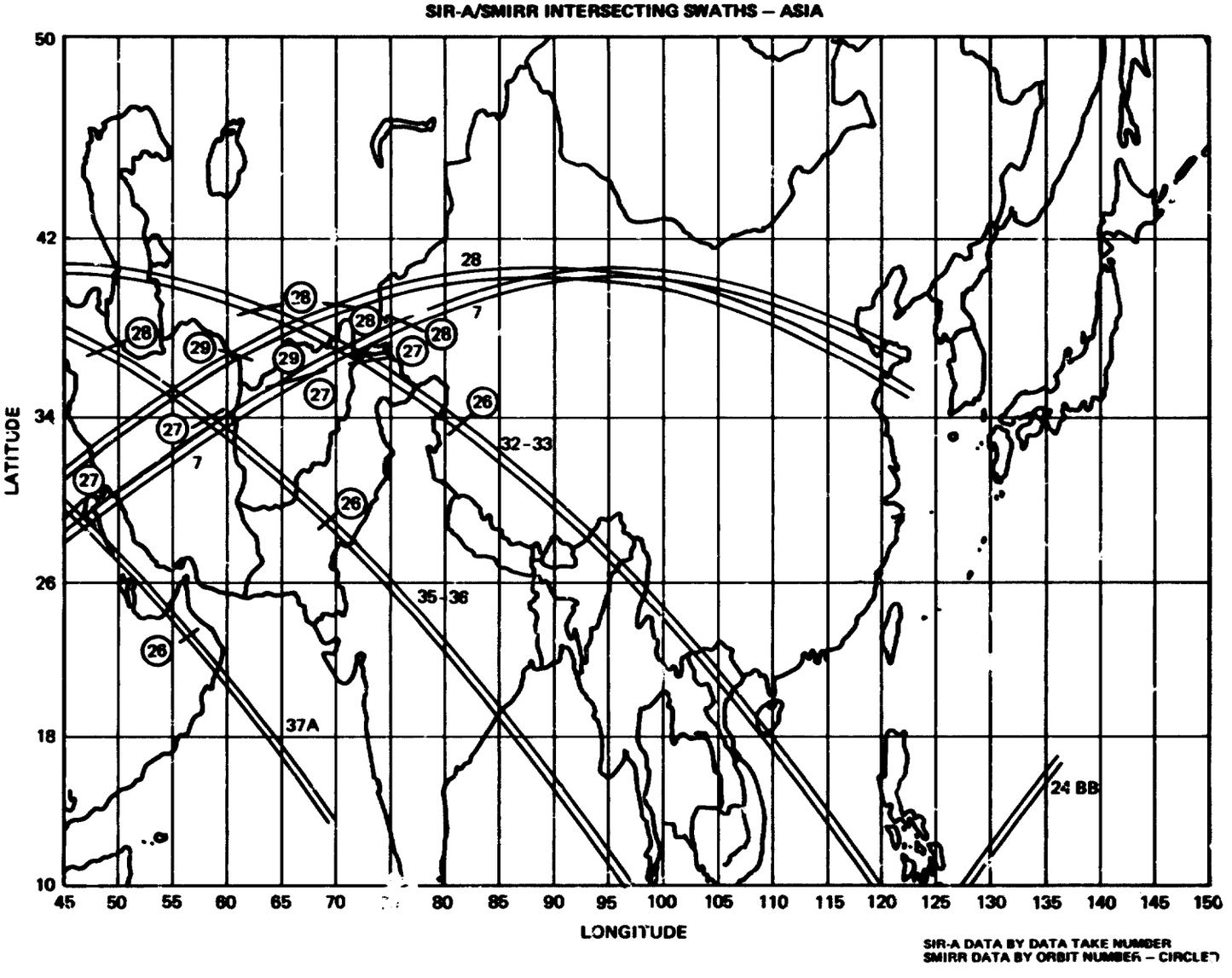

Figure 6-1(c)

SECTION VII

COVERAGE

Figures 7-1 through 7-8 show the coverage by continent in detail. The width of all swaths is 50 km and the length varies depending on the on/off times (Appendix A). Appendix B lists the latitude and longitude of the center of the swath in 1-min intervals for each data take.

C-3

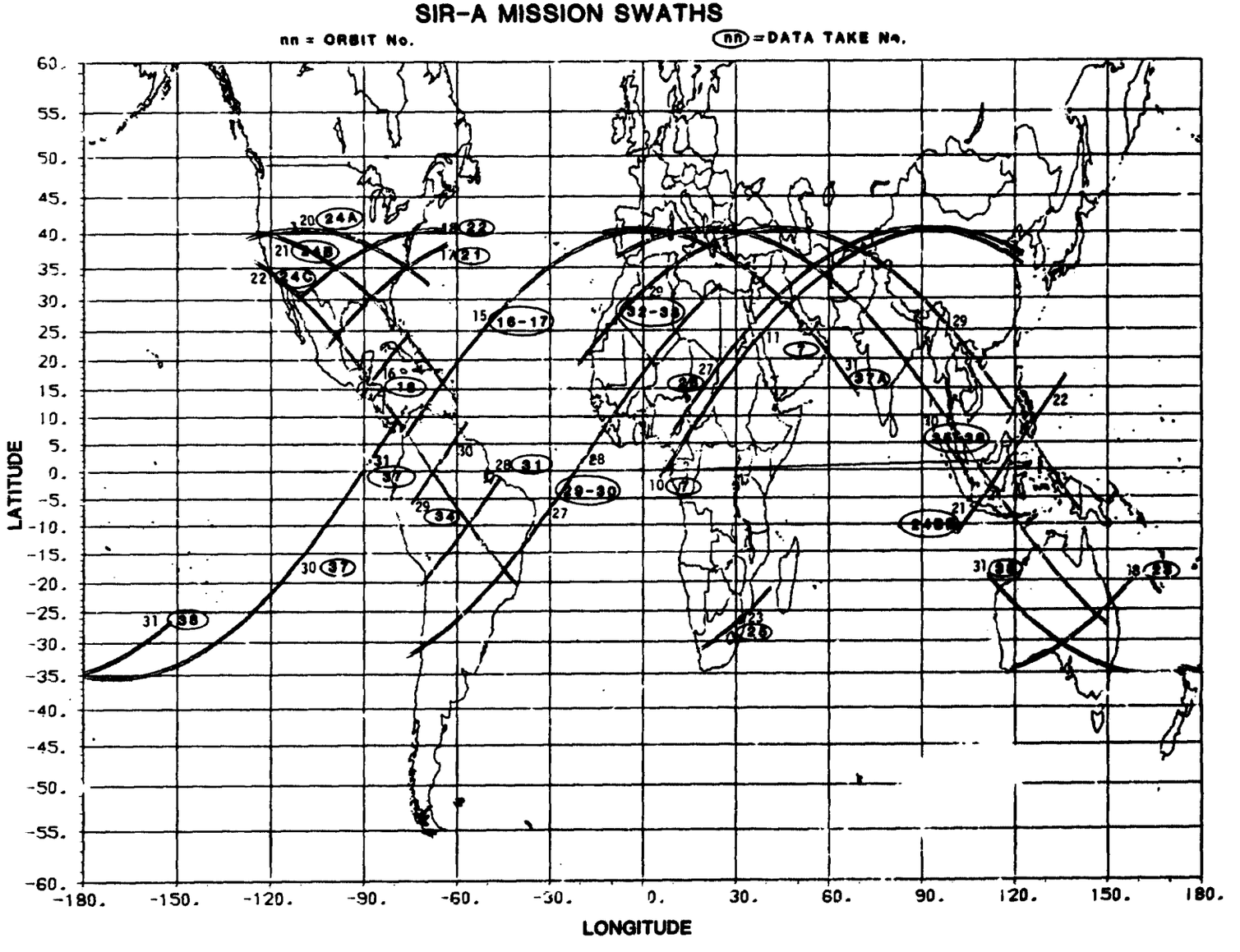

Figure 7-1

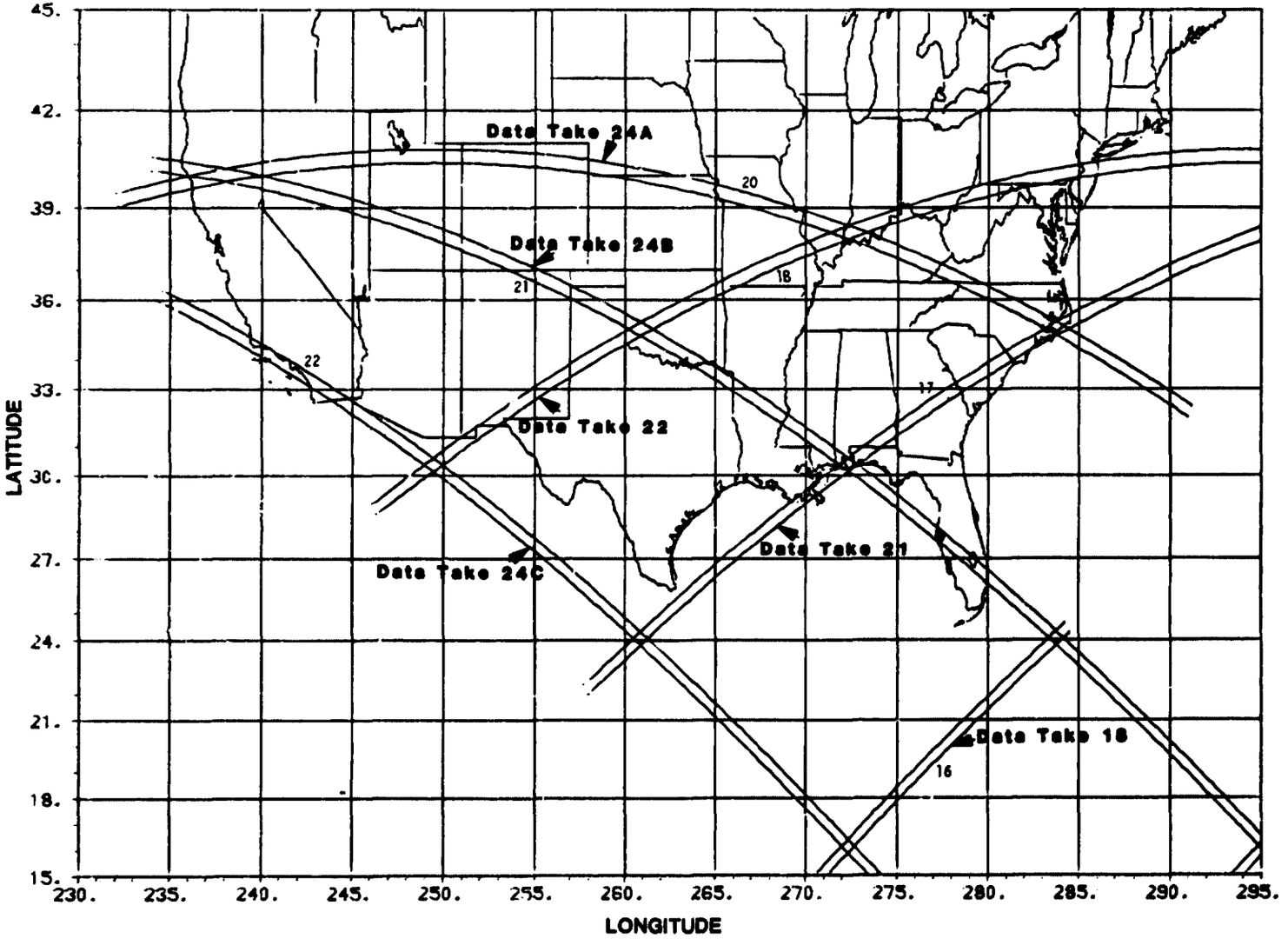

Figure 7-2

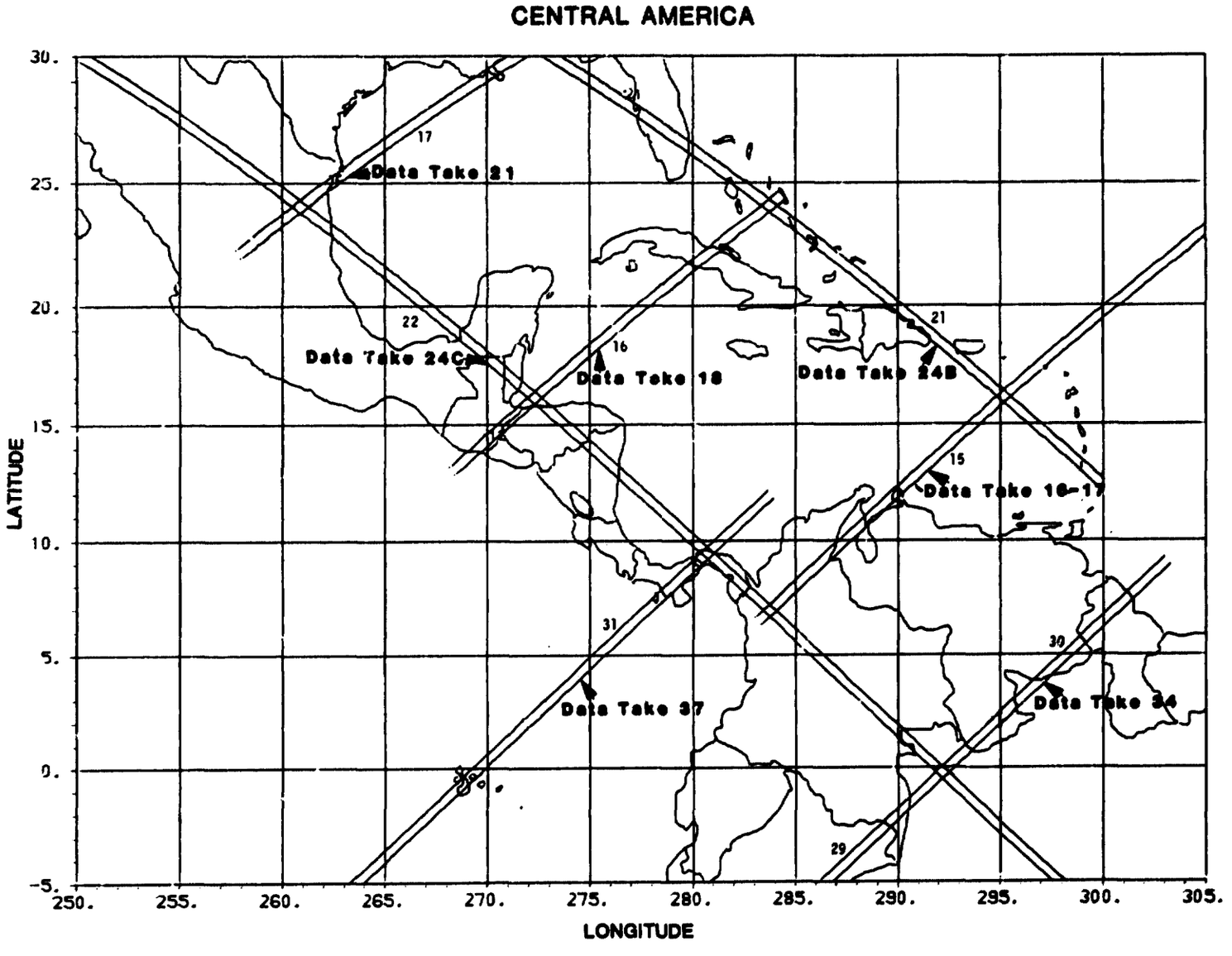

Figure 7-3

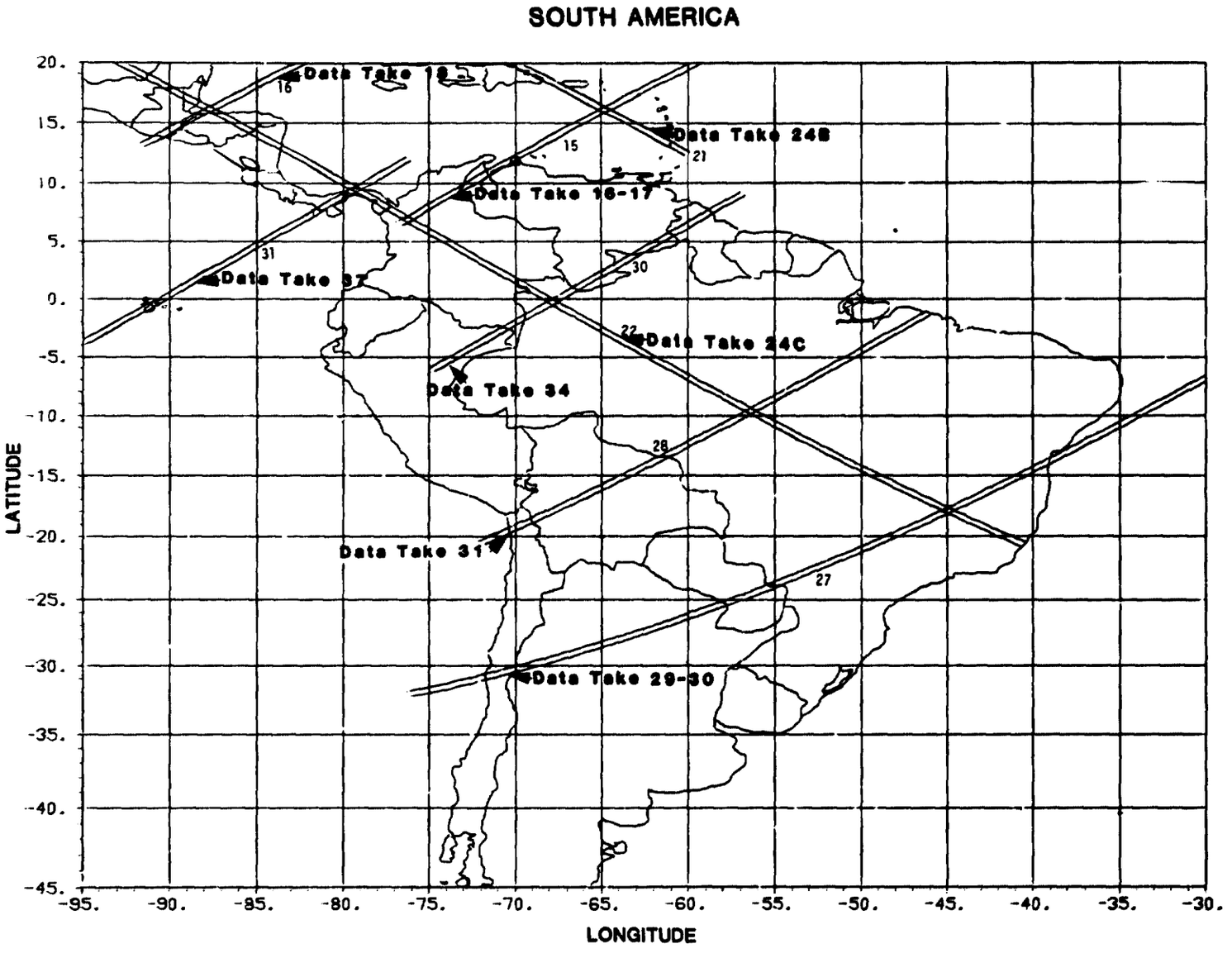

Figure 7-4

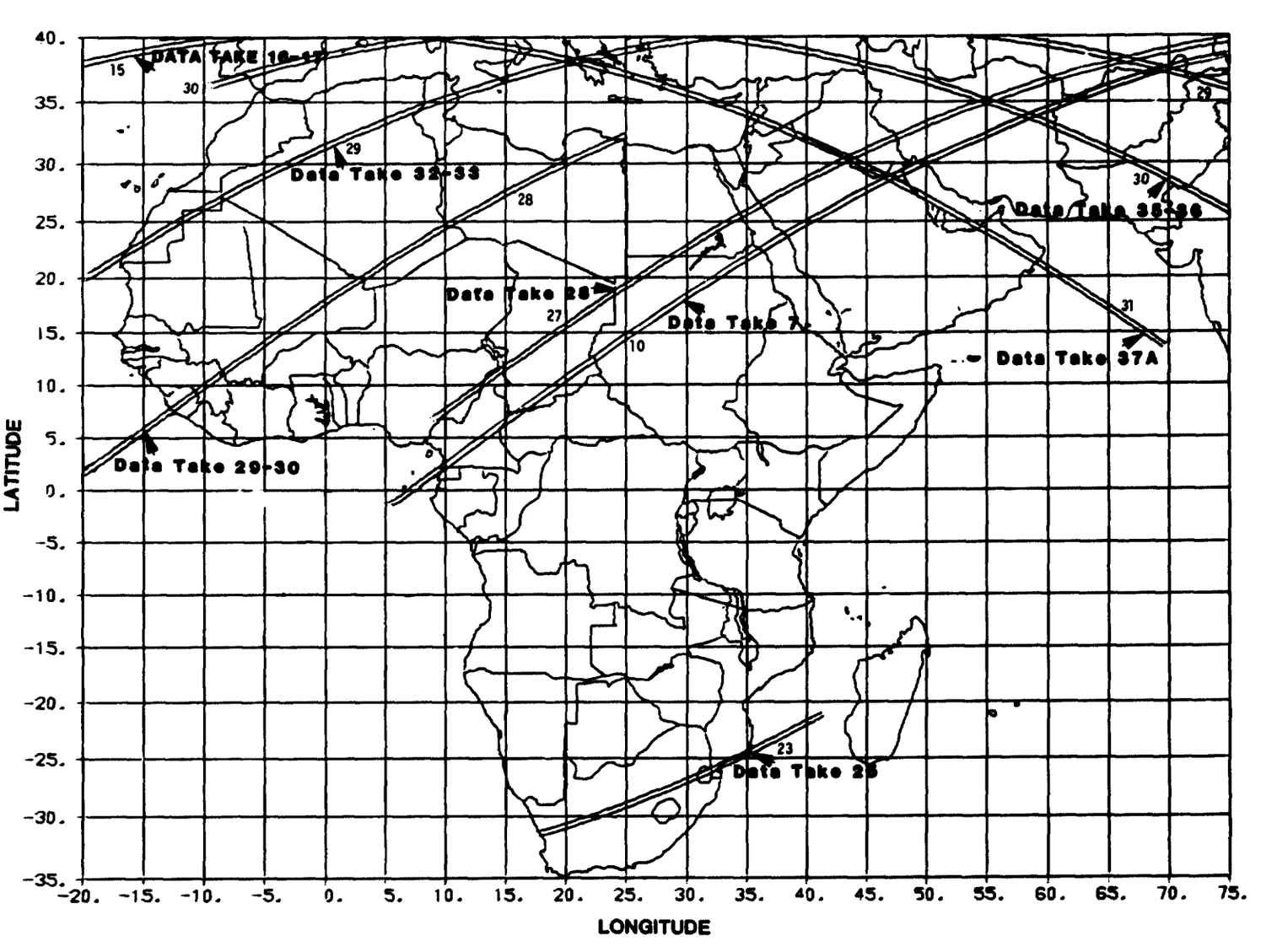

Figure 7-5

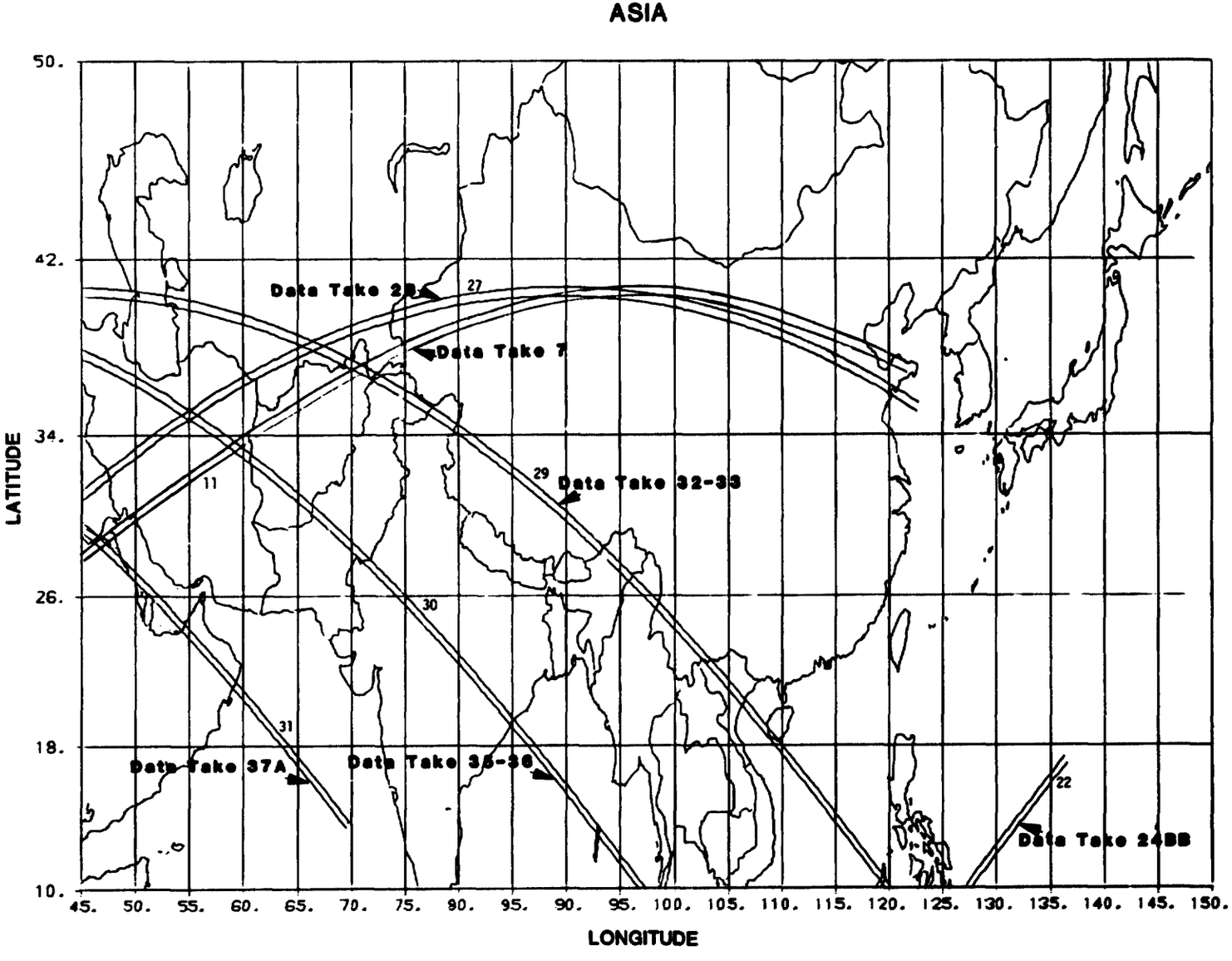

Figure 7-6

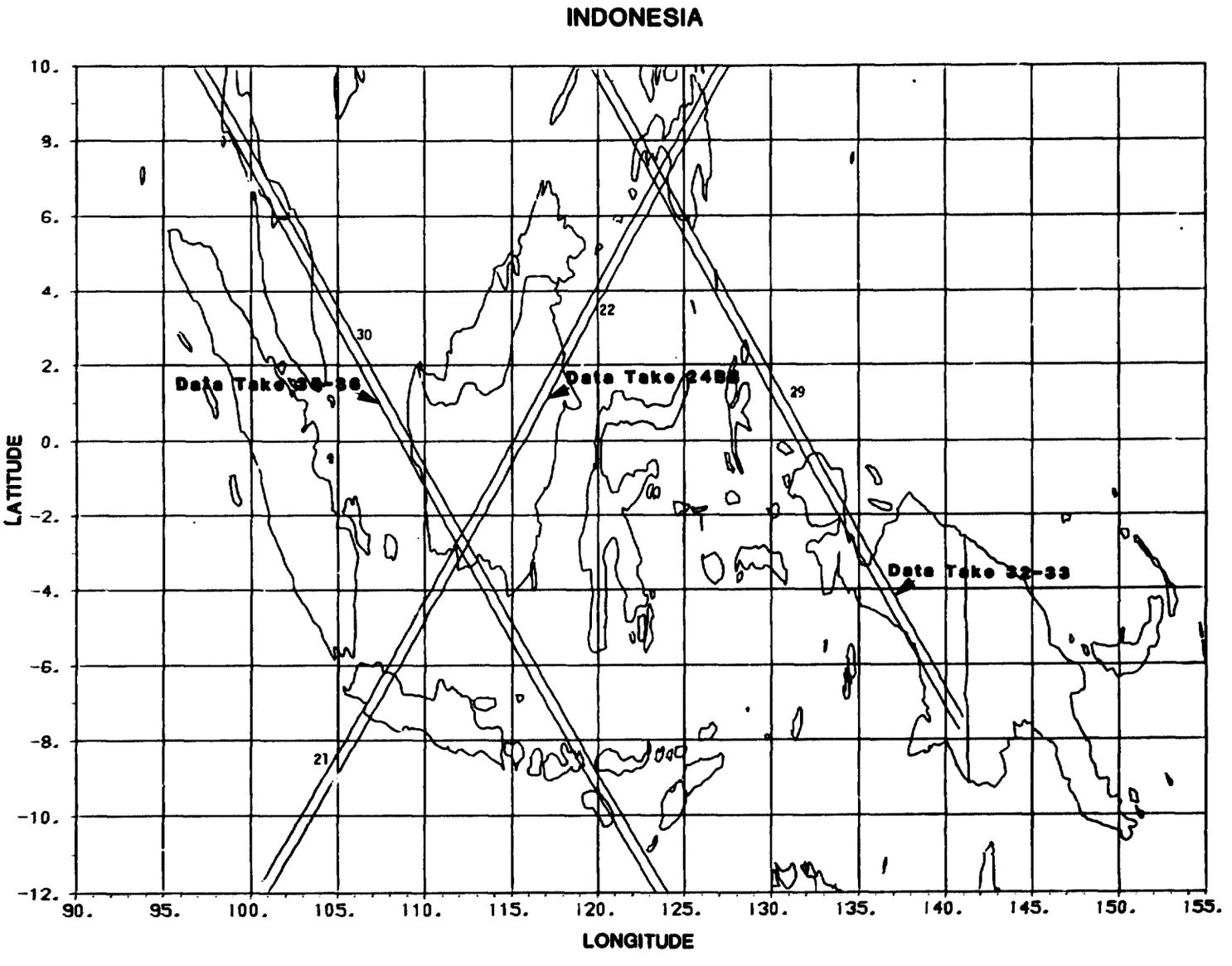

Figure 7-7

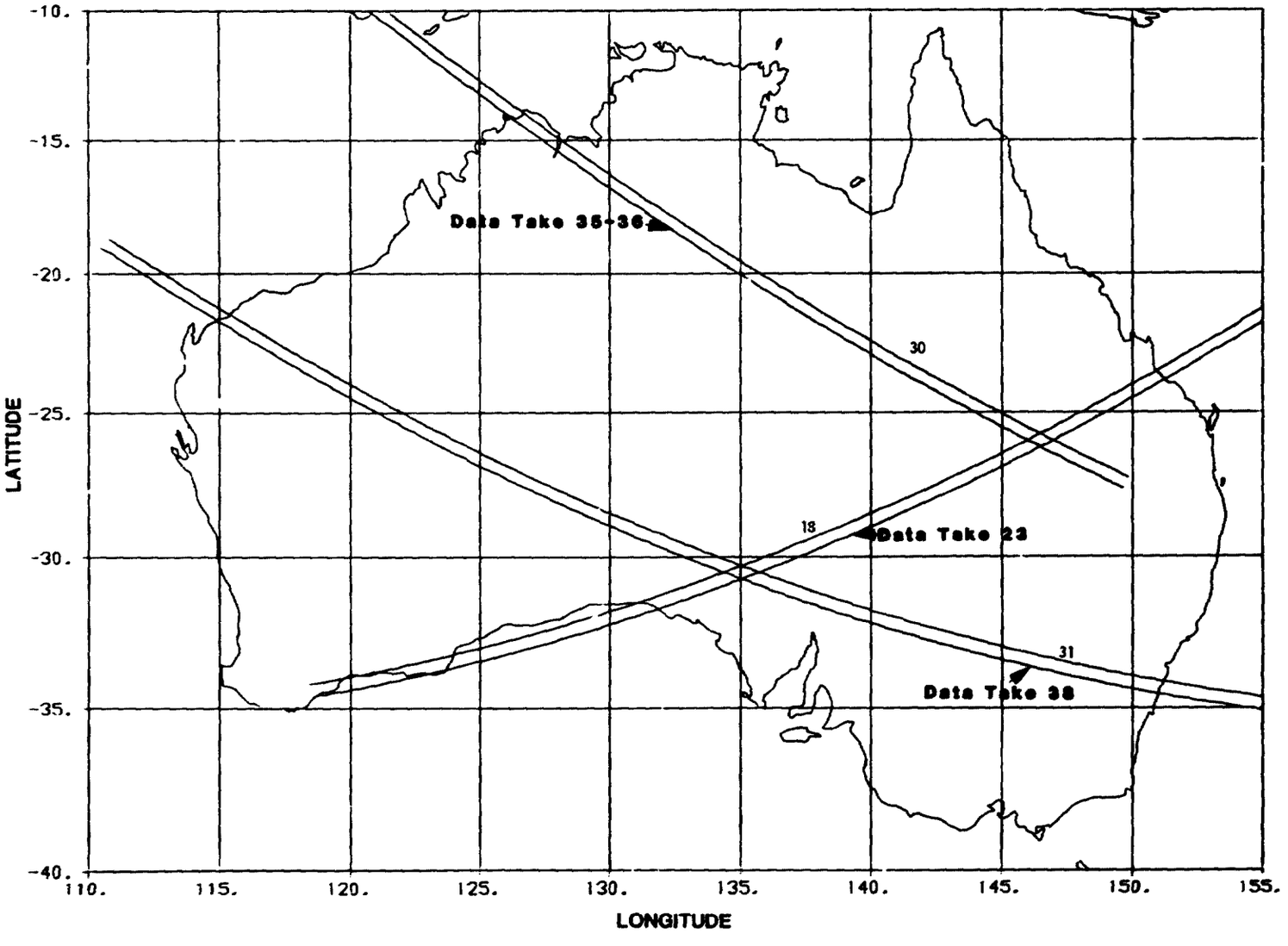

Figure 7-8

REFERENCES

Beadnell, H. J. L., (1909), An Egyptian Oasis (Kharga). London, p. 248.

Blom, R., and C. Elachi (1981), "Spaceborne and Airborne Imaging Radar Observations of Sand Dunes," J. Geophys. Res., Vol. 86, pp. 3061–3073.

Breed, C. S., (1977), "Terrestrial Analogs of the Hellespontus Dunes, Mars," Icarus, Vol. 30, pp. 326–340.

Breed, C. S., et al. (1979), "Regional Studies of Sand Seas Using ERTS (Landsat)," U.S. Geol. Sur. Prof. Paper, Chapter K, pp. 305–397.

Breed, C. S., M. J. Grolier, and J. F. McCauley (1979), "Morphology and Distribution of Common 'Sand' Dunes on Mars: Comparison With the Earth," J. Geophys. Res., Vol. 84, pp. 8183–8204.

Breed, C. S., and T. Grow (1979), "Morphology and Distribution of Dunes in Sand Seas Observed by Remote Sensing," U.S. Geol. Sur. Prof. Paper, Chapter J, pp. 253–303.

Defense Mapping Agency (1979), Operational Navigation Chart No. G2, Chott Merouane and Chott Melrhir Topographic Map, scale 1:1,000,000. Washington, D.C.

Dellwig, L. F., J. E. Bare, and R. L. Gelmett (1978), "SLAR--For Clear as Well as Cloudy Weather," Proceedings of the International Symposium on Remote Sensing for Observation and Inventory of Earth Resources and Endangered Environments, July 2-8, 1978, Freiburg, Fed. Rep. Germany, Int. Arch. Photogr., Vol. 3 of 22-7, pp. 1527–1546.

Elachi, C. E., (1980), "Spaceborne Imaging Radar: Geologic and Oceanographic Applications," Science, Vol. 209, pp. 1073–1082.

Elachi, C. C., et al. (1982), "Shuttle Imaging Radar (SIR-A) Experiment; Preliminary Results," Science (in press).

Elachi, C. C., L. Roth, and G. G. Schaber, "Radar Subsurface Imaging in Hyper-arid Regions," IEEE Ant. Prop. (in press).

Elder, C. H., P. W. Jeran, and D. A. Keck (1974), Geologic Structure Analysis Using Radar Imagery of the Coal Mining Area of Buchanan County, Va., Rpt. Inv., 7869, pp. 1–20. U.S. Bureau of Mines, Washington, D.C.

El Ramly, M. F., and M. H. Hermina (1978), Geologic Map of the Aswan Quadrangle, Egypt, scale 1:500,000, Egyptian Geological Survey/U.S. Geological Survey, Washington, D.C.

Engel, A. E. J., T. Dixon, and R. J. Stern (1980), "Late Precambrian Evolution of Afro-Arabian Crust From Ocean-Arc to Craton," Geol. Soc. Am. Bull., Vol. 91, pp. 699–706.

Engheta, N., and C. Elachi (1981), "Radar Scattering From a Smooth Surface With a Vegetative Layer Cover," in Proceedings of the IEEE International Geoscience and Remote Sensing Symposium, Vol. 1, pp. 631–635.

Falvey, D. A., (1974), "The Development of Continental Margins in Plate Tectonic Theory," Austral. Petrol. Explor. Assoc. J., Vol. 14, pp. 95–106.

Fryberger, S. F., (1979), "Dune Forms and Wind Regimes," U.S. Geol. Sur. Prof. Paper 1052, Chapter F, pp. 137–169.

Fullager, P. D., and J. K. Greenberg (1978), "Egyptian Younger Granites. A Single Period of Plutonism?" Precamb. Res., Vol. 6, p. A22.

Fulton, L. P., (1979), Structure and Isopach Map of the New Albany-Chattanooga-Ohio Shale (Devonian-Mississippian) in Kentucky: Eastern Sheet. Kentucky Geological Survey, Series XI. Lexington, Kentucky.

Gautier, E. F., and D. F. Mayhew (1935), Sahara--The Great Desert. Columbia University Press, New York, 280 pp.

Geologic Map of Northwestern Africa (Maroc-Algiers) (1952), sheet 1, scale 1:2,000,000. Published by the Organization Committee of the 19th International Geological Congress, Algiers.

Grolier, M. J., et al. (1980), "Yardangs of the Western Desert: in El Bazetah Journey to the Gilt Kebir and Uweinat," Geogr. J., Vol. 196, pp. 86–87.

Grove, A. T., (1970), "Rise and Fall of Lake Chad," Geogr. Mag., Vol. 42, No. 6, pp. 432–439.

Grove, A. T., and A. Warren (1968), "Quaternary Sand Forms and Climate on the South Side of the Sahara," Geogr. J., Vol. 134. No. 2, pp. 200–203.

Harris, L. D., and R. C. Milici (1977), "Characteristics of Thin-Skinned Style Deformation in the Southern Appalachians, and Potential Hydrocarbon Traps," U.S. Geol. Sur. Prof. Paper, Vol. 1018, pp. 1–40.

Hedin, S., (1905), "The Central Asian Deserts, Sand-Dunes, and Sands," in Scientific Results of a Journey in Central Asia, 1899-1902, Vol. 2, pp. 379–718. Swedish Army Lithographic Institute, Stockholm.

Hintze, L. F., and W. L. Stokes (1964), Geologic Map of Southeastern Utah, scale 1:250,000. Utah State Land Board, Salt Lake City, Utah.

Hussein, H. A., and I. A. El Kassas (1980), "Some Favorable Host Rocks for Uranium and Thorium Mineralization in the Central Eastern Desert of Egypt," Ann. Geol. Sur. Egypt, Vol. 10, pp. 879–908.

Instituto Geográfico Nacional (1970), Mapa Geológico de la Republica de Guatemala, scale 1:500,000. First edition. Guatemala.

Johnson, R. W., Jr. (1980), Residual Total Magnetic Map of Kentucky: Eastern Sheet, scale 1:250,000. Kentucky Geological Survey, Series XI. Lexington, Kentucky.

Krinsley, D. (1970), A Geomorphological and Paleoclimatological Study of the Playas of Iran: U.S. Geological Survey Final Science Report, Contract No. PRO CP 70-800; two vols., 486 pp. U.S. Geological Survey, Washington, D.C.

Krohn, M. D., et al., (1981), "Discrimination of a Chesnut-Oak Forest Unit for Geologic Mapping by Means of a Principal-Component Enhancement of Landsat Multispectral Scanner Data," Geophys. Res. Lett., Vol. 8, pp. 151–154.

McCauley, J. F., M. J. Grolier, and C. S. Breed (1977), "Yardangs," in Geomorphology in Arid Regions, Proceedings of the 8th Annual Geomorphology Symposium, Binghamton, N.Y., D. Doerling, editor. State University of New York, pp. 233–269.

McCauley, J. F., et al. (1982), "Subsurface Valleys and Geoarchaeology of Egypt and Sudan Revealed by Shuttle Radar," Science (in press).

McKee, E. D., (1966), "Structures of Dunes at White Sands National Monument, New Mexico," Sedimen., Vol. 7, No. 1, pp. 3–69 (special issue).

Muskat, J., personal communication, April 1981.

Nalivkin, D. V., (1973), Geology of the U.S.S.R. English translation by N. Rast. Oliver and Boyd, and U. of Toronto Press, Canada, p. 572–575.

National Oceanic and Atmospheric Administration (1980), Cape Hatteras Navigational Chart, scale 1:80,000. Washington, D.C.

Neary, C. R., I. G. Gass, and B. J. Cavanagh (1976), "Granitic Association of Northeastern Sudan," Geol. Soc. Am. Bull., Vol. 87, pp. 1501–1512.

Petrov, M. P., (1966), The Deserts of Central Asia: 1. Ordos, Ala Shan, and Peishan Desert. U.S. Department of Commerce Joint Publication Research Service, No. 39145, pp. 241–260.

Rogers, J., (1949), "Evolution of Thought on Structure of Middle and Southern Appalachians," Amer. Assoc. Pet. Geol. Bull., Vol. 33, No. 10, pp. 1643–1654.

Rogers, J. J. W., et al. (1978), "Varieties of Granitic Uranium Deposits and Favorable Exploration Areas in the Eastern United States," Econ. Geol., Vol. 73, pp. 1539–1555.

Schaber, G. G., G. L. Berlin, and W. E. Brown (1976), "Variations in Surface Roughness Within Death Valley, California: Geologic Evaluation of 25-m Wavelength Radar Images," Geol. Soc. Amer. Bull., Vol. 87, pp. 29–41.

Smith, H. T. U., (1965), Dune Morphology and Chronology in Central and Western Nebraska," J. Geol., Vol. 73, No. 4, pp. 557–578.

Stern, R. J., (1979), Late Precambrian Ensimatic Volcanism in the Central Eastern Desert of Egypt. Ph.D. Thesis, University of California San Diego, San Diego, California, 210 pp.

Stern, R. J., (1981), "Petrogenesis and Tectonic Setting of Late Precambrian Ensimatic Volcanic Rocks, Central Eastern Desert of Egypt," Precamb. Res., Vol. 16, pp. 195–230.

Stuckey, J. L., (1958), Geologic Map of North Carolina, scale 1:500,000. North Carolina Division of Mineral Resources.

Suslov, S. P., (1961), Physical Geography of Asiatic Russia. English translation by N. D. Gersheversky. W. H. Freeman and Co., London, San Francisco. 594 pp.

Tant, P. L., H. J. Byrd, and R. E. Horton (1974), General Soil Map of North Carolina, scale 1:1,000,000. U.S. Soil Conservation Service, Washington, D.C.

Trask, N. S., L. C. Rowan, and M. D. Krohn (1977), Lineament Map of Parts of Virginia, North Carolina, and South Carolina, scale 1:1,000,000. Open-file map MF 77-434. U.S. Geological Survey, Washington, D.C.

U.S. Geological Survey (1978), Middletown, North Carolina, Topographic Map, scale 1:24,000. Photo revision. Washington, D.C.

Waite, W. P., et al. (1981), "Wetland Mapping With Imaging Radar," IEEE Trans. Geosci. Elec., Vol. CE-9, No. 3, pp. 147–155.

Walker, A. S., (1982), "Deserts of China," Amer. Scien., Vol. 70, pp. 366–376.

Youssef, M. I., (1968), "Structural Patterns of Egypt and Its Interpretation," Am. Assoc. Petrol. Geol. Bull., Vol. 52, pp. 601–614.

Zhu, Z., W. Zheng, and L. Shu (1980), Zhongquo Shamo Gilumn (General Introduction to China's Deserts). Science Publishing House, Beijing, People's Republic of China, 117 pp. (In Chinese.)

APPENDIX A

SUMMARY OF RADAR PARAMETERS

Radar parameters, on/off times (in mission elapsed time), orbits, and continental coverage are listed for each data take. The mission elapsed time (MET) can be converted to GMT with the following equation:

1981 GMT = MET + 316 days + 15 h, 10 min, 10 s

Data Take	Orbit	Continent	Begin*	End*	Run Time	Alt. (n.m.)	STC	POSN	PRF	GAIN
7	10/11	AF/ASIA	0:14:43:09	0:15:12:17	1750	141.5	ON	18	1718	89
16-17	15/16	SA/ATLANTIC/EU	0:20:44:39	0:21:05:32	1253	140.8	OFF	15	1718	89
18	16	CA	0:22:16:54	0:22:21:47	293	140.0	OFF	15	1718	86
21	17	CA/US	0:23:50:15	1:00:01:20	665	141.4	ON	18	1718	89
22	18	US	1:01:23:00	1:01:34:00	660	142.1	ON	21	1718	89
23	18	AUST	1:02:21:45	1:02:31:15	570	141.8	ON	21	1718	89
24A	20	US	1:04:29:39	1:04:42:02	743	142.5	OFF	21	1670	86
24B	21	US	1:06:04:09	1:06:20:47	998	141.7	OFF	21	1718	86
24BB	21/22	INDON	1:07:04:09	1:07:16:02	713	139.0	OFF	15	1718	89
24C	22	US/SA	1:07:38:39	1:08:04:17	1538	141.6	OFF	21	1718	86
25	23	AF	1:09:52:54	1:09:57:02	248	141.7	OFF	21	1718	86
28	27	AF/ASIA	1:14:39:39	1:15:07:02	1643	140.6	ON	18	1718	89
29-30	27/28	SA/AFRICA	1:15:50:39	1:16:20:47	1808	140.4	OFF	18	1718	89
31	28	SA	1:17:27:09	1:17:35:32	503	139.4	ON	15	1718	89
32-33	29	AF/ASIA/INDON	1:17:43:54	1:18:25:32	2498	140.2	OFF	15	1718	86
34	29/30	SA	1:19:02:39	1:19:09:17	503	138.9	ON	15	1718	89
35-36	30	EU/ASIA/AUST	1:19:22:39	1:20:04:34	2515	141.2	OFF	18	1718	89
37	30/31	PACIFIC/CA	1:20:10:09	1:20:43:02	1973	138.8	ON	21	1770	89
37A	31	EU/ASIA	1:20:56:09	1:21:16:02	1119	141.3	ON	18	1718	95
38	31	AUST/PACIFIC	1:21:29:39	1:21:52:47	1388	141.0	ON	21	1718	89

*Accurate to 1 sec.

APPENDIX B

SWATH LOCATIONS

Latitude and longitude of the center of the radar swath and altitude of the Shuttle are listed for each data take in 1-min intervals. This data is based on the STS-2 post-OMS-4 ephemeris and should be regarded as preliminary.

Data Take: 7
Orbit: 10/11

Latitude	Longitude	MET* D	H	M	S	Altitude (N. Miles)
-1.49	5.38	0	14	43	00	139.51
0.99	8.29	0	14	44	00	139.50
3.48	11.20	0	14	45	00	139.52
5.98	14.13	0	14	46	00	139.58
8.46	17.08	0	14	47	00	139.68
10.94	20.70	0	14	48	00	139.81
13.39	23.11	0	14	49	00	139.97
15.81	26.22	0	14	50	00	140.16
18.18	29.39	0	14	51	00	140.38
20.51	32.66	0	14	52	00	140.61
22.78	36.01	0	14	53	00	141.87
24.98	39.49	0	14	54	00	141.13
27.09	43.08	0	14	55	00	141.41
29.10	46.81	0	14	56	00	141.68
30.99	50.68	0	14	57	00	141.95
32.76	54.68	0	14	58	00	141.22
34.40	58.84	0	14	59	00	142.47
35.87	63.14	0	14	0	00	142.70
37.17	67.59	0	15	1	00	142.91
38.31	72.18	0	15	2	00	143.10
39.24	76.88	0	15	3	00	143.25
39.96	81.69	0	15	4	00	143.37
40.48	86.57	0	15	5	00	143.46
40.75	91.51	0	15	6	00	143.51
40.82	96.48	0	15	7	00	143.52
40.65	101.42	0	15	8	00	143.49
40.27	106.35	0	15	9	00	143.43
39.65	111.20	0	15	10	00	143.33
38.84	115.96	0	15	11	00	143.20
37.82	120.59	0	15	12	00	143.03
37.51	121.67	0	15	12	15	142.98

*Accurate to 15 sec.

Data Take: 16-17
Orbit: 15/16

Latitude	Longitude	D	MET* H	M	S	Altitude (N. Miles)
6.75	-76.44	0	20	44	30	139.44
7.99	-74.97	0	20	45	00	139.49
10.46	-71.[illegible]	0	20	46	00	139.62
12.92	-68.[illegible]6	0	20	47	00	139.79
15.35	-65.87	0	20	48	00	139.98
17.73	-62.71	0	20	49	00	140.20
20.07	-59.46	0	20	50	00	140.44
22.35	-56.13	0	20	51	00	140.70
24.57	-52.67	0	20	52	00	140.97
26.69	-49.10	0	20	53	00	141.25
28.71	-45.40	0	20	54	00	141.54
30.63	-41.56	0	20	55	00	141.82
32.43	-37.58	0	20	56	00	142.09
34.10	-33.46	0	20	57	00	142.35
35.60	-29.18	0	20	58	00	142.60
36.95	-24.76	0	20	59	00	142.82
38.11	-20.20	0	21	0	00	143.01
39.08	-15.52	0	21	1	00	143.18
39.84	-10.72	0	21	2	00	143.31
40.39	-5.86	0	21	3	00	143.41
40.72	-0.92	0	21	4	00	143.47
40.83	4.02	0	21	5	00	143.50
40.76	6.52	0	21	5	30	143.49

Data Take: 21
Orbit: 17

Latitude	Longitude	D	MET* H	M	S	Altitude (N. Miles)
22.15	-102.17	0	23	50	15	140.66
24.36	-98.74	0	23	51	00	140.86
26.50	-95.18	0	23	52	00	141.14
28.54	-91.49	0	23	53	00	141.42
30.47	-87.66	0	23	54	00	141.70
32.28	-83.70	0	23	55	00	141.98
33.95	-79.57	0	23	56	00	142.24
35.47	-75.31	0	23	57	00	142.48
36.83	-70.91	0	23	58	00	142.71
38.01	-66.35	0	23	59	00	142.91
38.99	-61.69	0	0	0	00	143.08

*Accurate to 15 sec.

Data Take: 22
Orbit: 18

Latitude	Longitude	M E T* D	H	M	S	Altitude (N. Miles)
29.43	-112.63	1	1	23	00	141.49
31.31	-108.74	1	1	24	00	141.77
33.06	-104.70	1	1	25	00	142.04
34.66	-100.52	1	1	26	00	142.29
36.11	-96.19	1	1	27	00	142.53
37.39	-91.72	1	1	28	00	142.74
38.48	-87.11	1	1	29	00	142.93
39.37	-82.39	1	1	30	00	143.08
40.06	-77.57	1	1	31	00	143.20
40.53	-72.67	1	1	32	00	143.29
40.78	-67.72	1	1	33	00	143.34
40.80	-62.76	1	1	34	00	143.35

Data Take: 23
Orbit: 18

Latitude	Longitude	M E T* D	H	M	S	Altitude (N. Miles)
-34.35	119.61	1	2	21	45	142.46
-34.20	120.70	1	2	22	00	142.43
-33.33	125.22	1	2	23	00	142.29
-32.29	129.60	1	2	24	00	142.12
-31.09	133.84	1	2	25	00	141.92
-29.71	137.95	1	2	26	00	141.70
-28.19	141.93	1	2	27	00	141.47
-26.52	145.76	1	2	28	00	141.22
-24.74	149.47	1	2	29	00	140.97
-22.84	153.05	1	2	30	00	140.72
-20.83	156.53	1	2	31	00	140.47
-20.34	157.33	1	2	31	15	140.41

Data Take: 24A
Orbit: 20

Latitude	Longitude	M E T* D	H	M	S	Altitude (N. Miles)
39.67	-126.12	1	4	29	30	143.00
40.02	-123.69	1	4	30	00	143.06
40.50	-118.82	1	4	31	00	143.15
40.77	-113.87	1	4	32	00	143.21
40.81	-108.91	1	4	33	00	143.23
40.63	-103.95	1	4	34	00	143.21
40.21	-99.04	1	4	35	00	143.15
39.59	-94.19	1	4	36	00	143.06
38.74	-89.45	1	4	37	00	142.94
37.71	-84.81	1	4	38	00	142.78
36.48	-80.29	1	4	39	00	142.59
35.07	-75.92	1	4	40	00	142.38
33.51	-71.70	1	4	41	00	142.15
31.79	-67.63	1	4	42	00	141.91

*Accurate to 15 sec.

Data Take: 24B
Orbit: 21

Latitude	Longitude	D	M E T* H	M	S	Altitude (N. Miles)
40.46	-124.56	1	6	4	00	143.14
39.95	-119.67	1	6	5	00	143.07
39.22	-114.86	1	6	6	00	142.96
38.29	-110.17	1	6	7	00	142.83
37.16	-105.58	1	6	8	00	142.66
35.85	-101.13	1	6	9	00	142.47
34.37	-96.83	1	6	10	00	142.25
32.74	-92.68	1	6	11	00	142.02
30.96	-88.67	1	6	12	00	141.77
29.06	-84.81	1	6	13	00	141.51
27.05	-81.09	1	6	14	00	141.25
24.94	-77.49	1	6	15	00	140.99
22.75	-74.02	1	6	16	00	140.74
20.48	-70.66	1	6	17	00	140.50
18.15	-67.40	1	6	18	00	140.28
15.78	-64.22	1	6	19	00	140.07
13.36	-61.12	1	6	20	00	139.89
11.52	-58.84	1	6	20	45	139.78

Data Take: 24BB
Orbit: 21/22

Latitude	Longitude	D	M E T* H	M	S	Altitude (N. Miles)
-11.17	101.96	1	7	4	00	139.38
-8.80	104.97	1	7	5	00	139.22
-6.38	107.96	1	7	6	00	130.09
-3.94	110.90	1	7	7	00	139.00
-1.47	113.82	1	7	8	00	138.95
1.01	116.73	1	7	9	00	138.93
3.50	119.65	1	7	10	00	138.95
6.00	122.58	1	7	11	00	139.00
8.48	125.53	1	7	12	00	139.10
10.96	128.52	1	7	13	00	139.23
13.41	131.56	1	7	14	00	139.39
15.83	134.66	1	7	15	00	139.58
18.21	137.85	1	7	16	00	139.80

*Accurate to 15 sec.

Data Take: 24C
Orbit: 22

Latitude	Longitude	D	M E T* H	M	S	Altitude (N. Miles)
35.88	-124.19	1	7	38	30	142.45
35.18	-121.98	1	7	39	00	142.35
33.63	-117.77	1	7	40	00	142.13
31.94	-113.68	1	7	41	00	141.89
30.10	-109.74	1	7	42	00	141.64
28.15	-105.95	1	7	43	00	141.39
26.09	-102.28	1	7	44	00	141.13
23.94	-98.75	1	7	45	00	140.88
21.71	-95.33	1	7	46	00	140.63
19.42	-92.02	1	7	47	00	140.40
17.07	-88.79	1	7	48	00	140.19
14.66	-85.65	1	7	49	00	140.00
12.22	-82.58	1	7	50	00	139.83
9.76	-79.56	1	7	51	00	139.69
7.28	-76.60	1	7	52	00	139.59
4.79	-73.66	1	7	53	00	139.52
2.30	-70.73	1	7	54	00	139.48
-0.19	-67.82	1	7	55	00	139.48
-2.67	-64.91	1	7	56	00	139.51
-5.13	-61.98	1	7	57	00	139.58
-7.56	-59.02	1	7	58	00	139.68
-9.95	-56.03	1	7	59	00	139.81
-12.29	-52.98	1	8	0	00	139.96
-14.58	-49.87	1	8	1	00	140.14
-16.82	-46.68	1	8	2	00	140.34
-18.98	-43.41	1	8	3	00	140.56
-21.07	-40.03	1	8	4	00	140.79
-21.54	-39.20	1	8	4	15	140.85

Data Take: 25
Orbit: 23

Latitude	Longitude	D	M E T* H	M	S	Altitude (N. Miles)
-31.00	19.71	1	9	52	45	141.75
-30.71	20.71	1	9	53	00	141.69
-29.27	24.81	1	9	54	00	141.45
-27.70	28.74	1	9	55	00	141.19
-26.00	32.54	1	9	56	00	140.93
-24.18	36.21	1	9	57	00	140.66

*Accurate to 15 sec.

Data Take: 28
Orbit: 23

Latitude	Longitude	M E T* D	H	M	S	Altitude (N. Miles)
8.02	10.65	1	14	39	30	138.72
9.27	12.13	1	14	40	00	138.78
11.74	15.14	1	14	41	00	138.93
14.19	18.20	1	14	42	00	139.12
16.60	21.33	1	14	43	00	139.33
18.96	24.53	1	14	44	00	139.57
21.27	27.84	1	14	45	00	139.83
23.51	31.23	1	14	46	00	140.10
25.68	34.74	1	14	47	00	140.40
27.76	38.39	1	14	48	00	140.69
29.73	42.15	1	14	49	00	141.99
31.59	46.07	1	14	50	00	141.29
33.31	50.13	1	14	51	00	141.58
34.90	54.33	1	14	52	00	141.85
36.32	58.69	1	14	53	00	142.11
37.57	63.18	1	14	54	00	142.34
38.63	67.82	1	14	55	00	142.54
39.50	72.55	1	14	56	00	142.72
40.15	77.39	1	14	57	00	142.86
40.58	82.30	1	14	58	00	142.97
40.80	87.25	1	14	59	00	143.04
40.78	92.22	1	15	0	00	143.07
40.54	97.16	1	15	1	00	143.07
40.08	102.07	1	15	2	00	143.02
39.39	106.88	1	15	3	00	142.95
38.51	111.61	1	15	4	00	142.83
37.42	116.23	1	15	5	00	142.69
36.14	120.70	1	15	6	00	142.52
34.70	125.03	1	15	7	00	142.32

*Accurate to 15 sec.

Data Take: 29-30
Orbit: 27/28

Latitude	Longitude	D	M E T* H	M	S	Altitude (N. Miles)
-31.50	-73.42	1	15	50	30	141.55
-30.89	-71.32	1	15	51	00	141.44
-29.48	-67.22	1	15	52	00	141.19
-27.93	-63.26	1	15	53	00	140.94
-26.25	-59.45	1	15	54	00	140.67
-24.45	-55.77	1	15	55	00	140.40
-22.53	-52.21	1	15	56	00	140.13
-20.51	-48.76	1	15	57	00	139.86
-18.41	-45.41	1	15	58	00	139.61
-16.23	-42.17	1	15	59	00	139.37
-13.99	-39.00	1	16	0	00	139.16
-11.67	-35.91	1	16	1	00	138.97
-9.31	-32.88	1	16	2	00	138.80
-6.91	-29.89	1	16	3	00	138.67
-4.46	-26.94	1	16	4	00	138.58
-2.01	-24.01	1	16	5	00	138.52
0.48	-21.09	1	16	6	00	138.50
2.97	-18.18	1	16	7	00	138.52
5.46	-15.26	1	16	8	00	138.57
7.95	-12.32	1	16	9	00	138.67
10.43	-9.33	1	16	10	00	138.80
12.90	-6.30	1	16	11	00	138.97
15.32	-3.21	1	16	12	00	139.17
17.71	-0.04	1	16	13	00	139.40
20.05	3.20	1	16	14	00	139.65
22.33	6.54	1	16	15	00	139.92
24.54	10.00	1	16	16	00	140.21
26.66	13.57	1	16	17	00	140.51
28.59	17.27	1	16	18	00	140.81
30.62	21.10	1	16	19	00	141.11
32.42	25.08	1	16	20	00	141.41
33.65	28.16	1	16	20	45	141.59

Data Take: 31
Orbit: 28

Latitude	Longitude	D	M E T* H	M	S	Altitude (N. Miles)
-19.54	-70.04	1	17	27	00	139.68
-17.40	-66.75	1	17	28	00	139.44
-15.19	-63.55	1	17	29	00	139.21
-12.90	-60.41	1	17	30	00	139.01
-10.57	-57.35	1	17	31	00	138.83
-8.18	-54.34	1	17	32	00	138.68
-5.77	-51.37	1	17	33	00	138.57
-3.31	-48.43	1	17	34	00	138.49
-0.84	-45.51	1	17	35	00	138.45
0.41	-44.05	1	17	35	30	138.45

*Accurate to 15 sec.

Data Take: 32-33
Orbit: 29

Latitude	Longitude	D	M E T* H	M	S	Altitude (N. Miles)
20.54	-18.94	1	17	43	45	139.68
21.14	-18.09	1	17	44	00	139.75
23.38	-14.72	1	17	45	00	140.03
25.55	-11.21	1	17	46	00	140.32
27.63	-7.58	1	17	47	00	140.62
29.62	-3.81	1	17	48	00	140.93
31.47	0.09	1	17	49	00	141.23
33.21	4.13	1	17	50	00	141.52
34.81	8.34	1	17	51	00	141.80
36.24	12.68	1	17	52	00	142.06
37.50	17.17	1	17	53	00	142.30
38.57	21.79	1	17	54	00	142.51
39.45	26.53	1	17	55	00	142.69
40.12	31.35	1	17	56	00	142.84
40.56	36.26	1	17	57	00	142.95
40.79	41.21	1	17	58	00	143.03
40.79	46.17	1	17	59	00	143.07
40.56	51.12	1	18	0	00	143.07
40.11	56.03	1	18	1	00	143.03
39.44	60.86	1	18	2	00	142.95
38.57	65.59	1	18	3	00	142.84
37.49	70.21	1	18	4	00	142.70
36.22	74.69	1	18	5	00	142.53
34.80	79.03	1	18	6	00	142.34
33.20	83.23	1	18	7	00	142.12
31.46	87.28	1	18	8	00	141.89
29.60	91.18	1	18	9	00	141.65
27.62	94.93	1	18	10	00	141.40
25.54	98.57	1	18	11	00	141.14
23.36	102.07	1	18	12	00	140.89
21.12	105.46	1	18	13	00	140.65
18.80	108.75	1	18	14	00	140.43
16.44	111.94	1	18	15	00	140.22
14.04	115.07	1	18	16	00	140.03
11.59	118.12	1	18	17	00	139.87
9.12	121.12	1	18	18	00	139.73
6.63	124.09	1	18	19	00	139.63
4.14	127.01	1	18	20	00	139.56
1.65	129.94	1	18	21	00	139.52
-0.84	132.85	1	18	22	00	139.51
-3.32	135.76	1	18	23	00	139.54
-5.76	138.69	1	18	24	00	139.60
-8.18	141.67	1	18	25	00	139.70
-9.38	143.17	1	18	25	30	139.76

*Accurate to 15 sec.

Data Take: 34
Orbit: 29/30

Latitude	Longitude	M E T* D	H	M	S	Altitude (N. Miles)
-5.84	-74.33	1	19	2	30	138.53
-4.62	-72.86	1	19	3	00	138.49
-2.16	-69.92	1	19	4	00	138.43
0.32	-67.01	1	19	5	00	138.41
2.82	-64.09	1	19	6	00	138.43
5.33	-61.16	1	19	7	00	138.49
7.81	-58.16	1	19	8	00	138.58
10.27	-55.27	1	19	9	00	138.72
10.91	-54.48	1	19	9	15	138.76

*Accurate to 15 sec.

Data Take: 35-36
Orbit: 30

Latitude	Longitude	D	MET* H	MET* M	MET* S	Altitude (N. Miles)
37.44	-5.82	1	19	22	30	142.27
38.03	-3.52	1	19	23	00	142.38
39.01	1.13	1	19	24	00	142.58
39.79	5.92	1	19	25	00	142.75
40.35	10.79	1	19	26	00	142.88
40.69	15.72	1	19	27	00	142.98
40.82	20.68	1	19	28	00	143.03
40.70	25.64	1	19	29	00	143.05
40.38	30.56	1	19	30	00	143.04
39.82	35.44	1	19	31	00	142.98
39.05	40.23	1	19	32	00	142.89
38.08	44.91	1	19	33	00	142.77
36.91	49.46	1	19	34	00	142.61
35.58	53.88	1	19	35	00	142.43
34.06	58.16	1	19	36	00	142.22
32.40	62.28	1	19	37	00	142.00
30.60	66.26	1	19	38	00	141.76
28.68	70.09	1	19	39	00	141.51
26.64	73.79	1	19	40	00	141.26
24.53	77.36	1	19	41	00	141.01
22.32	80.81	1	19	42	00	140.76
20.03	84.15	1	19	43	00	140.53
17.70	87.39	1	19	44	00	140.31
15.31	90.55	1	19	45	00	140.11
12.88	93.64	1	19	46	00	139.93
10.43	96.67	1	19	47	00	139.78
7.95	99.65	1	19	48	00	139.66
5.46	102.60	1	19	49	00	139.57
2.96	105.53	1	19	50	00	139.51
0.47	108.43	1	19	51	00	139.49
-2.00	111.35	1	19	52	00	139.50
-4.47	114.27	1	19	53	00	139.55
-6.90	117.22	1	19	54	00	139.62
-9.31	120.21	1	19	55	00	139.73
-11.67	123.23	1	19	56	00	139.86
-13.97	126.33	1	19	57	00	140.02
-16.22	129.49	1	19	58	00	140.19
-18.41	132.73	1	19	59	00	140.39
-20.51	136.07	1	20	0	00	140.59
-22.52	139.52	1	20	1	00	140.80
-24.44	143.08	1	20	2	00	141.02
-26.24	146.76	1	20	3	00	141.23
-27.93	150.59	1	20	4	00	141.43
-28.69	152.55	1	20	4	32	141.53

*Accurate to 15 sec.

Data Take: 37
Orbit: 30/31

Latitude	Longitude	D	MET* H	M	S	Altitude (N. Miles)
-39.94	175.91	1	20	10	00	142.26
-40.44	-179.32	1	20	11	00	142.30
-35.53	-174.42	1	20	12	00	142.31
-35.59	-169.68	1	20	13	00	142.28
-35.44	-164.96	1	20	14	00	142.21
-35.07	-160.28	1	20	15	00	142.12
-34.51	-155.66	1	20	16	00	141.99
-33.73	-151.13	1	20	17	00	141.83
-32.77	-146.70	1	20	18	00	141.64
-31.64	-142.39	1	20	19	00	141.42
-30.32	-138.22	1	20	20	00	141.19
-28.87	-134.18	1	20	21	00	140.94
-27.26	-130.29	1	20	22	00	140.68
-25.52	-126.52	1	20	23	00	140.41
-23.67	-122.89	1	20	24	00	140.14
-21.72	-119.37	1	20	25	00	139.87
-19.67	-115.98	1	20	26	00	139.61
-17.52	-112.68	1	20	27	00	139.37
-15.31	-109.46	1	20	28	00	139.14
-13.04	-106.33	1	20	29	00	138.93
-10.71	-103.27	1	20	30	00	138.76
-8.32	-100.25	1	20	31	00	138.61
-5.91	-97.28	1	20	32	00	138.49
-3.46	-94.34	1	20	33	00	138.42
-0.98	-91.42	1	20	34	00	138.38
1.50	-88.50	1	20	35	00	138.37
4.00	-85.59	1	20	36	00	138.41
6.49	-82.65	1	20	37	00	138.49
8.98	-79.70	1	20	38	00	138.61
11.45	-76.70	1	20	39	00	138.76
13.90	-73.70	1	20	40	00	138.94
16.31	-70.52	1	20	41	00	139.16
18.68	-67.33	1	20	42	00	139.40
21.00	-64.04	1	20	43	00	139.66

*Accurate to 51 sec.

Data Take: 37A
Orbit: 31

Latitude	Longitude	D	M E T* H	M	S	Altitude (N. Miles)
40.54	-9.76	1	20	56	00	142.90
40.77	-4.82	1	20	57	00	142.98
40.80	0.14	1	20	58	00	143.02
40.58	5.09	1	20	59	00	143.02
40.14	10.00	1	21	0	00	142.98
39.48	14.84	1	21	1	00	142.91
38.62	19.58	1	21	2	00	142.81
37.55	24.20	1	21	3	00	142.67
36.31	28.69	1	21	4	00	142.50
34.88	33.04	1	21	5	00	142.31
33.29	37.24	1	21	6	00	142.09
31.57	41.30	1	21	7	00	141.86
29.71	45.21	1	21	8	00	141.62
27.73	48.99	1	21	9	00	141.37
25.66	52.61	1	21	10	00	141.12
23.49	56.13	1	21	11	00	140.87
21.25	59.53	1	21	12	00	140.63
18.94	62.82	1	21	13	00	140.40
16.58	66.02	1	21	14	00	140.19
14.17	69.15	1	21	15	00	140.00
11.73	72.21	1	21	16	00	139.83

Data Take: 38
Orbit: 31

Latitude	Longitude	D	M E T* H	M	S	Altitude (N. Miles)
-20.45	113.12	1	21	29	30	140.56
-21.46	114.80	1	21	30	00	140.67
-23.44	118.31	1	21	31	00	140.89
-25.30	121.93	1	21	32	00	141.10
-27.05	125.68	1	21	33	00	141.31
-28.67	129.55	1	21	34	00	141.51
-30.15	133.56	1	21	35	00	141.69
-31.48	137.73	1	21	36	00	141.86
-32.64	142.00	1	21	37	00	142.00
-33.63	146.42	1	21	38	00	142.12
-34.42	150.94	1	21	39	00	142.21
-35.02	155.55	1	21	40	00	142.26

*Accurate to 15 sec.

7:82:13